THE UNIVERSITY *of* EDINBURGH

This thesis has been submitted in fulfilment of the requirements for a postgraduate degree (e.g. PhD, MPhil, DClinPsychol) at the University of Edinburgh. Please note the following terms and conditions of use:

This work is protected by copyright and other intellectual property rights, which are retained by the thesis author, unless otherwise stated.
A copy can be downloaded for personal non-commercial research or study, without prior permission or charge.
This thesis cannot be reproduced or quoted extensively from without first obtaining permission in writing from the author.
The content must not be changed in any way or sold commercially in any format or medium without the formal permission of the author.
When referring to this work, full bibliographic details including the author, title, awarding institution and date of the thesis must be given.

Wave loadings and scaling effects on and within an Oscillating Water Column (OWC) caisson breakwater

Krisna Adi Pawitan

PhD Energy Systems – The University of Edinburgh – 2019

Table of Contents

Figures

Declaration

I declare that the thesis has been composed by myself and that the work has not be submitted for any other degree or professional qualification. I confirm that the work submitted is my own, except where work which has formed part of jointly-authored publications has been included. My contribution and those of the other authors to this work have been explicitly indicated below. I confirm that appropriate credit has been given within this thesis where reference has been made to the work of others.

The work presented in Chapter 4 was previously published in Coastal Engineering as A loading model for an OWC caisson based upon large-scale measurements by Krisna A. Pawitan (student), Aggelos S. Dimakopoulos, Diego Vicinanza, William Allsop, Tom Bruce (PhD supervisor). This study was conceived by all of the authors. I carried out the data analysis, the new prediction model proposal and validation, and the manuscript preparation and submission.

Okinawa, 20 August 2019

Krisna Adi Pawitan

PhD student

Declaration

I declare that the thesis has been composed by myself and that the work has not be submitted for any other degree or professional qualification. I confirm that the work submitted is my own, except where work which has formed part of jointly-authored publications has been included. My contribution and those of the other authors to this work have been explicitly indicated below. I confirm that appropriate credit has been given within this thesis where reference has been made to the work of others.

The work presented in Chapter 4 was previously published in Coastal Engineering as A loading model for an OWC caisson based upon large-scale measurements by Krisna A. Pawitan (student), Aggelos S. Dimakopoulos, Diego Vicinanza, William Allsop, Tom Bruce (PhD supervisor). This study was conceived by all of the authors. I carried out the data analysis, the new prediction model proposal and validation, and the manuscript preparation and submission.

Okinawa,

Krisna Adi Pawitan

PhD student

Lay Summary

In this ever-advancing world, the need for energy is expected to keep growing. Unfortunately, many current energy sources are not sustainable, especially with their associated CO_2 emission which one of the main causes of global warming. This emphasises the importance of supporting renewable energy sources to help with the energy generation needed. Among many recognised greener energy sources, wave remains one of the biggest in terms of resource availability, but still one of the least developed or utilised because of the engineering challenges of such harsh environment. There are many types of wave energy converter (WEC). The oscillating water column (OWC) has advantages due to its simplicity and low maintenance cost. The OWC-WEC uses a water column partially trapped inside a chamber with a power take-off system attached. As the waves rise and fall outside the OWC, the water column inside the chamber oscillates up and down and drives the air out of and in to the chamber through the power take-off system.

The development of OWC – WEC started around 1965 with the development of oscillating water columns to power wave buoys for navigation. Developments since have led to OWC pilot projects including: LIMPET- a wave power plant in Scotland, the Pico power plant in Azores, and the Mutriku wave energy plant in Spain. LIMPET proved that wave energy is a reliable source by operating for about 95% of its life time, however, LIMPET produced less than half of its expected performance, and both Mutriku and Pico plants structural problems during construction and operation. These experiences emphasise the uncertainty in the design process of this type of structure.

This thesis tries to tackle two major problems in the OWC when integrated in a vertical breakwater. The first one is related to the forces experienced inside the chamber. The model developed in this thesis enables the prediction of the chamber pressure generated and the wave force acting on the rear wall of the chamber. In order to validate the proposed model, data from a large-scale physical model experiment is explored. For the wave forces on the front of the OWC, new experiments prove that existing methods for conventional vertical breakwaters can be used for this type of structure with certain modification.

Prior to the prototype deployment on the actual site, OWC devices are developed, partly based upon lab experiments to check the performance of the device. The second uncertainty explored in the thesis is related to the scaling effect for a small-scale physical model testing in a laboratory. The scaling method used to scale down the structure dimension will work well in scaling wave effects but won't scale down the air characteristics inside the chamber correctly. The experiment is done by comparing the large-scale physical model measurement with the small-scale physical model results. This thesis showed that the small-scale tests will give information on pressure and forces which is comparable to, but on the safe side of those pressure and forces measured at large-scale.

The thesis results can reduce the uncertainty in an OWC-WEC installed vertical breakwater and push the development of the wave energy harvesting device.

Abstract

Even though wave energy has been established as one of the biggest sustainable energy sources over the last 70 years, the development of the wave energy harvesting device is proven to be challenging. Many types of wave converter device have been developed in the past to bring in some of this ocean energy while surviving the harsh conditions of the site. Among many types of wave energy converter invented, the Oscillating Water Column (OWC) has advantages due to its simplicity and low maintenance cost. Several OWC types have been designed and deployed from 1965 to date with many lessons learned. Most of deployed OWC designs, however, have focused on small, stand-alone structures. This thesis is focused on an OWC type wave energy converter (WEC) integrated in a vertical breakwater. This way, the OWC device can be placed in a very energetic location where a breakwater is most likely located. The integration of an OWC into the design of a new breakwater, furthermore, provides the opportunity for cost sharing between energy generation and coastal defence function.

This thesis aims to fill two knowledge gaps in methods for the design of breakwater integrated OWCs. The first one is the wave load uncertainty of the device. There is an extensive literature for conventional vertical breakwaters. There are, however, few studies for the OWC installed one. This thesis proposes a new wave load model for the inner chamber of an OWC. The model can be used to estimate the wave loads acting on the rear wall and the ceiling inside the caisson chamber. The model considers three conditions of the OWC chamber: the closed chamber condition, the fully open condition, and the operating condition. Both regular and irregular waves are considered. The model is validated by means of large-scale experimental data from the 2014 “GKW OWCs” project in the Large Wave Flume (GWK) facility in Hannover, Germany. The validation was done for the three chamber conditions. The model was successful in predicting the in-chamber pressure generated, rear wall landward force, and vertical force. It predicted to within a factor of 1.2 for the lower wave steepnesses and over-predicted the forces for the higher wave steepnesses with a more conservative agreement factor between 0.4 to 0.7. Furthermore, the number of front wall impact events comparison between the physical model observation and the existing conventional vertical breakwater probabilistic design tools show that the existing tools

can be used for the OWC installed vertical breakwater impact probability in the irregular wave condition.

In addition to the wave load prediction, this thesis also investigates the water column behaviour inside the chamber over various wave conditions for both regular and irregular waves. In particular, "sloshing" is explored where the water column behaviour is not according to the idealised piston movement. The conditions under which 'sloshing' is likely to occur have been characterised by means of in-chamber video. Impact pressure measurements of up to 12 $\rho g H_{mo}$ have been measured by means of pressure transducers within the chamber. Three different types of in-chamber wave impacts have been identified, characterised, and quantified: single impact, successional impact, and whole water column impact.

The second major contribution the thesis addresses is the scaling effect related to physical model testing of this kind of wave energy converter in a laboratory environment. Unlike common breakwater, an OWC includes an air chamber inside the structure. Froude scaling used for the scaled-down experiment in coastal structure only maintains the gravitational force and the inertia ratio between the prototype and the physical model. Consequently, Froude scaling is not sufficient to scale the influence of air stiffness in the OWC chamber correctly. A series of small-scale physical model of 1:79 to the prototype design of an OWC installed vertical breakwater experiment was done in the long wave flume in the University of Edinburgh. These experiments were designed to be as faithful a scaled down version of the large-scale GWK tests as possible, for both the dimensions of the structure and the wave conditions tested. This is done in order to facilitate the most direct comparison between the small-scale and large-scale experimental results. It can be concluded based on the chamber pressure comparison that on the optimum operating condition, the smaller scale physical model will over-estimate the pressure recorded in the large-scale by a factor of about 2.45. Similar results are obtained for both closed chamber and fully-open chamber conditions.

This thesis is expected to reduce the uncertainty in the design of breakwater integrated OWC by enabling the in-chamber loading estimation and more representative small-

scale physical model test in a laboratory. By reducing these uncertainties, the wave energy harvesting development could be push forward.

Acknowledgement

I would like to thank my advisors, Prof. Tom Bruce and Prof. William Allsop for the endless support and patients during my PhD study since the very first day. Without their guidance during the research and writing of this thesis, I will not be able to finish it and achieve what I have done today. I could not have imagined having a better advisor and mentor for my PhD study.

Besides my advisors, I would like to thank the rest of my thesis committee: Prof. Peter Troch and Prof. David Ingram for not only their insightful comments and encouragement, but also for the hard questions intended to deepen my analysis on my PhD project.

My sincere thanks also go to my fellow fighters: Duncan, Paul, Dan, and Rodrigo for the constructive discussion that we had and their usefull advice during the last four years of my study.

I would also like to thank Indonesia Endowment Fund for Education (LPDP) for the funding support during the four years of my study.

Last but not the least, I would like to say thank you for the endless morale support during my study and life in general to my lovely fiancé, Shirley Damian, my father and mother, Cipto Pawitan and Mijanti, and sister, Yosi.

Nomenclature

A_c	oscillating water column (OWC) chamber area
α_{bot}	rear wall chamber wave pressure at the bottom
α_{swl}	rear wall chamber wave pressure at still water pressure (swl)
A_o	OWC orifice area
$(B_c)_{wc}$	wave dissipating chamber width
β	angle between wave direction and a line normal to breakwater
C_r	wave reflection coefficient
d	in-chamber water depth
ΔE	current difference in sensors measurement
Δh	water elevation difference
Δp	pressure measured difference
D_{Ba}	air volume thickness in original Bagnold number
D_i	impact air volume thickness
D_{ori}	chamber orifice diameter
F_{goda}	force prediction using Goda formulae
F_i	impact force
$F_{i,max}$	impact force maximum
F_{meas}	measured wave force
F_{rw}	transmitted force
g	gravity acceleration
γ	JONSWAP peak enhancement factor
h	water depth
H	wave height
h_b	water depth at 5H seaward of the structure
H_{bc}	breaking wave height
H_{bs}	broken wave height
h_c	OWC/wave dissipating wave chamber height
H_{si}	incident wave height
H_{m0}	significant wave height
H_{max}	maximum wave height

h_s	fore-slope height
H_{tr}	transmitted wave height
k_{Ba}	height of effective water mass
k_i	height of impacting water mass
K_t	wave transmission coefficient
L	wave length
λ	scaling adjustment factor
L_{pi}	peak wave period wave length in irregular waves
N	total number of pressure transducers
η	elevation to which wave pressure is exerted
η_{tr}	elevation to which transmitted wave pressure is exerted
Ω	compression number
ρ_w	water density
P	proportion coefficient
$p_{1/250}$	average of the four highest pressure measured in an individual event
p_1	prediction of non-impulsive pressure on breakwater at swl
p_3	prediction of non-impulsive pressure on breakwater at the bottom
P_b	percentage of wave passed the non-breaking-to-breaking wave height
p_{Ba}	predicted peak air pressure
p_c	OWC chamber peak air pressure measurement
$(p_c)_{wc}$	wave dissipating chamber peak air pressure
$P_{i\%}$	probability of impact
$p_{i,max}$	impact pressure maxima
$(p_{max})_{Ba}$	prediction of the impact pressure maxima
$(p_{max})_m$	model impact pressure maxima
$(p_{max})_p$	prototype impact pressure maxima
p_n	pressure measured at n
p_o	atmospheric pressure
s_c	length ratio between model and prototype
s_w	wave steepness
t	time
T	wave period

t^*	relative time over wave period (t/T)
t_d	impact duration
$t_{i,max}$	time of the impact maxima occurrence
T_p	significant wave period
t_r	impact rise time
u_o	OWC water column impinging velocity
$(u_o)_{wc}$	wave dissipating chamber's water column impinging velocity
v_m	model air chamber volume
v_p	prototype air chamber volume
w	front wall penetration factor
x	varying air volume thickness
X_n	location of the pressure transducer n

1 Introduction

1.1 Background research and rationale

Even though wave energy has been established as one of the biggest potential sustainable energy sources over the last 70 years, the development of wave energy harvesting devices has proven to be challenging. Many types of wave energy converters (WECs) have been developed to harvest some of this ocean energy while surviving the harsh conditions of the site. There are many types of wave energy converter developed to date, among them the most researched are wave attenuator, point absorber, wave overtopping, and Oscillating Water Column (OWC). Wave attenuator is a floating WEC which generate energy from relative motion between two arms of the device, while point absorber utilised floating buoy which connected to a energy extraction mechanism. One of the advantages of wave attenuator is that the device can be directed toward the incoming wave for maximum efficiency, while point absorber can absorb wave energy from all direction. These types of WECs, however, are relatively difficult to be combined with other coastal structures such as breakwater, need to be positioned further from the coastline, and require additional effort for maintenance, such as towing to near-shore position.

Wave overtopping device collects overtopping water due to wave action inside a water reservoir and then channelled it back into the ocean through a power take-off mechanism. An OWC device, on the other hand, utilises the wave oscillation motion to force a volume of air to move into and out of the OWC chamber via a power take-off system (will be described further in Sub-chapter 2.2). Both wave overtopping devices and Oscillating Water Column (OWC) devices have advantages due to their simplicity, their shoreline or near-shore location, low maintenance cost, and their ability to be combined with breakwater. Recent finding, however, showed that the wave overtopping device may increase the overtopping rate to the area behind breakwater compared to a traditional breakwater (Vicinanza *et al.*, 2014). Due to these reasons, this thesis focuses on an Oscillating Water Column type WEC.

Several OWC types have been designed and deployed from 1965 to date with many lessons learned. Most of deployed OWC designs, however, have focused on small,

stand-alone structures. This thesis is focused on an OWC type wave energy converter (WEC) integrated in a vertical breakwater. This way, the OWC device can be placed in a very energetic location where a breakwater is most likely located. The integration of an OWC into the design of a new breakwater, furthermore, provides the opportunity for cost sharing between energy generation and coastal defence function.

OWC-WEC pilot projects including: LIMPET-a wave power plant in Scotland, Pico power plant in Azores, and Mutriku wave power plant in Spain. The Land Installed Marine Power Energy Transmitter or LIMPET for short was the Scotland's first full scale operating OWC-WEC. The device was operating in the Isle of Islay and developed by the Queen's University of Belfast. The device was designed to produce 500 kW of electricity and managed to operate 98% of its lifetime (The Queen's University of Belfast, 2002). It only produced, however, up to around 40% of its original designed capacity during peak production.

Pico power plant in the Azores on the Island of Pico, is a standalone single chamber OWC structure pilot project which construction started in 1992 and concluded in 1999. Unfortunately, most recent press release by the WavEc, the current owner of plant, revealed the partial collapse of the plant after 19 years of operation (WavEc – Offshore Renewables, 2018). The plant faced structural deficiencies during its operation time, especially in the sub-merged part of the plant, and WavEc finally suspended its operation in January 2017, despite of the combined effort between WavEc and the Azores Regional Government to recover the structure of the plant. Even though designed to survive longer than 19 years, the wave loads, and wave impacts may contribute greatly in the deterioration of the structure.

To date, the most ambitious OWC-WEC project is the Mutriku wave energy power plant which is the world's first grid connected OWC integrated breakwater in the port of Mutriku, Basque Country, Spain. Although fully operated since 2012, the plant suffered major storm damage during construction in 2009, resulting in a 2 to 3-year delay in the project. Four of the totals 16 OWC chambers which installed inside the breakwater were damaged. Figure 1 shows two of the four caissons which damaged by the storm. The OWC chamber opening is locate below the water surface and cannot be seen in the picture as shown by the diagram. As can be seen, the chamber on the

right hand side had a layer of the front wall disintegrated while the chamber on the left had the entire front wall “flown away”, exposing the in-chamber wall of the OWC caisson as explained by the red circle.

Figure 1 Damaged chamber in Mutriku Wave energy power plant during construction. The OWC chamber opening is locate below the water surface as demonstrated by the diagram (dotted line indicates the still water level). The chamber on the right hand side had a layer of the front wall disintegrated while the chamber on the left had the entire front wall “flown away”, exposing the in-chamber wall of the OWC caisson.

A more detailed exploration of LIMPET, Mutriku wave energy power plant, and Pico power plant can be found in Chapter 2.

The recent partial failures in Mutriku and Pico Wave energy power plant emphasise the threat of wave loading uncertainties for an oscillating water column design. This thesis aims to address some of these uncertainties, specifically the one related to the in-chamber wave loads and scaling effect in an OWC installed vertical breakwater design. Firstly, this thesis aims to propose a new method to model the wave loadings experienced by the ceiling and the rear wall inside the chamber caisson. This model includes the maximum pressure experience estimation and the pressure distribution pattern on the chamber ceiling and rear wall. Rather than starting over, this thesis will use the established and trusted methods as its starting point. The model draws inspiration from the widely used Goda prediction method for conventional breakwater. Unlike an OWC, there have been an extensive study for a conventional vertical

breakwater. Furthermore, the probability of wave impacts experienced by the front wall of the OWC integrated breakwater is compared with the conventional vertical breakwater estimation method. The water column impact inside the OWC chamber is identified, characterised, and quantified by means of large-scale physical model experiments.

Secondly, the thesis explores the scaling uncertainties in an OWC integrated breakwater physical model experiment. Prior to a prototype deployment, experimental testing plays an extremely important role in a design process of a coastal structure design. Since testing directly with a prototype or large dimensions is very costly, a designer starts with a scaled down version of the physical model. The scaled-down models, however, could be subject to "scale effects", which for simple coastal structure are well understood. This leads to the second gap to be tackled which would be the scaling effect uncertainties in a physical model testing of an Oscillating Water Column installed breakwater.

For conventional coastal defence modelling, Froude scaling method (Fr) is used to keep the gravity:inertia force ratio between the prototype and the scaled physical model. This scaling method, however, does not scale the air stiffness correctly between the prototype and the scaled physical model of an OWC chamber. In order to scale down the air volume correctly, another type of scaling method, such as Reynold scaling method (Re) or Cauchy scaling method (Ca), needs to be employed. Unfortunately, those scaling methods contradict Froude scaling method unless the model is 1:1 scale to the prototype. This thesis explores the effect of scaling in a physical model testing if only the Froude scaling method is considered, while the scaling in air stiffness is neglected.

1.2 Aims and objectives

This work's overall focus is on the development of a new model for estimating the in-chamber wave loadings of an OWC installed breakwater and on the scaling uncertainties of the air stiffness between the small-scale chamber and the large-scale chamber. Specific objectives are:

1. To develop a prediction method for the in-chamber wave loading for an OWC installed breakwater
2. To validate the prediction method based on the large-scale OWC physical model testing measurements
3. To compare the occurrence and magnitude of impacts on the front wall of the OWC breakwater with the conventional vertical breakwater wave impact design tools and adjusting the guidance as necessary
4. To identify, characterise, and quantify the water column behaviour of an OWC installed vertical breakwater during operation
5. To perform a small-scale physical model with wave condition based on the large-scale settings and compare the large-scale and small-scale measurement results
6. Conclude the findings in a form suitable for uptake by designers of OWC integrated breakwater

1.3 Thesis structure

Chapter 2 will begin with a concise history of the OWC-WEC. The literatures related to wave loading on OWC, conventional vertical breakwater, and OWC installed breakwater will be explored. The methodology used to obtain the objectives will be explained in Chapter 3. A conceptual model for OWC wave loadings will be proposed and a large-scale experiment to validate the model will be presented in detail in Chapter 4. Chapter 5 focused on the occurrence and magnitude of impacts loadings on the front wall of the OWC installed breakwater and then compare it to the conventional vertical breakwater design tools. Furthermore, the water column behaviour during operation and in-chamber wave impact will be identified, characterised, and quantified in this chapter. Chapter 6 contains the small-scale physical model test results analysis and the comparison of the experimental results between the large-scale testing and the small-scale testing for various kinds of chamber conditions to check the scaling effect between the two scales. Finally, the conclusions are presented in Chapter 7.

2 Literature review

2.1 Wave energy resource

The Intergovernmental Panel on Climate Change (IPCC) fifth assessment report (AR5) (IPCC, 2014) indicate a clear involvement of Human activities in the increase of average global temperature. It also stated that the global warming leads to an increase the sea level and diminishes the snow and ice. According to the AR5 IPCC report in 2014, the increase in global temperature is extremely likely to have been caused by anthropogenic greenhouse gasses which increases the concentration of CO_2 in the atmosphere. The latest IPCC (IPCC, 2018) report further indicates the sensitivity to change in excess of 1.5^{o}C above pre-industrial level. This is the clearest yet call for immediate action to reduce the amount of CO_2 emission. To reduce the amount of greenhouse gasses in the UK, Department of Energy and Climate Change releases the Carbon Reduction Commitment (CRC) which pursue the target of cutting the CO_2 emissions by 60% from 1990 levels by 2050. This plan pushed the development of greener energy generation such as the wave energy generators to replace conventional energy generation such as coal and natural gas. It is estimated that for every 1 kWh produced by marine renewables, the CO_2 emission can be reduced by 394g compared to Combined Cycle Gas Turbine (CCGT), 120g compared to Biomass, 937g compared to Coal powered energy generator, and about 1000g compared to Diesel power with 25% efficiency (Smart and Noonan, 2018). At the moment, Scotland's electricity generation using renewable energy (RE) tripled in the last 10 years with installed capacity of about 10GW by December 2018, or accounted to over 70% of total electricity used in Scotland. The biggest contributor for this at the moment is still onshore wind, which responsible for about 71% of the total electricity generated through renewable energy resources. Wave and tidal sector, furthermore, only responsible for about 0.18%. Starting 1st of April 2016, however, the UK government decided to remove onshore wind power plant from subsidy recipient and further tightened the regulation for new plan (Wintour and Vaughan, 2015). Consequently, this condition reduced the number of onshore wind turbine planning application by

94% in 2018 compared to 2015 (Gabbatiss, 2018). This gives room for improvement for wave energy sector to be developed (Renewables in Numbers, 2019).

Among the renewable energy sources, ocean remains as the biggest energy resource waiting to be harvested. It is calculated as much as 1000 GWh of wave energy reaches the British isle every day on average (Barstow *et al.*, 2008). The world energy council approximated no less than 29,500 TWh/yr of wave energy available, with the densest energy potential located in Europe and west coast of America (World Energy Council, 2016; IRENA, 2014). This source of energy, contrary to the theoretical energy potential suggested, remains under used compared to other renewable energy sources such as wind and solar (Quirapas *et al.*, 2015; Ly *et al.*, 2014), with conversion technologies at a relatively early stage of development with consequent high energy cost.

Waves is basically an energy passing through the surface of water. This energy mainly comes from the wind and then transmit across the ocean through the water. A stronger wind, which often occurs in the middle of the ocean, blows the surface of the ocean water and creates waves. These waves later travel toward the coastline transmitting the energy to an accessible location. This form of energy, along with offshore wind and tidal current, are commonly known as the marine renewables. Deployment of wave energy converter technologies are currently lagging to other two, due to its high cost of about EUR 330-630/MWh (IRENA, 2014) and poor performance of several projects to date. This thesis aims to boost the development of wave energy converters by reducing some key uncertainties associated with designing an Oscillating Water Column Wave Energy Converter.

2.2 Oscillating Water Column (OWC) energy converter

The general principle of an OWC can be seen in Figure 2. In general, an OWC device utilises wave crests and troughs to drive the water column trapped inside the OWC chamber to oscillate up and down. This oscillation occurs due to hydrodynamic pressure variation at the column base. These water column movements, furthermore, force the air inside the chamber to move out and in via an air channel. The power generation can then be done by placing a power take-off mechanism in this air channel.

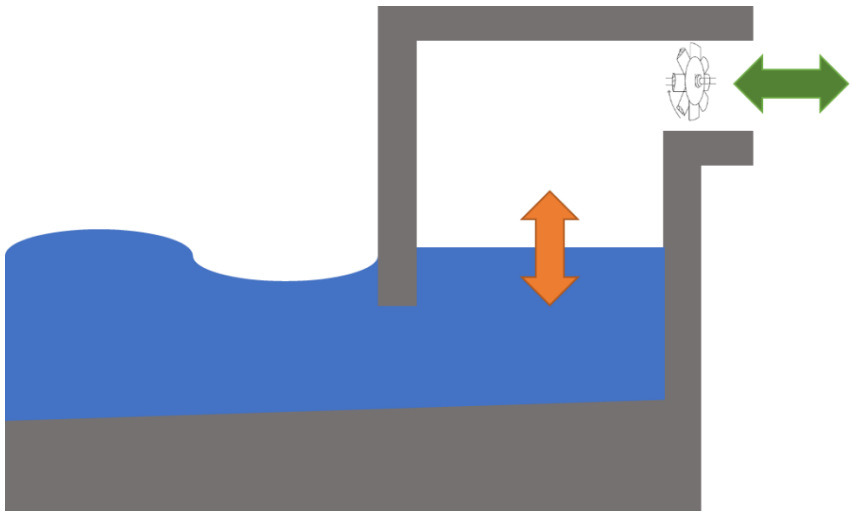

Figure 2 Schematic of Oscillating Water Column (OWC) wave energy converter.

The development of an Oscillating Water Column started in 1940s by the development of a floating OWC device to power a navigation buoy (Masuda, 1986; Falcão and Henriques ,2016). It was designed and developed due to its simplicity and potential for being relatively low maintenance. In the beginning, therefore the development was only focused on energy generation. Only after the idea of a perforated vertical breakwater was conceived in 1961 by Jarlan (1961), engineers then began to study the possibility of combining oscillating water column concept into a vertical breakwater (Takahashi, 1989). These studies found that integrating an OWC into a vertical breakwater is not only possible, but also has the theoretical potential of 100% energy absorption (Evans and Porter, 1995). Apart of the energy absorption capability, an OWC installed breakwater appears attractive compared to other wave energy converters (WECs), due to its simplicity in design, its ability to be located further into the ocean (higher energy exposure but remain connected to the coastline), and its ability to share the cost between the energy generation and coastal protection. The power take-off system, furthermore, does not require any submerged moving since it will be connected to the air chamber above the still water level (swl), although, it is important to note that the air flowing out of and into the chamber may be very humid and saturated with salt water spray.

Over the years, many researchers have explored the optimum design of an OWC. In general, the studies focused on the front wall wave loads, OWC caisson dimensioning,

and on power take-off optimisation. Small-scale physical model studies found that an inclined slope front wall will reduce the wave loads experienced by the front wall but will have higher wave transmission coefficient when compared to an ordinary vertical wall (Takahashi, 1989; Müller and Whittaker, 1993). Subsequent studies also found that the front wall geometry and the front wall penetration - defined as the depth of submerged part of the front wall divided by the distance between the swl and the OWC's chamber floor - also play a significant role in determining the overall efficiency of the device, with typical efficiencies of up to 70% reached (Morris-Thomas *et al.,* 2007). Preen and Robertshaw (2010) hypothesised that the total forces acting on the front wall will be the sum of wave pressure distribution and hydrostatic pressure distribution, and be reduced by the opposing pressure distribution acting on the in-chamber side of the front wall. Unfortunately, hitherto, there have been no experimental or numerical results to support this argument. The front wall wave load studies (*e.g.* Morris-Thomas *et al.,* 2007; Kuo *et al.,* 2015) mostly focused on non-impulsive wave loads, but one of the biggest concerns in a conventional vertical breakwater design is in impact loads. Recent findings suggested that introducing an OWC caisson may lead to a reduction in wave reflection of a vertical breakwater (He and Huang 2016; Viviano *et al.,* 2016). It is interesting to speculate whether the same effect can be seen in terms of impact loading experience by the front wall.

In addition to the wave loading, the OWC caisson dimension should also be selected based upon the wave characteristic. Takahashi (1988) recommended for the chamber width, submerged front wall, and chamber height to be designed depending on the local sea wave length and wave height. This will be discussed further in Methodology Section 3.1.2. Another important aspect in designing an OWC is the angle of wave incidence. Previous studies showed that under un-favourable oblique wave approach, the wave over topping type wave energy converter, Seawave Slot-cone Generator (SSG), performed 50% less efficiently compared to the 2-D study (Kofoed *et al.,* 2006). This thesis, however, device performance is not a central theme, and the analysis is limited to 2-D, so the effect of wave angle is excluded.

For OWC caissons, the exploration focus is further divided into the loads acting on the in-chamber walls and the water column condition during operation. Early exploration

on the rear wall wave pressure was done leading to the then proposed 4MW wave generator at Siadar bay, Scotland. Patterson *et al.* (2010) postulated the wave pressure distribution acting on the rear wall of the air chamber comes from the "missing" part of the front wall and the pressure distribution should be hydrostatic as illustrated in Figure 3.

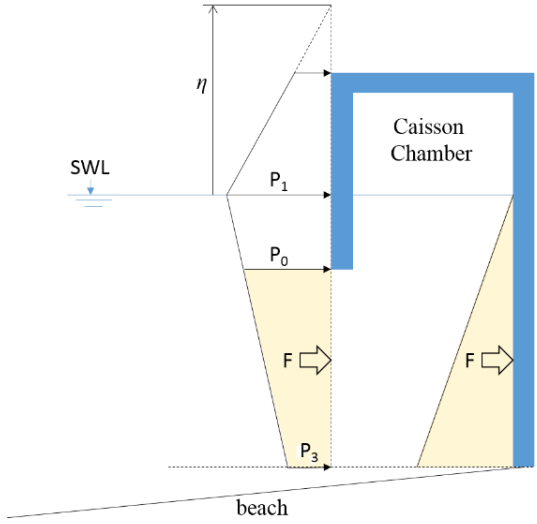

Figure 3 Hypothesised wave loading model for the OWC rear wall. Figure adapted from Patterson *et al.* (2010)

More recent small-scale physical model results, however, showed that the pressure acting on the rear wall is actually closer to a Goda-like pressure distribution (Kuo *et al.*, 2015). These experiments were, unfortunately, limited to regular wave tests and did not include the power take-off influence on the pressure distribution.

In addition to the in-chamber wave loads, the water column behaviour during operation is also crucial to the overall performance of the energy generator. To determine the device performance, the water column is mostly assumed to be well-behaved during the design stage. An experimental visualisation of the water column during operation, however, demonstrates that it might not always be the case (Müller and Whittaker, 1995). The authors found that there might be an impact acting on the rear wall of the chamber under certain wave conditions. More recent particle imaging velocimetry (PIV) results supported this by showing a vortex occurring behind the front wall opening when the water column is moving up (Lopez *et al.*, 2015). Medina-Lopez *et al.* (2015) further suggested that a pressure drop below the cavitation limit might

occurs on the opening of the front wall during extreme wave conditions. This condition may cause “cavitation erosion” to occur near the opening of the chamber. It is not impossible to imagine that this could initiate damage, *e.g.* by exposing reinforcing bar in concrete.

Apart from the structural influence, non-ideal water column conditions can be expected to have a negative effect on the wave energy conversion efficiency of the device. One could imagine that the chaotic water column movement may increase the amount of larger-scale turbulent motions in the chamber, which could lead to a significant reduction in energy extraction capability. Additionally, due to the moisture in the air chamber exceeds 65%, the power extraction capability may decrease by about 50 to 70% (Sheng *et al.*, 2013; Medina *et al.*, 2016). Although it has a significant effect on the performance of the device, there is very limited literature focused on the condition of the water column during operation, including looking on the wave condition under which the chaotic movement is more likely to occur.

Due to nonlinearity of the water chamber oscillation, there are two types of turbine most commonly used for an OWC power take-off mechanism: Wells turbine and Impulse turbine.

Wells turbine utilises a symmetrical aerofoil as the turbine blades in order to produce a uni-directional rotation independent of the direction of air flow. For this type of turbine to work, the incident angle of the turbine’s blade need to less than about 15^{o} or there is a high chance of stalling. Most of the time, pair of guide vanes are utilised to increase the efficiency of the turbine. Although commonly used, past repots showed that Wells Turbine has some disadvantges such as: narrow range of operating flow rates, poor starting characteristics, and high speed operation (700-1500 rpm) which resulted in high noise and high axial thrust (Setoguchi and Takao, 2006).

The second type of turbine which commonly used is Impulse turbine. This type of turbine utilised a jet of air or steam directed onto vanes in order to rotate the turbine. Similarly, pair of guide vanes are also utilised to increase the performance efficiency of the turbine. This type of turbine works in much less speed compare to Wells Turbine (about 350 rpm). Comparison between the two turbines showed that although Wells Turbine has higher peak efficiency, it stall at lower air flow rate while Impulse turbine

still giving useful output over a wider range of air flow rate. In other words, the impulse turbine may has a higher mean efficiency under high intensity waves (Setoguchi and Takao, 2006).

The PTO, furthermore, needs to be tuned to incident wave conditions to increase the performance of the device (Sarmento and Falcão, 1985; Jefferys and Whittaker, 1986). Although earlier study focused more on the utilisation of the Wells turbine, an impulse turbine was shown to have higher efficiency during starting and running condition in a separate study (Setoguchi *et al.*, 1999).

As mentioned in the Chapter 1, scaled testing plays an important role in the development of a coastal structure, including OWC. It is widely known that the Froude similitude law commonly used in coastal structure scaled model testing will not scale down the aero-thermodynamic characteristics inside the air chamber correctly (*e.g.* Takahasi *et al.*, 1985; Falcão and Henriques, 2014). This condition might then lead to the so-called small-scale effect in an Oscillating Water Column device scale testing. Falcão and Henriques (2014), furthermore, showed that these scale-effects can be reduced significantly by utilising a geometrically similar turbine in the model. Unfortunately, such application is limited to large-scale physical model of about 1:4 (at minimum) to ensure the fluid dynamic similitude between the prototype PTO and the scale PTO. In most cases, this scale effect is ignored, and Froude similitude is followed. Due to this, it is important to check what is the impact of ignoring the scale-effect and employ only Froude scaling in the physical model experiments.

2.3 Lessons learned from OWC projects

Over the years, there have been several OWC pilot projects in Europe. Early examples are shoreline OWC projects called LIMPET and Pico power plant in the UK and The Azores respectively. The world's first grid connected OWC installed breakwater was constructed at the port of Mutriku, Basque Country, Spain in 2009-2012, and the U-OWC type WEC in the Port of Civitavecchia in Italy followed in 2011 (Arena *et al.*, 2017). Apart of the bottom-stand OWC projects, there are also example of floating OWCs. This section will discuss the development of the OWC through the aforementioned OWC devices.

2.3.1 Land Installed Marine Power Energy Transmitter (LIMPET)

The Land Installed Marine Power Energy Transmitter (LIMPET) was designed and developed by the Queen's University of Belfast and constructed on the Isle of Islay, Scotland. When it started its operation in 2001, LIMPET was the first grid connected WEC in the world. The wave energy converter is an onshore oscillating water column device and was designed to generate 500kW of electricity. Figure 4 shows the schematic of LIMPET power plant which comprises a three 6m by 6m concrete chamber water columns and 40^{o} inclined front wall.

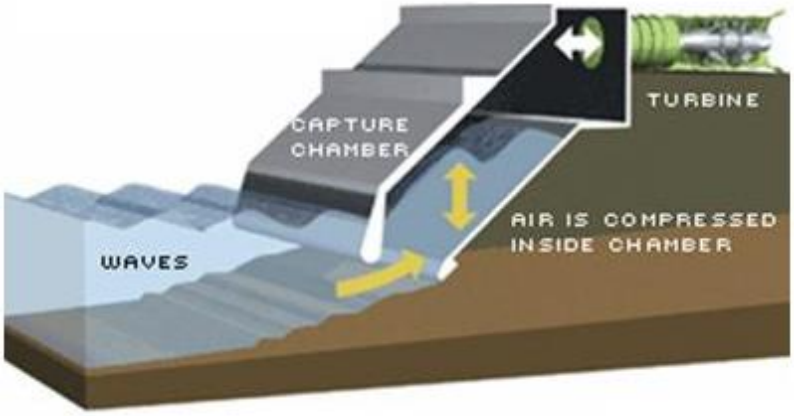

Figure 4 LIMPET on-shore oscillating water column (OWC) mechanism (Poullikkas, A., 2014).

The front wall inclination was selected after a small-scale test of 1/36 model experiments found that compared to a vertical structure, the 32.7^{o} front wall inclination led to a 36% wave pressure decrease, and the -32.7^{o} angle (experienced by the front wall facing the chamber) reduced the pressure as much as 56% (Müller and Whittaker, 1993). The experiment, however, only used a single regular wave period of 1.49s. The same small-scale test later showed large vortices appeared at the "lip" of the front wall during the water inflow and outflow and a breaking wave hitting the back wall in a high incident wave cases (Müller and Whittaker, 1995).

A LIMPET performance report indicated breaking wave loads of up to 690 kN/m^2 experienced by the prototype (Whittaker *et al.*, 2004) which is consistent with small-scale test. These results may show some of the reasons behind LIMPET poor performance during operation, only generating up to 100kW of its peak, about 20% of the rated capacity. Anecdotal evidence points also to a lot of wave energy being

dissipated by wave breaking in the shallow water offshore of the plant. Despite these performance issues, the project demonstrated that OWC wave energy converter's simplicity can offer excellent reliability by performing about 98% of its lifetime (The Queen's University of Belfast, 2002). This also shows that Wells turbine is suitable for an OWC type wave energy converter proven by the fact that the turbines used in Mutriku wave energy plant were designed and installed by WaveGen who grew out of the LIMPET project. A further conclusion was that the device did not require a lot of routine maintenance check-up, and was quite robust against any weather conditions.

2.3.2 Pico power plant

In parallel with LIMPET design and production, another full size fixed-structure OWC was initiated in the island of Pico, Azores, Portugal and under the coordination of Instituto Superior Tecnico (IST). The structure involves a single 12m x 12m cross section water column in a concrete chamber standing on the sea bottom as can be seen in Figure 5 (a) during a wave impact taken from the land and in (b) during calm water condition taken from sea. It was rated at 400 kW and was completed in 1999. The highest sustained energy output recorded was about 7500kWh during a near 400 hours of production in November 2010 representing an average of about 19 kW (Monk, 2012). The development of the device included a wide range of scales test from 1:35th test in a wave flume to 1:4th in actual sea water. After almost 20 years of operation, the wave power plant is finally closed due to some partial failure in the base of the wave energy converter, according to the latest press release by WavEc in 2018. Another site of the same island is currently under assessment for wave energy generation power plant following decommissioning of Pico power plant (Henriques *et al.*, 2013).

(a) (b)

Figure 5 Pico OWC-WEC in Portugal with the view (a) from the land during wave impact, and (b) from the sea during calm water condition (Aqua-RET, 2012).

2.3.3 Mutriku wave energy plant

Unlike coastline OWC structures like LIMPET and Pico plants, Mutriku wave energy plant is located in the deeper and more energetic location of the sea where a breakwater is needed as a harbour protection. The OWC type chamber is installed in an already designed approximately 440 meters long breakwater (Figure 6). The construction was promoted by Basque utility Ente Vasco de la Energía (EVE). The main challenges faced by the WEC's designers at that time were making a WEC design that will not interfere with the harbour accessibility and will not cause many alterations to the breakwater's original design (Torre-Enciso *et al.,* 2009). They later decided that an OWC concept could best fulfil both requirements. The final design of the OWC installed breakwater specified 16 OWC chambers, each connected to 18.5 kW self-rectifying Wells turbine with a rated power of 296 kW in total. The turbine used in this project is the same design as LIMPET's. Unlike LIMPET, however, this project used separate power take-off (PTO) system for each chamber. The developer claims that the power generator will avoid 600 tonnes of CO_2 emission annually, although it is interesting to consider the embodied CO_2 in the raw materials and the construction process. Another intention of the project is to make the place a reference point in marine energy development. This objective is successfully achieved upon the

commissioning of the project. This marked the world first grid-connected OWC installed vertical breakwater.

Although now operating, the construction was not a smooth process, suffering severe storm damage in December 2007, March 2008, and January 2009. These storms caused 4 of the 16 chambers to be partially destroyed, including the loss of the entire section of the front wall as shown in Figure 7 (a) and (b) (Horvath, 2009). A subsequent study suggests that the pressure experienced by the structure may have reached 6 times the 'operational' limits of the walls during these storms (Medina-Lopez *et al.*, 2015).

Figure 6 The bird's eye view of the current (after rebuilt) OWC installed breakwater in Mutriku port, Basque country, Spain. ("Mutriku break water and OWC wave power plant", *Ocean Energy System*, https://report2014.ocean-energy-systems.org)

(a) (b)

Figure 7 The damage of OWC installed breakwater in Mutriku caused by storm, showing (a) exposed chamber with the front wall missing, and (b) some of the layer of the front wall missing greatly reducing the front wall integrity (Horvath, 2009).

2.3.4 Resonant Wave Energy Converter (REWEC) or U-OWC

Europe's newest wave energy power plant project based on the OWC design is the Resonant Wave Energy Converter 3 (REWEC3) or as also known as the U-OWC type WEC (Boccotti, 2003). The design is unique because, unlike a simple OWC chamber, this type of OWC utilise an additional wall extending in front of the front wall (Figure 8) forming a "U" shaped wave duct – hence the "U" in U-OWC. By adding this vertical wall, the resonance of the device can be better tuned to a larger wave conditions (H_s > 1.5m), which lead to higher absorption of wave energy under these wave conditions. Bocotti (2007) estimated that for the identically size structure of OWC, the U-OWC could absorb 90.7% of the wave energy compared to only 15.6% of the simple OWC configuration when exposed to irregular sea condition with significant wave height (H_s) of 2.5m, making the U-OWC generate approximately 5.5 times more electricity power than the simple OWC.

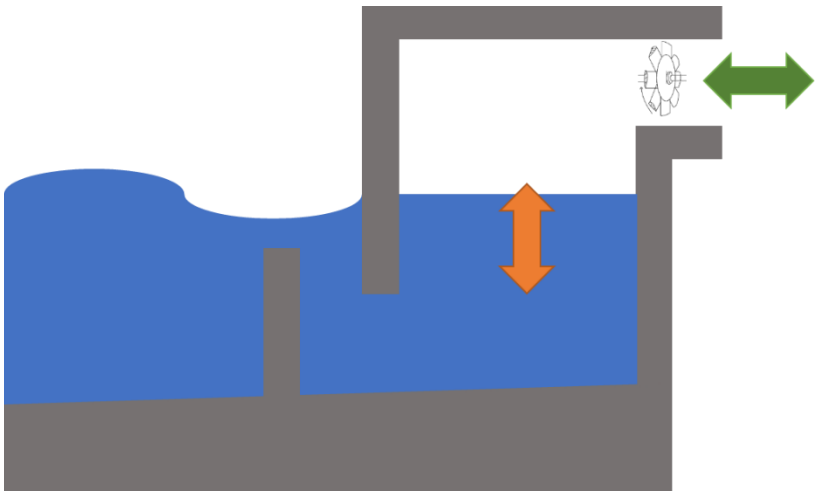

Figure 8 Schematic of U-Oscillating Water Column or Resonant Wave Energy Converter.

After much numerical and experimental testing, the world's first U-OWC prototype construction was started in the port of Civitavecchia in 2011 (Malara *et al.*, 2015). The 578m wave energy power plant consists of 124 chambers integrated into caisson breakwaters. One caisson comprises of 8 chambers. Early report of the first U-OWC plants can be seen in Arena *et al.* (2017). It is important to remember that addition an additional wall may increase the difficulty of the construction. Furthermore, this type of wave energy converter is still using the fundamental OWC wave absorption mechanism. Due to this reason, the current thesis limits investigation to a simple OWC. It will be very interesting to see the development of this wave power plant in its operation.

2.3.5 Siadar wave power project

In 2009, Npower proposed a 4MW wave energy plant, the largest in the world, in Siadar Bay, in Lewis, Scotland, shown in Figure 9. The proposal was submitted in 2010 as a result of Scotland's ambition to increase its renewable energy generation plan from 50% to 80% by 2020. A Scottish based wave energy company who had provided the turbine for LIMPET and Mutriku and would supply 36 Wells turbine to chamber over 220 m breakwater run, Wavegen, was then given the opportunity to build the wave power plant. Site measurements were used in a detailed study to establish the design wave conditions and the optimum orientation of the breakwater, which was established to be 310-315^{o} (Patterson *et al.*, 2010).

As can be inferred from the remote, island location, grid connection was one of the main challenges faced by this project. The project needed a subsea cable to connect the island to the national grid. The project was delayed due to the delays in the interconnector and high transmission charges, according to the spokesperson for Comhairle nan Eilean (Western Isle Council) in the Stornoway Gazette before its ultimate abandonment in 2012. WaveGen subsequently took on the promotion of the project and re-designed it to a 20 MW scheme. Sadly, it did not progress due to continued uncertainty on grid connection capacity. With the abandonment of the revised Siadar project, WaveGen sadly folded.

The cancellation of the project was a big blow to the wave energy development in the UK. This situation, however, emphasises the urgency for addressing the uncertainties in the breakwater installed OWC structure design. According to one of UK's leading technology research centre for offshore renewable energy, Catapult, there are 4 areas of improvements need to be achieved through innovation: (a) reliability and availability, (b) structures and moorings, (c) offshore operational cost reduction, and (d) electrical connectors (Smart and Noonan, 2018). This assessment, combined with lessons learned from Siadar design process and the damage suffered at Mutriku, shows that determining wave loads is crucial and one of the most important consideration in starting a wave energy plant project.

Figure 9 The location of the 4 MW Siadar wave energy converter project proposed, indicated by the red triangle.

2.3.6 Floating OWC development

The European projects discussed so far have all been fixed structure, either at the shoreline or integrated within a fixed breakwater. Elsewhere, the floating OWC has been explored too. An early example was an open sea test was done in Gokasho Bay, Nansei Town, Japan in September 1998. The device called 'Mighty Whale' was a floating oscillating wave power device consisting of three air chambers. It was tested in an open sea and even endured a typhoon with a significant wave height and period of 5.57 m and 12.5 s (Washio *et al.*, 2000). Unlike a fixed structure OWC device, a floating body of the a floating OWC structure enable the chamber to oscillate. This characteristic adds the mooring mechanism of the whole system to be very important in determining the efficiency of the energy generation. For a floating OWC design, the distance between the floater bottom and the top of the OWC is found to be the most influential factor in determining the annual average power output. One potential advantage of a floating OWC, due to the mobility of the device, is the peak frequency at which the device best operates. The device will have two peaks frequency due to the movement of the device itself and the water column inside the chamber. This allows the device to be tuned to a wider operating range (Gomez *et al*., 2011).

Another example of a floating OWC example was a 1: 3 scaled floating OWC tested in 2010 and deployed by Oceanlinx, an Australian company at Port Kembla (Figure 10). Extreme weather broke the mooring of the device in the same year, although fortunately, the structure was safely recovered soon after. The company continued to a development of the 1 MW energy generation device called greenWAVE in 2014. Unfortunately, the completed device was damaged beyond repair during its transport from Port Adelaide to Port McDonnell. The device is currently stranded in Yankalilla Bay, South Australia and waiting removal. This kind of failure was not unprecedented. In 1995, world's first offshore wave power plant OSPREY 1, which intended to be installed near Dounreay, Scotland, sank to the bottom of the ocean after caught by the 3 m swell of Hurricane Felix. The unfortunate wave energy device was developed by Applied Research and Technology of Inverness. It was concluded that repairing OSPREY 1 was unlikely to be viable and the project was abandoned. Those failures, with combined cost of more than US$ 9 million as reported by the Australian

Renewable Energy Agency and The Herald, further highlight the critical importance of sea-keeping in floating OWC devices.

The failures of OWC devices of greenWAVE and OSPREY 1 indicate the difficulties faced by such devices. Although they are not the reasons to give up an alternative mounting structure needs to develop which can withstand the harsh operating environment condition. Mutriku power plant has demonstrated that integrating an OWC within a breakwater is a practical, and perhaps the cheapest, solution to the problems. In this case, it is important to understand the use and aspects of breakwater.

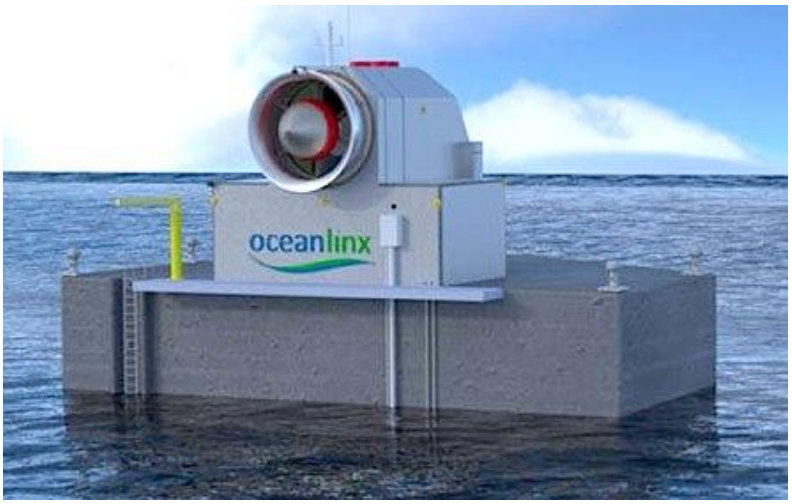

Figure 10 Oceanlinx floating OWC developed by Oceanlinx, Australia (Parkinson, G., 2013).

2.4 Wave loading on conventional vertical breakwaters

Generally, a breakwater is used as a protection for the coastal area behind it from the open ocean waves. The structure needs to be stable enough to avoid sliding and over-turning by wave loads.

These wave-loads include the slow-developing but longer-acting non-impulsive loads and short-lasting but high-intensity impulsive loads. The earlier modelling (Hiroi, 1919) modelled wave loads as a uniform water jet pressure, exerting to an elevation of about 1.25 times the wave height. This method supposed to estimate the wave pressure acting on the breakwater which includes both impulsive and non-impulsive wave loads. In 1928, another pressure formula based on non-linear wave theory for standing wave was introduced (Sainflou, 1928). The formula was immediately accepted by

many coastal engineers around the world as a basis to estimate the non-impulsive wave loads. The earlier formula was still used to estimate the impulsive wave loads in designing a breakwater. Both formulae, however, only used regular wave conditions with a single wave height for the calculation. This created a confusion when applied to the real sea waves since the wave height is not uniform (irregular sea conditions).

To resolve this confusion, Goda (1975) proposed a new set of wave pressure formulae for freeboard section of a simple vertical breakwater. These formulae were derived from many experimental data and theoretical considerations and have been shown to have a good estimation on the horizontal forces acting on a coastal structure (Weibe *et al.*, 2014; Kuo *et al.*, 2015; Tomiczek *et al.*, 2018). These formulae are currently accepted as the benchmark for non-impulsive wave loads estimation around the world. All of the non-impulsive wave loads estimation in this thesis utilise the extended version of the formulae which can be seen in Goda (2010).

Unlike the pulsating loads, impact loads which often come from a breaking wave have unpredictable pressure on various kind of breakwater structures (Kirkgöz, 1995; Allsop *et al.*, 1996; Laju *et al.*, 2005; Bullock *et al.*, 2007; Kisacik *et al.*, 2012).

The impact load of a breaking wave has always been one of the main uncertainties in a breakwater design, neglecting impact loads during the design process can be catastrophic (Oumeraci, 1994). To solve the uncertainties, it is important to know what makes a breaking wave create an impact pressure.

One of the earliest concepts of impact pressure generation was proposed by Bagnold (1939) who argued that the pressure is generated due to the enclosed air pocket, trapped between the impinging wave and the breakwater wall. The concept will be revisited and explained further in sub-chapter 2.6. An experiment done by Hattori *et al.* (1994) supported this argument and showed that the highest impact pressure may occur if there is a very small amount of air entrapped between the wall and the breaking wave. This experiment also showed that a larger amount of air entrapment might produce less impact. Cooker and Peregrine (1991a; 1991b), on the other hand, developed a computational model which shows that the pressure comes from the turning 'flip through' motion of the wave meeting a vertical wall, this argument later supported by an experiment done in 2001 (Oumeraci *et al*., 2001).

Allsop *et al.* (1997) then identified design methods used for wave impact loading prediction for a vertical breakwater and put them to an experimental test. The test results later used as a guidance to produce a decision chart for a simple or composite vertical breakwater which described the type of loadings will the structure face based on the berm height, the wave height, and berm length.

The Probabilistic Design Tools for Vertical Breakwaters (PROVERBS) project, led by Oumeraci and carried out between 1996 and 1999, established an enhanced design guidance for vertical breakwaters, with the integration of wave impacts into a probabilistic design methodology. The project differentiates the type of wave loads based on the duration of the load and the structure vibration natural period. The impulsive load occurs in a shorter duration than the structure vibration natural period, whereas the non-impulsive load occurs longer than twice the natural period. Separate prediction formulae are then developed to address each type of load. The large-scale experimental results, however, shows that the prediction formulae still gave a wide scatter showing room for improvement.

In addition to the plain vertical breakwater, designs have been explored to reduce reflection and dissipate incident wave energy. In 1961, a wave chamber was integrated into a vertical breakwater caisson in an attempt to reduce the wave reflection and overtopping characteristics of the structure (Jarlan, 1961). This so called perforated vertical breakwater's wave chamber is not unlike an OWC chamber. It is possible for the wave chamber to be modified into an OWC while still maintaining the wave reflection reduction ability (He and Huang, 2016). This made the integration of an OWC chamber into a vertical breakwater design so much simpler compared to other type of breakwaters, such as rubble mound breakwaters. Thus, this thesis aims to use these established methods (for plain vertical walls) as starting points, to be extended for application to OWCs integrated into a vertical breakwater.

2.5 Scaling methods for physical model test

Prior to a production of a coastal structure, it is always preferable to test the design first using a small-scale physical model. This is the most cost-effective estimation for the prototype behaviour when built. The physical model test conducted in a controlled

environment allow observation of multiple complex boundaries interaction which are difficult to simulate in current finite numerical calculation. In order to guarantee the similarity of physical characteristic between the physical model and the prototype, certain similarity requirements need to be met such as geometrical similarities, fluid dynamic similarity, and external effects similarities (Hughes, 1993). The external similarities, furthermore, include pressure, gravity force, wind shear stress, etc. In order to represent such variable similarities, several dimensionless parameters are then introduced using dimensional analysis as the base principle such as, Froude number, Reynolds number, Euler number, Weber number, Cauchy number, Mach number, and Strouhal number.

In modelling the hydrodynamic properties of a coastal structure site at smaller scale, both Froude number and Reynolds number are potentially important. Keeping one of these numbers the same, combined with geometric similarity, guarantee the hydrodynamic similitude in most coastal structure physical models. Which number need to be kept the same will be depending on the dominating force in the system. Froude number similarity or Froude criterion needs to be fulfilled when the relative influence of inertial force and gravity force are the most important influence of the system. The Reynolds number needs to be maintained if viscous forces dominate the hydraulic characteristic. Equations 1 and 2 describe the Froude number (Fr) and Reynolds (Re) numbers respectively.

$$Fr = \frac{v}{\sqrt{gl}} \tag{1}$$

$$Re = \frac{v\rho l}{\mu} \tag{2}$$

where: v = characteristic velocity, g = gravity acceleration, l = characteristic length, μ = dynamic viscosity of the fluid, and ρ = density of the fluid

2.6 Scaling effects in conventional vertical breakwater modelling for impulsive loads

Using a Froude scaling for non-impulsive wave loads experienced by a breakwater is commonly accepted. For impulsive wave loads, on the other hand, Froude similitude may not work correctly. In order to understand why, it is important to understand the

fundamental concept of impulsive loads. Impulsive loads usually generated by a breaking wave. The movement of breaking wave trapped a volume of air as illustrated by the dashed line in Figure 11. Figure 12 show the action of impulsive loads due to breaking wave on a vertical wall in a wave flume. As can be seen, a volume of air is trapped due to "flipping" motion of the breaking wave.

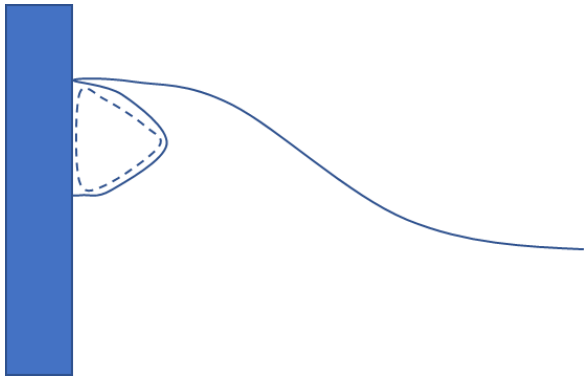

Figure 11 Impulsive loads on a vertical breakwater due to breaking wave illustration.

(a) (b) (c)

Figure 12 Impulsive loads; a breaking wave moving toward the wall (a), hitting the wall with an air pocket formed between a water mass and the breakwater (b), and the water mass hitting the wall (c).

Bagnold (1939) proposed formulae to estimate the impact pressure generated by an entrapped air cushion during breaking wave on a vertical breakwater by modelling it as a volume in a chamber compressed by an impinging mass of water column as illustrated in Figure 13. The generated air pressure (p_{Ba}) relationship with the water mass is linear with the effective height of the water mass (k_{Ba}) (water volume / area) over the air volume thickness (D_{Ba}) as can be seen in $p_{Ba} - p_o = \rho_w k_{Ba} \left(\frac{d^2x}{dt^2}\right)$, where

x denotes the varying thickness of the air volume over time t and ρ_w denotes the water density. If adiabatic compression is assumed in the air volume, the generated pressure (p_{Ba}) and atmospheric pressure (p_o) will be given by $p_{Ba} = p_o \left(\frac{D_{Ba}}{x}\right)^{1.4}$.

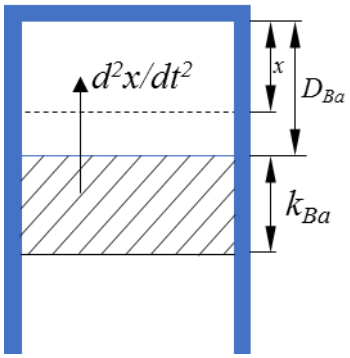

Figure 13 Air pocket with length (D) compressed by an impinging water mass with length (k) model (Bagnold, 1939).

Based on initial conditions at $t = 0$ of $x=D$ and $dx/dt = -u_o$ with u_o denotes the velocity of impinging water mass, the ratio between the peak air pressure generated (p_{max}) and atmospheric pressure (p_o) is approximated by Equation 3.

$$\frac{(p_{max})_{Ba}}{p_o} = 1 + 2.7\left(\frac{\rho_w k_{Ba} u_0^2}{p_o D_{Ba}}\right) \quad (3)$$

The non-dimensional parameter on the right side of the formula is called "Bagnold number". In this model, the water column movement is assumed to be a simple piston with a flat surface at all time. Mitsuyasu (1967) expanded this formula to include the effect of air leakage to the peak pressure generation.

By drawing upon the similarity between the situation of a generated impact pressure (p_{Ba}) and chamber pressure generation in a wave chamber $(p_c)_{wc}$, Takahashi *et al.* (1985) proposed a modified Bagnold equation to calculate the impulsive vertical forces acting on the ceiling of a wave dissipating caisson installed in a perforated vertical breakwater due to breaking wave. In this case k_{wc} defined as a quarter of the added mass of a plate whose width equal to 2 times chamber width ($k_{wc} = \frac{\pi B_c}{4}$) and D_{wc} is equal to the height of trapped air. The modified definition of k_{wc}, D_{wc}, and $(u_o)_{wc}$ can be seen in Figure 14. The value of water column vertical velocity $(u_o)_{wc}$ is depending on the incident wave height and impact rise time (t_r). The same modification can be

applied for the case of the oscillating water column by substituting the height D_{Ba} with the chamber height h_c (Takahasi, 1988).

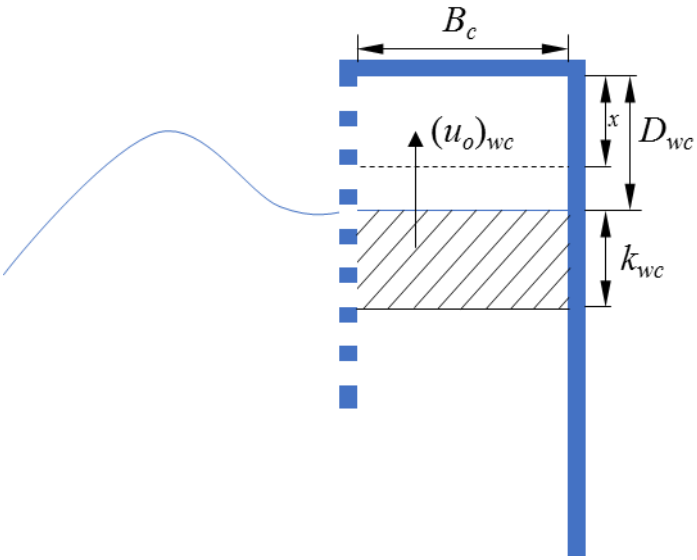

Figure 14 Air compressed by a mass of water model application on a perforated vertical breakwater with wave dissipating chamber (Takahashi *et al.*, 1985).

Takashi *et al.* (1985) and Takahashi (1989) tested the formula by means of small-scale physical model and found that the model measurement tended to over-estimate the peak pressure at the prototype scale. The model used was a 1/20 scale model, scaled down using Froude similitude law. The over-estimation may happen because the characteristic of the trapped air may not follow the Froude similitude correctly.

As can be inferred from the Bagnold number relationship (see Equation 3), unless the ambient pressure during experiment is scaled down in proportion to the scaling ratio, the peak air pressure generated will not follow the scaling ratio between the model and the prototype. Since controlling the ambient pressure is generally difficult to achieve even in a controlled laboratory environment, an adjustment factor (λ) was introduced by Takahashi *et al.* (1985) in order to adjust the small-scale physical model measurement. The factor can be calculated by comparing the measured peak pressure in a model $(p_{max})_m$ with the estimated peak pressure in a prototype scale $(p_{max})_p$ (Equation 4).

$$\lambda = \frac{(p_{max})_m \cdot s_c^{-1}}{(p_{max})_p} \quad (4)$$

where s_c denotes the length ratio between the model and prototype. The experimental observation showed an adjustment factor (λ) equal to 3.01 for the case of no leakage and 2.43 for the case of 0.75% orifice:chamber area ratio.

It is important to note that these formulae were developed to calculate the peak pressure caused by impulsive loads of a breaking wave on a vertical wall and inside a wave dissipating chamber. Although similarity can be drawn for a compressed air chamber by water column oscillation, the peak pressure resulted from water column induced by non-impulsive loads may act differently when scaled down. This needs to be investigated further.

The introduction of adjustment factor (λ) to the modified Bagnold equation by Takahasi *et al.* (1985) highlighted the uncertainty in impulsive loads experiments in small-scale model of a conventional vertical breakwater. Allsop *et al.*, (1997) suggested an adjustment factor between 2.22 to 2.5 for a 1/32 model of a vertical breakwater, tested using fresh water. A wider range of scale effect correction factor for conventional vertical breakwater was also proposed by Cuomo *et al.* (2010b) for multiple Froude scale numbers as a function of model Bagnold number (Bgn_M) in the Y-axis and prototype Bagnold number (Bgn_p) on the X-axis shown in logarithmic scale (Figure 15).

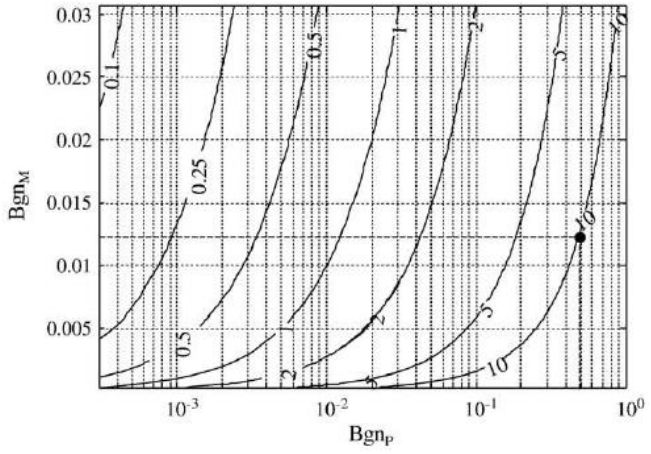

Figure 15 Scale factor as a function of Bagnold number of the model (Bgn_M) in the Y-axis and Bagnold number of the prototype (Bgn_p) on the X-axis shown in logarithmic scale, taken from Cuomo *et al.* (2010b). The solid lines indicate the scale factor that need to be used when up-scaling the impact pressure measured using the small-scale model.

2.7 Scaling effects in modelling OWC breakwaters

For a small-scale model testing of an OWC structure, the air and water interaction characteristics inside the chamber will not scale properly using Froude scaling method (similarly to the problems in testing impulsive loads on a breakwater scale model). To simulate the air viscous characteristic properly in this case, Reynolds similitude law should be fulfilled. Unfortunately, for both scaling methods to be satisfied in the same model is practically impossible except at 1:1 scale, since Froude similitude law dictate the model-to-prototype chamber volume ratio $(v_m/v_p) = s_c^{1/2}$, while Reynolds require $(v_m/v_p) = s_c^{-1}$. Since the gravity force is much more important than the in-chamber air characteristics in a physical model testing, the effects related to Reynolds number are often neglected, especially for cases where the Reynolds number is higher than 10^5.

Falcão and Henriques (2014) proposed the model-to-prototype chamber volume ratio (v_m/v_p) should be s_c^2 instead of s_c^3 to compensate for the air compression uncertainty based on non-dimensional analysis. Since the geometric scaling of the structure will give the air volume to be s_c^3, not the desired s_c^2, an additional variable air volume is suggested to be connected to the OWC model chamber to compensate for the lack of air volume. This suggestion, however, may present significant practical challenges in an experimental test since the external air tank need to be mounted in a close proximity to the OWC chamber and the pipe connection need to be relatively large diameter to avoid pressure loss when the air is circulating between the chamber and the tank. In addition, connecting a model OWC chamber to an external air volume may alter the in-chamber loading and water column behaviour. Weber (2007) suggests keeping the representative air chamber height for all scale to be the same, thus following the s_c^2 requirement. This method, however, may mean that any wave overtopping effect of the incident wave will not be modelled correctly, with possible knock-on effect on wave loadings. Viviano, *et al.* (2018) showed that preserving prototype the chamber height in a 1:9 model only had slightly increased natural period of the device (by less than 10%), while it may increase the over-estimation of the front wall wave loads measurements of the small-scale model by a factor of 1.5. Due to this consideration, Froude scaling similitude will be followed for overall dimensions in this thesis and

consequently keeping the in-chamber air volume ratio between the model and the prototype to be s_c^3, instead of s_c^2.

To reduce the uncertainty caused by the small-scale affect, Dimakopoulos *et al.* (2017) proposed a non-dimensional compression number omega (Ω) for the air chamber characterisation in a scaled physical model. The number can be used to calculate the ratio between the volumetric flow rate of the air passing through the power take-off and the air displaced by the water movement as shown by $\Omega = \sqrt{\frac{1+\left(q_c/Q_c\right)^2}{(q_c/Q_c)^2}}$, where: q_c = air flow rate through the power take-off, and Q_c = air displacement flow rate from the water movement. When Omega (Ω) is less then and equal to 0.1 then the air can be considered as incompressible, while Omega (Ω) bigger than 0.1 means the air compressibility is significant.

By utilising this method, the consistency of the energy performance between a small-scale model and a full-scale model should be ensured. The scaling effects related to the wave loading experienced by the structure, on the other hand, have not been explored. Chapter 6 of this thesis will explore the scaling effects associated to the wave loadings uncertainties in the small-scale model of an oscillating water column wave energy converter installed in a vertical breakwater.

3 Methodology

Original work presented in this thesis draws primarily upon two sources of physical model data of an Oscillating Water Column with a vertical front wall. The thesis is divided into three parts: in-chamber wave loads model, extreme wave impacts on the front wall and inside the chamber, and scaling effect of a scaled OWC physical model testing. A theoretical study is done for the first part of the analysis by drawing similarity between a conventional breakwater design tools and modify it to be applied in in-chamber wave loads model of an OWC installed vertical breakwater. The model is then validated using the large-scale model data because the large-scale is assumed to be more similar with a prototype scale compared to the small scale. Furthermore, the wave generator used during the large-scale campaign is capable to produce a wider range of wave conditions compare to the small-scale experimental campaign.

The second part of the thesis involved the impulsive loads experienced by the front wall and the inside the chamber. For the front wall, the experimental observation is compared with a conventional vertical breakwater estimation design tools for the non-impulsive and impulsive loads transition, impulsive force and rise time relationship, and the probability of impact in certain number of wave cycles. Furthermore, the in-chamber water column behaviour during operation is mapped under various sea states for the first time to investigate the wave conditions under which sloshing is more likely to occurs by means of video recorder placed inside the chamber. The water column behaviour then identified, characterised, and quantified for the extreme conditions which includes in-chamber ceiling impact.

The third and last part of the thesis investigates the scaling effect involved in a scaled physical model experiments of an OWC wave energy converter. The comparison is done especially for the chamber pressure generated inside the chamber during operation. An adjustment factor will be established based on the comparison to adjust the smaller scale physical measurements to estimate the prototype scale measurements.

3.1 Large-scale test (GWK)

3.1.1 Wave channel

The large-scale experiments were carried out in the large wave channel (Grosse Wellenkanal, GWK) in Hannover, Germany. The "GWK OWCs" project was an EC Hydralab III access project led by University of Edinburgh in collaboration with HR Wallingford, Second University of Naples, Queen's University of Belfast, and the University of East Anglia. Although these experiments were done prior to the start of the PhD, it has been raw data from those tests that has been the starting point for all the large scale data analysis presented in this thesis.

The flume size is 307m long, 5m wide, and 7m deep. The hydraulics driven machine shaft can generate wave heights (H) up to 2m are achievable for regular waves, with significant wave height (H_{m0}) up to 1.3m achievable for the irregular waves. The wave generator also capable of producing wave period between 3.0s and 6.0s with good accuracy. The structure installed was consisted of three chambered caissons and located approximately 100m from the wave maker. The three OWC caissons were hydraulically identical, although only the middle caisson was instrumented. The power take-off is simulated by means of circular orifice opening.

The OWC caisson geometry was fixed, but the still water depth (h), orifice opening diameter (D_{ori}), and front wall 'lips' penetration (w) were controlled. Orifice opening diameters (D_{ori}) were selected between zero (closed chamber) to 0.3 m (where orifice-to-chamber area ratio A_o/A_c = 2.0% - approximating a fully open situation), still water depth (h) was selected as 3.5m, and front wall 'lips' penetration (w) was selected as 0.38m. Schematics of the experimental arrangement at GWK are shown in Figure 16 from the side view (a) and the plan view (b).

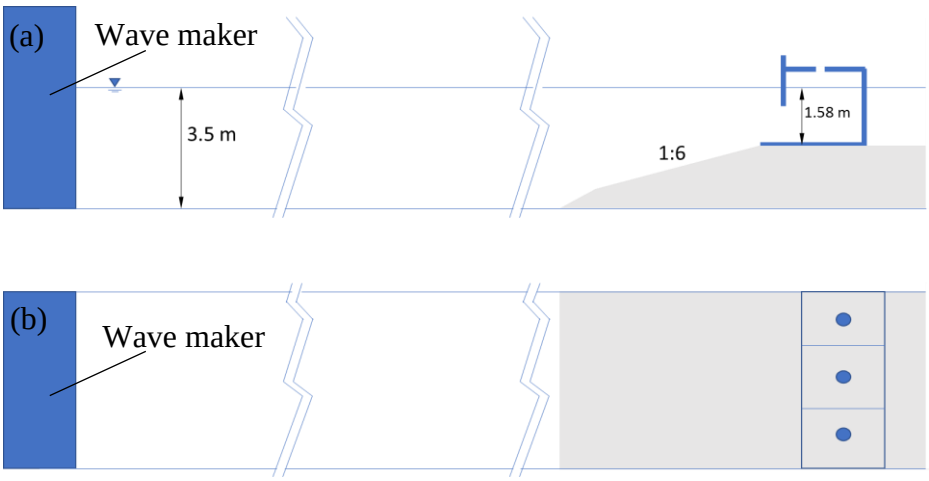

Figure 16 Experimental setup at GWK from (a) longitudinal section with the water depth for both the deeper part and the shallower part in m, and (b) top view. The waves travel from left to right with the paddle to OWC length = 97.47 m.

3.1.2 Oscillating Water Column physical model configuration

The detailed longitudinal section of the centre caisson of the structure and the location of the pressure sensors is indicated in Figure 18 with dimension in mm. The vertical front wall structure was selected due to its simplicity and constructability. Furthermore, wave energy converter device in the port of Mutriku showed that such configuration is working and simple enough to be built. In an OWC design, there are three most important geometries: chamber width (B_c), submerged front wall (w), and chambers height (crest freeboard) (h_c) (Figure 17).

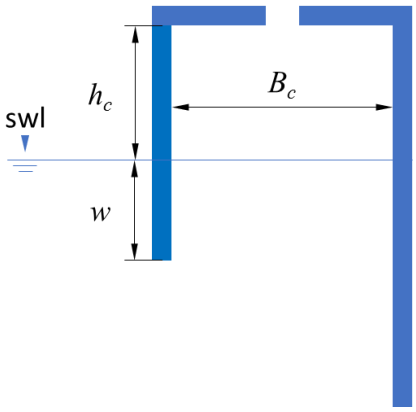

Figure 17 Most important geometries in designing an OWC chamber after Takahashi (1988): chamber width (B_c), submerged front wall (w), and chamber height (h_c).

Takahashi (1988) recommends several values for the OWC installed breakwater design based on the hydrodynamic efficiency and structural stability as follows: B_c equal to about 0.13L (wavelength), w equal to about 0.25H_{max} (highest incident wave height), and h_c equal to about 1.0H_{m0}. The chamber width is about 0.17L. The submerged front wall is about 0.3 H_{max}. The chamber height (crest freeboard) is selected to be about 1.2 H_{m0} to reduce the wave overtopping possibility (Bourke, 2013).

For the experiment, eight wave gauges measured the wave conditions: four wave gauges (WG01-04) were located at the full depth zone where the bottom is flat; the other four wave gauges (WG05-08) were located 1 m in front of the structure where the bottom has a 1:6 inclination. These arrangements allow the wave reflection to be analysed using both 3 probes method and 4 probes method – see Mansard and Funke (1980); Faraci *et al*. (2014). If it can be imagined that the reflected wave is the amount of incoming energy being reflected back into the ocean, then the power take-off setting which resulted in the least wave reflection, "absorb" the most of that energy, thus has the highest efficiency. The wave reflection analysis results conclude that under irregular waves conditions, the 0.2m orifice diameter yields the least reflection and therefore optimum energy extraction (Viviano *et al*., 2016). Five further wave gauges (WG09-13) are located inside the caisson chamber – one close to each corner and one in centre of the chamber – to measure the water surface elevations inside the chamber.

A line of five pressure transducers were placed vertically on the front wall facing outside (P1-P5) and on rear wall facing into the chamber (P8-12). Two pressure sensors are mounted in the ceiling facing down into the chamber (P6 and P7). Figure 19 (a) and (b) show the photograph of the facility where the experiments were done, along with the three identical structures used for the experiment before the installation of the load-bearing front wall. Figure 19 (c) shows the inside view of the caisson chamber. The lines drawn on the wall represent the distance from the ceiling. The orifice used to provide damping was mounted 1.4m above the chamber ceiling, in a 0.5m diameter 'chimney' above the centre of the chamber, both to avoid influence of overtopped water and to enable the orifice to serve the additional purpose of giving a further (approximate) measure of air flowrate. Figure 20 shown the complete structure

with the front wall just before the experiment (a) and during the experiment with an additional "stop log" installed on the very top of the wall (b) to avoid wave overtopping. The front wall of the structure was formed of a "stop log" previously used by the facility to dam the flume, which was thicker than the chamber wall and anchored at both sides of the flume. Although only the central chamber (of the three) was instrumented, other two chambers were hydraulically identical, with the same PTO arrangement and setting.

In the operating condition, the air damping characteristics inside the chamber will change depending on the power-take-off (PTO) resistance. To vary the damping characteristic of the PTO, five different orifice diameters were used = 0.05m, 0.1m, 0.2m, and 0.3m. In addition, a fully closed caisson chamber (orifice diameter = 0m) was tested. The 0.3m orifice approximates the fully open condition, offering very little resistance to the air flow. The opening diameters from 0.05m to 0.2m represent the operating conditions.

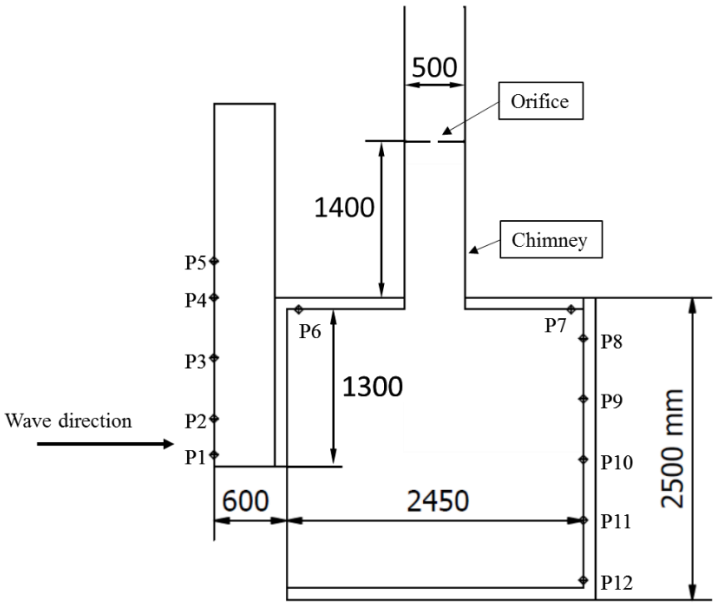

Figure 18 Detailed longitudinal section of the OWC device. P1 to P12 indicate the location of the pressure transducers used during the experiments. All the dimensions are in mm.

(a)

(b)

(c)

Figure 19 Photos of (a) the GWK facility, (b) Three structures of the OWC caisson tested, and (c) Inner view of the caisson chamber.

(a)

(b)

Figure 20 The complete structure (a) before the experiment and (b) during the experiment with an additional board installed on the very top of the wall to avoid wave overtopping.

3.1.3 Tested wave conditions

Both regular and irregular waves were generated at various wave steepness as shown in Figure 21 (a) and (b) respectively. The dots represent the test setting used, while various coloured solid lines represent various wave steepnesses. These wave conditions were selected to cover range of wave steepnesses with the limitation of the wave generator capability. The further detailed tested wave conditions along with the reference name are listed in Table 1 for the regular waves and Table 2 for the irregular wave conditions with T represents the wave period in regular wave condition and T_p represents the significant wave period in irregular wave condition. The irregular waves were generated using JONSWAP spectrum with a peak enhancement factor (γ) of 3.3.

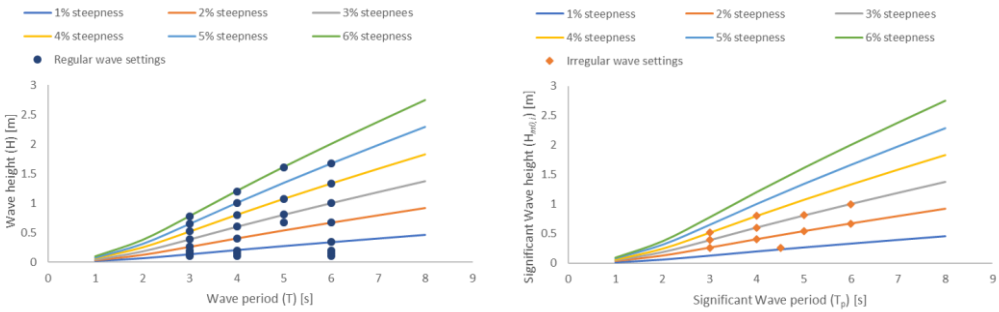

(a) (b)

Figure 21 Wave conditions used for the experiments at various wave steepness for (a) Regular wave, and (b) Irregular wave.

Name	GWK	
	T [s]	H [m]
Reg01	3.0	0.26
Reg02	3.0	0.39
Reg03	3.0	0.52
Reg04	3.0	0.65
Reg05	3.0	0.78
Reg06	4.0	0.40
Reg07	4.0	0.60
Reg08	4.0	0.80
Reg09	4.0	1.00
Reg10	4.0	1.20
Reg11	5.0	0.67
Reg12	5.0	0.81
Reg13	5.0	1.07
Reg15	5.0	1.61
Reg16	6.0	0.67
Reg17	6.0	1.00
Reg18	6.0	1.33
Reg19	6.0	1.67
Reg20	6.0	0.34
Reg21	3.0	0.20
Reg22	3.0	0.15
Reg23	3.0	0.10
Reg24	4.0	0.20
Reg25	4.0	0.15
Reg26	4.0	0.10
Reg27	6.0	0.20
Reg28	6.0	0.15
Reg29	6.0	0.10

Table 1 Large-scale (GWK) regular sea states.

Name	GWK	
	T_p [s]	H_{m0} [m]
Irr01	3.0	0.26
Irr02	3.0	0.39
Irr03	3.0	0.52
Irr04	4.0	0.40
Irr05	4.0	0.60
Irr06	4.0	0.80
Irr07	5.0	0.54
Irr08	5.0	0.81
Irr10	6.0	0.67
Irr11	6.0	1.00
Irr13	4.5	0.26

Table 2 Large-scale (GWK) irregular sea states.

3.2 Small-scale test (University of Edinburgh)

3.2.1 University of Edinburgh long wave flume

The small-scale experiments were carried out in the 20 m long University of Edinburgh long wave flume as shown in Figure 22. The schematic of the flume is illustrated in Figure 23. The waves were generated using a flap-type wave maker with good absorption capability based upon force feedback control. The sloping foreshore was made using two 3 m long boards made of plastic and installed in two different elevations angle as indicated in the figure. Since the depth of the long wave flume is not geometrically similar with the GWK facility, several modifications need to be made such as changing the leading foreshore to be 1:10 and adding a second slope to maintain the water depth on the front wall of the chamber to be scaled correctly with the large-scale model. It is also important to be noted that the dissimilarity in full water depth and in the foreshore angle may resulted in different wave conditions at the toe of the structure even though the nominal wave height and wave period are scaled down faithfully. For example, according to wave shoaling effect calculation proposed by Goda (2010), when the large- and small-scale wave period equal to 6s and 2s respectively, the wave height at the toe of the structure are about 1.17H and 1.12H for large- and small-scale respectively. Here H denotes the wave height measured on the deeper side of the flume or the nominal wave height.

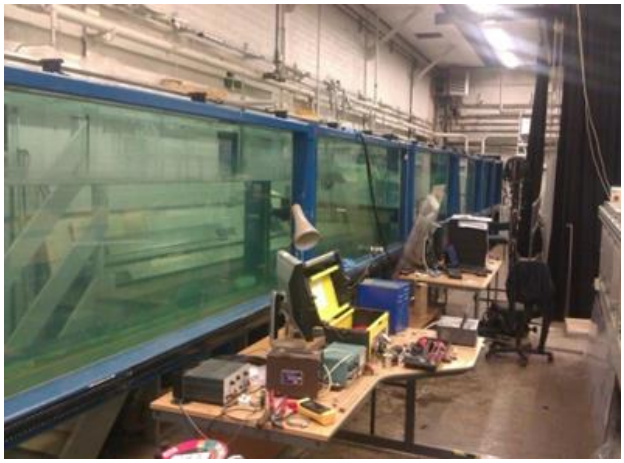

Figure 22 Image of the UoE long wave flume for the experiment.

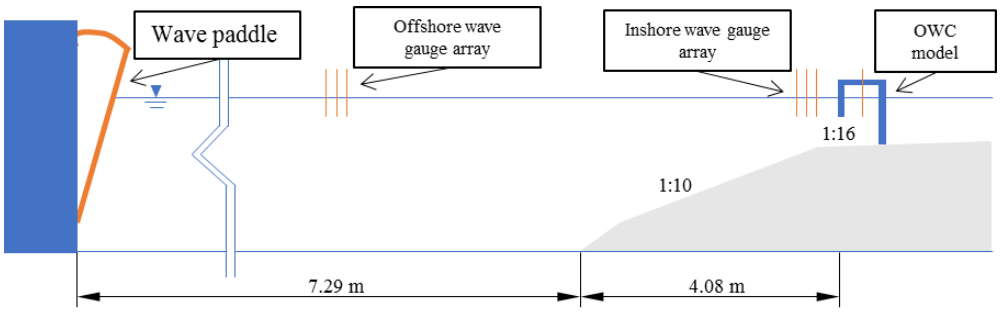

Figure 23 Schematic diagram of set up for small-scale tests.

The wave paddle is capable of producing wave heights of up to 0.12m, and wave periods in the range of 0.5s to 3s. According to Airy wave theory, the wave occurred on the still water depth (h) of 0.7m is classified as transitional wave on the deeper part of the flume and shallow wave on the fore-slope part in front of the structure.

3.2.2 Small-scale physical model

The small-scale physical model is approximately 1:9 ratio to a single chamber in the large-scale model as shown in Figure 24 with T1-T8 indicate the location of pressure transducer and dimension is shown in mm. This ratio is selected to match the wave flume wave height and wave period generation capability and to ensure the incident wave experienced by the structure remains unaffected by the side walls of the flume. Because both the small-scale and the large-scale experiments are strictly 2-D, there is an assumption that the chamber widths are not important, and no attempt was made to replicate the GWK width at small scale. The cross-sectional dimensions are shown in Figure 25 in details with dimension shown in mm and the diamond mark indicates the location of the pressure transducer (PT). The small-scale model was made of clear perspex which as a typical Young's Modulus range in between 2.7-3.3 GPa. The large-scale physical model, on the other hand, was made of concrete with typical Young's Modulus range in between 10-30 GPa. Because the stiffness can be scaled linearly, the small-scale model's stiffness is enough to represent the large-scale model stiffness. Although the resonant frequency of both GWK and UoE structures was not measured directly, even under wave impact, no evidence of the structures' oscillation could be discerned in the pressure transducer signals, indicating frequencies higher than the sampling frequencies of 1000 Hz for both large- and small-scale tests.

The model utilised pressure transducers (PTs) to measure the wave loads on the front wall, rear wall, and ceiling. Due to the limitation of space, only 3 PTs can be placed on the front wall: one PT placed 50 mm below the still water level and 20 mm above the front opening (T1), one PT placed on the still water level (T2), and one PT placed 50 mm above the still water level (T3). As suggested by the conventional vertical breakwater pressure distribution, is it expected for the highest wave pressure to be located on the still water level (swl) and less above and below the swl. This configuration was selected to get the representative pressure points of the pressure distribution which includes the highest-pressure point. The three pressure transducers located on the rear wall (T4-T6) are all below the swl in accordance to the water pressure distribution postulated by Preen and Robertshaw (2010). The last two pressure transducers (T7 and T8) are located on the centre of the ceiling to measure the chamber pressure. It is expected for the chamber pressure to be the uniform inside the chamber, so theoretically only one PT is needed. The location of the PT, however, can't be placed on the centre of the chamber due to the orifice opening, so the PT has to be placed near the side wall. Due to this limitation, another PT is placed on the same lateral position but near the opposite chamber wall to ensure the uniformity of the chamber pressure measured.

The physical model air chamber is 290 mm height, 285 mm wide, and 280 mm long, and equipped with an orifice opening installed in the centre of the ceiling. Similar to the large-scale model, the orifice opening plate can be changed. This allows multiple orifices plate diameter to be used to simulate different Power Take-Off (PTO) resistance during the experiment.

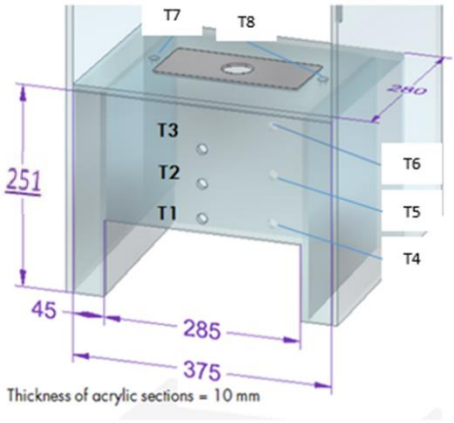

Figure 24 3-D image of the small-scale physical model used with dimension in mm and T indicates the pressure transducer location.

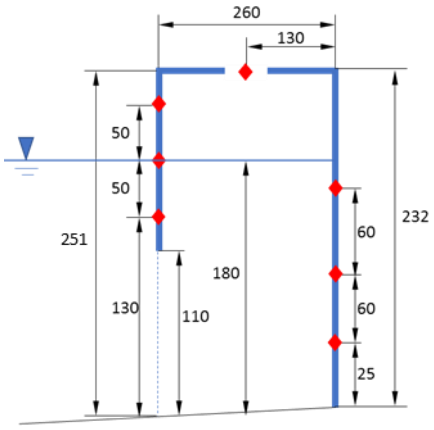

Figure 25 Cross-section of the small-scale physical model used with dimension shown in mm.

3.2.3 Power take-off simulation and instrumentations

The experiments utilised 8 different orifice diameters ranging from 0 mm (fully closed) to 75 mm (fully open) to simulate the power take-off resistance. For simplification, the orifice size will be presented as the orifice:chamber area ratio percentage (A_o/A_c). Figure 26 shows the range of orifices used starting from: (a) 6.18%, (b) 3.95%, (c) 2.22%, (d) 0.99%, (e) 0.44%, (f) 0.25%, (g) 0.11%, and (h) closed orifice (0%). It should be noted that the circular orifice area will have a quadratic connection between the chamber pressure generated and the diameter of the orifice, instead of the linear relationship expected for a Wells turbine.

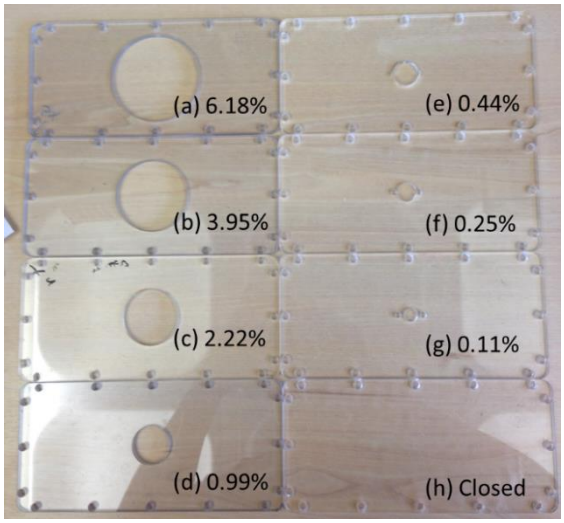

Figure 26 Photograph of the eight rectangular plates which can be selected for the roof of the chamber.

To measure the wave height up to seven Edinburgh Designs resistance-type wave gauges were used. Three wave gauges were installed in front of the structure on the shallow part, and another three wave gauges were installed in the deeper part of the flume. The distance between the three wave gauges and the location of the wave gauges from the model were varied in accordance to the wavelength of each wave condition. Another wave gauge is installed at the middle of the small-scale model in order to measure the wave movement inside the chamber with the exception of closed chamber case. The in-chamber wave gauge was placed through the opening orifice, so it is practically impossible for the closed orifice to use the same method without compromising the airtight characteristics of the chamber. For the orifice diameter smaller than the wave gauge dimensions, two small holes with diameter of 5 mm was drilled. The gap area between the edge of the hole and the WG is very small relative to the orifice opening area, thus can be neglected.

The wave height measurement was done twice, once without the model installed and another one with the model installed during experiment. When the model is removed, the wave gauge used to measure the water height inside the chamber is moved to the position of the front wall. This is necessary to measure the incident wave height without any wave reflection caused by the physical model. It needs to be noted,

however, there is still a minimum wave reflection from the slopping foreshore installed.

Since the water level recorded is the water level on the shallow part of the water in front of the structure, the wave height recorded will be slightly different with the nominal water level on the setting. For all of the calculation in this thesis, the incident wave height will be utilised instead of the nominal wave height.

The resistive type wave gauges will produce an output voltage as the measurement signals. This signal needs to be translated into water level by means of electrical voltage difference (ΔE) to water level difference (Δh) calibration. The calibration is done by recording the voltage output of the wave gauge at several known water levels. The recorded ΔE for each water level then plotted against the calculated Δh. Figure 27 shows an example of the calibration result with the data points (solid circle) and the linear regression line (dotted line). The data shows a very good agreement between the data points and the regression. The calibration water level range was always similar with the measurement range for this study to ensure the accuracy of the water level measurement during experiment. The calibration was carried out at least once a day before the first test.

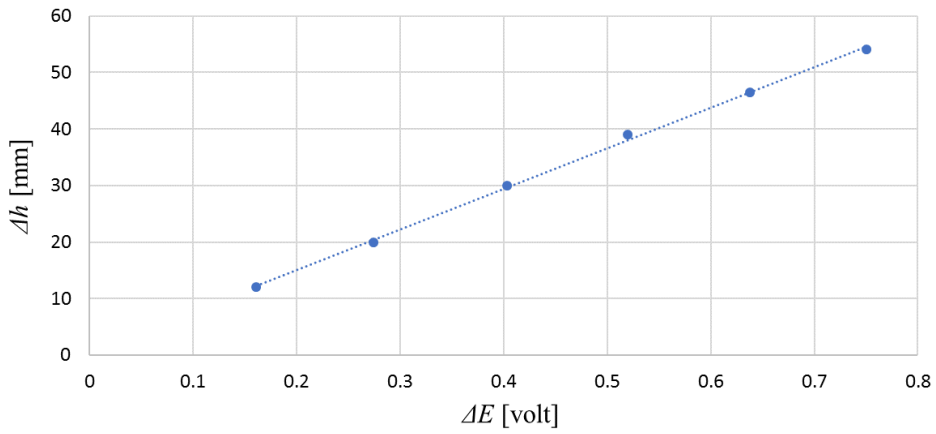

Figure 27 Calibration results for the resistant-type wave gauge used for the experiment.

The eight pressure transducers used for the experiment are the General Electric Druck sensing type PDCR 1830 pressure sensors. This type of PT has the maximum pressure measurement of 7.5kPa with pulse power excitation of 10ms. The maximum wave induced pressure anticipated in this investigation is below the limit capability of the

pressure transducer. According to the manufacturer's data sheet, the sensors have a combined effect of non-linearity, hysteresis, and repeatability of 0.06% maximum for pressure measurement up to 7.5kPa which is higher than the pressure measured in current experiments.

One problem encountered during the experiment is the position of the pressure sensor of the pressure transducer. The pressure sensor is recessed and the thread to fasten the sensor to the physical model was located on the outer side of the recessed wall. Figure 28 shows the original design of the pressure transducer. The problem occurs when there is an air volume trapped in the flush while the incident wave hit the front wall or the rear chamber wall. This condition leads to an uncertainty in the measured pressure, and at the same time will cause a vibration signal for the pressure data recorded due to the oscillation of the small pocket of trapped air. In the event of an impact, furthermore, the flush would protect the sensor from measuring the actual impact pressure which probably leading to an under-estimation of the actual impact pressure. A modification then had to be made in order to remove the flush and add a new thread. Figure 29 show: (a) the modified pressure transducer and (b) when they are installed to the physical model's wall. A small recessed is still visible, but no further modification can be made without risking damage to the pressure sensor. Because the outer front surface of the pressure sensors was positioned flush with the front wall surface, there is an unavoidable small gap, in the plane of the wall, around the circumference of the sensor's membrane.

Figure 28 Image of the original pressure transducer used with the pressure sensor protected by the flush.

(a)

(b)

Figure 29 (a) The modefied pressure transducer with the pressure sensor exposed and protective flush removed and (b) when it was mounted on the front wall of the model.

A common sealant tape is used to make sure there is no leakage between the pressure transducer and the structure's mount. A leakage test is done before the actual

experiment is started. The leakage test was done by turning the assembled structure upside down and fill it with water. Figure 30 demonstrates the process. The test showed no water leakage on the chamber. Because the maximum in-chamber air pressure during operation is less than the water pressure acting on the ceiling surface during the leakage testing, it is safe to assume the chamber is airtight under closed chamber condition.

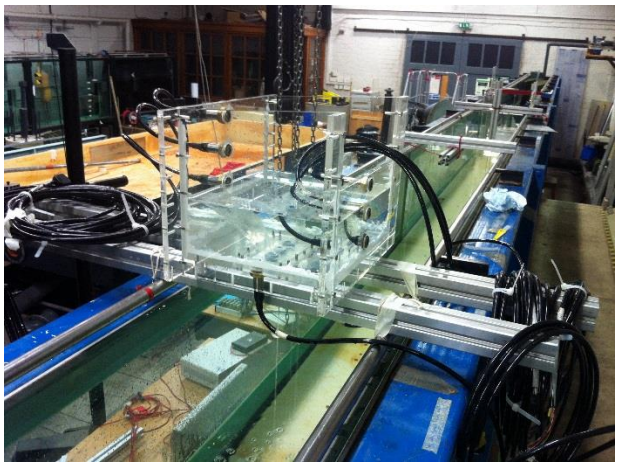

Figure 30 Leakage testing of the small-scale physical model.

To ensure the static pressure accuracy, the pressure transducers were calibrated by varying the water level in flume and positioned each pressure transducer in a specific location to measure the hydrostatic pressure of that particular position. The calibration then done by comparing the output voltage (ΔE) given by the transducers with the difference in hydrostatic pressure (Δp) given by different known water level. Figure 31 shows an example of one of the pressure transducer calibration result. Similar to the wave gauges, the calibration pressure range was also similar to the measurement range and done at least once a day prior to the first test of the day.

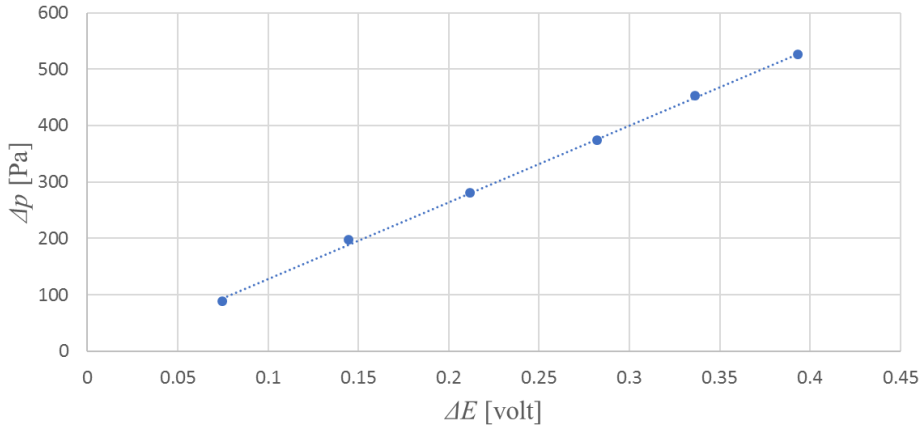

Figure 31 Calibration example results for the pressure transducer.

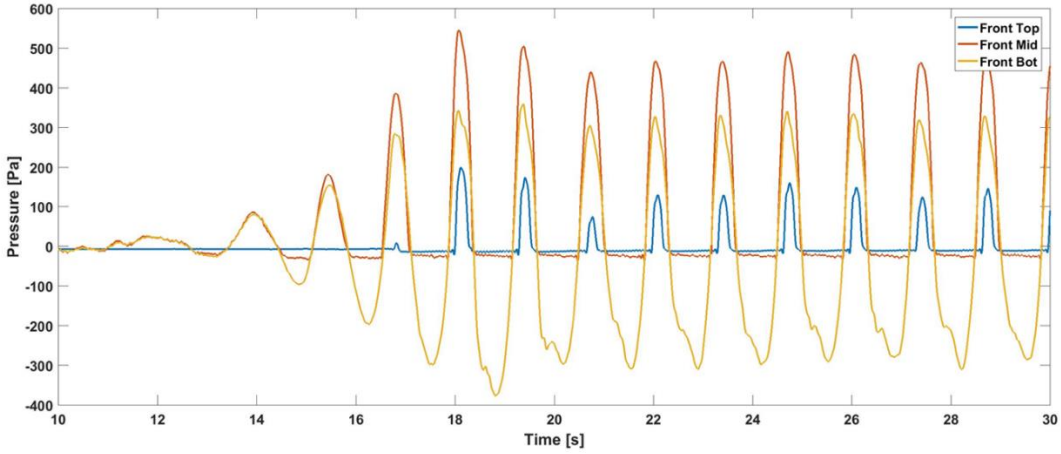

Figure 32 Pressure measurement example for the front wall at various elevation during the regular wave testing.

Figure 32 shows an example of the front wall pressure measurement for a regular wave condition. In the figure, y-axis shows the pressure measurement in Pascal and x-axis shows the time in s. It should be noted that zero value indicates the still water level condition of all pressure transducer measurement. Since the middle and the top pressure transducer is located above the still water level (and on still water level), zero value means the atmospheric pressure when the test was carried out. The bottom pressure transducer, on the other hand, located below the still water level, so zero pressure indicates the hydrostatic pressure correspond to the location of the PT

(relative to the swl) and the negative pressure shown here means the water level at that particular time is below swl.

An additional video camera was also deployed outside of the flume facing the structure from the side. Unlike the large-scale model, the small-scale is constructed with a clear perplex. The flume wall is also constructed with a clear glass. These materials enable the video camera to be placed outside the flume and the in-chamber water column condition visible in the recording.

3.2.4 Tested wave conditions

This experiment utilised two different sets of the wave condition; the regular wave conditions and the irregular wave conditions for a range of wave steepnesses as shown in Figure 33 for both (a) regular wave conditions (solid circle) and (b) irregular wave conditions (solid diamond). The irregular wave conditions were generated with JONSWAP spectra and peak enhancement factor (γ) equal to 3.3. The nominal wave conditions were selected to replicate the large-scale physical model test and includes the (nominal) wave steepnesses of s_w = 0.01, 0.02, 0.03, and 0.04. Unfortunately, due to the limitation of the flap paddle wave generator, not all of the wave condition tested in the large-scale physical model test could be replicated, especially the one with higher wave height or longer wave period than the wave paddle capability. Table 3 and Table 4 list the sea state code name, wave height, and wave period for the experiment.

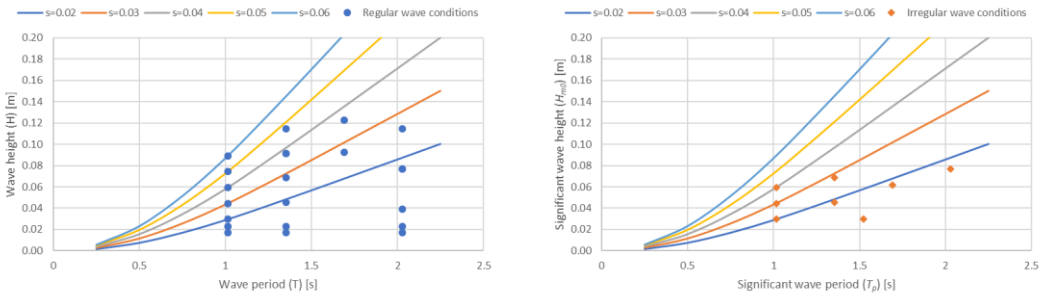

(a) (b)

Figure 33 The wave steepness conditions used for the experiment for (a) regular wave (solid blue circle) and (b) irregular wave (solid orange diamond) conditions.

Name	UoE	
	T [s]	H [m]
Reg01	1.01	0.03
Reg02	1.01	0.04
Reg03	1.01	0.06
Reg04	1.01	0.07
Reg05	1.01	0.09
Reg06	1.35	0.05
Reg07	1.35	0.07
Reg08	1.35	0.09
Reg09	1.35	0.11
Reg10	1.35	0.09
Reg11	2.03	0.08
Reg12	1.69	0.09
Reg13	1.69	0.12
Reg16	2.03	0.08
Reg17	2.03	0.11
Reg20	2.03	0.04
Reg21	1.01	0.02
Reg22	1.01	0.02
Reg24	1.35	0.02
Reg25	1.35	0.02
Reg27	2.03	0.02
Reg28	2.03	0.02

Table 3 Small-scale (UoE) regular wave sea states.

Name	UoE	
	T_p [s]	H_{m0} [m]
Irr01	1.01	0.03
Irr02	1.01	0.04
Irr03	1.01	0.06
Irr04	1.35	0.05
Irr05	1.35	0.07
Irr07	1.69	0.06
Irr10	2.03	0.08
Irr13	1.52	0.03

Table 4 Small-scale (UoE) irregular sea states.

Both Pressure and wave height data were taken using National Instrument Data Acquisition system (DAQ). For the regular wave conditions, the sampling frequency was 2000 Hz in order to capture any impact pressures that may happen on the front wall and the back wall. All of the regular wave test uses the same recording duration of 90 seconds. This duration was chosen to make sure each test has at least five stable wave cycles.

For the irregular wave condition, on the other hand, the observation was done for at least 1000 wave cycles. The duration of the recording varies depending on the significant wave period, so it varies between 15 minutes to 27 minutes. The sampling rate for the irregular wave condition it is limited to between 500 Hz and 1000 Hz depending on the period of the recording due to limitation on the recording and processing memory. It is understood that lowering the sampling rate may increase the risk of not capturing the maximum impact pressure should the corresponding impact rise time is faster than the frequency of the recording. Figure 34 shows an example for the highest impact rise time in this experiment recorded. The x-axis shows the time in seconds and the y-axis shows pressure measurement in pascal. In this example the rise time is measured to be 0.0086s which is more than twice the sampling interval of 0.004s (500 Hz), thus fulfilling the Nyquist criterion. It is safe to say that 500 Hz is enough to capture the impulsive pressure during this test. The DAQ system is shown in Figure 35 with [1] showing the Pressure Transducer connector, [2] showing the National Instrument Data Acquisition System, and [3] showing the Edinburgh Design wave gauge box.

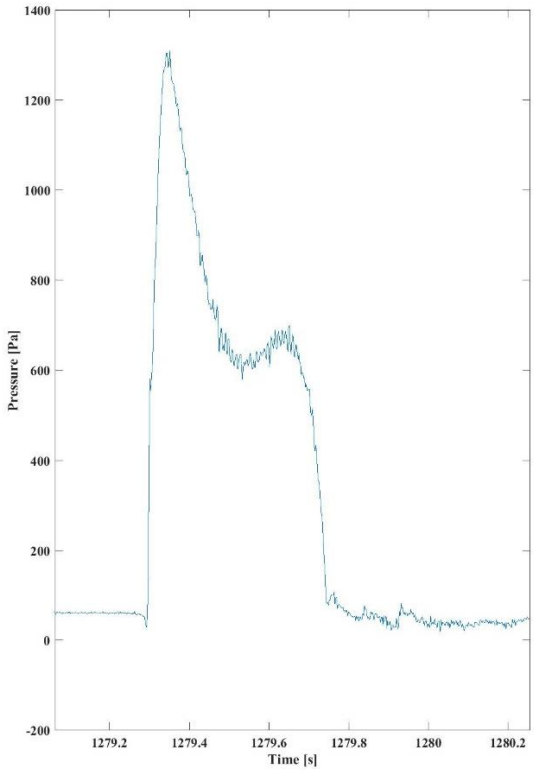

Figure 34 Pressure measurement on the still water level of the front wall with T_p = 2.01s and H_{m0} = 0.08m.

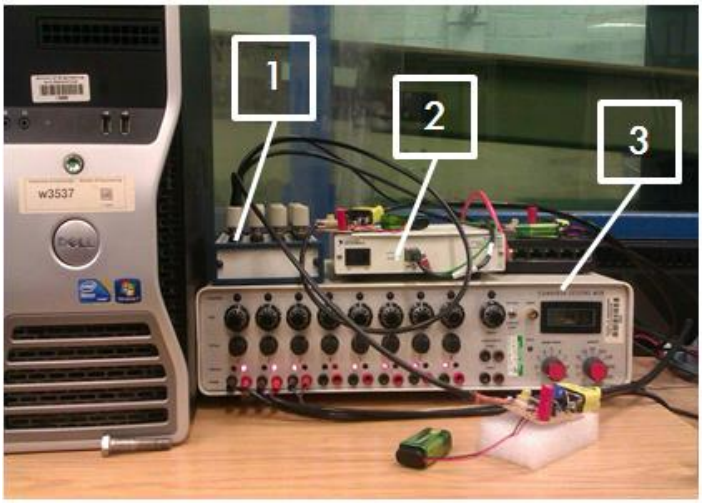

Figure 35 The Data Acquisition System used for both the wave gauges and pressure transducers measurement: (1) pressure transducer connector, (2) National Instrument® Data Acquisition System, and (3) Edinburgh Design® wave gauge box.

3.3 Force calculation consideration and method for measurement results

The force calculation used in this study is a conservative model with the pressures acting seaward on the inside of the front wall are not considered. These pressures will be small compared to the landward front wall and rear wall pressures, and in any case, would reduce the sliding and over-turning moment of the structure, thus improving the structure stability. The areas included in the force acting on the structure are illustrated by the blue arrows in Figure 36.

One wave cycle is defined using zero-up crossing method as illustrated in Figure 37. This method assumed a single wave cycle to start when the water level rises up from the still water level from below. It then ends when the water reaches the still water level from below. Model validation in regular and irregular seas will be done separately but using the same methodology.

The force calculation for the model is done using a 2D integrated pressure method. The experimental force, on the other hand, will be calculated using centred rectangle method. This method assumes a pressure measurement at the transducer location to be representative of the pressure over an associated area. The scheme is illustrated in Figure 38, with the integrated pressures (*i.e.* contributing forces) (F_{meas}) for N number of sensors calculated using Equation 5. The rear wall force calculation uses the same method as used for the front wall.

There are two ways to explore and quantify forces for design, both of which could be interesting. The first way is to calculate the integrated pressure at each time step to give a time history of total forces on the rear wall and ceiling. The second way takes the worst-case approach using the maximum pressure identified for each pressure transducer location (which will not in general be simultaneously experienced). These forces then integrated to give the maximum imaginable forces on the rear wall and chamber ceiling.

$$F_{meas} = \sum_{n=1}^{N} F_n = \sum_{n=1}^{N} (X_n - X_{n-1}) p_n \quad (5)$$

Here p_n denotes the pressure measured at the location X_n. For the large-scale test example, N is equal to 5 for the front wall and the front wall higher than X_5 is not

considered for the for calculation. For the rear wall, *N* is equal to 5 and X_5 is equal to the chamber ceiling. For the small-scale's front wall, *N* is equal to 3 and the front wall higher than X_3 is not considered. For the rear wall, *N* is also equal to 3 and since the PTs are only positioned below the still water level, X_3 is equal to swl.

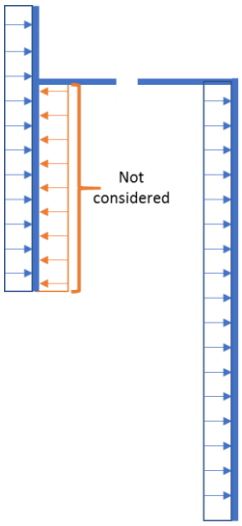

Figure 36 The area considered for the force calculation, the area of the front wall facing the chamber is not considered.

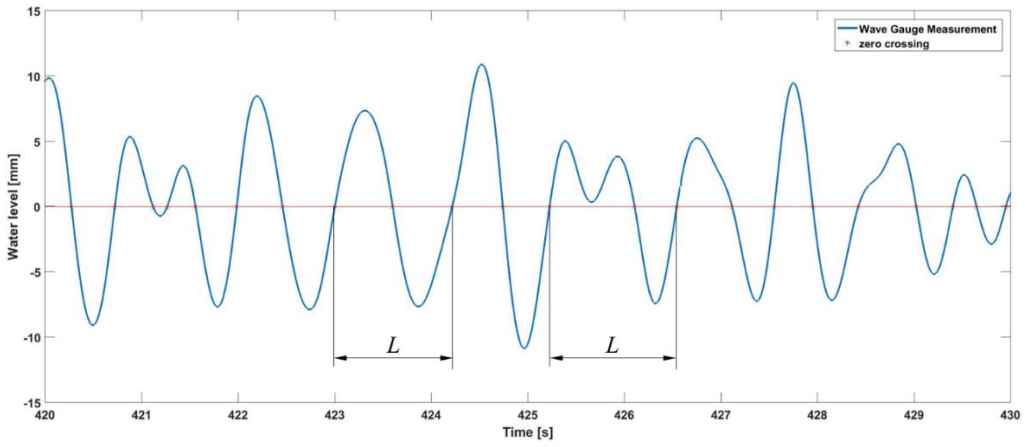

Figure 37 A single wave length (L) based on the zero up-crossing method.

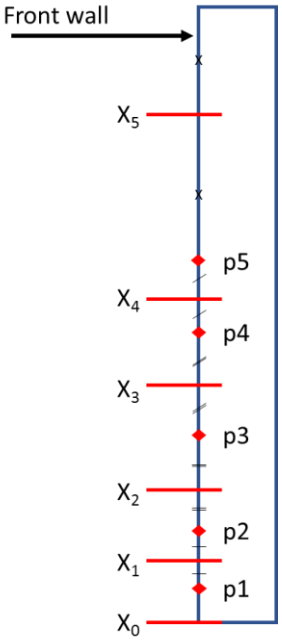

Figure 38 The interval calculation for the rectangular integrated pressure method.

4 In-chamber wave loading and air chamber pressure conceptual model and validation

There are wide and trusted literatures that discuss the pressure distribution of a conventional vertical breakwater against sliding or overturning due to wave loads. For OWC installed breakwater, however, there is no such established method in the literature. Additionally, there is almost no literature exploring the pressures inside the OWC chamber. A prediction tool for the loadings experienced by an OWC caisson must in addition contain a prediction tool to give practical and conservative estimates of the pressure distributions which occur inside the chamber such as on the rear wall and on the ceiling. Only with all of these can the whole structure of OWC installed breakwater be designed for stability.

This chapter introduces a prediction model to enable the estimation of the pressure distribution on the real wall and the caisson ceiling. The starting point is the development of a conceptual model for these forces based upon physical rationale, in turn based upon established methods. For this model, the water column is assumed to be well behaved without sloshing, and the water level inside the chamber is assumed never to reach down to the 'lip' of the front wall, *i.e.* no 'venting' occurs. The pressure acting on the inside of the front wall curtain will have an opposite direction with the pressure acting on the rear wall, so it is safe to assume that calculating this pressure can only increase the stability of the overall structure. This condition allows the conceptual model to add a degree of safety by removing the pressure estimation acting on the inside of the curtain wall from the integrated pressure (force by metre run equation).

The conceptual model for in-chamber pressure estimation is described in the following sub-sections.

4.1 Proposed model and definition

Goda (2010) presents an estimation method for design wave loads for a conventional vertical breakwater. The conceptual model proposed in this section adopts the Goda pressure estimation method as the starting point of the calculation. F_{Goda} is taken as

the force estimation acting on the front wall of an ordinary breakwater calculated using Goda (2010). The pressure occurring on the rear wall of the OWC chamber then can be postulated as a result of a wave momentum transmitted under the front wall of the structure. This situation is therefore closely similar to the situation of a skirt breakwater as shown in Figure 39. As can be seen from the figure, the breakwater in this case does not reach the local seabed. This situation is not dissimilar with the water before and after the front wall of an OWC installed breakwater structure and is therefore used as a tentative basis for the conceptual model.

Kriebel & Bollman (1997) introduced a transmission coefficient (K_t) for the skirt breakwater. The method calculates K_t based on the in-chamber water depth (d), wave length (L), and the submergence depth of the front wall (skirt) into the water (w). The K_t calculation is adopted in this conceptual method, given by Equation 6 and 7 with w/d defined as the *wall penetration factor*. In accordance to Kriebel & Bollman (1997), the wall penetration factor is only considered up to 0.9, because it is assumed that at higher factor, no wave momentum will be able to pass through the wall opening as if the chamber is fully shut. On the contrary, the wall penetration factor less than 0.3 is considered to have a negligible effect to the transmitted wave momentum as if the front wall does not exist. In summary, the calculation processes can be seen in Figure 40.

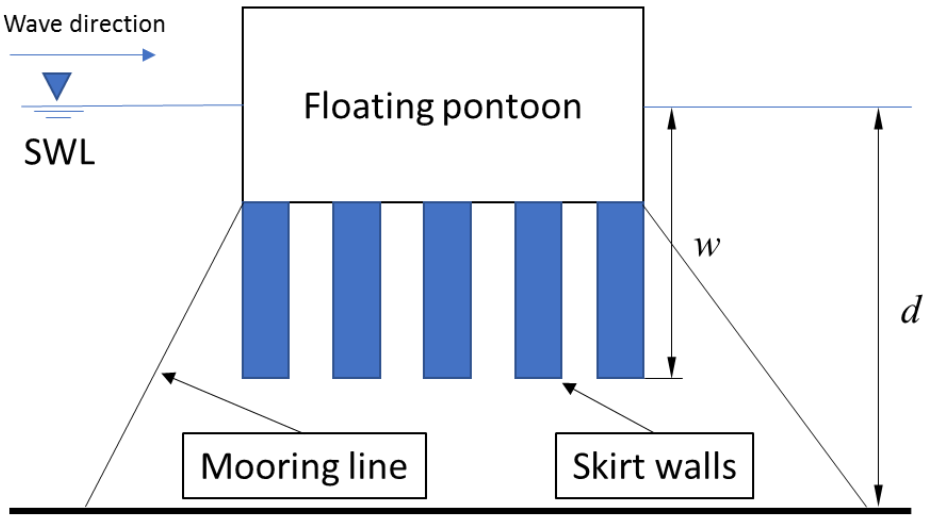

Figure 39 Skirt breakwater schematics.

$$0 \leq \frac{w}{d} \leq 0.3 \rightarrow \quad K_t = 1 \tag{6}$$

$$0.3 < \frac{w}{d} \leq 0.9 \quad \rightarrow \quad K_t = \frac{0.81-0.7(^w/_d)}{0.6} \tag{7}$$

$$\frac{w}{d} > 0.9 \rightarrow \quad K_t = 0 \tag{x}$$

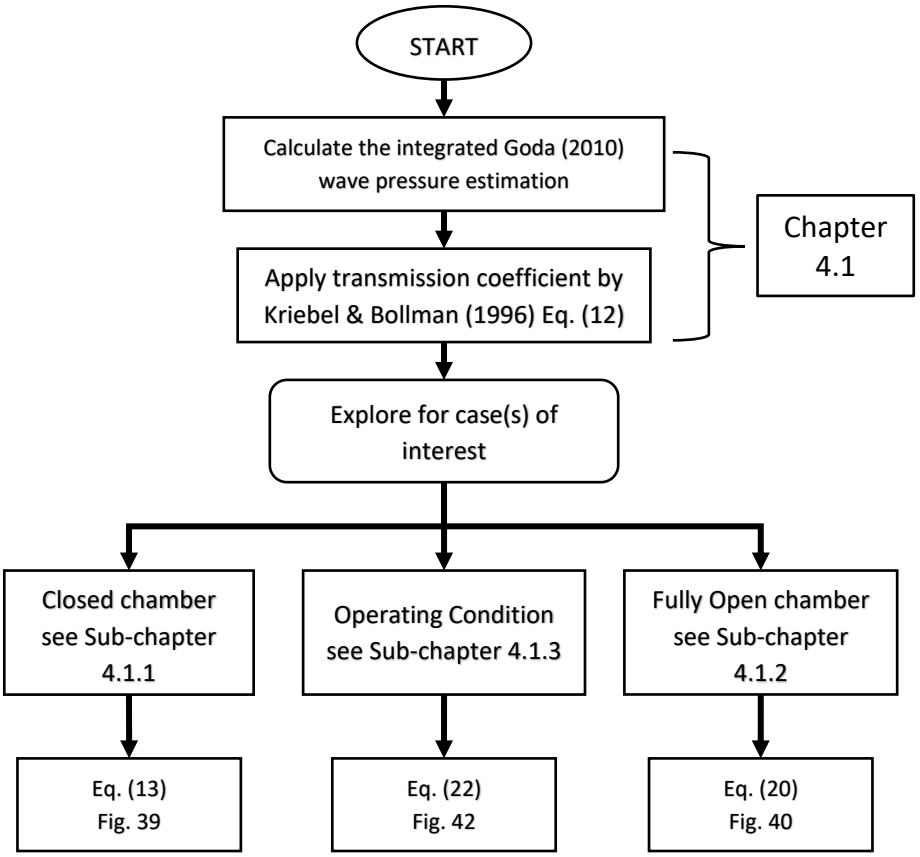

Figure 40 The flowchart of proposed model calculation process.

If F_{rw} is taken as the total transmitted force, then the relationship between F_{Goda} and F_{rw} can be expressed using Equation 8.

$$F_{rw} = F_{Goda}.K_t \tag{8}$$

Because Equation 7 only estimates the total transmitted force acting on the rear wall of the OWC chamber, the next step is to postulate the pressure distribution acting of the rear wall of the OWC chamber. This pattern may change significantly depending on the power take-off (PTO) resistance. A realistic resistance, however, should lie between the two extreme conditions of a closed OWC chamber (100% PTO resistance) and a fully open chamber (0% PTO resistance). It is practical and useful to discuss

initially these extremes in 4.1.1 for closed chamber and 4.1.2 for fully open chamber. After this, an intermediate “operating condition” is explored in 4.1.3.

4.1.1 Closed chamber condition

The fully closed chamber means there is no air movement into or out of the chamber, with the consequence that water movement into or out of the chamber is minimal, depending on the air compressibility characteristics inside the chamber. As a result, it can be anticipated that this closed condition will result in the highest chamber pressures. Whilst air is inherently compressible, the hydraulic forces in small-scale tests are very small in absolute terms so the air in the (model) OWC chamber will be very stiff relative to the (model) wave forces. In effect, small scale air can be treated as incompressible (Weber, 2007, Dimakopoulos *et al*. 2017). The motion of water level within the chamber is minimal and can therefore be assumed to be stationary. Because the in-chamber water is not moving into or out of the chamber, pressure variations due to velocity and cyclical / rotational motions that would create a non-uniform distribution are not expected to occur. Hence the wave pressure will transmit as an increment to the hydrostatic pressure at still water level and will be uniform in both air and water phases, giving a rectangular pressure distribution for the transmitted force (F_{rw}) acting on the rear wall as shown in Figure 41.

Here F_{Goda} denotes the front wall integrated pressure explained in the previous sub-section. Since the chamber pressure (relative to atmosphere) is driven by the dynamic water pressure, the chamber pressure will therefore be the same as the water pressure. Due to these similarities, the water pressure inside the chamber, denoted by p_c, can be calculated using Equation 9.

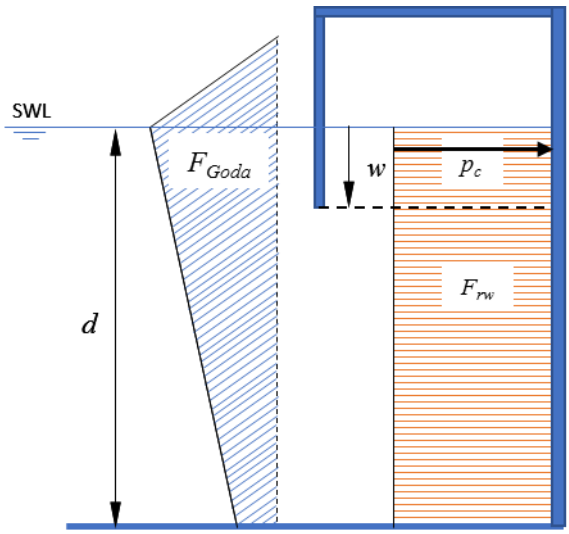

Figure 41 The pressure distribution schematics for the closed chamber case.

$$(F_{rw})_{closed} = K_t . F_{Goda} = p_c d \tag{13}$$

4.1.2 Open chamber condition

The other extreme condition of the system is the fully open condition. In this case, air damping in the chamber will be zero and pressures inside the chamber will remain very close to atmospheric. This condition, then, allows the water inside the chamber to move freely up and down depending on the transmitted wave height without any chamber pressure being generated. Since water motion will only be driven by the wave height transmitted into the caisson. The conceptual model takes the pressure distribution inside the chamber to be similar to the pressure distribution on the front wall. The pressure distribution on the rear wall for the fully open case is illustrated in Figure 42 together with annotations showing key parameters. The distribution follows the Goda distribution with the pressure loss due to wall penetration incorporated in the calculation. In this model, H_{tr} which denotes the transmitted wave height is introduced in Equation 10. Equation 11 and 12 define the coefficients α_{swl} and α_{bot} to calculate the pressure acting on the still water level (P_{swl}) and the pressure acting on the rear wall bottom of the chamber (P_{bot}). The pressure at the still water level (P_{swl}) and the pressure at the bottom of the rear wall (P_{bot}) are given by Equations 13 and 14. The elevation to which the pressure distribution due to the transmitted wave extends is denoted by η_{tr}, calculated using Equation 15.

$$H_{tr} = H_{max}\, K_t \tag{10}$$

$$\alpha_{swl} = \left[0.6 + 0.5\left(\frac{4\pi h/L}{\sinh\left(4\pi h/L\right)}\right)^2\right] + \left[\min\left\{\frac{h_b - d}{3h_b}\left(\frac{H_{tr}}{d}\right)^2, \frac{2d}{H_{tr}}\right\}\right] \tag{11}$$

$$\alpha_{bot} = 1 - \frac{d}{h}\left[1 - \frac{1}{cosh\left(2\pi h/L\right)}\right] \tag{12}$$

$$P_{swl} = \alpha_{swl}\, \rho_w\, g\, H_{tr} \tag{13}$$

$$P_{bot} = \alpha_{bot}\, P_{swl} \tag{14}$$

$$\eta_{tr} = 1.5\, H_{tr} \tag{15}$$

Here h denotes the still water depth of the incoming wave in front of the structure, L denotes the deep-water wave length, and h_b denotes the water depth at 5H seaward of the structure.

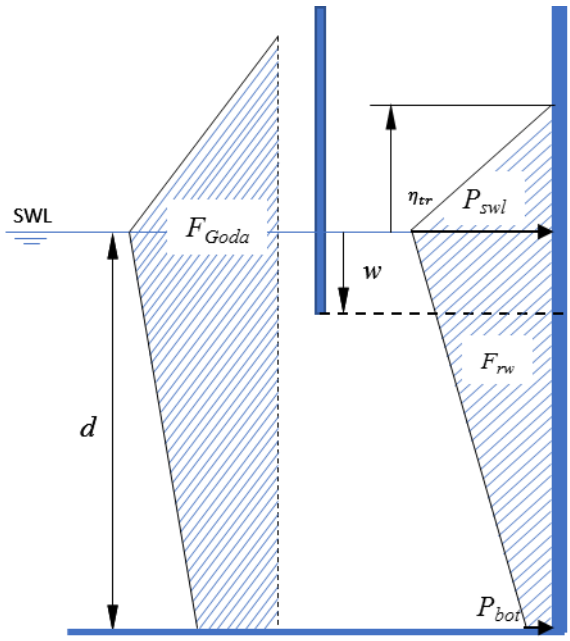

Figure 42 The pressure distribution schematics for the fully open chamber case

Based on the pressure distribution, Equations 13, 14 and 15 can be substituted to Equation 7 to give an expression for the total force on the rear wall, for fully open chamber (Equation 16).

$$(F_{rw})_{open} = 0.5\left((\eta_{tr} + d)P_{swl} + dP_{bot}\right) \tag{16}$$

4.1.3 Operating condition

As mentioned earlier, the "operating condition" indicates the condition where a power take-off resistance is considered and lies between the two extremes – open and closed – already modelled. Because it lies between the two extremes (0% < PTO resistance< 100%), the pressure distribution is also imagined to be an intermediate condition between the two. If the proportion of the closed chamber in the whole transmitted integrated pressure (F_{rw}) is denoted by P (with $0 \leq P \leq 1$), then the F_{rw} pressure distribution for this operating condition can be modelled as $(F_{rw})_{operate}$ (Equation 17).

$$(F_{rw})_{operate} = P(F_{rw})_{closed} + (1 - P)(F_{rw})_{open} \tag{17}$$

This equation combines both extreme conditions with the first term on the right hand representing the closed chamber pressure distribution and the second term on the right-hand side represent the open chamber pressure distribution. Note that the assumption of fixed chamber water elevation in Equation 8 is no longer applicable in the operating case, so the elevation η_{tr} needs to be included for the closed chamber influence. This adjustment makes the full pressure distribution in operating condition (Equation 18) with the adjusted η_{tr} being Equation 19.

$$(F_{rw})_{operate} = P\big(p_c(d + \eta_{tr})\big) + 0.5(1 - P)\big((\eta_{tr} + d)P_{swl} + dP_{bot}\big) \tag{18}$$

$$\eta_{tr} = \begin{cases} 0, \ if \ P = 1 \\ \min(1.5\, H_{tr}\, , h_c)\, , \ if \ 0 \leq P < 1 \end{cases} \tag{19}$$

Here h_c denotes the height of the chamber ceiling, since the water column surface elevation will not be able to exceed the chamber ceiling elevation. The proportion coefficient (P) varies depending on the air damping characteristic of the OWC chamber, which is ultimately related to the PTO resistance. A highly simplified relationship between the proportion coefficient P with the air damping characteristic can be imagined as that shown in Figure 43. According to this definition for this conceptual model, P = 1 means the chamber can be considered to be in a closed condition and P = 0 means the chamber can be considered to be fully open.

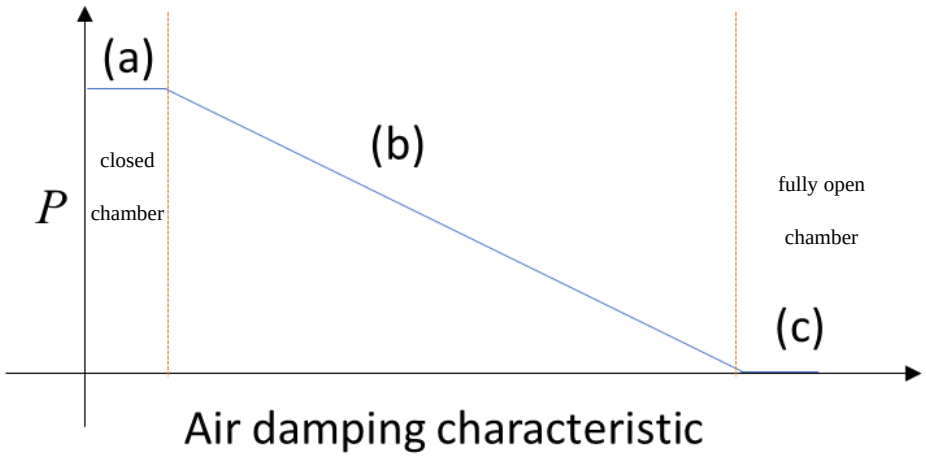

Figure 43 The P coefficient expected relation with the air damping characteristics divided into three zone: (a) the air damping reduction is small enough to be neglected with P = 1, (b) the air damping reduced toward zero leading to the chamber pressure reducing considerably with P=f(Air damping), and (c) the air damping is small enough to be considered as fully open with P=0.

Figure 44 (a) – (e) show the schematic diagrams of the pressure distribution on the rear wall of an OWC chamber formed in a vertical breakwater, with *P* ranging from 1, 0.75, 0.5, 0.25, and 0 respectively. The diagrams are schematics only but are intended to show the way in which the pressure distribution reconfigures, moving from closed chamber to fully open via a smooth transition through the "operating" region.

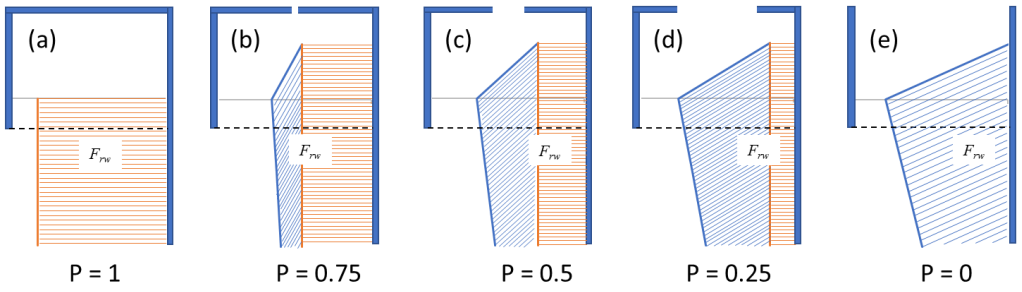

Figure 44 The pressure distribution schematics for the operating condition case at various proportion coefficient P values. Opening sizes exaggerated for illustrative purpose. P=1, subfigure (a) illustrate closed chamber, P=0 (e) illustrate fully open chamber, and (b) – (e) illustrate the intermediate cases identified as "operating cases".

4.2 Validation for regular wave conditions

To validate the proposed model, the large-scale physical model results are utilised. The large-scale model is selected because it is closer to how a prototype design act compare to the small-scale physical model and the wave generator for the large-scale experiments was able to produce a wider range of wave conditions. The measured force is calculated as described in Chapter 3.3.

4.2.1 Closed chamber condition

The effectiveness of the model is explored in Figure 45 in which the ratio of measured:predicted pressures, $(p_c)_{\text{measured}}$: $(p_{predict})$, for the fully closed chamber is plotted over the range of the wave steepnesses tested. Pressure transducers P6 and P7 at the chamber ceiling are averaged and used for the pressure comparison. Different symbols represent different wave periods. The solid line here represents perfect agreement, so that points above the line are unsafe (under-estimation) and the points below the line are safe (over-estimation). The agreement is generally very encouraging, with all data lying within a factor of approximately 1.25 of the predictions.

Moving from the pressures to the forces, Figure 46 shows the ratio of the measured forces to those predicted by the model. As expected, the results do not differ too much from the those for the pressures because this case assumed that the momentum from the incident wave is transmitted instantaneously to the rear wall and distributed uniformly on the rear wall, as proposed in Sub-section 4.1.1. Although there a few more points above the line (unsafe), all data is still within the factor of 1.25. These results give confidence in the model for the fully closed condition.

Figure 47 (a)-(c) illustrate pressure distributions acting on the rear wall for the model (solid line) and the measurements (solid circles). Here pressures are plotted against the vertical elevation of the corresponding pressure transducer. As expected, Figure 47 (a) and (b) show that the calculated pressures don't differ too much from the measurements because this case assumed that the momentum from the incident wave is transmitted instantaneously to the rear wall and distributed uniformly on the rear wall (Section 3). Figure 47 (c), on the other hand, shows a conservative model

prediction for the higher wave steepness sea condition (Reg08). These give confidence in the model for the fully closed condition.

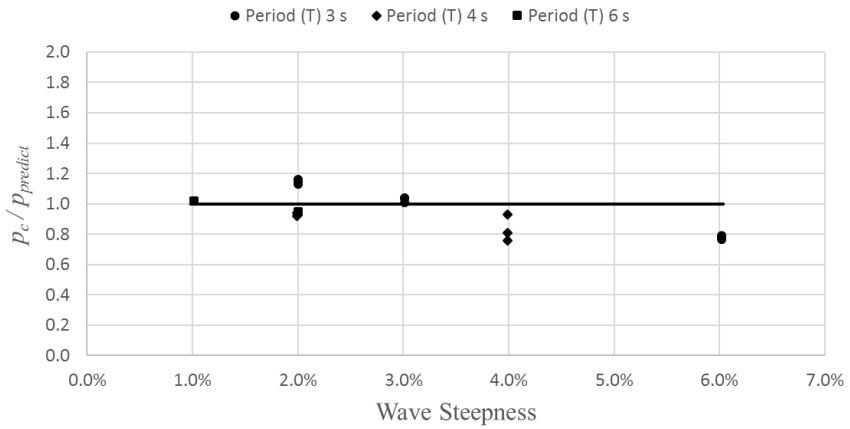

Figure 45 The chamber pressure ratio between the measurement and the model prediction at various wave period for closed case and regular waves, solid line represents the prediction model.

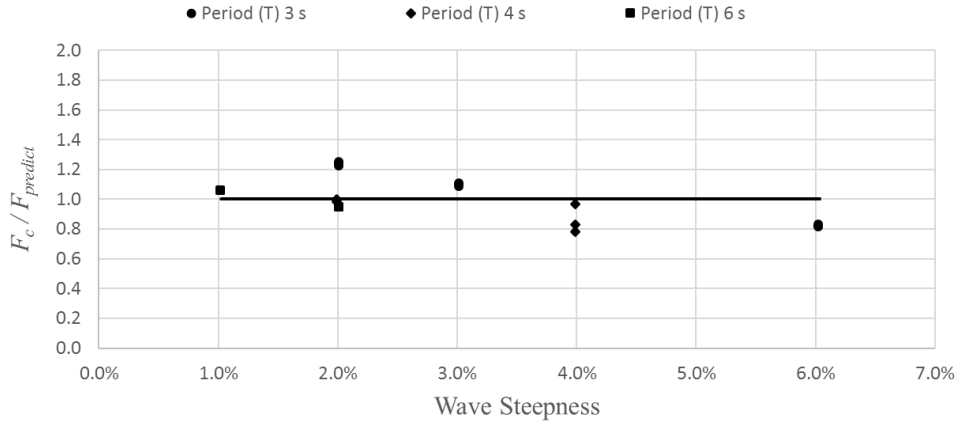

Figure 46 The total force acting on the structure ratio between the measurement and the model prediction at various wave period for closed chamber and regular waves, solid line represents the prediction model.

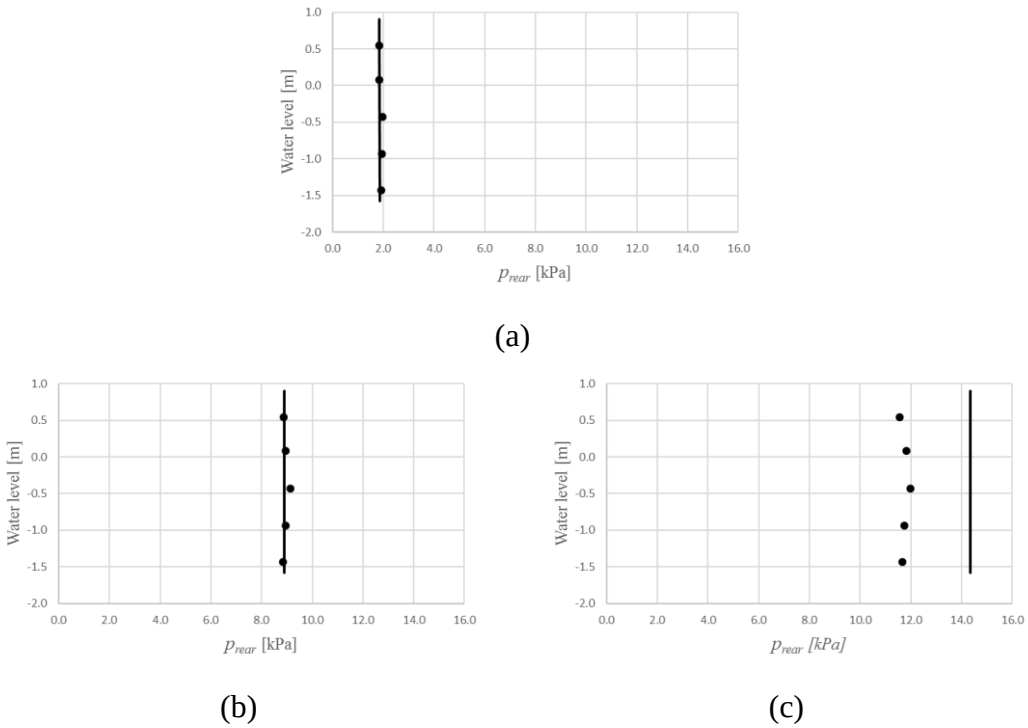

Figure 47 Measured (bullet point) and predicted (solid line) distributions of pressure maxima, for closed case; regular waves; (a) Reg01, (b) Reg05, and (c) Reg08, solid line represents prediction model.

4.2.2 Fully open chamber condition

Under the fully open condition, the chamber pressure remains very close to atmospheric pressure, so there is no value in investigating the chamber air pressures. The biggest orifice opening in the experiment is 0.3 m (2.0%) and the fully open condition is expected in this ratio. In order to separate the cases which can be considered as fully open a discrimination method need to be employed. The discrimination is done by calculating the chamber pressure increase rate in [kPa/s]. This is calculated by dividing the maximum pressure chamber measured by the pressure rise time (from atmospheric pressure to maximum – about ¼ of the wave period). Plotting the pressure rise rates against wave steepness gives Figure 48. As can been seen, every case above a pressure rise rate of 1.5 kPa/s (red line) is considered in the operating condition. Based on the figure, it can be inferred that if the wavelength is long enough, and the wave height is relatively low, the air inside the chamber can flow out of and into the chamber without raising and lowering the chamber pressure.

This no pressure change assumption may not hold for steeper wave conditions, so it is important to differentiate which of the cases may be treated as fully open and which should instead be considered as in “operating condition”

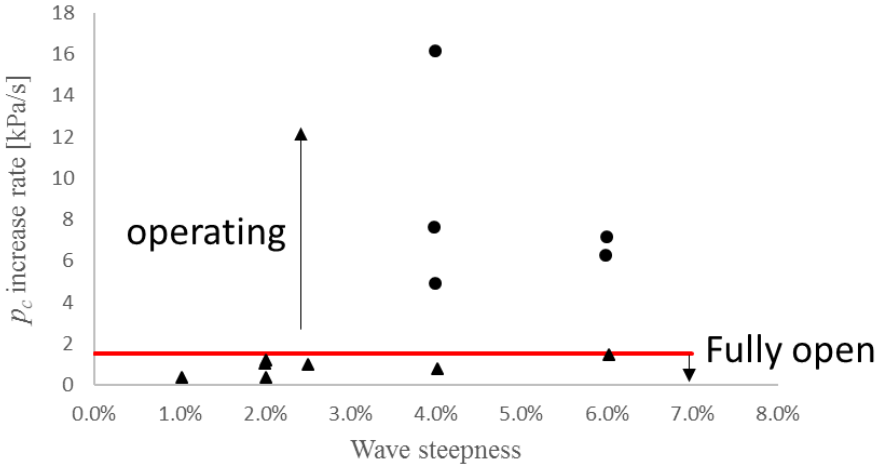

Figure 48 The pressure chamber increase rate for the 2.00% orifice to chamber ratio case, regular wave, solid red line represents the cut-off line.

Five of the total 12 cases tested in this opening condition have chamber pressure increase rate above the cut-off line and excluded from further analysis in this sub-chapter. For the conditions identified as ‘fully open’ the force ratio between the measured and the predicted force are plotted in Figure 49. It can be seen that the model works best for lower wave steepnesses (predictions to within a factor of 1.2). For the steeper wave conditions, the model gives safe prediction by factors ranging from 0.7 to 0.4. The discrepancy between the measurement and the prediction can occur because in the steeper wave condition, the in-chamber pressure may build up because the orifice opening is not large enough to allow the air flow smoothly out and into the chamber. This chamber pressure generation may affect the force acting on the rear wall resulting in the pressure measured located in the safe-zone, below the prediction line.

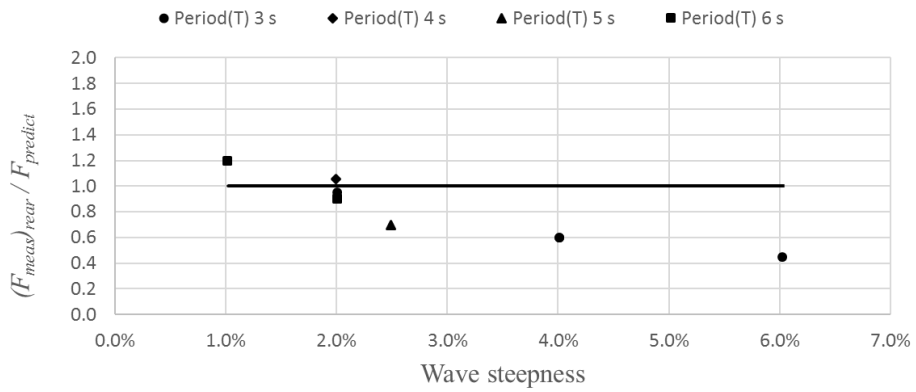

Figure 49 The total force acting on the rear wall of the structure ratio between the measurement and the model calculation at various wave conditions for fully open case, regular wave, solid line represents the prediction model.

The maximum measured pressure at each vertical elevation is now compared with the pressure estimated by the model at the corresponding vertical elevation on the rear wall (Figure 50). In the figure, the different data sets show the measured to predicted pressure ratio for different regular waves, with the wave steepness shown in the brackets. The solid line represents perfect agreement with the model. The points located on the right side of the line are under-estimations (unsafe) and the points located on the left side of the line are over-estimations (safe). The data shows that the measurement mostly fell in the 1±0.2 factor region to the model except for the highest wave steepnesses (Reg03 with 4% wave steepness and Reg05 with 6% wave steepness).

Figure 51 (a)-(g) show example pressure maxima distributions from measured data and model predictions on the rear wall with waves Reg01, Reg03, Reg05, Reg06, Reg11, Reg16 and Reg20 respectively. In the figure, subfigures (a) and (d) show cases where the models are in excellent agreement with the measurement, while (b), (c), (e) and (f) shows a safe prediction by a factor between 0.45 to 0.7 in the maximum pressure. Figure 4.20 (g) shows the example where the measurement is located on the un-safe prediction with an under-estimation by a factor of 1.15, although the pressure pattern still matched the prediction well.

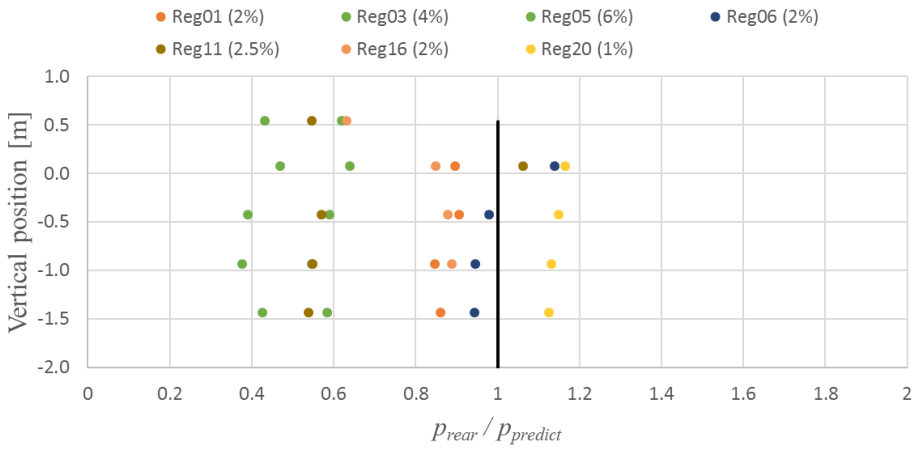

Figure 50 The rear wall pressure ratio between the measurement:prediction at various wave conditions and vertical elevations, fully open case, solid line represents the prediction model.

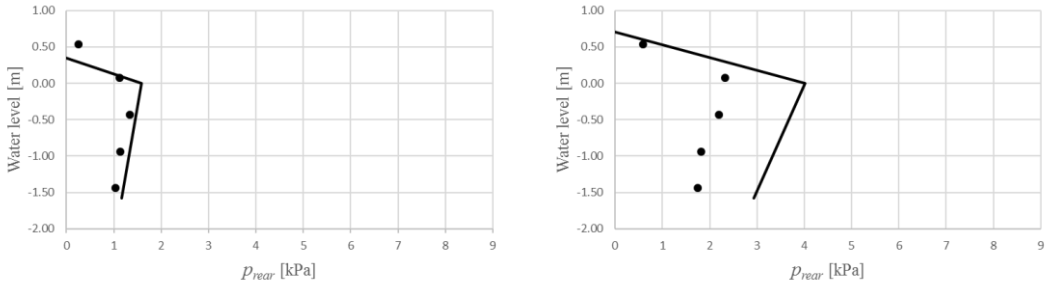

(a)

(b)

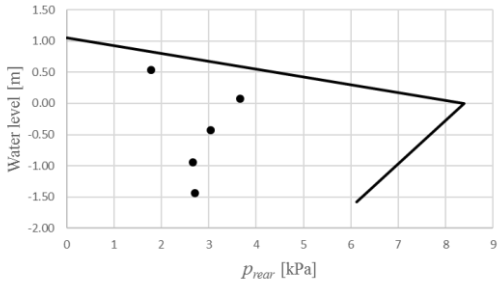

(c)

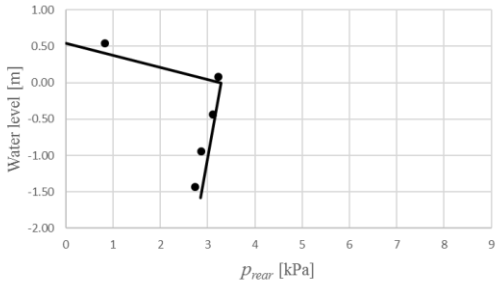

(d)

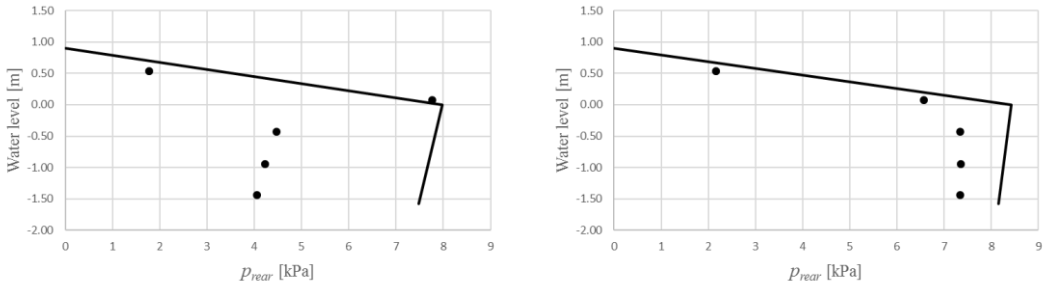

(e) (f)

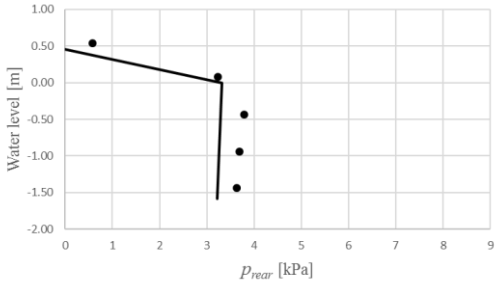

(g)

Figure 51 The rear wall measured pressure at various elevation, solid line represents prediction mode, regular wave, fully open case: (a) Reg01, (b) Reg03, (c) Reg05, (d) Reg06, (e) Reg11, (f) Reg16, and (g) Reg20.

4.2.3 Operating chamber condition

In the "operating condition", the orifice opening of the caisson chamber was changed, simulating the power take off resistance during operation. The model is validated using multiple orifice openings. Although in reality the location of the orifice opening and the shape of the orifice might have a minor role, the air chamber pressure will mainly be affected by the orifice area relative to the chamber cross-sectional area. For the purpose of simplicity, it is assumed that only this ratio determines the PTO influence on the chamber pressure. This assumption along with the simplification between the air damping characteristic and the proportion coefficient (P) introduced in Section 2.4, resulted in an empirically derived Equation 20.

$$P = f\left(\frac{A_o}{A_c}\right) = 1 - 45.55\,(\frac{A_o}{A_c}) \tag{20}$$

Figure 52, Figure 53, and Figure 54 show the ratio of measured to predicted chamber pressures against the wave steepness, wave height, and wave period respectively. The model validation includes the test results for 0.06%, 0.22%, and 0.88% orifice to chamber area ratio as explained in Section 3, and the 2.00% ratio that considered to be in operating condition as explained in Section 4.1.2. It is clear that wave period is less significant in influencing the change of pressure chamber measured:predicted chamber pressure ratio. From the results, it can be inferred that the prediction is safe for the higher wave height. This may happen because of the momentum loss during the water level movement inside the chamber is neglected in the model. It is also notable that higher and steeper wave conditions have a higher likelihood of 'sloshing' occurring within the chamber which will be discussed further in Chapter 5.

In addition to the chamber pressure comparison, Figure 55 shows the pressure distribution of both measurements (solid circle points) and model (solid line) for various wave conditions for the 0.88% orifice to chamber ratio. The pressure plotted in these figures has the chamber pressure subtracted at every time step leaving only the pressure induced by the motion of the water. Figure 55 (a), (c), (f), (n), and (o) show a very good agreement between the measurement and the model. Figure 55 (b), (e), (g), (h), and (m) show rather less good agreement, but still to within a factor of 0.6 (a safe prediction). Figure 55 (j) and (k) show an interesting feature where the pressures change dramatically over the vertical water level. The maximum pressure acting near the still water level is however similar with the model, to within factor of 0.72 to 0.76. This unusual pattern may happen because the water surface is sloshing during the experiment, while the model assumes the water surface to be well behaved, like a water piston. Figure 55 (d) and (l) show the model giving quite significant over-estimations (a factor of 0.3 to 0.4 between model and measurements). Nevertheless, almost all of the data show a safe prediction.

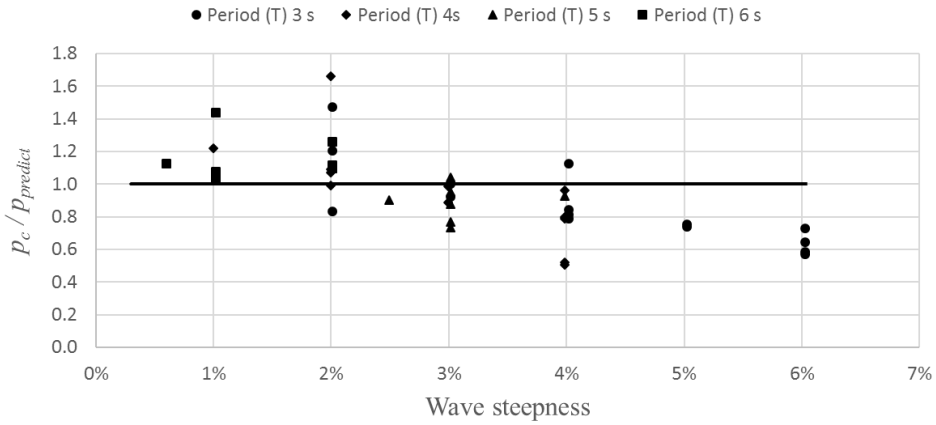

Figure 52 Measured:predicted chamber pressure against the wave steepness, operating condition, regular waves, solid line represents prediction model.

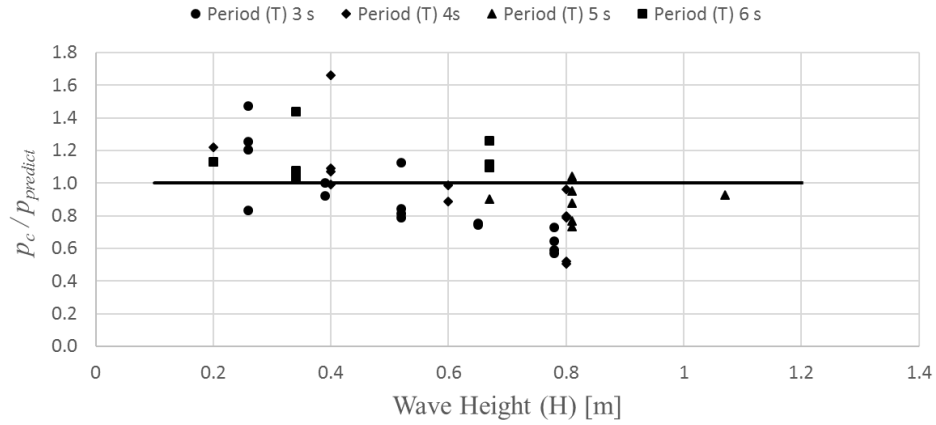

Figure 53 Measured:predicted chamber pressure against the wave height, the operating condition, regular wave, solid line represents prediction model.

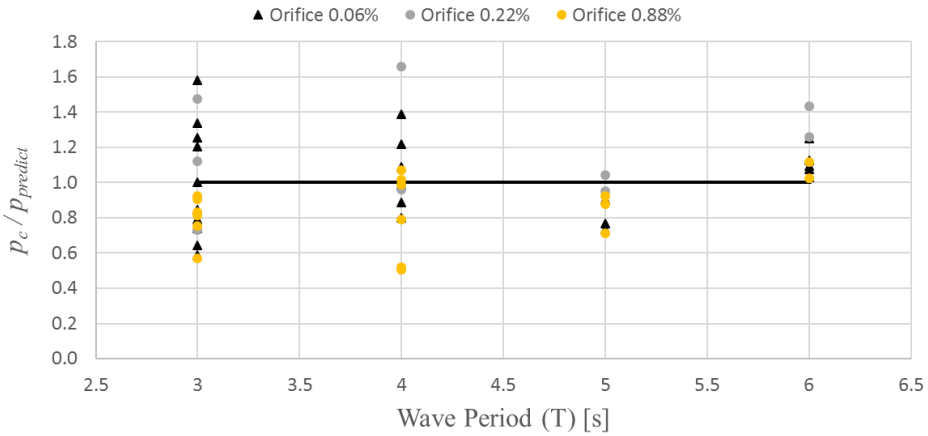

Figure 54 Measured:predicted chamber pressure against the wave period, operating condition, regular waves, solid line represents prediction model.

4.2.4 Vertical force on the chamber ceiling

Unlike an ordinary breakwater, an OWC breakwater has a pressure acting on the ceiling of the chamber within the caisson. This pressure leads to a vertical force which contributes to lowering the threshold for sliding (by reducing the available friction) and also contributes to the overturning moment of the complete structure. It is therefore important for the model to estimate the ceiling vertical force. Only the positive (upwards) force acting on the ceiling will be explored and validated because the negative force will always result in the structure being in a safer state against sliding and overturning. The success of the model is evaluated in Figure 56 where the measured to predicted vertical force ratio is plotted over the range of wave heights for the closed chamber condition. It can be seen that the model accurately predicts the measured vertical force to within a factor of 1 ± 0.2.

Since the maximum chamber pressure will be experienced in the closed chamber case, it is assumed that the biggest vertical force will also occur during the closed chamber experiments and only this case is plotted. Figure 57, which shows the ratio of the measured vertical forces in the closed and operating conditions, supports this assertion. The fully open condition is not included in this figure because it is assumed to have zero chamber pressure. As predicted, the ratio decreases as the orifice opening gets bigger. Note that some of the 0.06% orifice cases are located above the line of perfect agreement. This may be because the orifice to chamber area ratio is very small (0.06%)

making the difference between the closed chamber and the operating condition negligible, especially for the larger wave height conditions.

When compared to the total horizontal force, the vertical force for the regular wave conditions is always less by a factor of approximately 0.78 times. This result is in line with the suggestion of the previous research (Ashlin *et al.,* 2017).

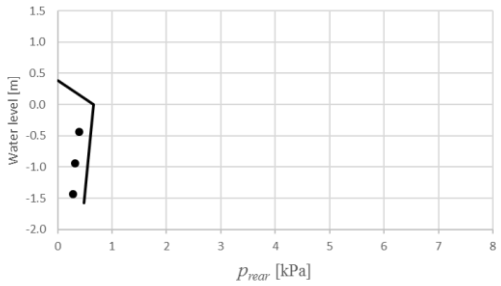
Water level [m]
1.5
1.0
0.5
0.0
-0.5
-1.0
-1.5
-2.0
0 1 2 3 4 5 6 7 8
p_{rear} [kPa]

(a)

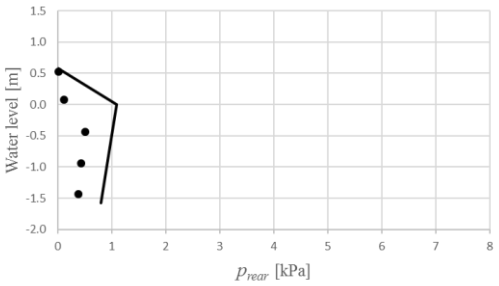
Water level [m]
1.5
1.0
0.5
0.0
-0.5
-1.0
-1.5
-2.0
0 1 2 3 4 5 6 7 8
p_{rear} [kPa]

(b)

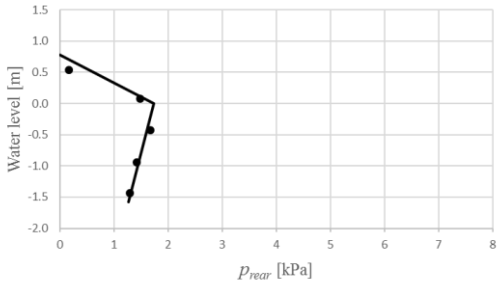
Water level [m]
1.5
1.0
0.5
0.0
-0.5
-1.0
-1.5
-2.0
0 1 2 3 4 5 6 7 8
p_{rear} [kPa]

(c)

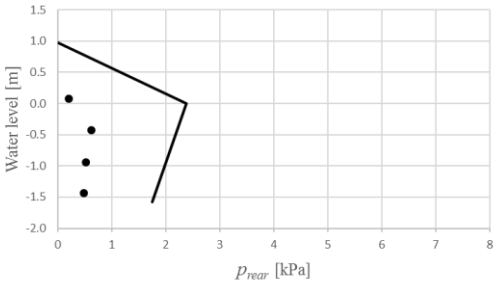
Water level [m]
1.5
1.0
0.5
0.0
-0.5
-1.0
-1.5
-2.0
0 1 2 3 4 5 6 7 8
p_{rear} [kPa]

(d)

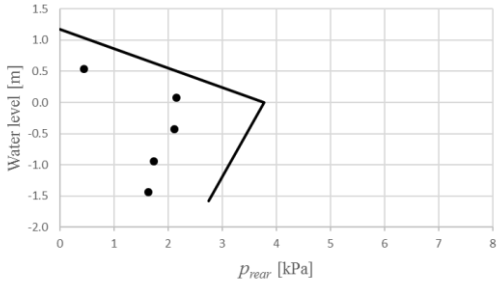
Water level [m]
1.5
1.0
0.5
0.0
-0.5
-1.0
-1.5
-2.0
0 1 2 3 4 5 6 7 8
p_{rear} [kPa]

(e)

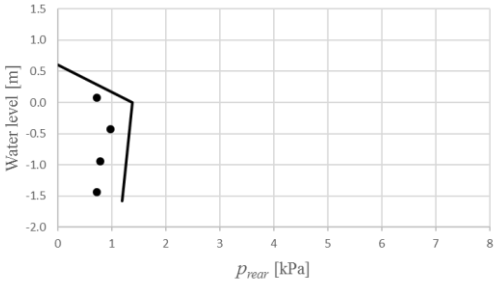
Water level [m]
1.5
1.0
0.5
0.0
-0.5
-1.0
-1.5
-2.0
0 1 2 3 4 5 6 7 8
p_{rear} [kPa]

(f)

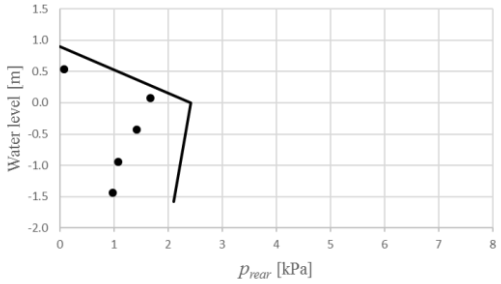
Water level [m]
1.5
1.0
0.5
0.0
-0.5
-1.0
-1.5
-2.0
0 1 2 3 4 5 6 7 8
p_{rear} [kPa]

(g)

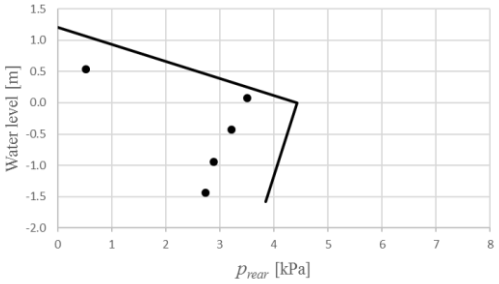
Water level [m]
1.5
1.0
0.5
0.0
-0.5
-1.0
-1.5
-2.0
0 1 2 3 4 5 6 7 8
p_{rear} [kPa]

(h)

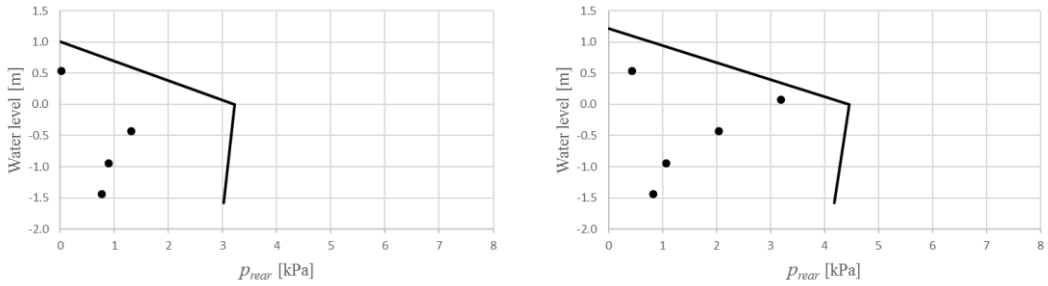

(i)

(j)

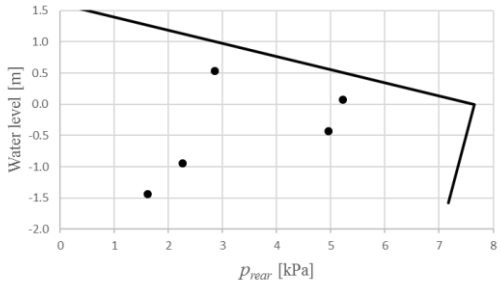

(k)

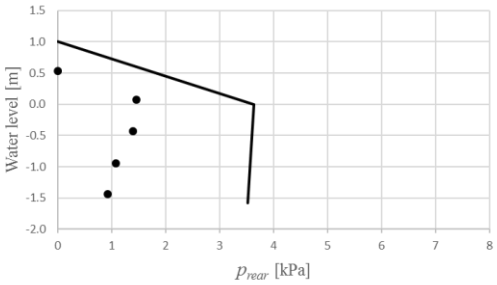

(l)

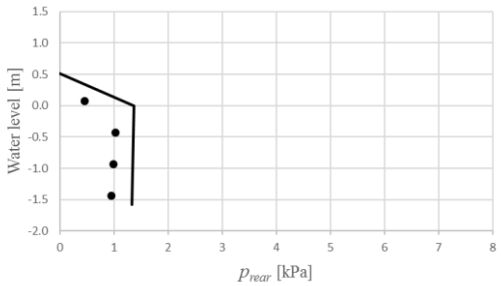

(m)

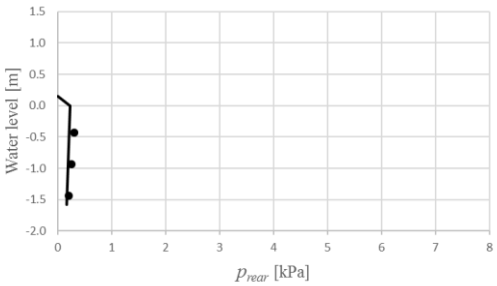

(n)

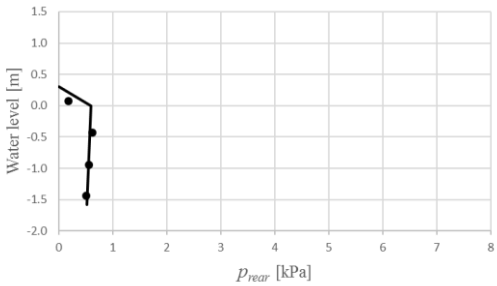

(o)

Figure 55 (a) – (o) Measured pressure distributions acting on the rear wall at various vertical elevation, regular wave, solid line represents the prediction model, and various wave conditions: (a) Reg01, (b) Reg02, (c) Reg03, (d) Reg04, (e) Reg05, (f) Reg06, (g) Reg07, (h) Reg08, (i) Reg11, (j) Reg12, (k) Reg13, (l) Reg16, (m) Reg20, (n) Reg23, (o) Reg24.

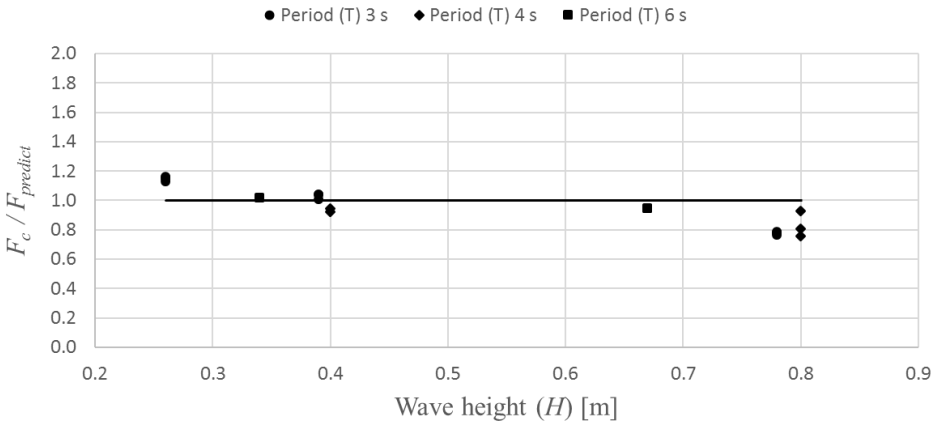

Figure 56 Caisson chamber vertical force ratio measured:predicted ratio against the wave height, closed chamber case, regular waves, solid line represents the prediction model.

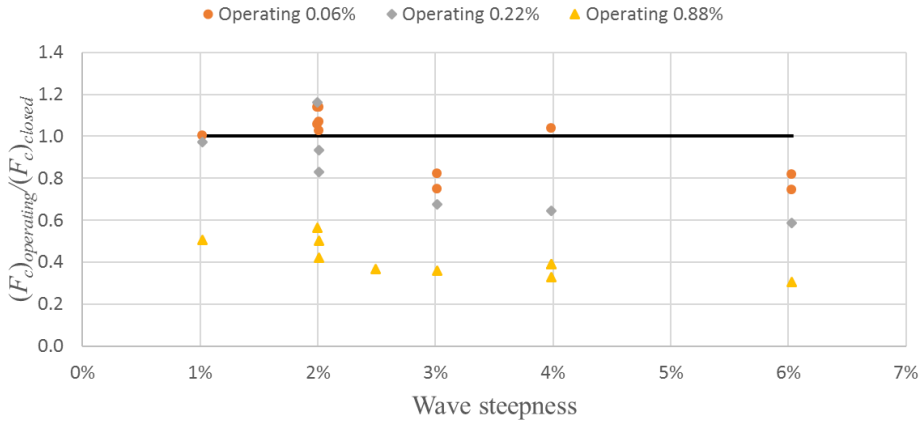

Figure 57 Caisson chamber vertical forces ratio between the closed chamber case and the operating condition orifice cases for regular waves

4.3 Result and analysis for irregular wave test

For Rayleigh-distributed wave heights, the maximum wave height will be approximately 1.8 times the significant wave height for a sequence of 1000 irregular waves. A simple approach to adjusting the conceptual model is therefore to multiply the significant wave height by this factor of 1.8. This change will affect integrated pressure on the front wall (F_{Goda}) calculation in Equation 9 for closed chamber, Equation 16 for the fully open chamber, and Equation 18 for the operating condition.

Due to the required test lengths, rather fewer experiments for the irregular case were carried out so the validation data set is sparser than for the case of regular waves.

4.3.1 Closed chamber condition

The ratio between the maximum measured to predicted chamber pressure is presented in Figure 58 in the usual way.

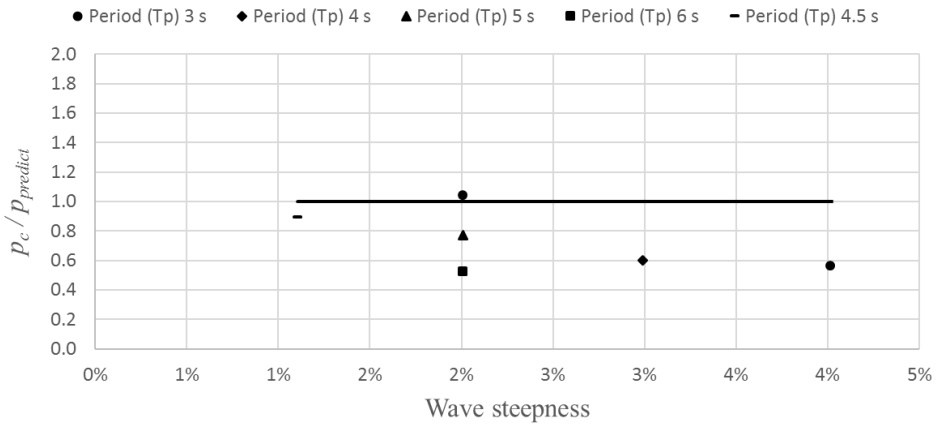

Figure 58 The Chamber pressure ratio measured:predicted at various irregular wave periods and wave steepnesses for closed chamber case, irregular waves

It is clear that the model fits quite well with the measurements especially for the lower wave steepness, where the measured/predicted ratio is 1 ± 0.1. For higher waves, the prediction factor is about 0.6 to 0.8, all falling in the safe zone.

4.3.2 Fully open chamber condition

First, it is necessary to distinguish, carefully, the tests which are truly in an 'open condition' from those still located in the 'operating condition'. The method used to distinguish these cases for regular waves – discriminating on the chamber pressure increase rate – cannot be applied straightforwardly here. If the maximum pressure is considered, then most of the tests would be defined to be in the 'operating condition'. Instead, $p_{1/250}$, equal to the mean of 4 largest pressure maxima of the individual events, is used as the basis for the pressure increase rate measure. Figure 59 shows the pressure increase rate of each cases and the pressure increase rate higher than 1.5 kPa/s is considered as operating chamber condition and excluded in this analysis. Figure 60 shows the ratio of the measured rear wall force and the force calculated by the model

for the cases which the $p_{1/250}$ increase rate suggests fully open conditions (< 1.5 kPa/s).

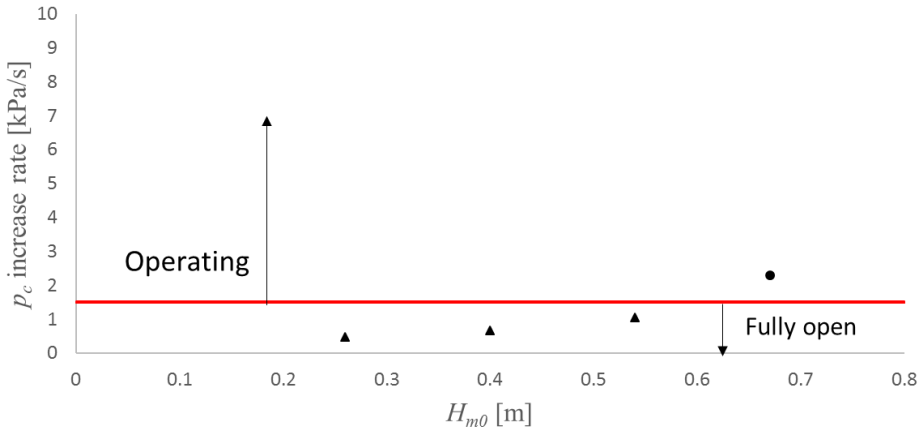

Figure 59 Pressure increase rate for irregular wave conditions plotted against significant wave height, H_{m0}. The pressures increase rate is based upon the $P_{1/250}$, solid red line represents the cut-off rate.

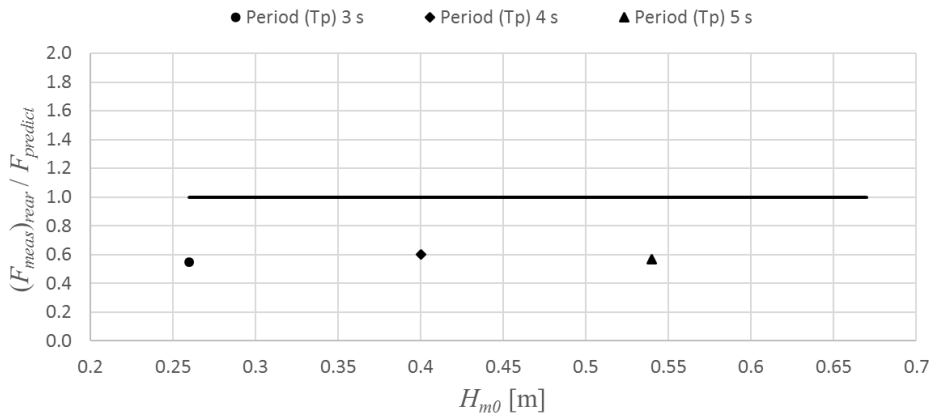

Figure 60 rear wall force measured:predicted ratio for various irregular wave conditions, fully open case, irregular waves, the solid line represents the prediction model.

Note that the x-axis shows the significant wave height because all of the data shown has the same wave steepness of 2%. The model generally overpredicts the measurements, with the comparison factor of about 0.6. Since the maximum pressure acting on the rear wall depends upon the vertical location, it is important to see how well the model predict the pressure distributions on the rear wall. Figure 61 (a) – (c) shows the comparison between the model (solid black line) and the (non-simultaneous)

maximum measured pressure distribution, with the irregular wave cases Irr01 (a), Irr04 (b), and Irr07 (c).

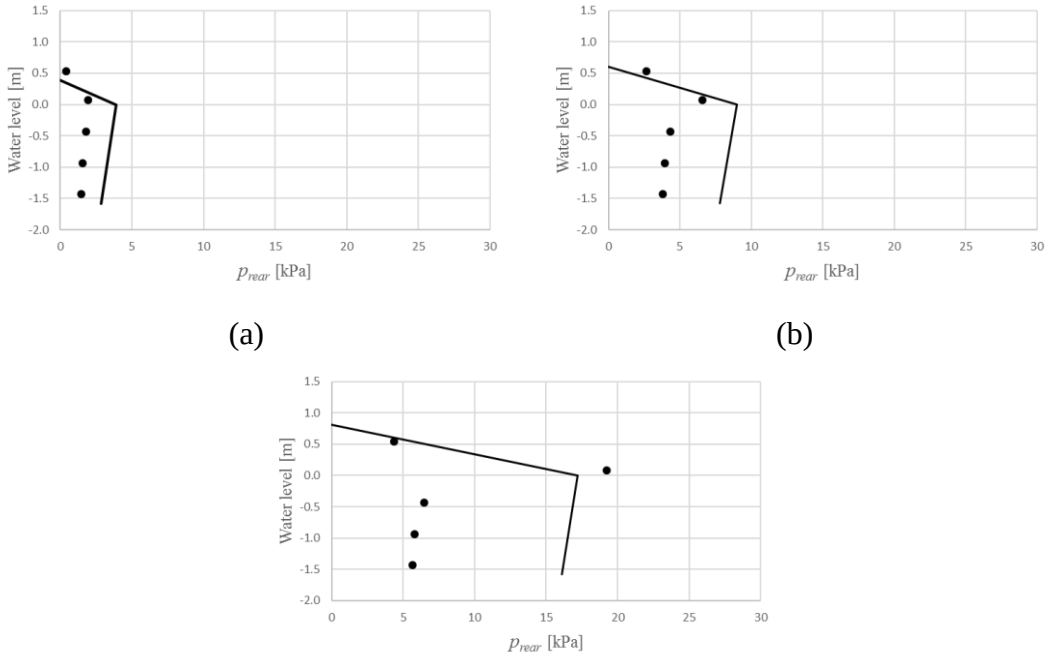

Figure 61 Measured rear wall pressure distributions (circle) and the model prediction (solid line), for fully open case for; (a) Irr01, (b) Irr04, and (c) Irr07.

As can be observed from Figure 61, the measured pressure maxima are still mostly well-predicted, and with the exception of that in Figure 61 (c), slightly on the safe side. The total force prediction for this case, however, is still safe. This effect is evidenced in detail in Figure 62 which shows the associated 'sloshing' (a) the instant of the pressure maximum, and (b) immediately afterwards. It is clear that the in-chamber behaviour is far from an idealised up and down oscillation, but instead, the water located near the rear wall is observed to run up the rear wall very rapidly, before hitting the ceiling. The water mass is then reflected to the front part of the chamber. For the underpredicted case, the very steep gradient in the measured pressure distribution could be due to water column moevement in the chamber during experiment. The in-chamber water column behaviour, including violent motion, will be explored in more detail in Chapter 6 in this thesis.

(a) (b)

Figure 62 (a) At the instant of violent in-chamber water column movement and (b)immediately after. Irregular waves (Irr07).

The water surface movement can be compared with the well-behaved oscillation taken from the Irr01 test shown in Figure 63 (a) and (b).

(a) (b)

Figure 63 The negative (a) and the positive (b) water movement of Irr01 irregular wave conditions. The still water level is located at 0.73 m level on the painted scale visible.

4.3.3 Operating chamber condition

Figure 64 shows the ratio of maximum measured chamber pressure to the prediction, plotted against the wave steepness. It can be seen that that in these ‘operating

conditions' in irregular waves, the model predictions are on the safe side, within a factor of 0.8 ± 0.2.

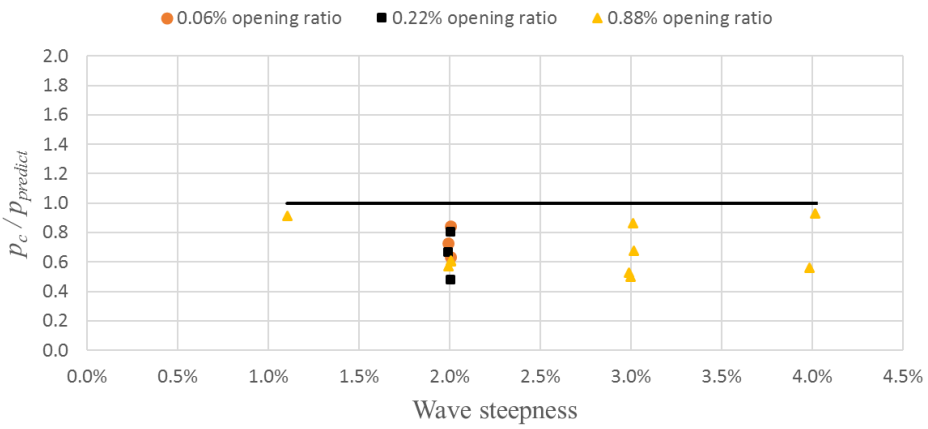

Figure 64 Measured to predicted chamber pressure ratio, operating conditions, irregular wave conditions, solid line represents the prediction model.

These validation results give confidence that the loading model works very well in estimating the non-impulsive in-chamber wave loads acting on the rear wall and the chamber pressure generated (including the vertical force acting on the in-chamber ceiling).

5 OWC installed vertical breakwaters: impact loads on front face and in-chamber

Since previous chapter focused only on the in-chamber non-impulsive wave loads for design of an Oscillating water column (OWC) formed in a vertical breakwater, this chapter will explore the impact wave loads experienced by both the front wall and the in-chamber wall of the structure. The experimental measurement will be compared to prediction based upon established methods for vertical breakwaters. Sub-chapter 5.1 will explore the wave loads experienced by the front wall, the sub-chapter 5.2 will focused on the in-chamber wave loads, and finally the in-chamber water column behaviour will be characterised in sub-chapter 5.3.

5.1 Front wall wave loads and impact

Adding an OWC chamber inside a vertical breakwater would be anticipated to affect the wave loads experienced by the front wall of the structure. This may include both the non-impulsive wave pressure and any impact wave pressures experienced by the front wall. This chapter explores the commonly used front wall pressure and force design tools for a conventional vertical breakwater and then compare the results with the large-scale measurement data introduced in the previous chapter.

5.1.1 Front wall non-impulsive loads

A non-impulsive or pulsating load is a slow acting wave load produced by a non-breaking wave. To estimate the pressure received by a vertical breakwater, Yoshimi Goda (Goda, 2010) proposed formulae based on the elevation to which the wave pressure is exerted (η), significant wave height (H_{m0}), and significant wave period (T_p) of the wave condition as shown in Equation 21 to 23.

$$\eta = 0.75(1 + \cos\beta)H_{max} \tag{21}$$

$$p_1 = \frac{1}{2}(1 + \cos\beta)(\alpha_1 + \alpha_2 cos^2\beta)\rho_w g H_{max} \tag{22}$$

$$p_3 = \alpha_3 p_1 \tag{23}$$

Here p_1 is the non-impulsive water pressure at still water level (swl) and p_3 is the water pressure at the bottom of the breakwater, and H_{max} is the maximum incident wave

height and can be taken as approximately $1.8H_{m0}$ based on the individual wave height Rayleigh-distribution. The α_1, α_2, and α_3 coefficients can be calculated by Equation 24, 25, and 26 respectively. The symbol g denotes the gravity and ρ_w denotes the water density. Finally, β denotes the angle between the direction of the wave and a line normal to the breakwater.

$$\alpha_1 = 0.6 + \frac{1}{2}\left[\frac{4\pi h/L}{\sinh(4\pi h/L)}\right]^2 \quad (24)$$

$$\alpha_2 = min\left\{\frac{h_b - d}{3h_b}\left(\frac{H_{max}}{d}\right), \frac{2d}{H_{max}}\right\} \quad (25)$$

$$\alpha_3 = 1 - \frac{d}{h}\left[1 - \frac{1}{\cosh(2\pi h/L)}\right] \quad (26)$$

Here h denotes the full water depth, d denotes the water depth from swl to the bottom of the breakwater, h_b denotes the water depth at $5H_{m0}$, and L denotes the deep-water wave length associated to the significant wave period T_p (where $L = (gT_p^2)/2\pi$). The pressure distributions are shown in Figure 65 with the highest pressure located at the still water level (swl).

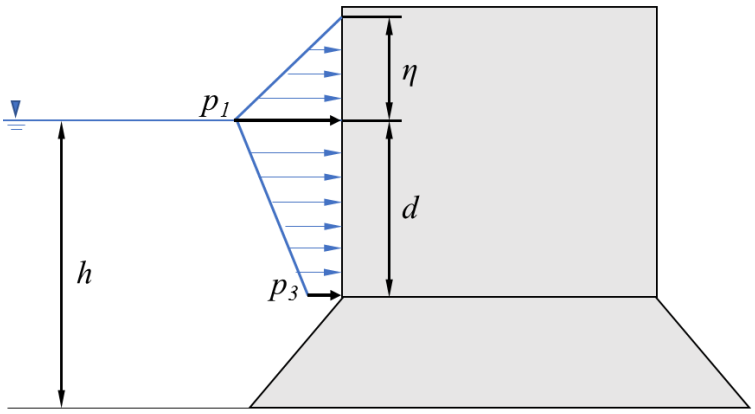

Figure 65 Pressure distribution adopted from Goda (2010).

Figure 66 show the average of four biggest pressure measured on the front wall $(p_{1/250})_{front}$ for (a) H_{m0}= 0.26m and T_p= 3s; (b) H_{m0}=0.39 T_p=3s; (c) H_{m0}=0.54m and T_p=3s; and (d) H_{m0}=0.26 and T_p=4.5s. The solid line represents the estimation calculated using the techniques mentioned above, and the measured data points are for orifice:chamber area ratio of closed (orange circle), 0.10% (grey rectangular), 0.20% (yellow diamond), 0.88% (blue triangle), and 2.0% (green star). The estimation line is

stopped at water elevation equal to -0.7m because that is the end of the front wall penetration. As can be seen, the incorporation of the chamber, especially with open orifice, may be resulted in less wave pressure on the front wall. This condition become more profound in a higher wave height and wave period as shown in Figure 66 (c). This can be explained because under very high wave condition, the water column inside the chamber may experience a lot of turbulence which resulted in enhanced dissipation of momentum and consequent reduction of wave loads acting on the in-chamber rear wall.

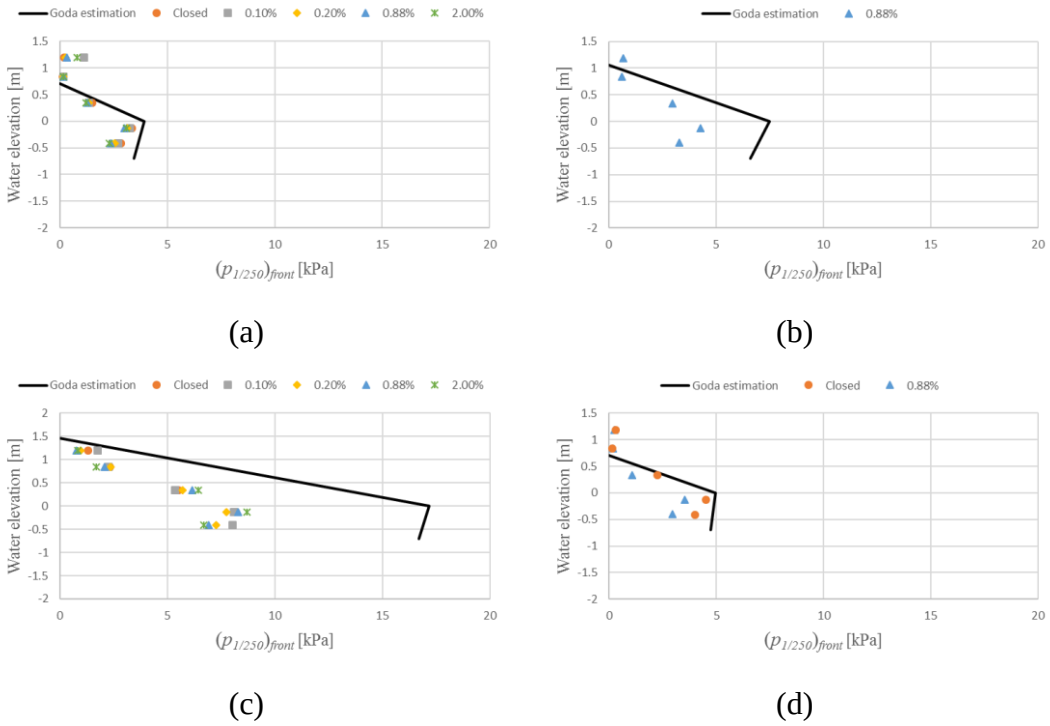

Figure 66 Non-impulsive front wall measured $p_{1/250}$ for closed chamber (circle), opening:chamber area ratio 0.10% (rectangle), 0.20% (diamond), 0.88% (triangle), and 2.0% (*) and Goda estimation (solid line) for (a) H_{m0}= 0.26m and T_p= 3s; (b) H_{m0}=0.39 T_p=3s; (c) H_{m0}=0.54m and T_p=3s; and (d) H_{m0}=0.26 and T_p=4.5s.

Due to the limitation of time, only the closed case and 0.88% case were tested for the H_{m0}=0.26m and T_p=4.5s, and only the 0.88% case was tested for the H_{m0}=0.39m and T_p=3s. The trend, however, remains the same for all of cases so it is safe to say that the result will be similar for the cases that haven't been tested in both wave conditions.

5.1.2 Front wall impulsive loads

Allsop *et al.* (1996) and Oumeraci (1994) characterised three types of impact pressure experienced by the font wall. The first type (Figure 67) is a severe impact pressure on the vertical wall which characterised by a short rise time ($t_r < 0.01T_p$) and the highest-pressure peaks. The second type is a less severe impact pressure with smaller pressure maximum and a second smaller peak after the impact (Figure 68). The rise (t_r) for this type is longer than the first type ($t_r < 0.1T_p$). The final type characterised is a double peaked pressure resulted from steep near-breaking waves with more obvious double pressure peaks and of similar magnitude (Figure 69) and longer rise time ($t_r \approx 0.2T_p$). The rise time (t_r) is defined as the time between the start of an impact and the force maximum of the impact. The time from the impact's start to its end is called the duration (t_d). Figure 71 illustrates the rise time (t_r), duration (t_d), and maximum impact pressure measured ($p_{i,max}$) of Figure 67. Weggel and Maxwell (1970) proposed a semi-empirical relation equation between the rise time (t_r) and the impact force (F_i) (Equation 27).

$$F_i = a.t_r^b \tag{27}$$

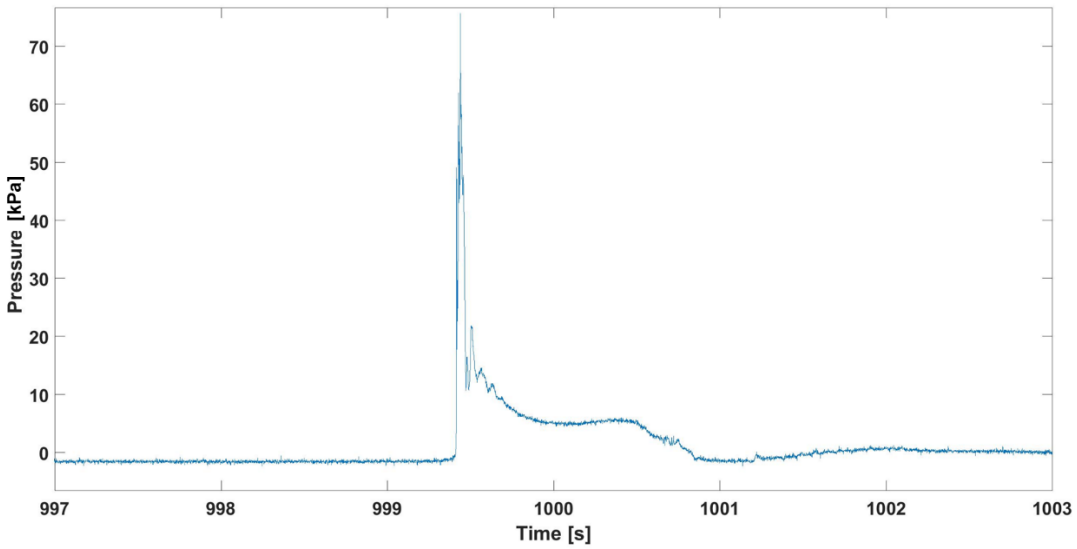

Figure 67 Severe pressure impact characteristics (Type 1) with rise time (tr) < 0.01 Tp from the large-scale model experimental measurement

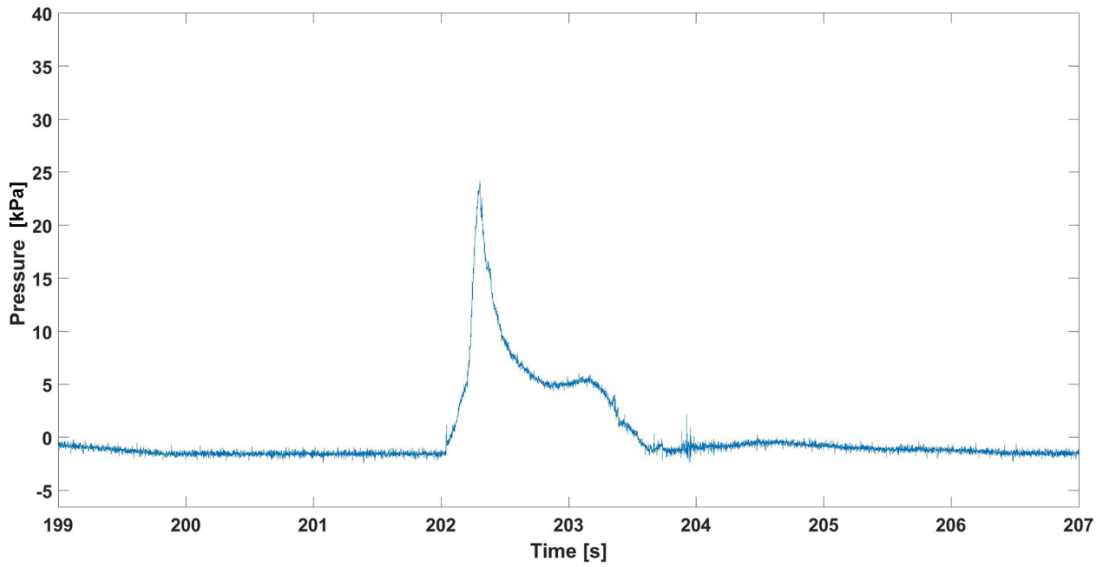

Figure 68 Less severe pressure impact characteristics (Type 2) with rise time (tr) < 0.1 Tp from the large-scale model experimental measurement

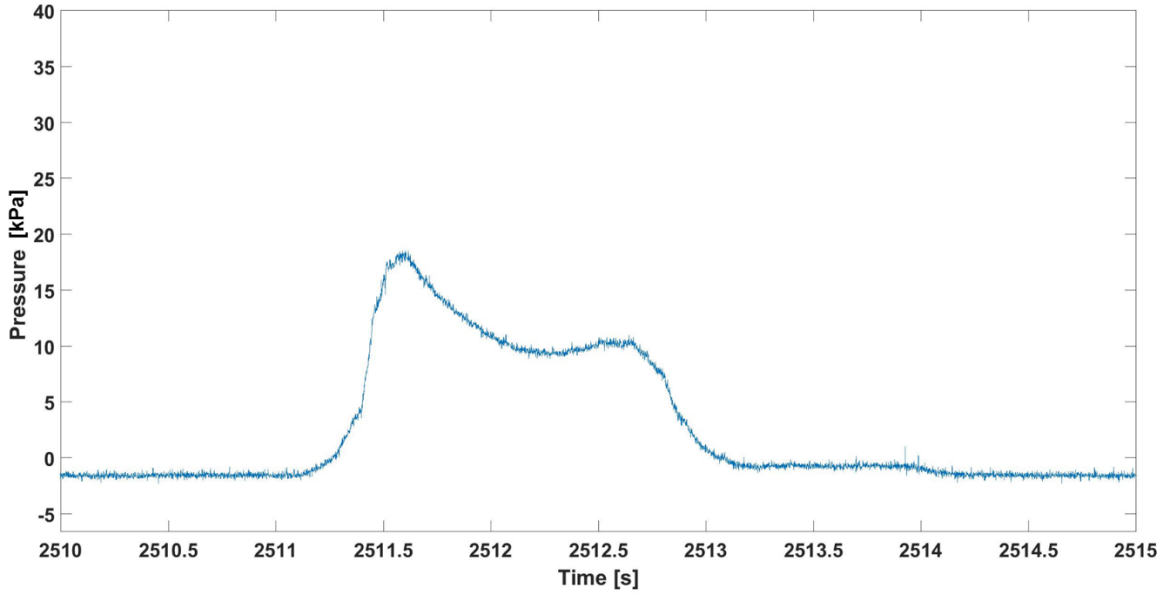

Figure 69 Near breaking pressure impact characteristics (Type 3) with rise time (tr) ≈ 0.2 Tp from the large-scale model experimental measurement

where *a* and *b* are empirical coefficient chosen to include all of the experimental measurement scatter under the impact force (F_i) line. Large-scale experimental testing (Cuomo *et al.*, 2010a) shows for conventional vertical breakwater, the impact force

(F_i) should not exceed a line created by Equation (27) and a = 7 and b = -0.6 as shown in Figure 70. McKenna and Allsop (1999) further suggested that Weibull distribution can be used to describe the wave forces experienced by the front wall and a change in gradient (an "elbow") represents the change from a non-impulsive force to an impulsive force in an irregular wave conditions given the offshore wave length and the water depth ratio of less than 17 (L/h<17) and offshore wave high and water depth ratio of less than 0.425 (H/h<0.425). These conditions are taken based on the wave steepness transition between the breaking and broken wave supporting the argument that impulsive loads are caused solely by breaking wave. The Weibull distributed forces outside those parameters will have a curved distribution.

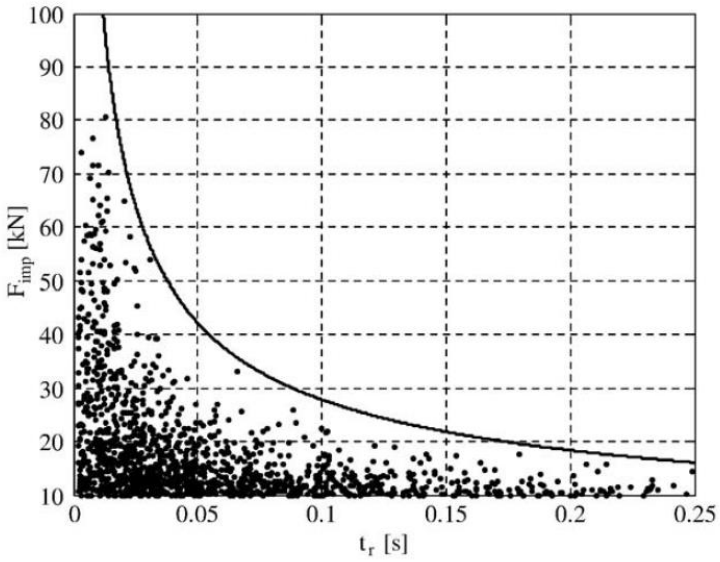

Figure 70 Impact force maxima (Fi) plotted against the rise time (tr) for conventional breakwater with solid line calculated based on Equation (27) and a = 7 and b = -0.6 taken from Cuomo *et al.* (2010a).

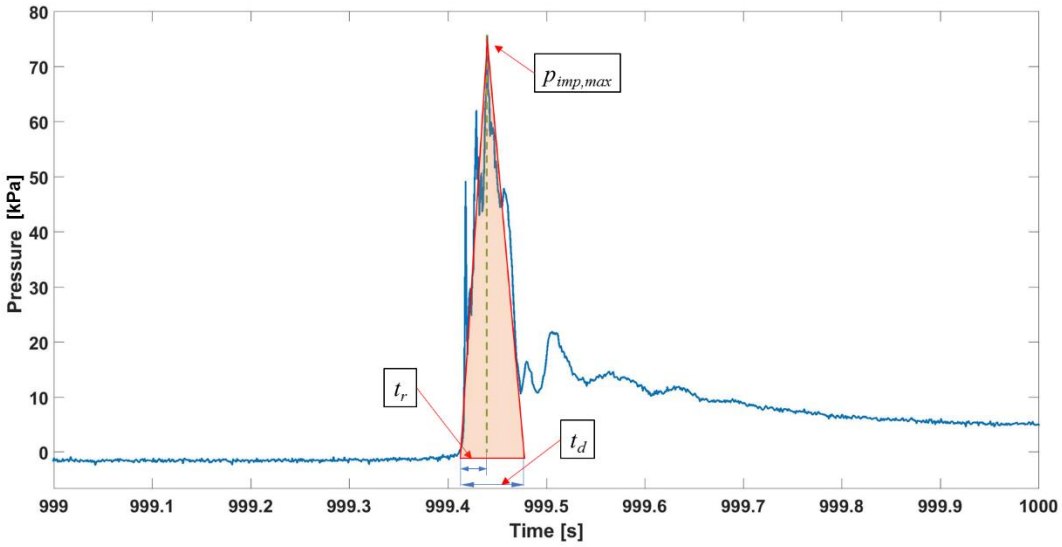

Figure 71 The break-down of rise time (t_r), duration time (t_d), and peak pressure ($p_{i,max}$)

In order to compare the experimental data on impacts on the OWC model with the literature, the same rectangular force calculation and zero-up crossing methods are employed for the front wall to get the force maxima for each wave event in irregular wave conditions. The measured force maxima for each wave event are then plotted against the non-exceedance probability (*ln(-ln(1-P))*) and the results are shown in Figure 72 – Figure 98. In addition to the force maxima, a solid diamond is utilised to mark the observed transition from a non-impulsive wave force to an impulsive wave force. The observation of the transition is done qualitatively and compared with the "elbow" transition of the Weibull distribution. Figure 77,Figure 78, Figure 86, Figure 90, Figure 92, and Figure 95 show that the non-impulsive-to-impulsive transition is consistent with the change in the distribution gradient or the so called "elbow". Although, it can be seen that Figure 72, Figure 74, Figure 75, Figure 76, Figure 79, Figure 82, and Figure 83 also have the change of gradient even though no impact observed. It can be concluded that for the OWC installed vertical breakwater, the change "elbow" does not accurately indicate a non-impulsive-to-impulsive wave load transition.

To explore the relationship between the impact force (F_{imp}) and the rise time (t_r), the normalised measured force is plotted against the associated normalised rise time in Figure 99. The normalisation is done by dividing the measured impact force with the

average of four biggest non-impulsive force of the same irregular wave train ($F_{imp}/F_{ni,1/250}$) and the rise time with the peak wave period (t_r/T_p). The line presented is the relationship proposed by Cuomo *et al.* (2011) at various non-exceedance (as shown in the figure). The top line is the 99.9% non-exceedance level with 25% relative error line. As can be seen from the figure, the F_{imp} and t_r relationship for the OWC installed vertical breakwater also follows the relationship proposed by Weggel and Maxwell (1970) with only 2 out of 160 impacts observed fell above the non-exceedance 99.9% relative error line.

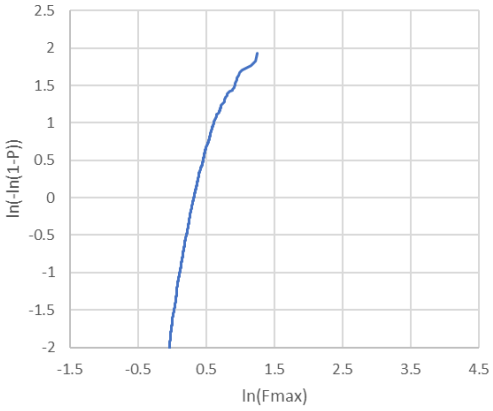

Figure 72 Non-exceedance probability distribution for irregular wave with T_p = 3s, H_{m0} = 0.26m, and closed chamber.

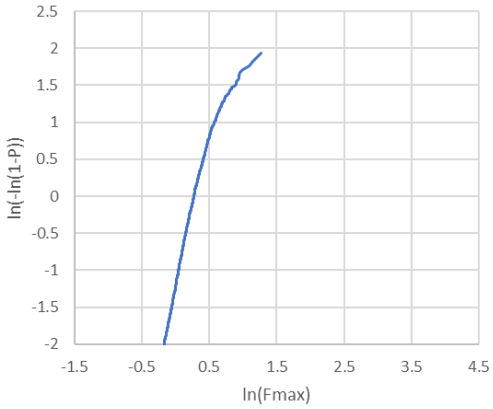

Figure 73 Non-exceedance probability distribution for irregular wave with T_p = 3s and H_{m0} = 0.26m and A_o/A_c = 0.1%.

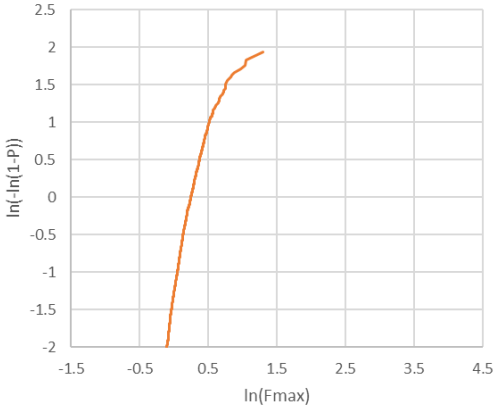

Figure 74 Non-exceedance probability distribution for irregular wave with T_p = 3s and H_{m0} = 0.26m and A_o/A_c = 0.2%.

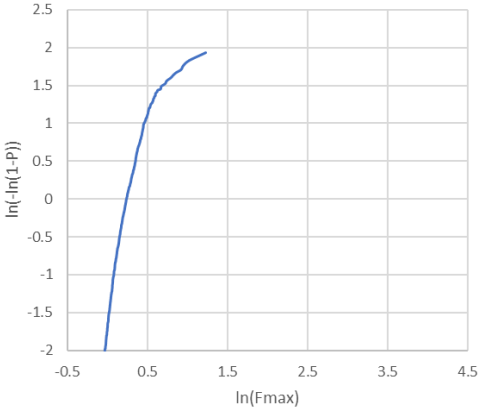

Figure 75 Non-exceedance probability distribution for irregular wave with T_p = 3s and H_{m0} = 0.26m and A_o/A_c = 0.88%.

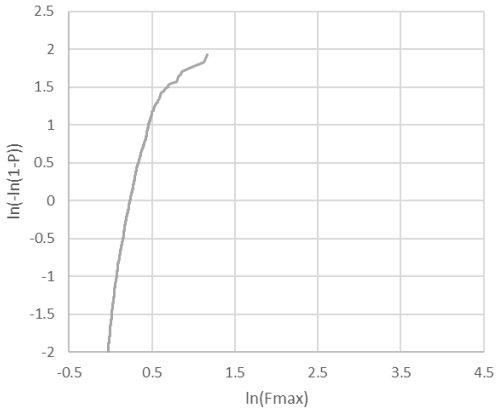

Figure 76 Non-exceedance probability distribution for irregular wave condition with T_p = 3s and H_{m0} = 0.26m and A_o/A_c = 2.0%.

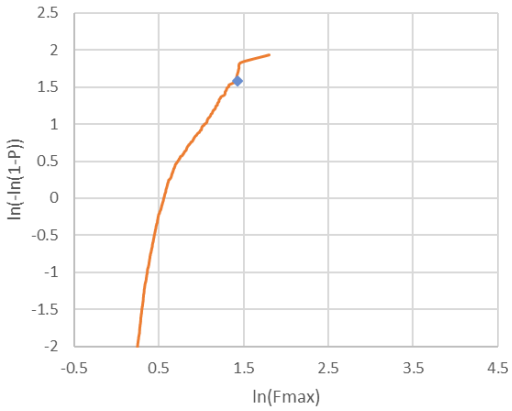

Figure 77 Non-exceedance probability distribution for irregular wave condition with T_p = 3s and H_{m0} = 0.39m and A_o/A_c = 0.88%.

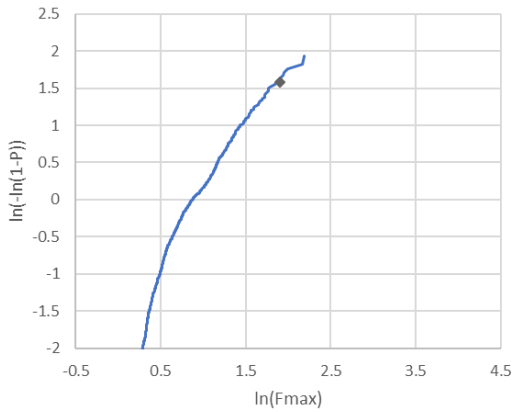

Figure 78 Non-exceedance probability distribution for irregular wave with T_p = 3s and H_{m0} = 0.52m and closed chamber.

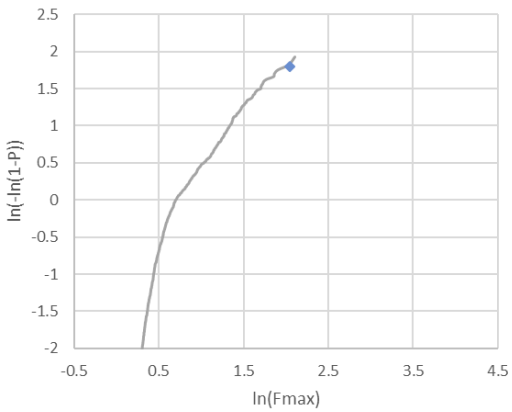

Figure 79 Non-exceedance probability distribution for irregular wave with T_p = 3s and H_{m0} = 0.52m and A_o/A_c = 0.88%.

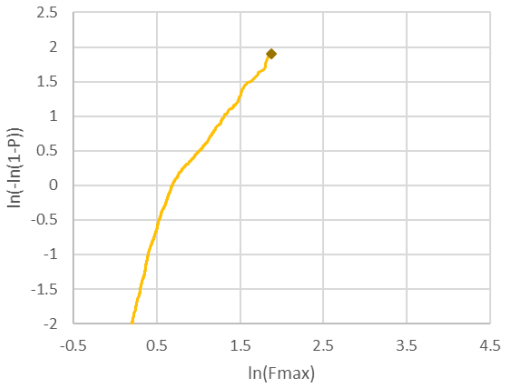

Figure 80 Non-exceedance probability distribution for irregular wave with T_p = 4s and H_{m0} = 0.4m and A_o/A_c = 0.1%.

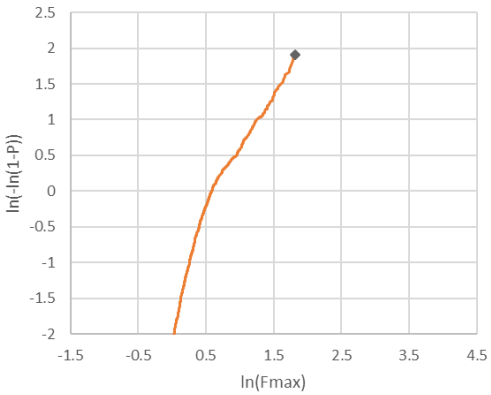

Figure 81 Non-exceedance probability distribution for irregular wave with T_p = 4s and H_{m0} = 0.4m and A_o/A_c = 0.2%.

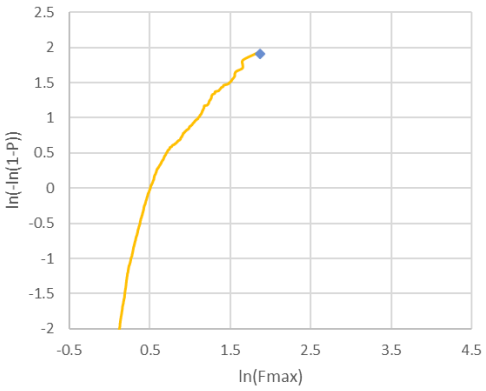

Figure 82 Non-exceedance probability distribution for irregular wave with T_p = 4s and H_{m0} = 0.4m and A_o/A_c = 0.88%.

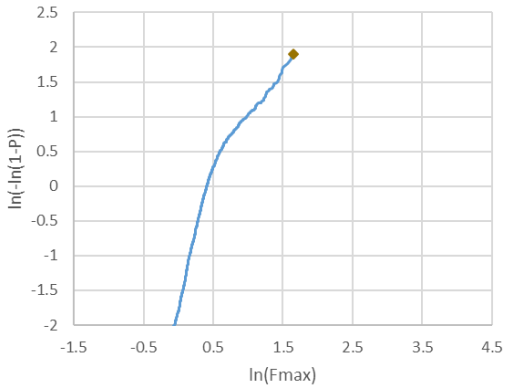

Figure 83 Non-exceedance probability distribution for irregular wave with T_p = 4s and H_{m0} = 0.4m and A_o/A_c = 2.0%.

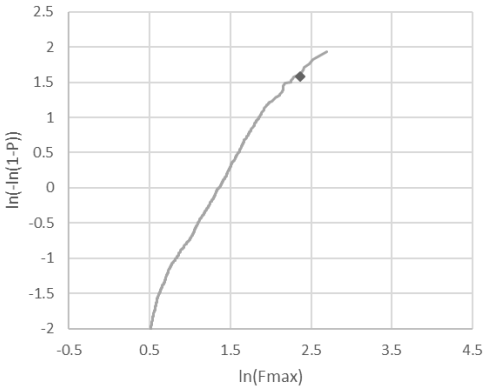

Figure 84 Non-exceedance probability distribution for irregular wave with T_p = 4s and H_{m0} = 0.6m and closed chamber.

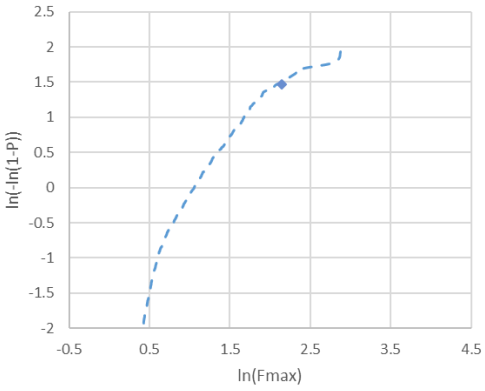

Figure 85 Non-exceedance probability distribution for irregular wave with T_p = 4s and H_{m0} = 0.6m and A_o/A_c = 0.88%.

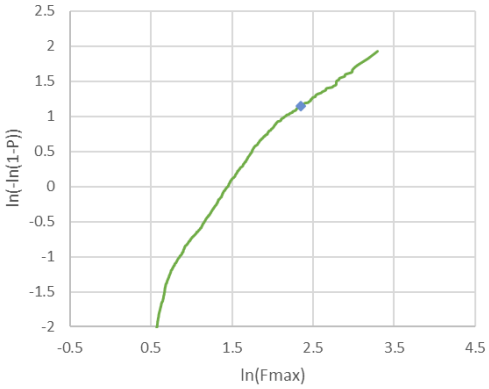

Figure 86 Non-exceedance probability distribution for irregular wave with T_p = 4s and H_{m0} = 0.8m and A_o/A_c = 0.88%.

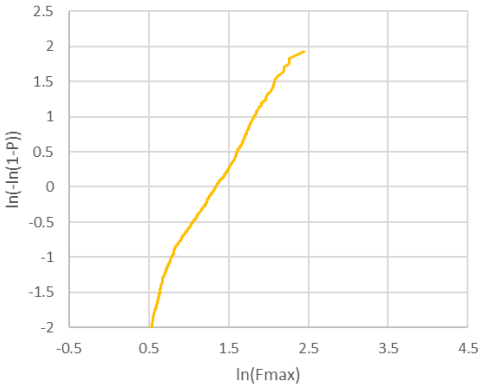

Figure 87 Non-exceedance probability distribution for irregular wave with T_p = 5s and H_{m0} = 0.54m and closed chamber.

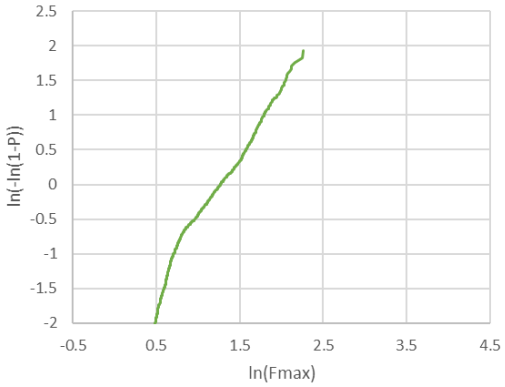

Figure 88 Non-exceedance probability distribution for irregular wave with T_p = 5s and H_{m0} = 0.54m and A_o/A_c = 0.1%.

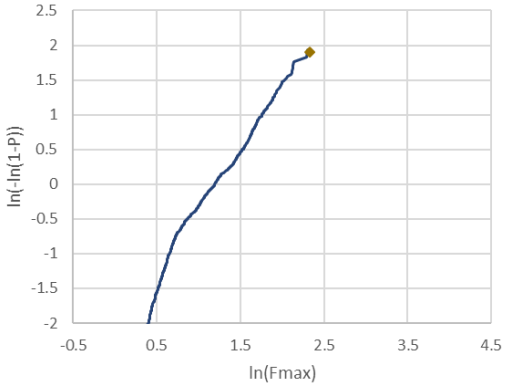

Figure 89 Non-exceedance probability distribution for irregular wave with T_p = 5s and H_{m0} = 0.54m and A_o/A_c = 0.2%.

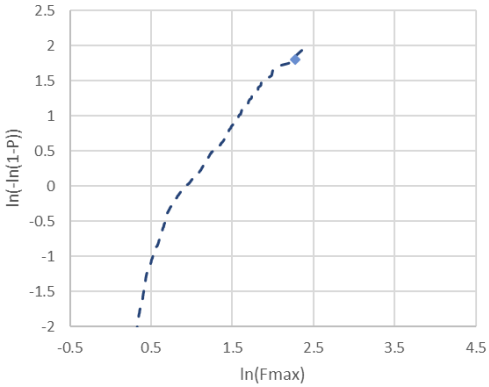

Figure 90 Non-exceedance probability distribution for irregular wave with T_p = 5s and H_{m0} = 0.54m and A_o/A_c = 0.88%.

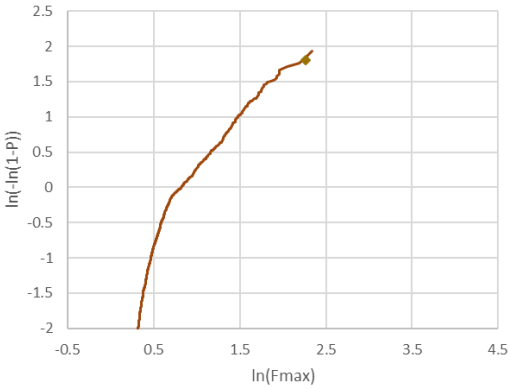

Figure 91 Non-exceedance probability distribution for irregular wave with T_p = 5s and H_{m0} = 0.54m and A_o/A_c = 2.0%.

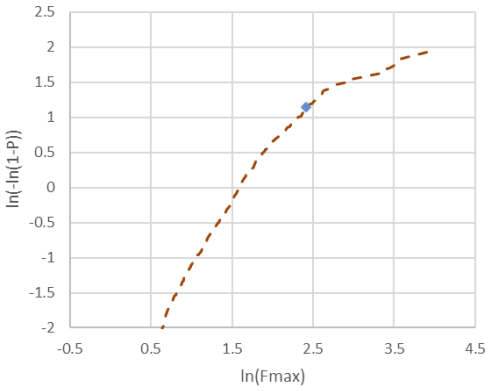

Figure 92 Non-exceedance probability distribution for irregular wave with T_p = 5s and H_{m0} = 0.81m and A_o/A_c = 0.88%.

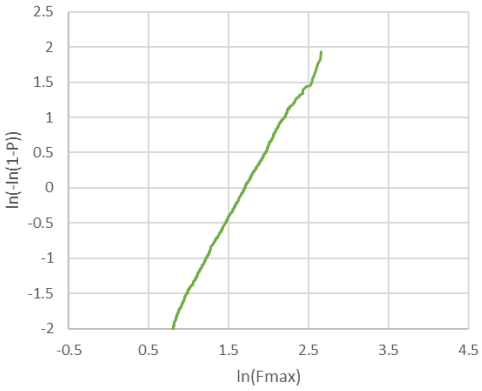

Figure 93 Non-exceedance probability distribution for irregular wave with T_p = 6s and H_{m0} = 0.67m and closed chamber.

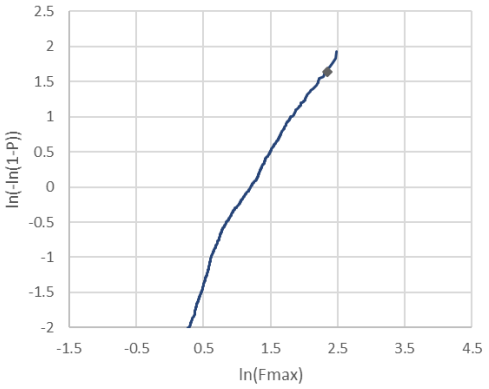

Figure 94 Non-exceedance probability distribution for irregular wave with T_p = 6s and H_{m0} = 0.67m and A_o/A_c = 2.0%.

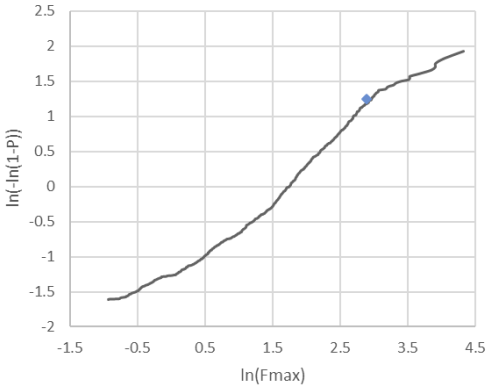

Figure 95 Non-exceedance probability distribution for irregular wave with T_p = 6s and H_{m0} = 1.0m and A_o/A_c = 0.88%.

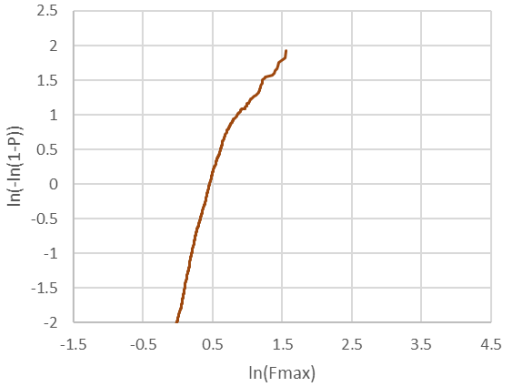

Figure 96 Non-exceedance probability distribution for irregular wave with T_p = 4.5s and H_{m0} = 0.26m and closed chamber.

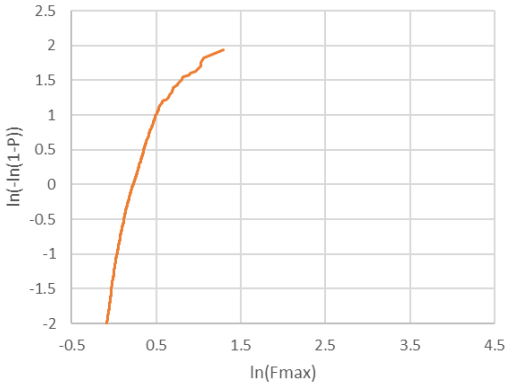

Figure 97 Non-exceedance probability distribution for irregular wave with T_p = 4.5s and H_{m0} = 0.26m and A_o/A_c = 0.88%.

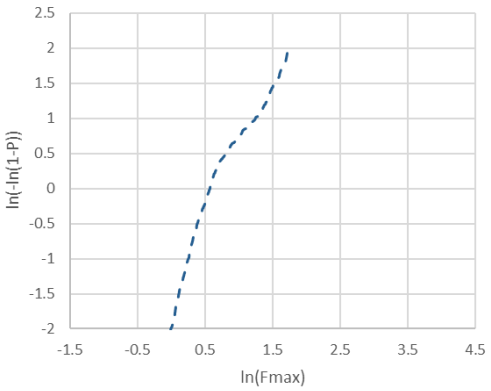

Figure 98 Non-exceedance probability distribution for irregular wave with T_p = 6.5s and H_{m0} = 0.4m and A_o/A_c = 0.88%.

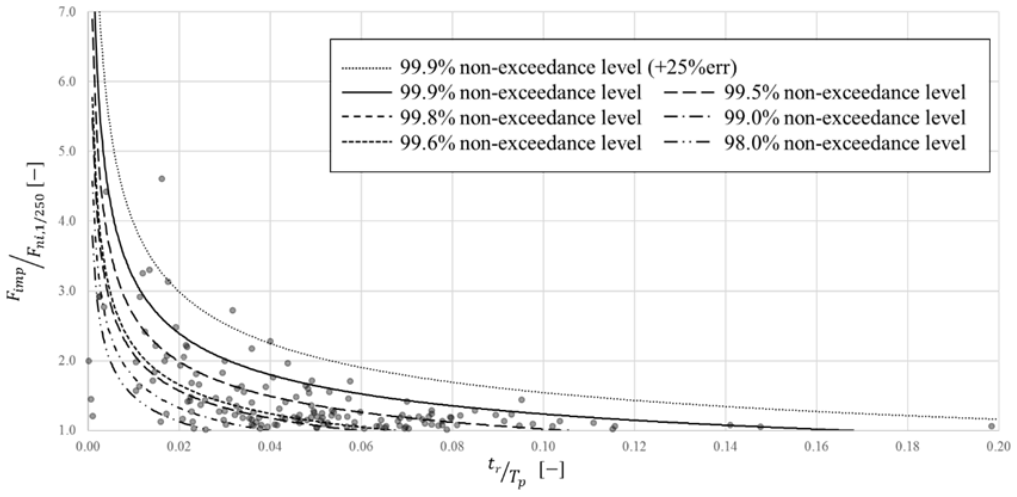

Figure 99 Impact force maxima against rise time for the front wall impact force with the lines represents the Weggel and Maxwell (1970) relationship for multiple non-exceedance level after Cuomo *et al.* (2011).

In 1939, a method to predict the impulsive pressure magnitude for a prototype scale was proposed by Bagnold (1939). This method utilised the peak pressure of a compressed air by an impinging mass of water column as explained in Chapter 2. This method, which commonly known as "Bagnold method", is later used to establish an adjustment factor by Takahashi *et al.* (1985) and they proposed an adjustment factor (λ) of 3.01 to be used to adjust the impulsive loads measured using a 1:16 physical model of a vertical breakwater which scaled down using Froude similitude law (see Equation 1). This adjustment factor then extended to include multiple scale model by Cuomo *et al.* (2010b) with several parameters defined for a scaled model Bagnold number calculation. The water mass velocity (u_o) is defined as the propagation velocity of a wave with height equal to the significant wave height (H_{m0}) over a constant water depth d (Equation 28). The air chamber thickness (D_i) can be considered as a circular air pocket with diameter equal to 1/12 of the H_{m0} (Equation 29), and, finally, the water mass thickness (k_i) is taken as Equation 30 as observed by Bagnold (1939) and Mitsuyasu (1967).

$$u_o = \sqrt{g(d + H_{m0})} \tag{28}$$

$$D_i = \frac{\pi}{12} H_{m0} \tag{29}$$

$$k_i = 0.2\left(1 - \frac{\pi}{12}\right) H_{m0} \tag{30}$$

The same method is used to find the adjustment factor (λ) for the large-scale test results. For example, for the Irr11 wave conditions, the significant wave height (H_{m0}) is 1.00 m so the Bagnold number of the model is equal to 0.153. Since the large-scale model is about 1:9 to the prototype, the Bagnold number of the prototype will be 1.378, thus the predicted ($p_{i,max}$) is about 377 kPa. The experimental results of Irr11 (Figure 100) show the impact pressure ($p_{i,max}$) measured is 224 kPa, so the model is over-estimating the prototype impact pressure by a factor (λ) of 5.34. Since the scale factor proposed by Cuomo *et al.* (2010b) (Figure 15) does not include model Bagnold number (Bgn_M) higher than 0.03 and prototype Bagnold number (Bgn_p) higher than 1.00, current experimental results cannot be compared directly. A simple extrapolation, however, put the adjustment factor of higher than 5 for current experiment, which supported the result.

It is important to remember that an impact load occurs locally and may not occurred exactly at the pressure transducer location during the experiment. For example, the previous $p_{i,max}$ example of λ calculation was measured at the pressure transducer elevation of P2 (see Figure 12). Different wave conditions with H_{m0} equal to 0.81m (Irr08) result (Figure 101), on the other hand, shows $p_{i,max}$ occurred at elevation of P1 (see Figure 12) and shows an adjustment factor of 2.41. Table 5 lists several the $p_{i,max}$, λ, and the location corresponding to $p_{i,max}$ observed in current experimental campaign. As can be seen in the adjustment factor varies widely with maximum number of 5.43. This may happen because of the nature of impact as explained above. The $p_{i,max}$ of number 3 and 4 experiments in the table, for instance, occurred on different PT location (P4 and P3, respectively) even though happened during the same irregular wave event.

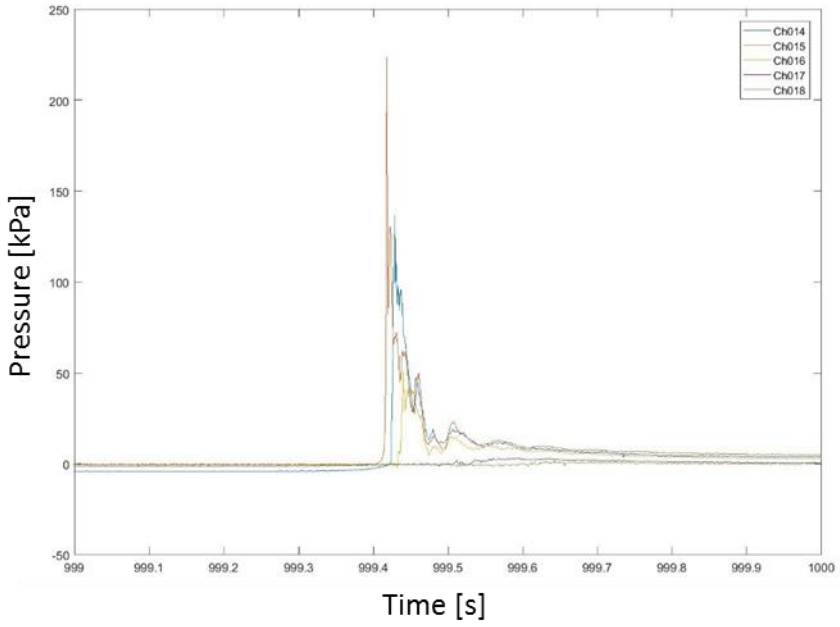

Figure 100 impulsive load time series measured on the front wall of the Large-scale OWC model with H_{m0} = 1.00m and T_p = 6s.

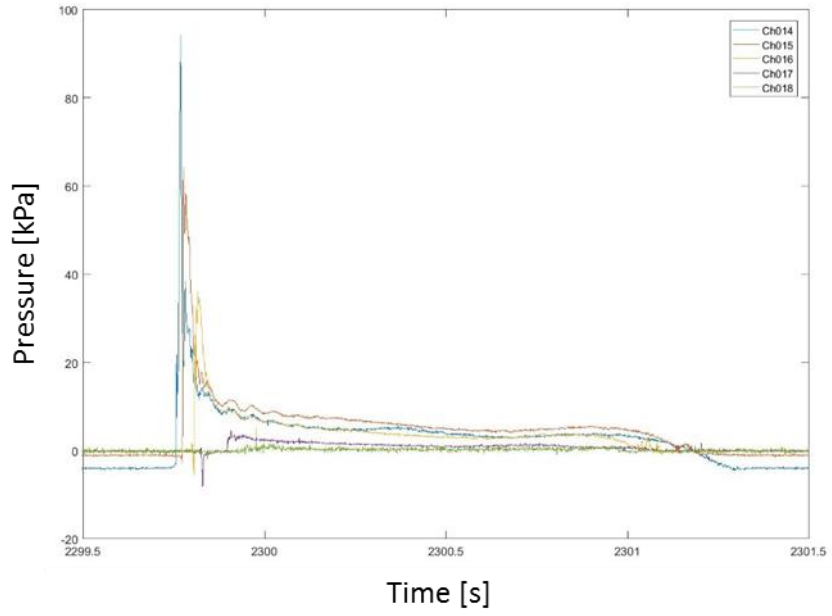

Figure 101 Figure 5. 1 impulsive load time series measured on the front wall of the Large-scale OWC model with H_{m0} = 0.81m and T_p = 5s.

No	Wave	Tp [s]	Hmo [m]	Model				Prototype		Adjustment λ
				$p_{i,max}$	PT location	$t_{i,max}$	Bagnold	Bagnold	$p_{i,max}$	
1	Irr04	4	0.400	6	P2	1437.946	0.120	1.083	296	0.182
2		4	0.400	6	P2	3165.378	0.120	1.083	296	0.172
3	Irr06	4	0.800	26	P4	1014.480	0.142	1.280	350	0.678
4		4	0.800	26	P3	1377.500	0.142	1.280	350	0.663
5	Irr08	5	0.810	94	P1	2299.770	0.143	1.285	351	2.412
6	Irr10	6	0.670	13	P2	3951.729	0.135	1.216	333	0.364
7	Irr11	6	1.000	224	P2	999.418	0.153	1.378	377	5.343

Table 5 Adjustment factor (λ) estimation for the large-scale model experiments when compared with the prototype impact load ($p_{i,max}$) estimation.

5.1.3 Probability of impacts (Pi%) – prediction method

A simple method to estimate the percentage of impacts in a single irregular wave train on a vertical breakwater was developed by Calabrese and Vicinanza (1999) as part of PROVERBS (Oumeraci *et al.*, 2001). The estimation depends on the water depth in front of the structure (h) and the depth of the water just in front of the front wall which in this case equal to the in-chamber water depth (d). It basically uses the breaking wave height (H_{bc}) calculation to predict the state of each incident wave when it hits the structure - whether it be in the condition of non-breaking (more likely to give a non-impulsive wave loads), near breaking (Figure 69 type of impact loads) and breaking (Figure 67 and Figure 68 type of impact loads) or broken (non-impulsive wave loads). Equations 31 to 33 are the formulae for wave height at breaking.

$$L_{pi} = \left(gT_p^2/2\pi\right) tanh\left(2\pi\, h/L_{pi}\right) \quad (31)$$

$$C^* = (1 - C_r)/(1 + C_r) \quad (32)$$

$$H_{bc} = (0.1025 + 0.0217\, C^*)\, L_{pi}\, tanh\left(2\pi\, k_b h/L_{pi}\right) \quad (33)$$

where k_b is the empirical berm constant and equal to 1 when no berm utilised, L_{pi} is the peak period wave length in the water depth h, C^* is the reflection constant depending on the overall reflection coefficient C_r, and H_{bc} is the wave height at breaking. Table 6 listed the reflection coefficient of each experimental test calculated

based on the four-probe reflection analysis. The calculation is directly taken from Viviano *et al*. (2016) which was based on Faraci *et al.,* (2014) four probes method.

As can be seen from Table 6, the reflection coefficient (C_r) of the device while the orifice is closed is near to 0.9. At or near maximum operating efficiency, however, the reflection is reduced significantly to about 0.41 to 0.64 depending on the irregular wave condition. The reflection coefficient at optimum operation condition is also consistently the lowest compared to other operating conditions settings and compared to the closed and fully open settings.

To give the maximum possible percentage of impact, the percentage of wave which passed the non-breaking-to-breaking point (P_b) has to be estimated first using Equation 34 with H_{si} denoting the incident wave height and H_{bc} denoting the breaking wave height.

$$P_b = \exp\left[-2\left(\frac{H_{bc}}{H_{si}}\right)\right] \tag{34}$$

These waves might include both the breaking wave and the broken wave. In other words, P_b can be seen as the maximum percentage of impact ($P_{i\%}$) possible in a single sequence. In order to estimate the actual percentage of impact ($P_{i\%}$), the transition point between breaking wave impact to broken waves needs to be found. PROVERBS (Oumeraci *et al.*, 2001) suggested that the transition should occur when $C_r = 0$ and the breaking to broken transition wave height (H_{bs}) can be estimated using Equation 35.

$$H_{bs} = 0.1242\, L_{pi}\, tanh\left(2\pi\, h_s/L_{pi}\right) \tag{35}$$

Thus, the percentage of impacts can be calculated by subtracting the number of broken waves in P_b according to Equation 36.

$$P_{i\%} = \left\{exp\left[-2\left(\frac{H_{bc}}{H_{si}}\right)^2\right] - exp\left[-2\left(\frac{H_{bs}}{H_{si}}\right)^2\right]\right\}.100\% \tag{36}$$

No	Test ref.	Wave Condition	T_p [s]	H_{m0} [m]	D_{ori} [m]	C_r
1	32708	Irr01	3	0.26	0	0.89
2	31814		3	0.26	0.05	0.82
3	32007		3	0.26	0.1	0.66
4	32107		3	0.26	0.2	0.64
5	31410		3	0.26	0.3	0.73
6	40202	Irr02	3	0.39	0.2	0.59
7	32709	Irr03	3	0.52	0	0.9
8	40203		3	0.52	0.2	0.57
9	31902	Irr04	4	0.40	0.05	0.9
10	32008		4	0.40	0.1	0.67
11	32108		4	0.40	0.2	0.48
12	31701		4	0.40	0.3	0.52
13	32710	Irr05	4	0.60	0	0.89
14	40204		4	0.60	0.2	0.49
15	40205	Irr06	4	0.80	0.2	0.48
16	32711	Irr07	5	0.54	0	0.91
17	32009		5	0.54	0.1	0.71
18	32109		5	0.54	0.2	0.48
19	31702		5	0.54	0.3	0.52
20	40206	Irr08	5	0.81	0.2	0.5
21	32801	Irr10	6	0.67	0	0.91
22	31704		6	0.67	0.3	0.54
23	40207	Irr11	6	1.00	0.2	0.514
24	32712	Irr13	4.5	0.26	0	0.9
25	32401		4.5	0.26	0.2	0.41
26	32402	Irr14	6.5	0.40	0.2	0.48

Table 6 Reflection coefficients based on Faraci *et al.*, (2014) after Viviano *et al.*, (2016) for the large-scale physical model.

Figure 102 shows the percentage of the impact estimation for each event based on the reflection coefficient (blue circle) for the large-scale test and the simple vertical breakwater $P_{i\%}$ calculation taken from Allsop *et al.* (1997) (orange rectangle). As can be seen from the figure, the large-scale test result is in good agreements with the example. Although the percentage of impact for H_{si}/d between 0.5 and 0.6 seems to be less agreeable, but the trend line is still following the overall data where the impact started to appear between H_{si}/d = 0.3 and H_{si}/d = 0.4. The data, furthermore, shows a good agreement for 0.6 < H_{si}/d < 0.7. It should be noted that the orange rectangle data is based on the conventional vertical breakwater.

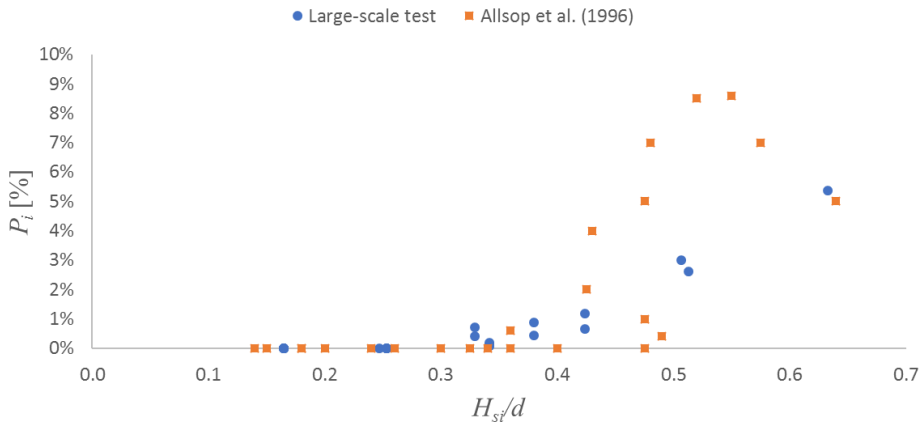

Figure 102 Impact probability calculation plotted against the normalised incident wave height (H_{si}) for the large-scale measurements (blue circle) and Allsop et al (1996) (orange square).

5.1.4 Impact Probabilities ($P_{i\%}$) - -comparison of prediction with OWC experiments

To compare the $P_{i\%}$ estimations with the experiment, the rectangular force calculation is applied for the front wall based on pressure transducers P1-P5 (Figure 18) measurement. The percentage of impact is estimated for 1000 wave cycles for each irregular condition. Table 7 shows the number of impacts predicted and observed for each test and Figure 103 shows the plotted comparison between the estimation (circle) and the observation (square) against the normalised incident wave height (H_{si}/d). The event maxima are then plotted on the same non-exceedance graphs in Figure 104-Figure 112. Plots are only presented for the irregular wave tests in which impact were observed. The predicted onset of impacts (by $P_{i\%}$) is shown by the horizontal line.

No	Test ref.	Wave Condition	T_p [s]	H_{m0} [m]	D_{ori} [m]	$P_{i\%}$ for 1000 events	# Impact observed
1	32708	Irr01	3	0.26	0	0	0
2	31814		3	0.26	0.05	0	0
3	32007		3	0.26	0.1	0	0
4	32107		3	0.26	0.2	0	0
5	31410		3	0.26	0.3	0	0
6	40202	Irr02	3	0.39	0.2	0	7
7	32709	Irr03	3	0.52	0	7	7
8	40203		3	0.52	0.2	4	2
9	31902	Irr04	4	0.40	0.05	0	1
10	32008		4	0.40	0.1	0	1
11	32108		4	0.40	0.2	0	1
12	31701		4	0.40	0.3	0	1
13	32710	Irr05	4	0.60	0	9	7
14	40204		4	0.60	0.2	4	12
15	40205	Irr06	4	0.80	0.2	30	40
16	32711	Irr07	5	0.54	0	2	0
17	32009		5	0.54	0.1	1	1
18	32109		5	0.54	0.2	1	2
19	31702		5	0.54	0.3	1	2
20	40206	Irr08	5	0.81	0.2	26	39
21	32801	Irr10	6	0.67	0	12	0
22	31704		6	0.67	0.3	7	5
23	40207	Irr11	6	1.00	0.2	54	28
24	32712	Irr13	4.5	0.26	0	0	0
25	32401		4.5	0.26	0.2	0	0
26	32402	Irr14	6.5	0.40	0.2	0	0

Table 7 Number of impacts based on the calculation and observed number of impacts of the large-scale experiment comparison.

As can be seen from Table 7, the predicted number of impacts seems to have a fairly good agreement with the observation. The prediction over-estimates the number of impacts observed in cases no. 15, 21 and 23, while the prediction under-estimates the number of impacts observed in cases no. 6, 14, and 20. The prediction method predicts the number of impacts observed for the rest of the cases quite well within ±2 impacts.

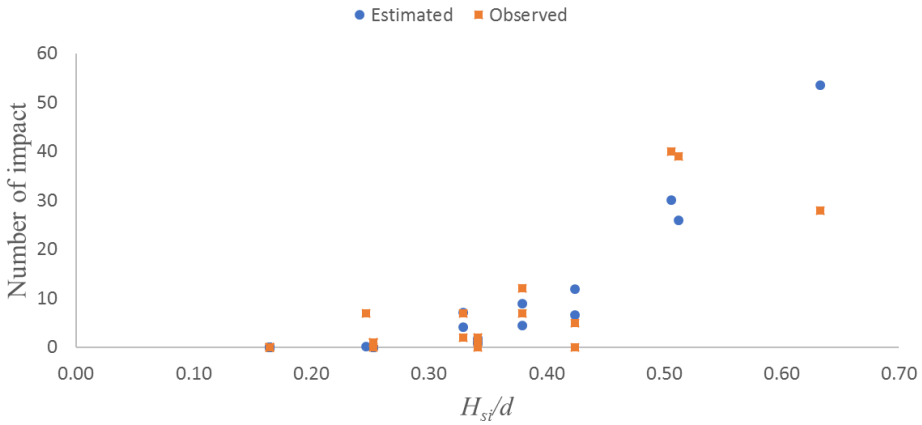

Figure 103 Estimated (circle) and observed (square) number of impacts plotted against the normalised incident wave height (H_{si}), large-scale measurements, irregular wave.

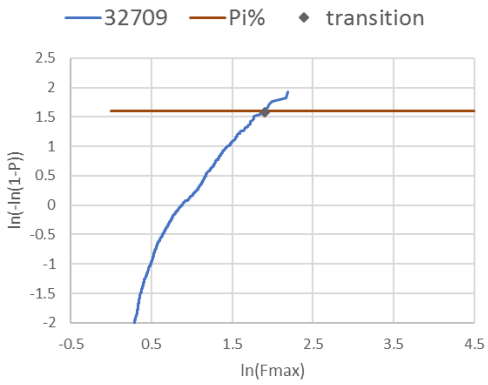

Figure 104 Non-exceedance probability distribution for irregular wave with T_p = 3s and H_{m0} = 0.52m and closed chamber, solid line represents the predicted number of impacts ($P_{i\%}$).

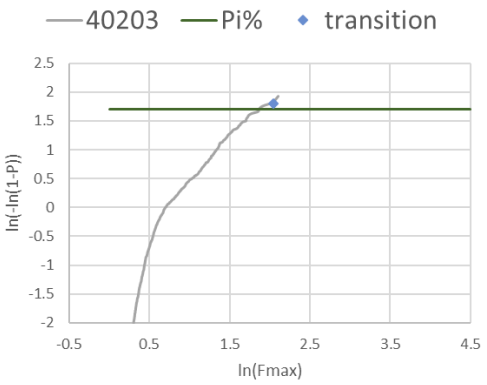

Figure 105 Non-exceedance probability distribution for irregular wave with T_p = 3s and H_{m0} = 0.52m and A_o/A_c = 0.88%, solid line represents the predicted number of impacts ($P_{i\%}$).

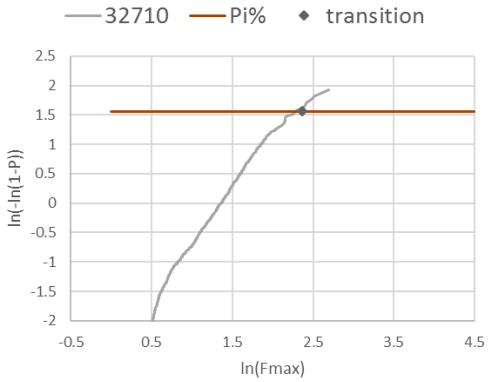

Figure 106 Non-exceedance probability distribution for irregular wave with T_p = 4s and H_{m0} = 0.6m and closed chamber, solid line represents the predicted number of impacts ($P_{i\%}$).

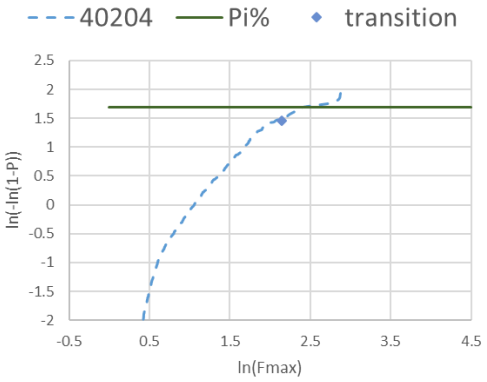

Figure 107 Non-exceedance probability distribution for irregular wave with T_p = 4s and H_{m0} = 0.6m and A_o/A_c = 0.88%, solid line represents the predicted number of impacts ($P_{i\%}$).

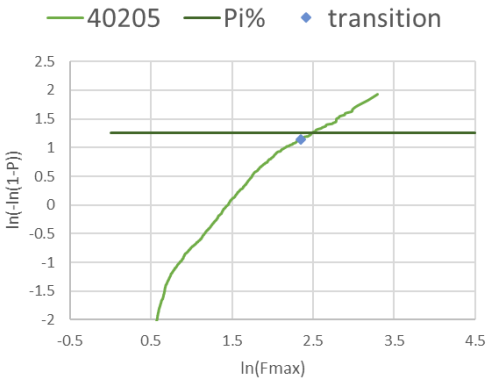

Figure 108 Non-exceedance probability distribution for irregular wave with T_p = 4s and H_{m0} = 0.8m and A_o/A_c = 0.88%, solid line represents the predicted number of impacts ($P_{i\%}$).

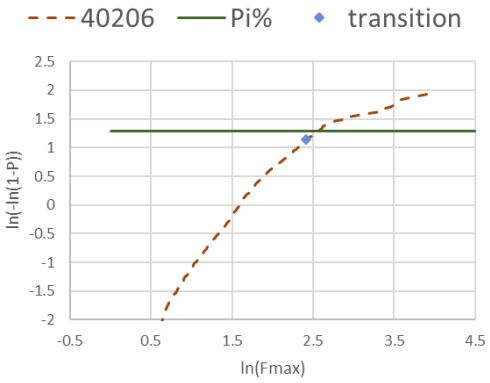

Figure 109 Non-exceedance probability distribution for irregular wave with T_p = 5s and H_{m0} = 0.81m and A_o/A_c = 0.88%, solid line represents the predicted number of impacts ($P_{i\%}$).

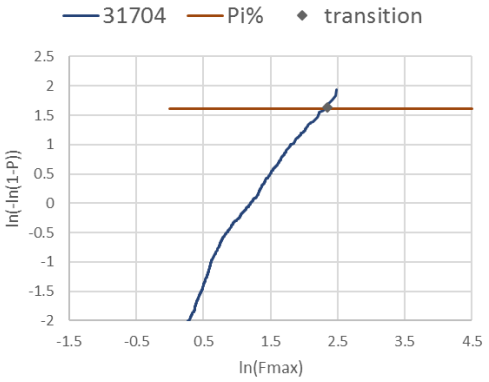

Figure 110 Non-exceedance probability distribution for irregular wave with T_p = 6s and H_{m0} = 0.67m and A_o/A_c = 2.0%, solid line represents the predicted number of impacts ($P_{i\%}$).

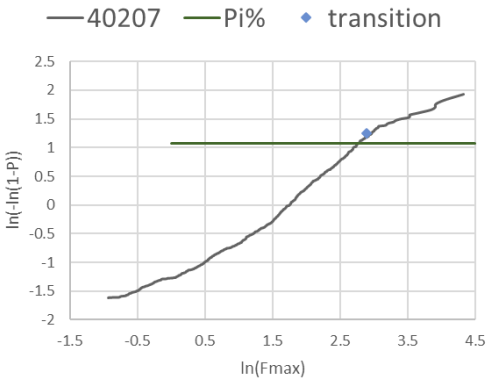

Figure 111 Non-exceedance probability distribution for irregular wave with T_p = 6s and H_{m0} = 1.0m and A_o/A_c = 0.88%, solid line represents the predicted number of impacts ($P_{i\%}$).

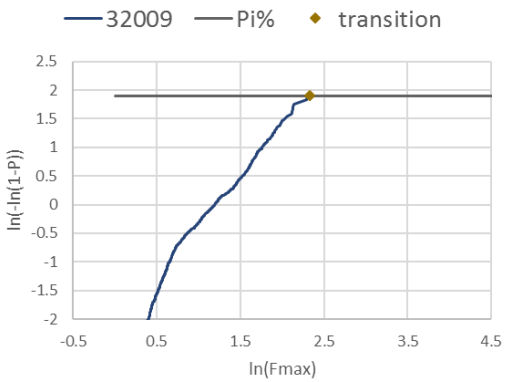

Figure 112 Non-exceedance probability distribution for irregular wave with T_p = 5s and H_{m0} = 0.54m and A_o/A_c = 0.2%, solid line represents the predicted number of impacts ($P_{i\%}$).

Figure 104, Figure 106, Figure 110 and Figure 112 show a very good agreement between the prediction of $P_{i\%}$ and the measurements in a 1000 wave cycles test set. It should be noted that the force impact calculation is done using a rectangular method based on the pressure measurement from transducers with a very small surface area. It is inevitable, however, that the pressure maxima may be extremely sensitive to the exact location of the impact. Consequently, it is possible that some impact pressure maxima are underestimated, or indeed, impacts could be missed altogether.

Based on the results shown, it can be concluded that the impacts probability method developed for the conventional breakwaters can be used to predict the number of impacts experienced by an OWC installed vertical breakwater with fairly good accuracy.

5.2 In-chamber wave loads behaviour

5.2.1 Violent In-chamber ceiling impact characterisation

Unlike the front wall, in the idealised view of the in-chamber water column, the in-chamber ceiling would never experience a wave pressure directly from the incident wave except in the event where the whole water column rises up and meets the ceiling. Under normal operating conditions, the ceiling should only experience the air pressure

generated inside the chamber. This will be the case if the water column is behaving well as demonstrated in Figure 113 (a) and (b). In-chamber video observation, however, shows sloshing phenomena occurring during some of the experiments. This phenomenon is characterised by a turbulent surface water movement inside the chamber, with an impact on the chamber ceiling in some extreme cases.

Four different regimes are now proposed to differentiate the intensity of the in-chamber water column movement inside the chamber. The first one is "well-behaved" water column movement as previously demonstrated in Figure 113. The second is "low movement" where the water column vertical oscillation is still easily observed, but the water surface is not calm (Figure 114). The third level is "medium movement" where the water column vertical movement is harder to distinguish and there is an obvious difference in water level between the front and the rear parts of the water column, as apparent in Figure 115. The final and probably most important characterisation is the "violent movement" where there is a very little water column oscillation visible while the water surface is very chaotic. In some extreme cases, impact pressures are observed on the ceiling during this level of water column movement as shown in Figure 116.

A separate research using the Particle Imaging Velocimetry (PIV) measurement for an OWC water column behaviour is done by López, *et al.* (2015). The research shows vortices appear near the front opening as the water enters the water column under certain wave conditions. This is in line with the unsteady water column behaviour found in the present work although due to the limitation of the camera, the image of such vortices inside the water column cannot be seen in the large-scale physical model test.

In addition to the water column behaviour characterisation, three types of violent ceiling impact were observed. The first type is the one generating highest impact pressure of up to $12\rho g H_{m0}$, which is "single ceiling impact" on the front or the rear part of the chamber. Figure 117 (a) shows the single impact event pressure measurement on the rear ceiling, (b) shows the location of each corresponding colour, and (c) shows the corresponding image on the rear part of the chamber. In addition to the high magnitude of impact, this condition is worsened by the unpredictability of the impact pressure generated as shown by the bigger pressure measurement in Figure 118, even

though the wave condition has less wave steepness. The impact, unfortunately, cannot be seen in the video since the location of the impact is very close to the in-chamber video recorder location.

The second type of violent ceiling impact is “successional ceiling impact” in which event there is, in succession, either an impact on the rear of the ceiling followed by an impact in the front of the chamber, or vice versa. Figure 119 (a) to (d) show the breakdown event of this type of impact with t^* indicates the relative time of each breakdown event to a single wave period ($t^* = t/T_p$). In the example in the figure, the impact occurs on the front part of the ceiling, directly followed by an impact on the rear part of the ceiling.

Figure 120 shows the time series pressure measurement on the ceiling and the rear wall of the chamber. Figure 121 is a second example of a “successional celling impact”, but this time, the first impact occurring on the rear part of the ceiling followed by the impact on the front part. In this instance, the impact pressure maxima generated are similar between the two successive impacts.

The third ceiling impact type is the “whole water column ceiling impact” when the whole, or nearly the whole water column hits the ceiling of the chamber. This type of ceiling impact is usually indicated by a big hydrostatic wave pressure leading up to, and immediately following the impact pressure, with the impact occurring at the peak of the chamber pressure. Figure 122 shows a pressure time series of such events under regular wave condition. As can be seen, the non-impulsive pressure is similar, if not identical, for each single wave cycle. The impact magnitude, however, looks random. This further emphasis the uncertainty in ceiling impact.

(a) (b)

Figure 113 "Well behaved" upward (a) and downward (b) water column oscillation behaviour in T=4.0s, H=0.4m and A_o/A_c=0.1% test.

(a) (b)

Figure 114 "Low sloshing" during upward (a) and downward (b) water column oscillation in in T=4.0s and H=0.8m and A_o/A_c=0.1% test.

(a)

(b)

(c)

Figure 115 "Medium sloshing" water column behaviour with less obvious upward (a) and downward (b) oscillation and an impact observed on the rear wall in (c) in T=5.0s and H=0.67m and A_o/A_c=0.88% test.

Figure 116 "Violent sloshing" water column behaviour with no observable water column oscillation and an impact on the ceiling in T_p=5.0 s and H_{m0} = 0.8m and A_o/A_c=2.0% test.

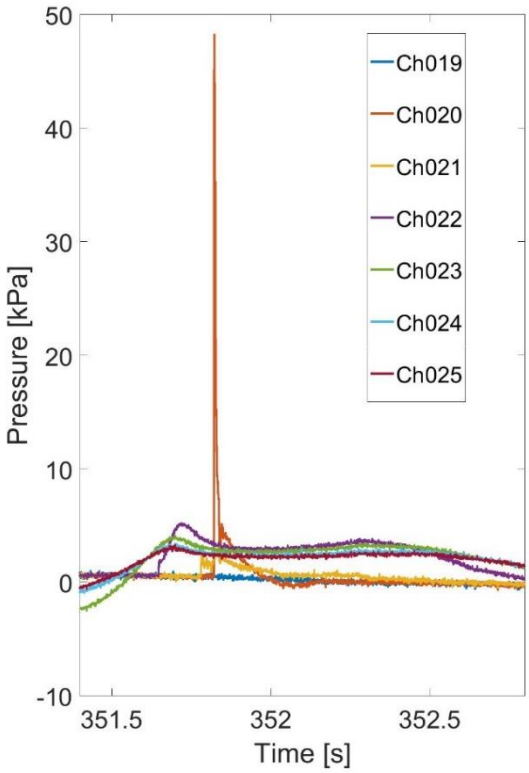

(a)

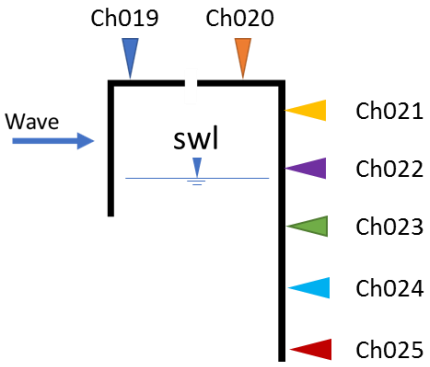

(b)

(c)

Figure 117 Example of "single ceiling impact" type with (a) Time series of chamber pressure measured with the line colour key in (b), and (c) showing the corresponding impact event.

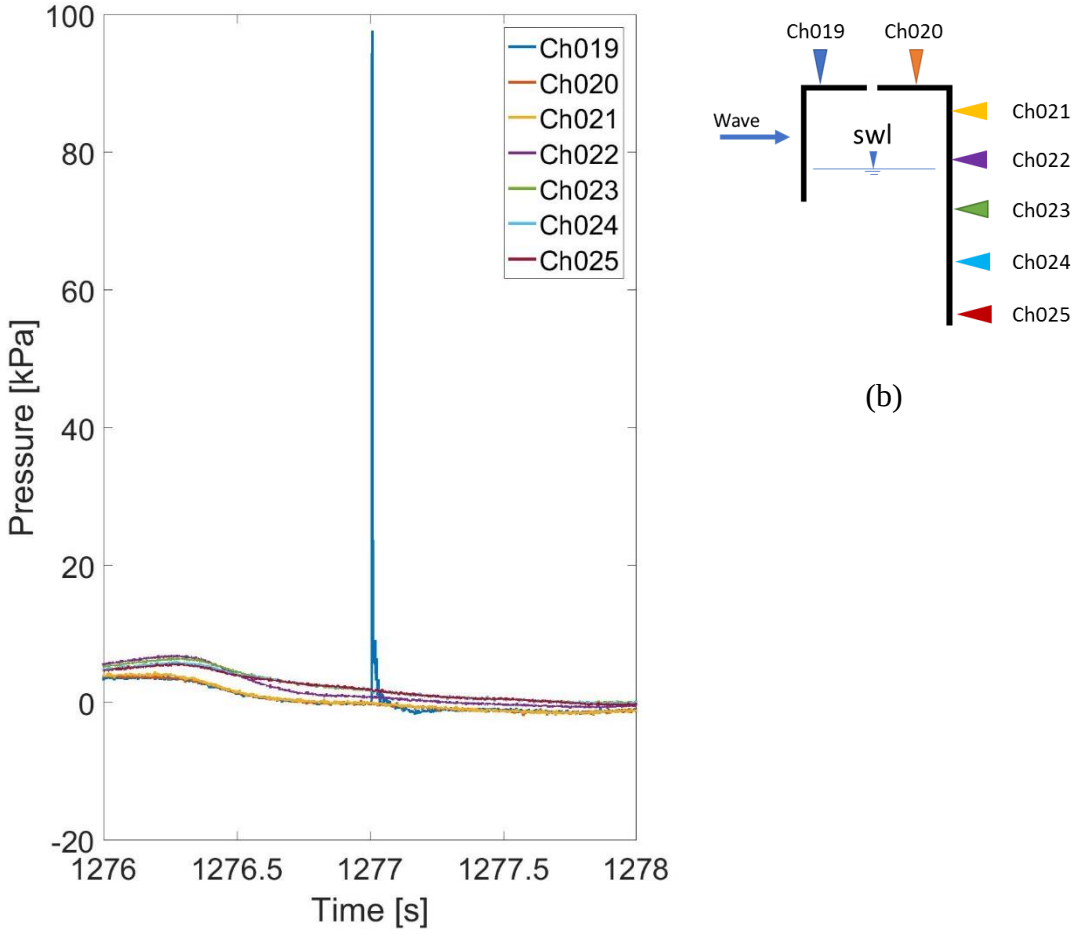

(a)

(b)

Figure 118 Example of "single ceiling impact" type with (a) time series of chamber pressure measured with the line colour key in (b).

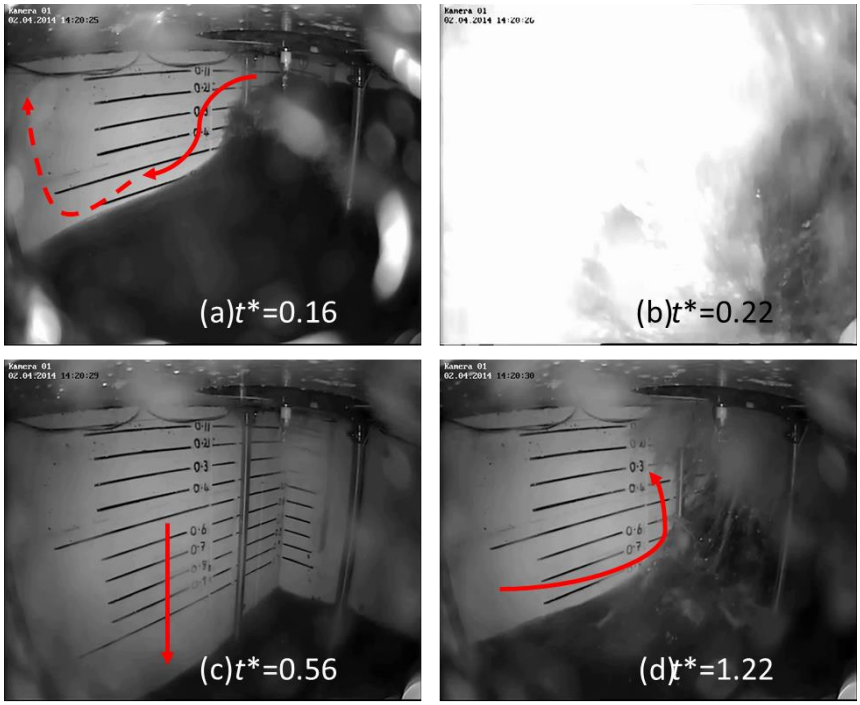

Figure 119 Sequence of events in a "successional ceiling impacts" example with (a) The water column rises and is reflected by the rear wall. (b) The reflected water flows to the front part of the chamber and an impact occurs on the front part of the ceiling, followed by (c) the water column falling and (d) rising up again to give a second impact on the rear part of the ceiling. Here *t indicates the relative time of each breakdown event to a single wave period (*t** = t/T_p).**

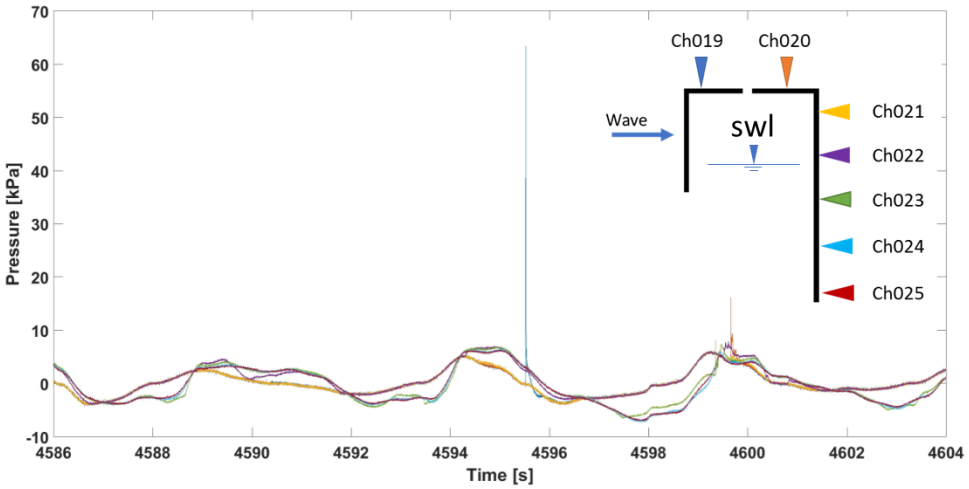

Figure 120 The pressure time series of the in-chamber pressure transducers for "successional ceiling impacts" type, corresponds to the one shown in Figure 119, line colours corresponds the diagram.

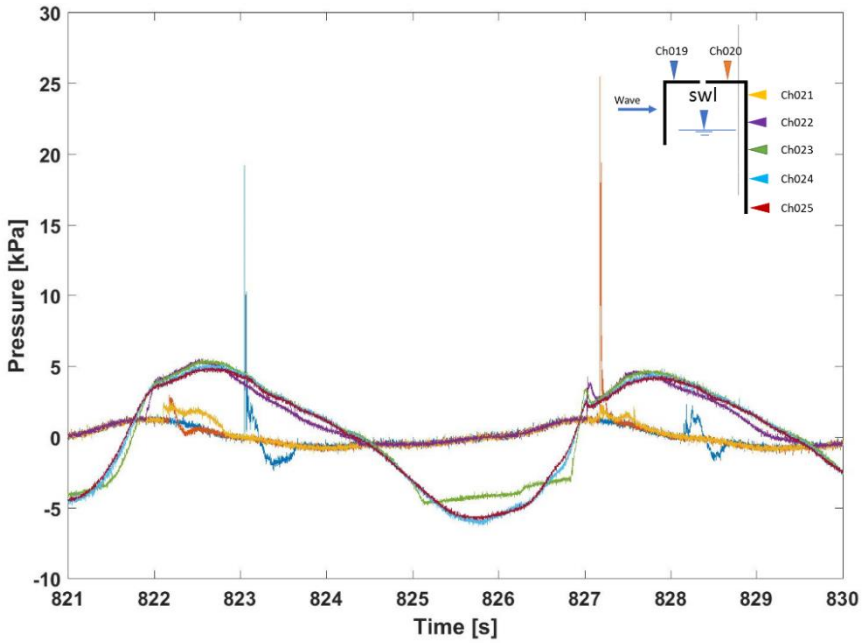

Figure 121 Pressure time series measurement example of the "successional ceiling impacts" with line colour corresponds the diagram.

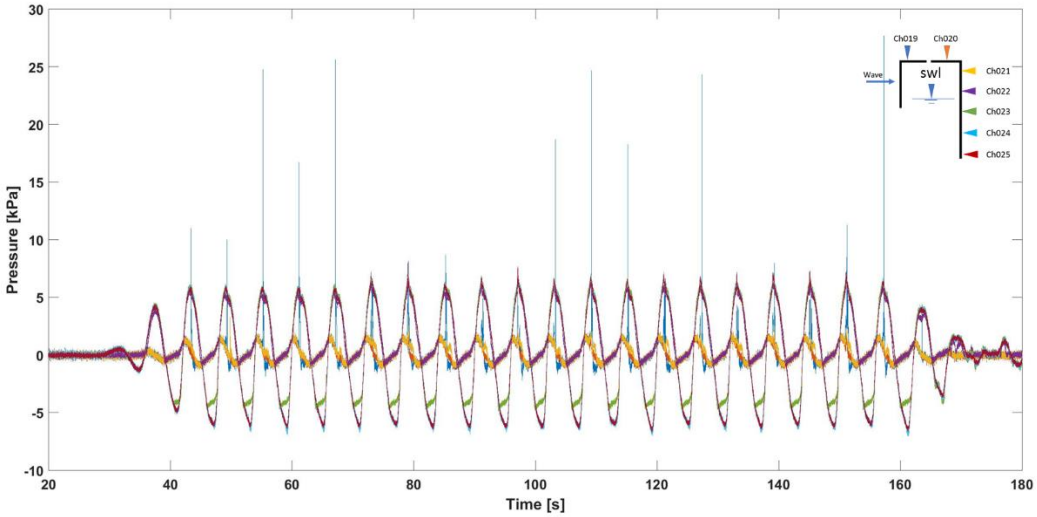

Figure 122 A time series pressure measurement example of "whole water column ceiling impact", line colour corresponds the diagram.

5.2.2 Front wall and in-chamber ceiling impact comparison

Because the method for the estimation of the percentage of impacts has been shown (Subchapter 3.1.4) to work quite well for the front wall of the OWC breakwater, it is

interesting to explore whether the ceiling impacts have any connection with the front wall impacts. The importance is highlighted because the impact pressures measured are at least comparable to the front wall impact pressures. Table 8 summarises the impact force maxima ($F_{i,max}$), time of the force maxima ($t_{i,max}$) and rise time (t_r) for both the front wall and in-chamber ceiling. The table includes only the cases where the ceiling impact is observed. One important similarity that all of the cases shared is that they are closer to the fully open regime, event tough no all the same orifice opening (D_{ori}). This is possible because the chamber pressure generation is much less in the bigger orifice opening (especially the fully open orifice setting), so larger water column motion is anticipated. Furthermore, the force impact maxima measured are consistently larger on the ceiling than the front wall and are accompanied by much shorter rise time (t_r). Biggest impacts occurring on the front wall, on the other hand, do not generally result in the biggest impacts on the ceiling - all of the $t_{i,max}$ for the front and the ceiling are different, apart from case number 3. Cases number 3 and 4 share the same wave condition with the difference only in the orifice opening. The force impact maximum of the front wall is shown to occur at the same time (4727s). The ceiling impact maxima, however, occurred at different time (4728s and 3718s). This further emphasises the uncertainty in impact force experienced by the ceiling.

In the previous chapter, D_{ori} equal to 0.3 m is shown to be in “fully open” regime. From the albeit somewhat limited set of impact cases studied, the observation shows that in the fully open condition, when there is an impact on the front wall, there will be an impact on the ceiling.

No	T_p [s]	H_{m0} [m]	D_{ori} [m]	front			ceiling		
				$F_{i,max}$	$t_{i,max}$	t_r	$F_{i,max}$	$t_{i,max}$	t_r
1	4	0.4	0.3	5.08	1436.82	0.101	59.81	351.82	0.002
2	4	0.8	0.2	27.09	1328.31	0.107	51.46	2594.45	0.001
3	5	0.54	0.2	10.51	4727.53	0.384	41.34	4728.24	0.001
4	5	0.54	0.3	10.42	4727.01	0.353	60.55	3718.74	0.001
5	5	0.81	0.2	49.69	3178.47	0.082	77.71	4595.52	0.001
6	6	0.67	0.3	11.91	3954.09	0.454	84.33	282.59	0.001
7	6	1	0.2	75.66	999.44	0.025	119.50	1277.01	0.001

Table 8 Impact force maxima ($F_{i,max}$), time of the force maxima ($t_{i,max}$) and rise time (t_r) for both the front wall and in-chamber ceiling.

Figure 123 compares the front wall and in-chamber ceiling force maxima for non-impulsive loads and impulsive (impact) loads. Data located above the solid line means the in-chamber ceiling impact force maxima exceeds the front wall impact force maxima for the given test. As can be seen, almost all of the impact force data is located above the solid line. This demonstrates that in-chamber impact forces are at least comparable and potentially just as important as the front wall impacts.

Figure 124 shows the rear wall and in-chamber ceiling impact force maxima comparison, while Figure 125 shows the front wall and rear wall impact force maxima comparison. It is apparent that the ceiling impact forces maxima are always bigger than the impact force experienced by the rear wall (data located above the solid line).

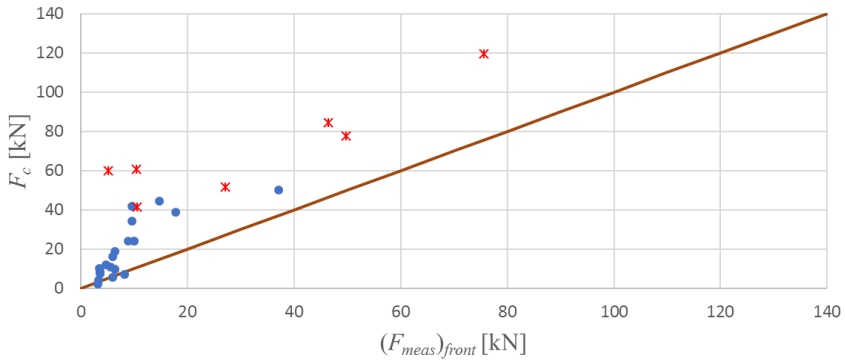

Figure 123 Front wall and in-chamber ceiling force maxima comparison, for both non-impulsive loads (solid blue circles) and impulsive (impact loads) (red stars).

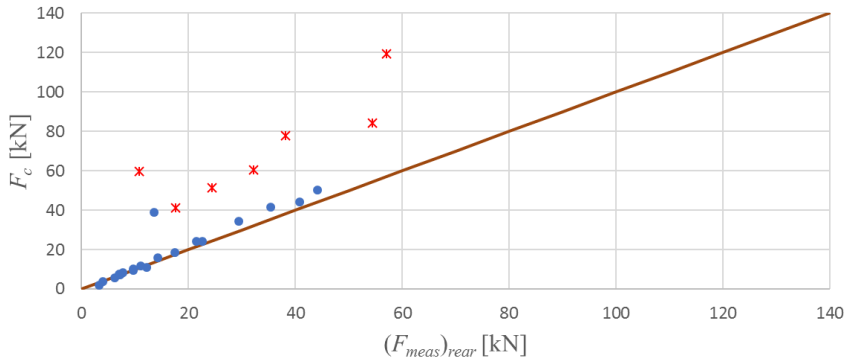

Figure 124 Rear wall and in-chamber ceiling force maxima comparison, for both non-impulsive loads (solid blue circles) and impulsive (impact loads) (red stars).

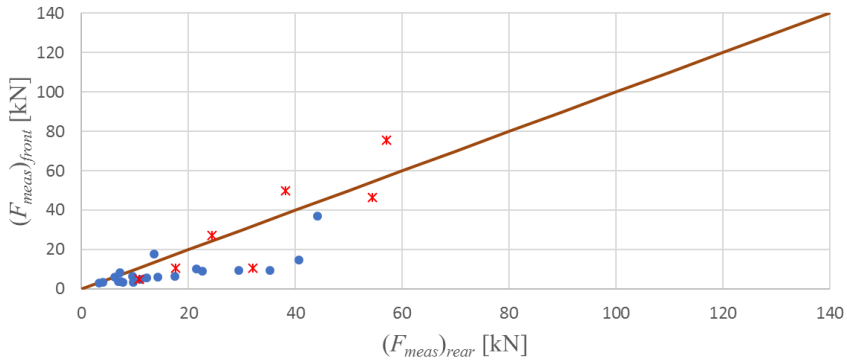

Figure 125 Front wall and rear wall force maxima comparison, for both non-impulsive loads (solid blue circles) and impulsive (impact loads) (red stars).

5.3 Mapping the wave conditions at risk of sloshing

In addition to the inefficiency caused by sloshing (in-chamber water column movement), it may also lead to a severe impact pressure on the in-chamber walls. Furthermore, the large-scale measurements show that some amount of sloshing is not an uncommon situation of an OWC breakwater during operation. It should thus be considered as part of the design and performance assessment. In order to understand the conditions under which sloshing is most likely to occur, the in-chamber video record was studied for both the regular and irregular wave conditions.

5.3.1 Conditions at risk – large-scale tests

For each test, the sloshing regime was identified and recorded alongside the wave height or significant wave height (H or H_{m0}), chamber width characteristics (B_c/L), and

the opening:chamber ratio (A_o/A_c). A colour code is utilised to indicate the sloshing intensity observed. If the water surface looks calm while oscillating, then it can be recorded as “no sloshing” (Figure 113) and it is represented in green. Blue represents “low sloshing”, the condition where the water surface is not calm, but the oscillation is still obvious within the video (Figure 114). Yellow indicates “medium sloshing” with a very visible water height difference between the front and the rear end of the chamber while the oscillating motion is still visible (Figure 115). Finally, red indicates “violent sloshing” where the water movement inside the chamber is very violent with almost no obvious water oscillation observed within the video (Figure 116). In addition to the colour code, several symbols are used for additional information: no test available (/), water level touch the ceiling (^), and major ceiling impact observed (!).

The results for the sloshing regime for the regular wave conditions can be seen in Table 9. One characteristic that can be seen right away is that the sloshing is more likely to occur with the bigger orifice openings. The chamber pressure generated by the smaller orifice (the closed case condition included) inhibits the water column from sloshing, although some low sloshing phenomena still can be observed in some of the cases. It is also clear from the result that when low sloshing occurs in the closed/near-closed chamber conditions, it is likely to be a higher sloshing in the bigger orifice condition. In general, the sloshing is more likely to occur in higher wave height conditions.

In order to see the effect of the of the front wall penetration, the curtain used as the front wall of the physical model structure was lowered for the 0.88% orifice:chamber area ratio case. The results show that it has some effect for the B_c/L = 0.1394 cases. It changes the sloshing condition from low sloshing (blue) to no sloshing (green) for the H = 0.26 m and H = 0.52M cases. The lower curtain wall also causes change from medium sloshing (yellow) to low sloshing (blue) for the H = 0.78m case. This influence, however, does not seem to appear in the smaller B_c/L cases. For example for the B_c/L = 0.1045 and 0.8m, both the original and lowered curtain wall cases regain the same level of sloshing intensity, even though the impact pressure observed in the H = 0.8 m original curtain height did not appear in the lowered curtain case. Interestingly, the converse is observed for the B_c/L = 0.0697 and H = 0.67m case where the sloshing intensities from the medium sloshing (yellow) to the high sloshing (red)

state. Nevertheless, lowering the front wall usually has a calming impact to the sloshing characteristics.

B_c/L	H [m]	Orifice Diameter (A_o/A_c)					
		Closed	0.1%	0.2%	0.88%	0.88% (lowered)	2.00%
0.1394	0.1	/		/		/	
	0.15	/	/	/	/	/	
	0.2	/		/	/	/	
	0.26						
	0.39	/		/	/	/	/
	0.52						
	0.65	/		/		/	/
	0.78						!
0.1045	0.1	/		/	/	/	
	0.15	/	/	/	/	/	
	0.2	/		/		/	
	0.4						
	0.6	/		/		/	/
	0.8				!		!
	1	/	/	/	!	/	/
	1.2	/	/	/	/	/	!
0.0836	0.54				!		!
	0.81	/			!	/	/
	1.07	/	/	/	!	!	!
	1.61	/	/	/	/	/	!
0.0697	0.1	/		/	/	/	
	0.15	/	/	/	/	/	
	0.2	/		/	/	/	
	0.34						
	0.67						^
	1	/	/	/	!	/	/
	1.33	/	/	/	/	/	!

Table 9 Sloshing regime for regular wave conditions (/) indicates a case not tested, (^) indicates a situation where the water column touches the ceiling, and (!) indicates a ceiling impact.

Table 10 shows the observations irregular wave conditions. The wave height listed in the figure is the nominal significant wave height (H_{m0}) and the wave length in the relative chamber width is calculated using fictitious significant wave period and denoted by L_p. The maximum individual wave height according to the Rayleigh distribution could be up to 1.8 times the significant wave height for these 1000-wave sequences. This condition seems to exacerbate the water column condition inside the caisson – in all cases, a higher sloshing intensity is observed compared to the corresponding regular waves case. The trend, however, remains the same with the sloshing more likely to occur for higher wave heights and bigger orifice openings. Lowering the front wall penetration, however, seems to bring a calming effect across different B_c/L_p. This can be seen in the 0.88% opening ratio results, the original front

wall position and the lowered curtain wall results. It is worth noting that lowering the front wall is expected to lead to higher energy losses due to increased vortex formation on the inflow and associated with viscous lost.

B_c/L_p	H_{m0} [m]	Orifice Diameter (A_o/A_c)					
		Closed	0.1%	0.2%	0.88%	0.88% (lowered)	2.00%
0.1394	0.26						
	0.39	/	/	/		/	/
	0.52		/	/			/
0.1045	0.4	/				/	!
	0.6		/	/			/
	0.8	/	/	/	!	/	/
0.0929	0.26		/	/		/	/
0.0836	0.54				!		!
	0.81	/	/	/	!	/	/
0.0697	0.67		/	/	/		!
	1	/	/	/	!	/	/
0.0643	0.4	/	/	/		/	/

Table 10 Sloshing regime for irregular wave condition, (/) indicates a case not tested, (^) indicates the situation where the water column touches the ceiling, and (!) indicates a ceiling impact.

5.3.1 Conditions at risk – small-scale tests

There are several detail differences between the large-scale and the small-scale models. In the large-scale model, the front wall is separated with the main OWC chamber and assembled later before the experiment started, as shown in Figure 126 (a) without and (b) with the front wall installed. This mechanism allows the front wall to be lowered for the additional experiments as presented in the previous sub-chapter. The front wall also protruded above the caisson ceiling protecting the orifice opening from an over topping. Secondly, the chimney above the large-scale chamber in which the orifice was located is not reproduce in the small-scale. Instead, the orifice was simple in the chamber ceiling itself.

(a) (b)

Figure 126 Images of the large-scale physical model without (a) and with (b) the front wall installed.

The small-scale model was a single structure for the entire front wall and side front wall as shown in Figure 127. This allowed wave overtopping to occur during the experiments, but a lowered curtain walls were not practical. The main concern is the overtopping water poured back into the chamber. Due to these, additional symbols are added to the tables to describe wave overtopping occurrence (*) and the situation where a significant volume of overtopped water poured back into the chamber and increase the chamber water height (Π). Furthermore, the (/) symbol now indicates a test with no video available, while (-) is used for conditions that are not tested. The same colour code is used for the sloshing intensity, with green (no sloshing), blue (low sloshing), yellow (medium sloshing), and red (high sloshing).

Figure 127 The front wall of the small-scale physical model. The opening to the chamber is visible underneath the curtain wall, in which three pressure transducers are mounted.

For the small-scale experiments, the camera is located on the side of the wave flume since the material of the wave flume side wall (glass) and the structure (perspex) allow the water column inside the chamber to be seen from the outside. Figure 128 shows the sloshing condition associated with colour code green (a), blue (b), yellow (c), and red (d) - (e). The solid red lines approximate the water column water surface inside the chamber at each instant.

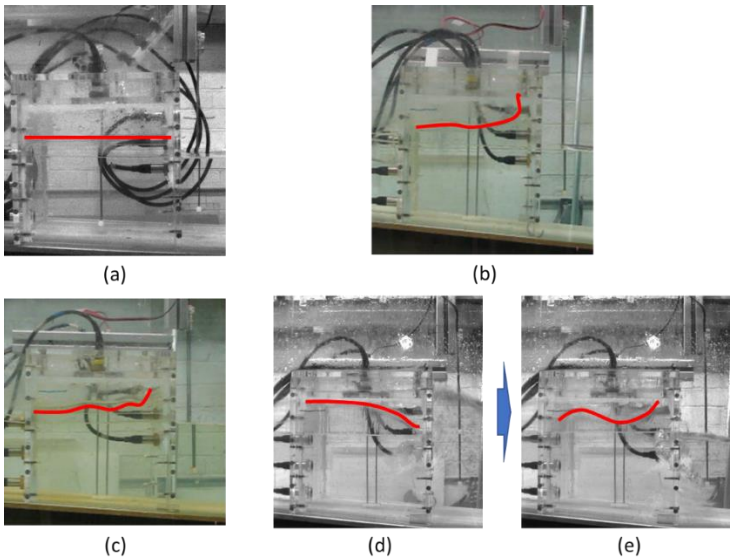

Figure 128 Sloshing conditions for the small-scale model with associated colour code green (a), blue (b), yellow (c), and red (d) - (e). Each colour code indicates the same behaviour as the large-scale physical model (section 5.2).

B_c/L	H [m]	Orifice opening (A_c/A_c)							
		closed	0.11%	0.25%	0.44%	0.99%	2.22%	3.95%	6.18%
0.165	0.02	/	/	/	/				
	0.03								
	0.04								
	0.06								
	0.07								
	0.09								
0.099	0.02	/	/	/	/				
	0.05								
	0.07								
	0.09								
	0.11	*	* Π	* ^	*			-	
0.070	0.08								^
	0.09								
	0.12	*	*Π	*Π	*Π				
0.055	0.02	/	/	/	/				
	0.04								
	0.08							^	^
	0.11	*	*Π	*Π	*Π				^

Table 11 Sloshing regimes for regular wave condition in small-scale physical model. (-) indicates the video not available, (^) indicates the situation where the water column touches the ceiling, (Π) indicates the overtopped water pouring back into the chamber and (!) indicates a ceiling impact.

Table 11 shows the sloshing regime characteristics for the small-scale physical model regular wave conditions. The regime is indicated alongside the same properties as per the large-scale results, relative chamber width, wave height (m), and orifice: chamber area opening ratio. The small-scale tests explored a wider range of orifice opening (as mentioned in chapter 3). This allowed the gradual onset and growth of the sloshing to be observed, such as the B_c/L = 0.07 and H = 0.09 m and 0.12 cases. The water surface was initially calm and well behaved (green) even though wave overtopping was observed in the closed chamber case for H = 0.12m. The sloshing, however, developed in the bigger orifice opening to high sloshing (red) in the ratio of 3.95%. The trend of sloshing occurrence in the higher wave height and wider orifice diameter remains the same between the large-scale and the small-scale.

B_c/L_p	H_{m0} [m]	Orifice opening (A_o/A_c)							
		closed	0.11%	0.25%	0.44%	0.99%	2.22%	3.95%	6.18%
0.1650	0.030						/	/	/
	0.045	/					/	/	/
	0.059	*	*	*	*				
0.0991	0.046	*	*		*		/	/	/
	0.069	v	v*	*	*	*	^ *	^	^
0.0702	0.062	*	*	*		*	^*	^	^
0.0547	0.077	v	v*	v*	*Π	^*	^*	^*	^*
0.0823	0.030	/				/	/	/	/

Table 12 Sloshing regimes for regular wave conditions in small-scale tests. (-) indicates video not available, (^) indicates the water column touches the ceiling, (Π) indicates overtopped water pouring back into the chamber and (!) indicates a ceiling impact.

Table 12 shows the sloshing regime characteristics for the irregular wave conditions. The wave height listed in the figure is the nominal significant wave height (H_{m0}) and the wave length in the relative chamber width is calculated using fictitious significant wave period and denoted by L_p. Just like the large-scale test results, the in-chamber water column behaviour is generally more prone to sloshing for the irregular wave conditions. The figure uses the same colour code as the previous figure. An additional symbol used here is "v" to indicate "venting" event. Venting occurs when the incident water level falls below the front wall and the air flow into the chamber through the front wall opening instead of the power take off (simulated by the orifice in the experiment). Figure 129 captures the "venting" which occurs on B_c/L_p = 0.0991, Hm0 = 0.069 m, for the closed orifice. It can be seen that the air passes under the front wall and adds to the air volume inside the chamber as demonstrated by the red arrow. Figure 130 shows the chamber pressure time history (corresponding to the venting phenomenon in Figure 129), of the closed orifice, B_c/L_p = 0.0991, and H_{m0} = 0.069m. The zero value in the graph represents the atmospheric pressure. As can be seen, after venting, the average pressure increases above the atmospheric pressure and generate less negative pressure. One can imagine that such a phenomenon could negate the negative pressure generated during operation.

It is possible that this phenomenon also occurs during the large-scale experiment shown in Figure 131. The solid red line approximate elevation of the lower 'lip' of the front wall. The measurement lines on the chamber wall indicate the distance between

the line and the chamber ceiling. The front wall “lips” is located at 1.3 m from the ceiling.

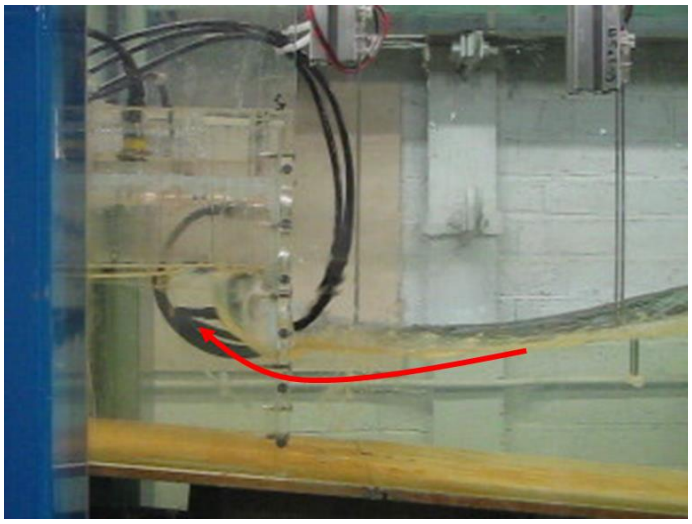

Figure 129 Venting event which occurred during a small-scale physical model experiment. The red arrow indicates where the water level has fallen below the front wall and a volume of air has entered the chamber.

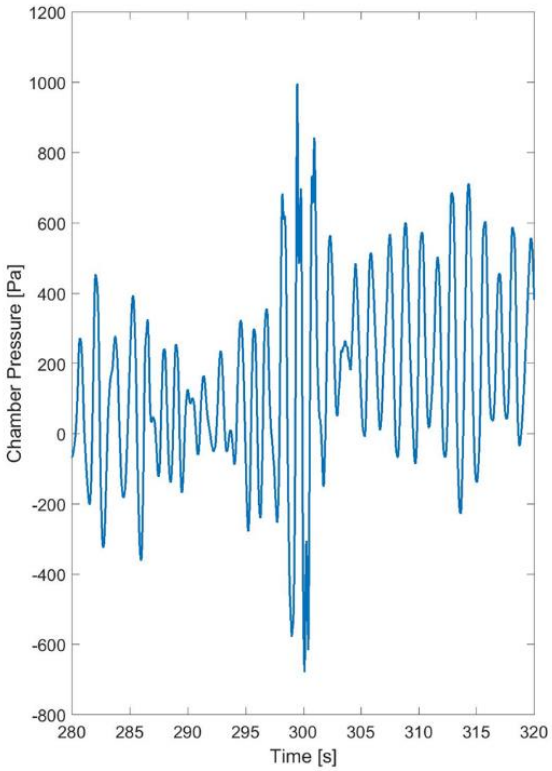

Figure 130 Chamber pressure time series during the venting event. The signature of the venting is increase in average pressure between t = 295s and t = 300s.

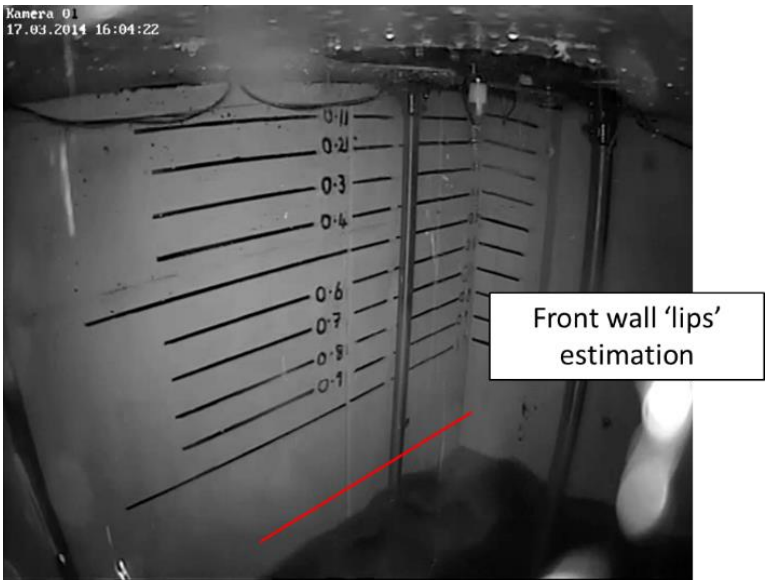

Figure 131 Video image of a suspected venting event during the large-scale physical model testing. The red line indicates the approximate elevation of the front wall opening.

6 Small-scale results and comparison

This chapter explores the small-scale measurements, and then compares them with the wave loading prediction model developed for the in-chamber wave loads. A comparison is then presented between the small-scale results for the in-chamber rear wall and generated chamber pressure and the large scale (GWK) results of the same location to investigate the scaling effects.

6.1 Small-scale physical model performance analysis

To establish the maximum energy which can be captured by the small-scale model, the peak power generated is determined for each test. The various orifice openings and wave conditions of the small-scale model are then compared (Figure 132) for regular wave condition because power generated varied for each wave within an irregular wave train. The power generated is calculated by multiplying the volumetric flowrate of the air flowing in and out of the chamber in a single wave cycle by the chamber pressure maxima of the corresponding wave cycle.

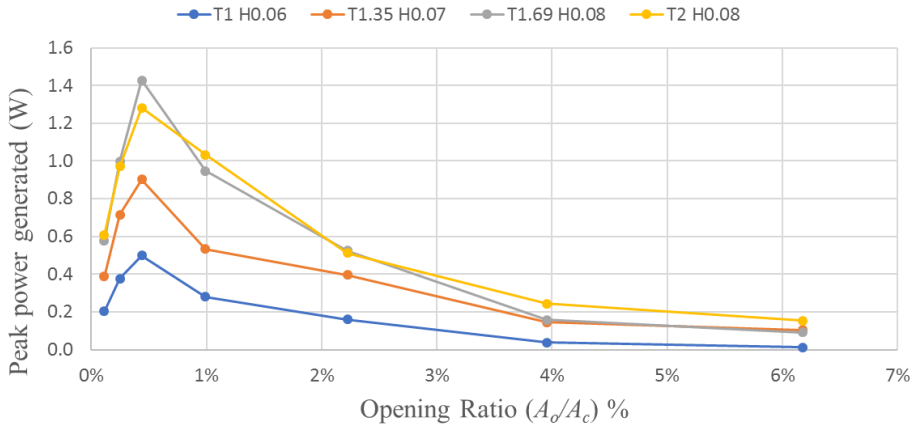

Figure 132 Power generating performance: comparison between various opening:chamber ratio for multiple wave settings.

The figure shows that the OWC works most efficiently in the 0.44% orifice to chamber area ratio – a finding that is consistent across all tested regular wave conditions.

6.2 Small-scale model: comparison of wave loads with new prediction method

6.2.1 Closed chamber case

For the small-scale closed chamber results, the measured chamber pressure is compared with the prediction model (Subchapter 4.1.1 and Equation 13) and the results is shown in Figure 133. The Y-axis of the figure shows the measured/predicted pressure ratio. The X-axis show the maximum measured chamber pressure. As can be seen from the figure, the prediction model under-estimates the small-scale chamber pressure maxima for the one less than 200 Pa by a factor of 2.0. On the other hand, the prediction model over-predicts for the higher in-chamber pressure maxima (> 200Pa), by a factor of 0.7. These discrepancies might occur due to the air stiffness of the small-scale structure. In a smaller chamber dimension, the air stiffness is higher compared to that of a bigger air volume in a prototype's caisson chamber. Under lower wave steepnesses, this characteristic may be under-estimate by the prediction mode which explain the results shown in the figure. Nevertheless, the pressure magnitude is relatively small compared to the steeper wave steepnesses.

Figure 134 shows the landward force acting on the rear wall of the chamber, comparing small-scale measurements with the prediction model. The figure shows the similar trend as Figure 133, with the larger magnitude forces being over-predicted by a factor of 0.7.

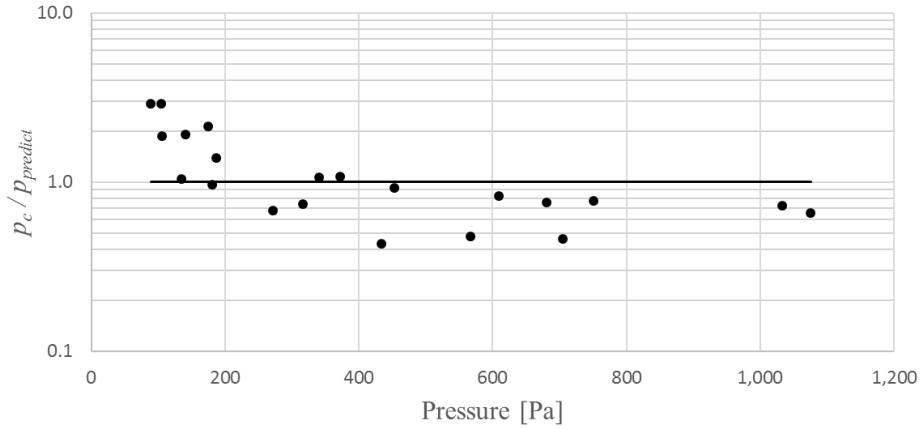

Figure 133 Measurement:prediction ratio of the closed chamber cases against pressure magnitude for the regular wave conditions, small-scale measurements. Solid line represents the model prediction.

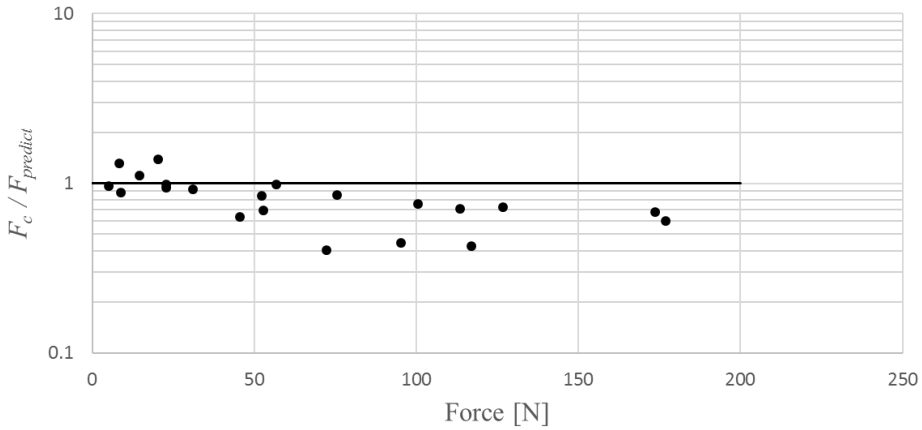

Figure 134 Measurement:prediction ratio of landward near wall force of the closed case cases against force magnitude for the regular wave conditions. Solid line presents the model prediction.

It is interesting to explore the influence of the wave steepness on the measured:predicted comparison, so Figure 133 and Figure 134 are reworked using wave steepness as the X-axis to give Figure 135 (chamber pressure, p_c) and Figure 136 (rear wall landward forces, $F_{meas,rear}$). A slight declining trend is observed from the figures showing which is possibly because higher wave steepness may have bigger energy loss then the less steep waves when passing through the front wall opening. The transition from under-estimation to the over-estimation by the prediction model

for both force and pressure comparisons here falls around the same region of 1% to 2% wave steepness.

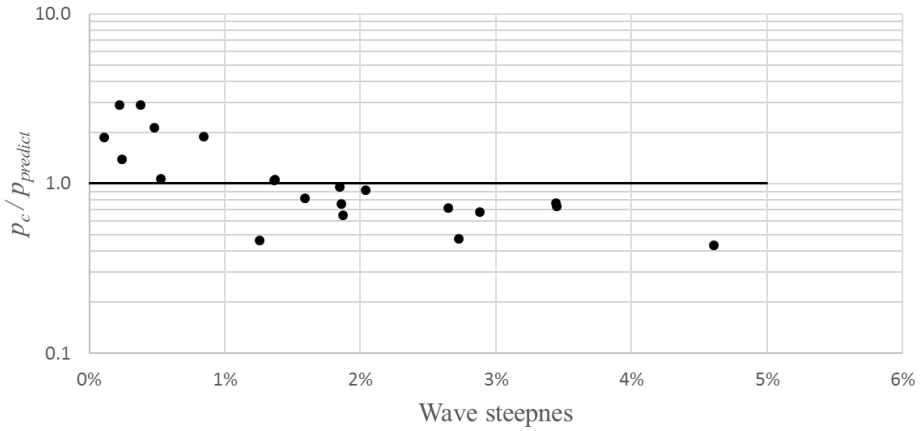

Figure 135 Measurement:prediction ratio of the closed chamber cases against wave steepness for the regular wave conditions, small-scale measurements. Solid line represents the model prediction.

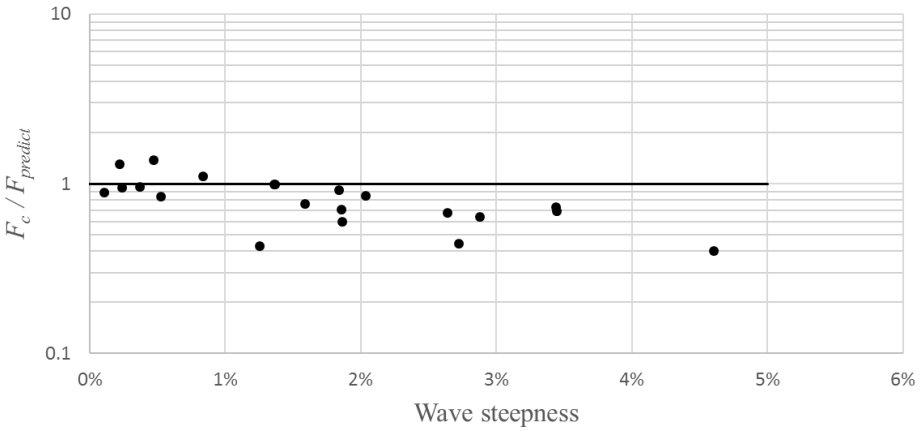

Figure 136 Measurement:model ratio of landward near wall force of the closed case cases against wave steepness for the regular wave conditions. Solid line presents the model prediction.

For the irregular sea conditions, the measurements used the JONSWAP spectra with significant wave heights and wave periods described in detail in the Chapter 3. The model for irregular waves assumed a wave height of 1.8 times the significant wave height as the basis of its calculation. The maximum chamber pressure comparison for the irregular sea conditions is presented in Figure 137, and the landward rear wall force comparisons presented in Figure 138. Here, the x-axis shows the wave steepness

calculated based on the significant wave height and period, and y-axis shows the chamber pressure measured:predicted ratio and rear wall force measured:predicted ratio. It is observed that unlike the regular test result, all of the test data in the irregular test for both chamber pressure maxima and rear wall force maxima are located on the safe side of the prediction and closer to the estimation by a factor of 0.85 and 0.73 respectively. The results trend, furthermore, seems to be flat, not declining as was seen for the regular wave results. This could be because in the irregular sea conditions, the wave steepness is not constant on a wave-to-wave basis, so the dissipating effect of the front wall varied for each wave cycle in the same test set. This also shows that the small-scale physical measurements have better agreement with the prediction for the irregular wave conditions than for the regular wave conditions.

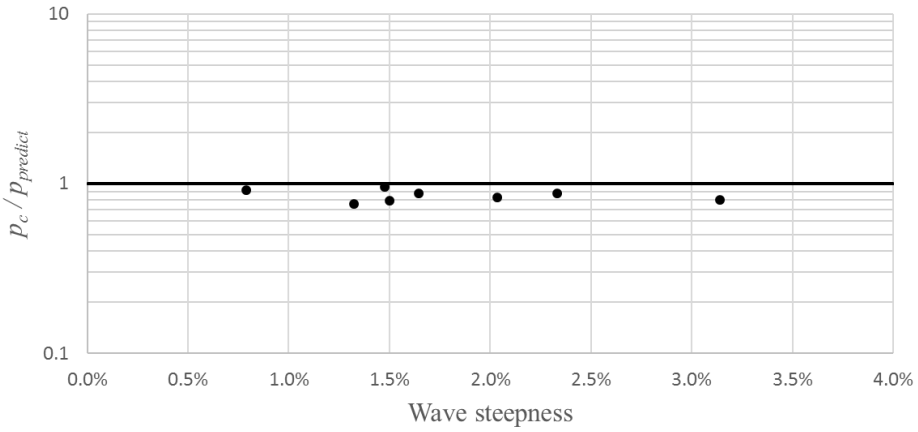

Figure 137 Pressure maxima measurement:prediction ratio of the closed chamber cases against wave steepness for the irregular wave conditions. Solid line represents the model prediction

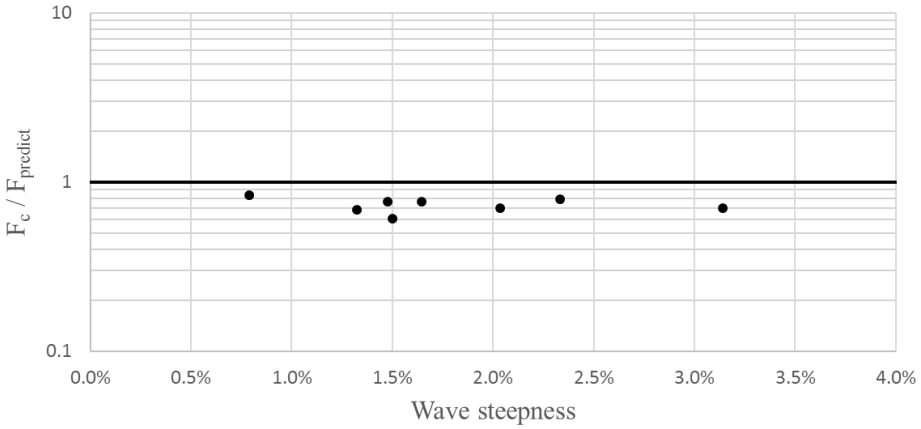

Figure 138 Measurement:prediction ratio of landward rear wall force of the closed case cases against wave steepness for the irregular wave conditions. Solid line presents the model prediction

6.2.2 Fully open chamber case

The second extreme case which explored in these experiments is the fully open condition. In order to distinguish between the cases that can be included in the fully open and the cases that are still in the operating condition (Section 6.2.3), the chamber pressure increase rate is plotted in Figure 139 for the regular wave conditions. The solid red line (200 Pa/s) indicates the cut-off between the operating condition and the fully open condition. This cut-off pressure increase rate is determined based on the linear scaled-down of the large-scale cut-off measurement of 2 kPa/s. Note that all of the tests at 3.93% and 6.18% orifice:chamber ratio falls in the fully open condition. All of the cases located above the solid red line are hence forth excluded in this sub-chapter analysis. In the fully open case, the chamber pressures in all cases are assumed to be very close to atmospheric pressure and assumed not to change with the water column oscillation inside the chamber. This assumption is supported by the chamber pressure increase rate remaining almost the same regardless of the wave steepness in the figure.

Since a chamber pressure comparison is not meaningful, only the landward force acting on the chamber rear wall is compared, and the result plotted against the wave steepness is presented in Figure 140. The measurements have a very good agreement with the model prediction (Subchapter 4.1.2 and Equation 16) for most of the cases,

however the declining trend is more obvious here compared to the closed chamber case. This may be because the energy dissipation due to front wall penetration is bigger in the fully open case because the in-chamber water column movement is not restricted by the chamber pressure which increases the water movement in and out of the chamber. Since the measurements exceeds some of the model predictions, is it important to check whether the under-prediction (unsafe) cases are associated with significant force magnitudes. Figure 141 shows that they are actually located in the smaller force magnitude zone, whereas the biggest magnitudes are all located in the safe-zone, close to the prediction line. Thus, the rear wall force comparisons show that the small-scale physical measurement agrees well with the rear wall force prediction with an average factor of 0.88 for the regular wave conditions. Furthermore, many of the data points with the same wave conditions for 2.22%, 3.95% and the 6.18% over-lapped each other, showing that the orifice opening has little effect on the results and supporting the fully open assumption for these cases.

Next, rear wall pressures at various elevation are explored. Figure 142 and Figure 143 show the pressures acting on the rear wall at different elevations for 3.95% and 6.18% opening ratios respectively. Measured:predicted comparison shows that the under-estimation of the pressure acting on a few specific elevations of the chamber rear wall is about a factor of 0.75. The detailed comparison between the pressure distribution prediction and the measured pressure acting on the rear wall at various elevation of the structure can be seen in Figure 144 (a)-(r) for the 3.95% cases and Figure 145 (a)-(r) for the 6.18% cases.

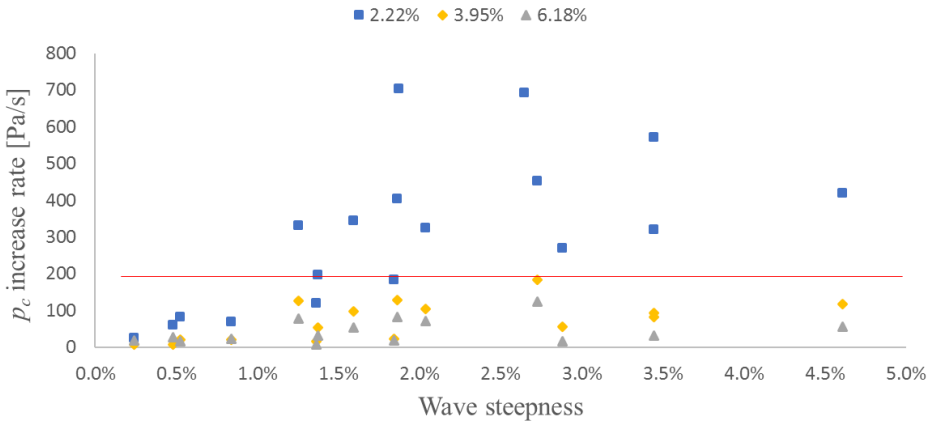

Figure 139 Chamber pressure increase rate for the opening:chamber ratio of 2.22% (blue solid square), 3.95% (yellow solid diamond), and 6.18% (grey solid triangle) for regular wave conditions, small-scale measurements. The solid line represents the cut-off line between the operating condition (above) and fully open condition (below).

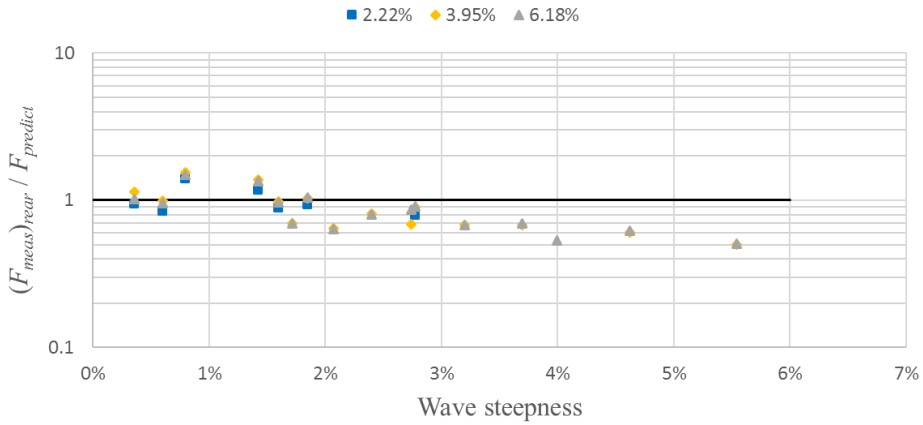

Figure 140 Measurement:prediction ratio of landward rear wall force for the fully open cases vs wave steepness, for the regular wave conditions, small-scale measurements. Solid line presents the model prediction

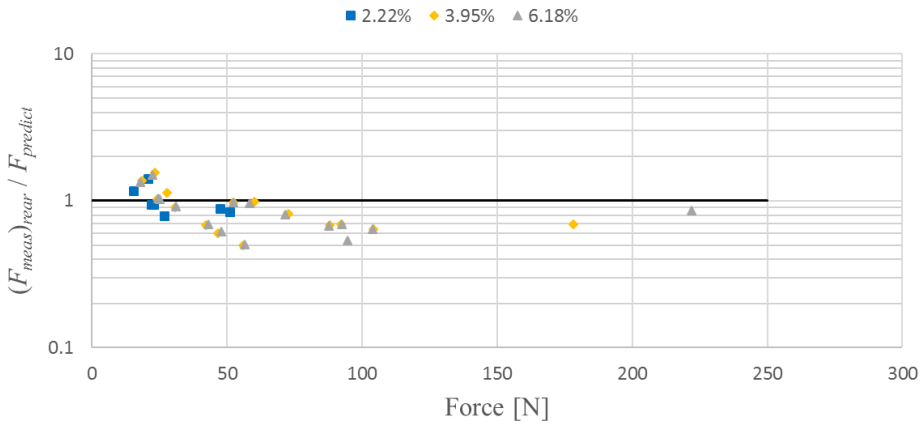

Figure 141 Measurement:prediction ratio of landward rear wall force of the fully open case vs force magnitude, for the regular wave conditions, small-scale measurements. Solid line presents the model prediction

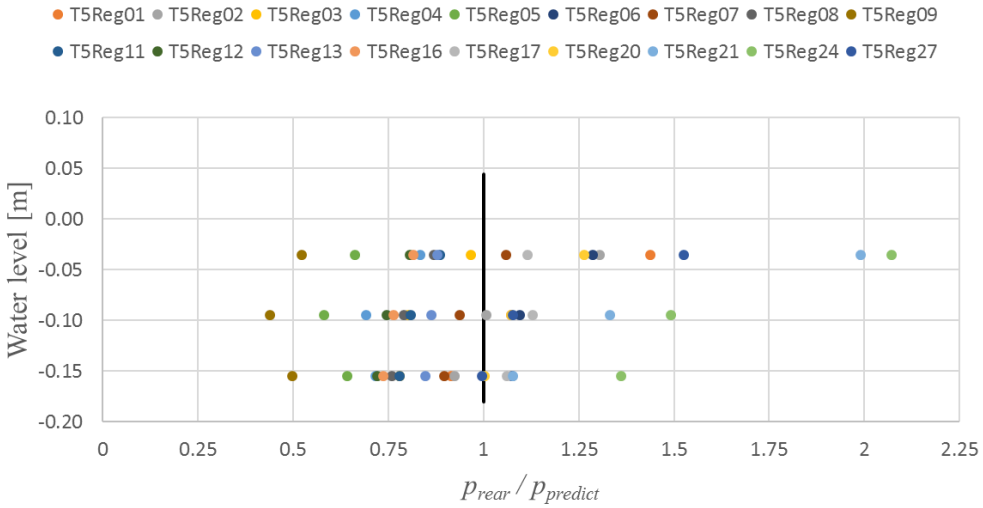

Figure 142 Ratio of measurement:prediction for rear wall landward pressures at various vertical elevations for the 3.95% opening:chamber ratio, small-scale measurements, regular wave conditions, open chamber. The solid line represents the model prediction.

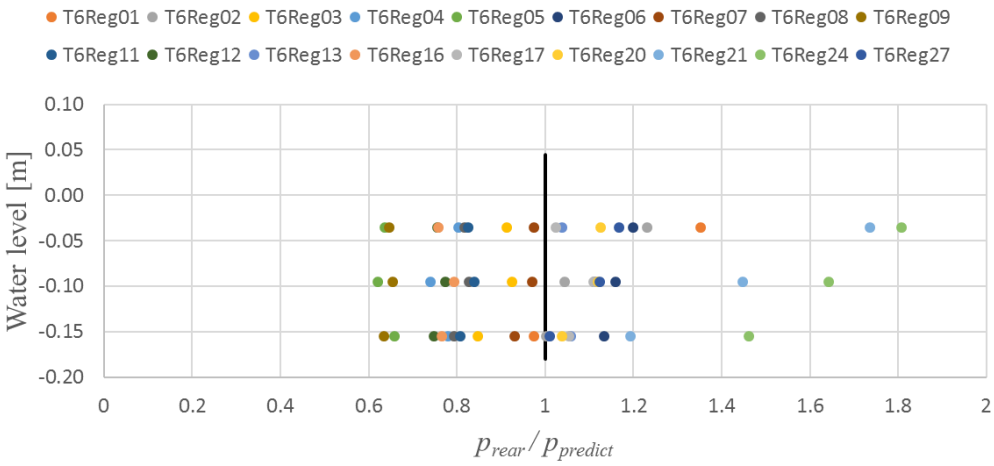

Figure 143 Ratio of measurement:prediction rear wall landward pressure at various vertical elevations for the 6.18% opening:chamber ratio, small-scale measurements, regular wave conditions, open chamber. The solid line represents the model prediction.

For the irregular wave conditions the wave steepness is determined based on the significant wave height and period. In reality, however, the wave steepness varies for each wave in an irregular sea. Due to this characteristic, the pressure increase rate also changed depending on each wave cycle. For simplification the fully open condition is determined using the $p_{1/250}$ pressure increase rate, which is the average of 4 biggest chamber pressures of each test set. The results of the calculation are presented in Figure 146. The y-axis of the graph shows the $p_{1/250}$ increase rate and the x-axis shows the wave steepness. The cut off rate of 200 Pa/s is applied and, just as for the regular wave tests, all of the 3.95% and 6.18% opening ratio cases are fall into the fully open regime. For the 2.22% ratio, on the other hand, only one test is included. Based on the pressure rate cut-off, the maximum landward force acting the rear wall comparisons between the small-scale measurements and the prediction model for the fully open chamber are shown in Figure 147. Just like the closed chamber case, all of the maximum force measured in this condition also located on the safe-side of the prediction by a factor of 0.62. The trend of the data is similar to that for the regular wave conditions, with the declining trend observed for the higher wave steepness, possibly due to higher energy losses. It can also be seen that the maximum forces for different orifice opening:chamber ratios have about the same force maxima ratio,

supporting the assumption that the diameter of the orifice opening has little effect in the open chamber.

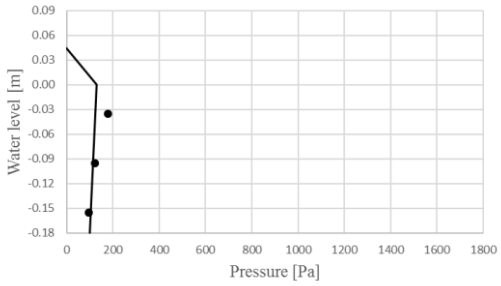

(a)

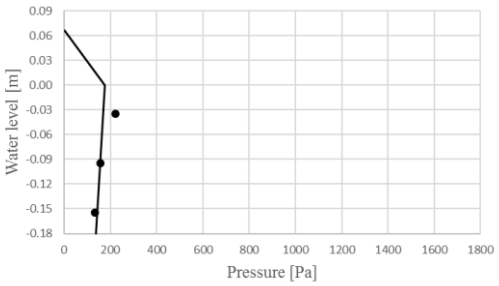

(b)

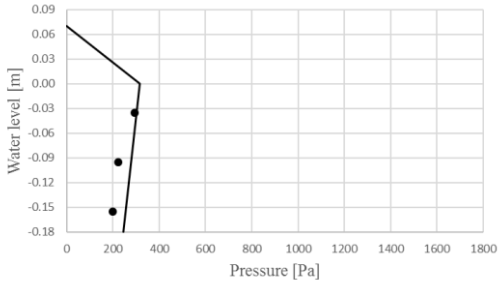

(c)

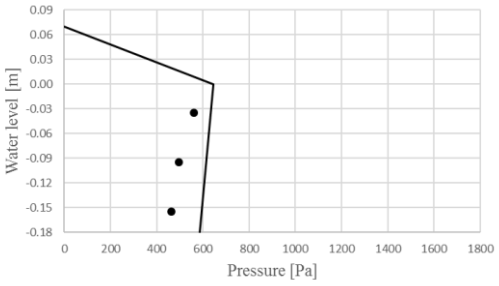

(d)

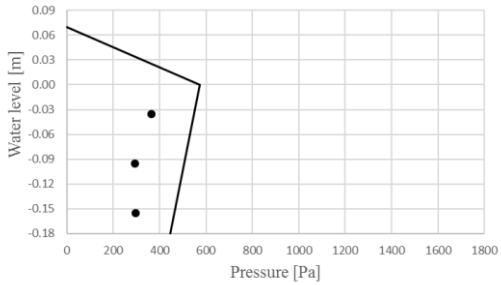

(e)

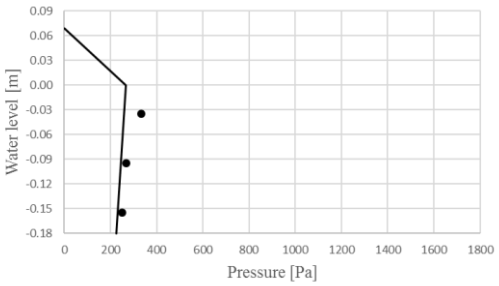

(f)

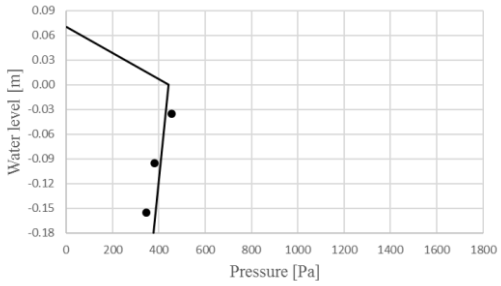

(g)

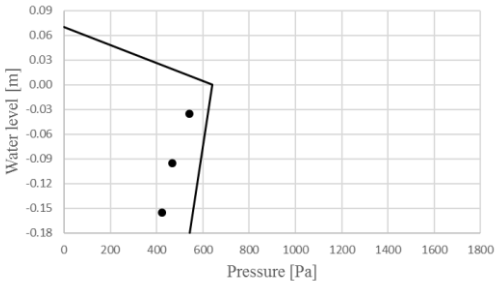

(h)

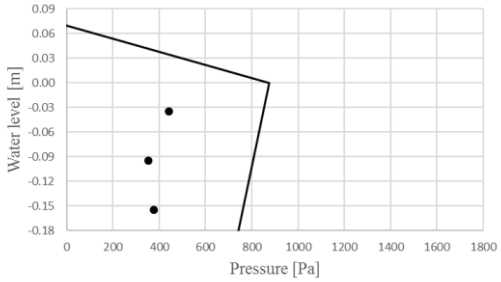
Water level [m]
0.09
0.06
0.03
0.00
-0.03
-0.06
-0.09
-0.12
-0.15
-0.18
0 200 400 600 800 1000 1200 1400 1600 1800
Pressure [Pa]

(i)

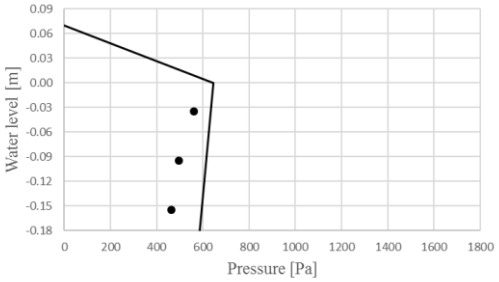
Water level [m]
0.09
0.06
0.03
0.00
-0.03
-0.06
-0.09
-0.12
-0.15
-0.18
0 200 400 600 800 1000 1200 1400 1600 1800
Pressure [Pa]

(j)

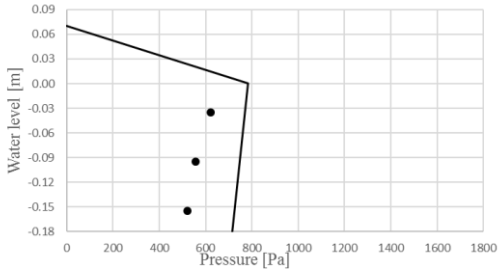
Water level [m]
0.09
0.06
0.03
0.00
-0.03
-0.06
-0.09
-0.12
-0.15
-0.18
0 200 400 600 800 1000 1200 1400 1600 1800
Pressure [Pa]

(k)

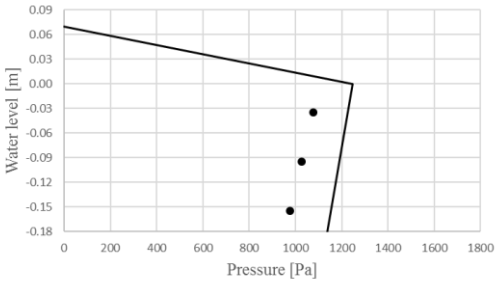
Water level [m]
0.09
0.06
0.03
0.00
-0.03
-0.06
-0.09
-0.12
-0.15
-0.18
0 200 400 600 800 1000 1200 1400 1600 1800
Pressure [Pa]

(l)

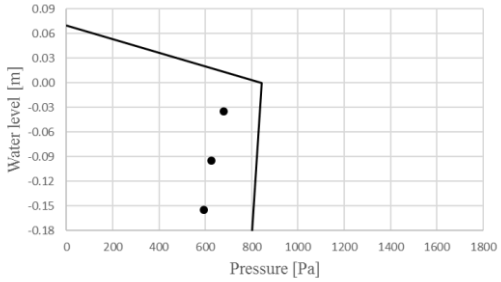
Water level [m]
0.09
0.06
0.03
0.00
-0.03
-0.06
-0.09
-0.12
-0.15
-0.18
0 200 400 600 800 1000 1200 1400 1600 1800
Pressure [Pa]

(m)

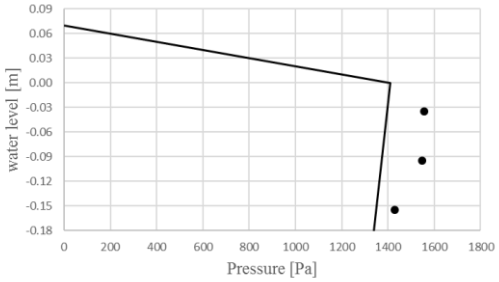
water level [m]
0.09
0.06
0.03
0.00
-0.03
-0.06
-0.09
-0.12
-0.15
-0.18
0 200 400 600 800 1000 1200 1400 1600 1800
Pressure [Pa]

(n)

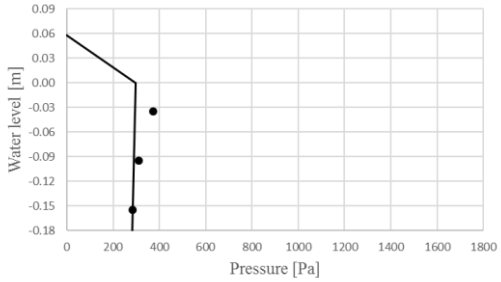
Water level [m]
0.09
0.06
0.03
0.00
-0.03
-0.06
-0.09
-0.12
-0.15
-0.18
0 200 400 600 800 1000 1200 1400 1600 1800
Pressure [Pa]

(o)

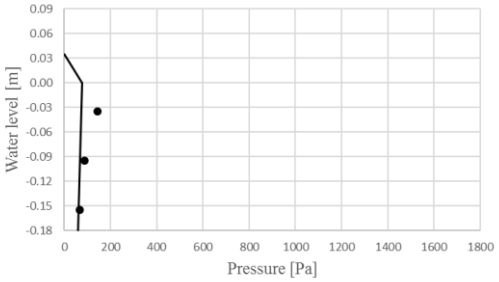
Water level [m]
0.09
0.06
0.03
0.00
-0.03
-0.06
-0.09
-0.12
-0.15
-0.18
0 200 400 600 800 1000 1200 1400 1600 1800
Pressure [Pa]

(p)

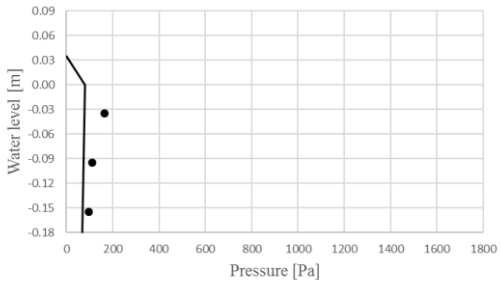

(q)

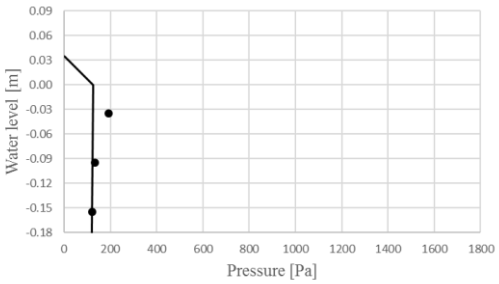

(r)

Figure 144 (a)-(r) Measured (solid circle) and predicted (solid line) pressure distributions for fully open case 3.95% opening:chamber ratio, and regular wave conditions of: (a) Reg01, (b) Reg02, (c) Reg03, (d) Reg04, (e) Reg05, (f) Reg06, (g) Reg07, (h) Reg08, (i) Reg09, (j) Reg11, (k) Reg12, (l) Reg13, (m) Reg16, (n) Reg17, (o) Reg20, (p) Reg21, (q) Reg24, (r) Reg27.

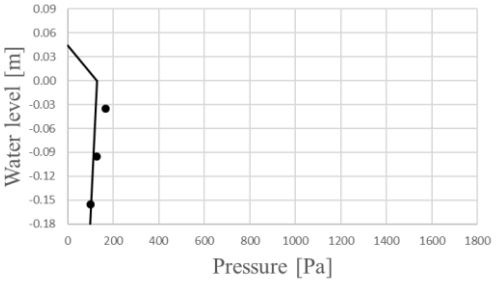
Water level [m]
0.09
0.06
0.03
0.00
-0.03
-0.06
-0.09
-0.12
-0.15
-0.18
0
200
400
600
800
1000
1200
1400
1600
1800
Pressure [Pa]

(a)

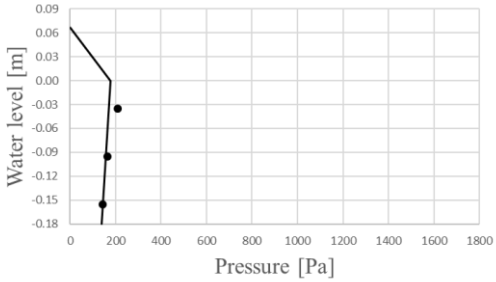
Water level [m]
0.09
0.06
0.03
0.00
-0.03
-0.06
-0.09
-0.12
-0.15
-0.18
0
200
400
600
800
1000
1200
1400
1600
1800
Pressure [Pa]

(b)

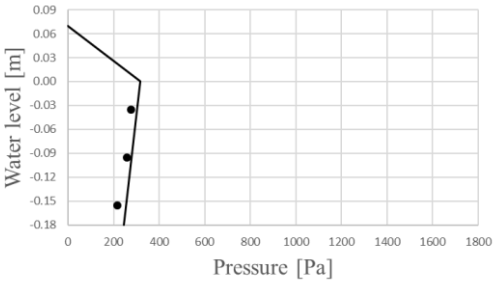
Water level [m]
0.09
0.06
0.03
0.00
-0.03
-0.06
-0.09
-0.12
-0.15
-0.18
0
200
400
600
800
1000
1200
1400
1600
1800
Pressure [Pa]

(c)

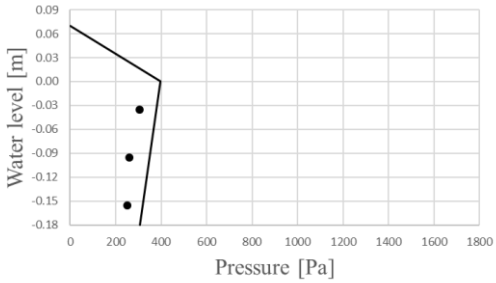
Water level [m]
0.09
0.06
0.03
0.00
-0.03
-0.06
-0.09
-0.12
-0.15
-0.18
0
200
400
600
800
1000
1200
1400
1600
1800
Pressure [Pa]

(d)

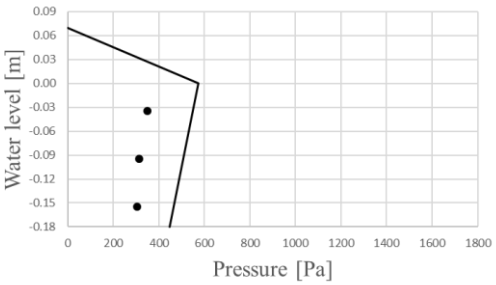
Water level [m]
0.09
0.06
0.03
0.00
-0.03
-0.06
-0.09
-0.12
-0.15
-0.18
0
200
400
600
800
1000
1200
1400
1600
1800
Pressure [Pa]

(e)

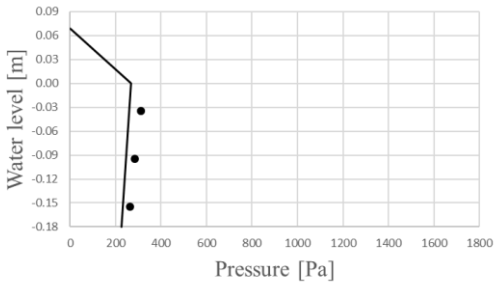
Water level [m]
0.09
0.06
0.03
0.00
-0.03
-0.06
-0.09
-0.12
-0.15
-0.18
0
200
400
600
800
1000
1200
1400
1600
1800
Pressure [Pa]

(f)

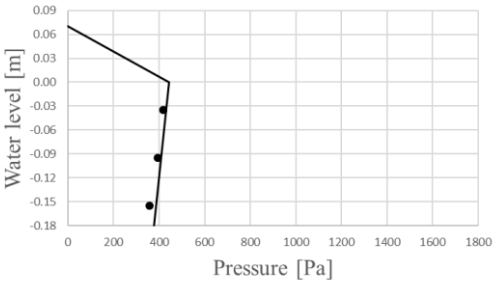
Water level [m]
0.09
0.06
0.03
0.00
-0.03
-0.06
-0.09
-0.12
-0.15
-0.18
0
200
400
600
800
1000
1200
1400
1600
1800
Pressure [Pa]

(g)

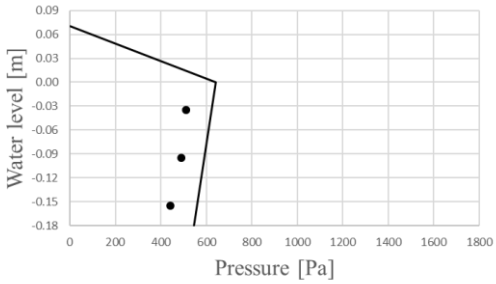
Water level [m]
0.09
0.06
0.03
0.00
-0.03
-0.06
-0.09
-0.12
-0.15
-0.18
0
200
400
600
800
1000
1200
1400
1600
1800
Pressure [Pa]

(h)

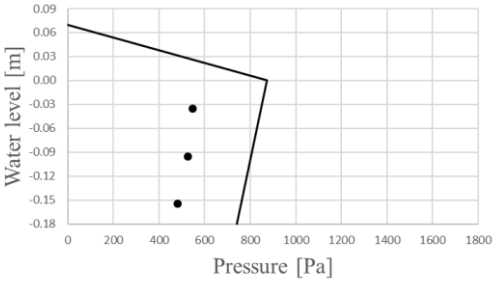
Water level [m]
0.09
0.06
0.03
0.00
-0.03
-0.06
-0.09
-0.12
-0.15
-0.18
0 200 400 600 800 1000 1200 1400 1600 1800
Pressure [Pa]

(i)

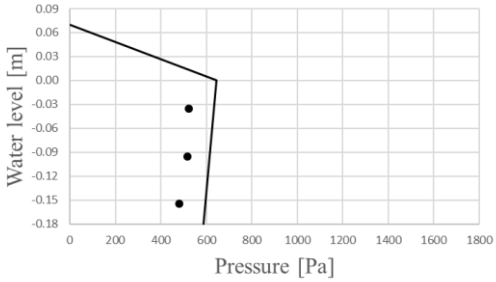
Water level [m]
0.09
0.06
0.03
0.00
-0.03
-0.06
-0.09
-0.12
-0.15
-0.18
0 200 400 600 800 1000 1200 1400 1600 1800
Pressure [Pa]

(j)

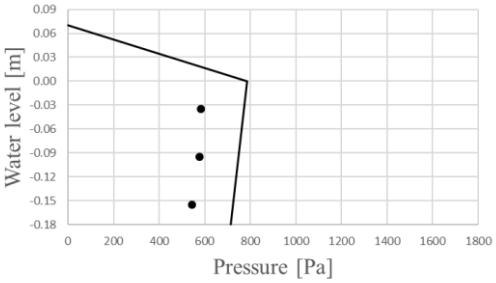
Water level [m]
0.09
0.06
0.03
0.00
-0.03
-0.06
-0.09
-0.12
-0.15
-0.18
0 200 400 600 800 1000 1200 1400 1600 1800
Pressure [Pa]

(k)

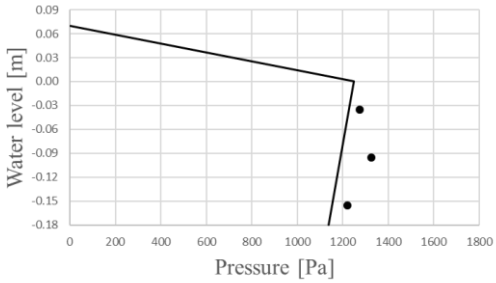
Water level [m]
0.09
0.06
0.03
0.00
-0.03
-0.06
-0.09
-0.12
-0.15
-0.18
0 200 400 600 800 1000 1200 1400 1600 1800
Pressure [Pa]

(l)

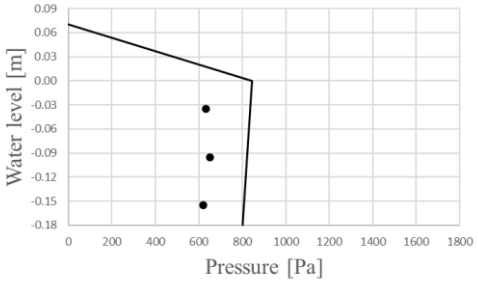
Water level [m]
0.09
0.06
0.03
0.00
-0.03
-0.06
-0.09
-0.12
-0.15
-0.18
0 200 400 600 800 1000 1200 1400 1600 1800
Pressure [Pa]

(m)

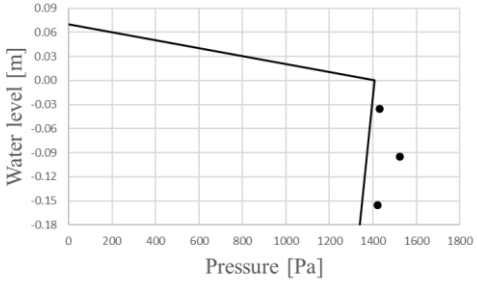
Water level [m]
0.09
0.06
0.03
0.00
-0.03
-0.06
-0.09
-0.12
-0.15
-0.18
0 200 400 600 800 1000 1200 1400 1600 1800
Pressure [Pa]

(n)

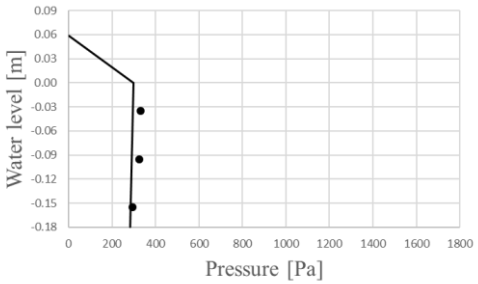
Water level [m]
0.09
0.06
0.03
0.00
-0.03
-0.06
-0.09
-0.12
-0.15
-0.18
0 200 400 600 800 1000 1200 1400 1600 1800
Pressure [Pa]

(o)

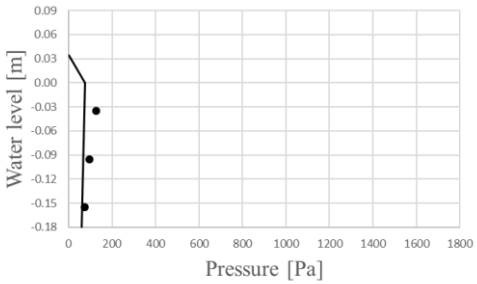
Water level [m]
0.09
0.06
0.03
0.00
-0.03
-0.06
-0.09
-0.12
-0.15
-0.18
0 200 400 600 800 1000 1200 1400 1600 1800
Pressure [Pa]

(p)

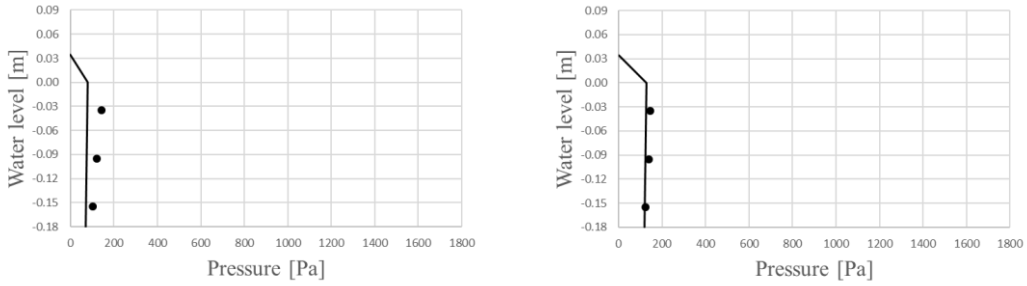

(q) (r)

Figure 145 (a)-(r) Measured (solid circle) and predicted (solid line) pressure distributions for fully open case, 6.18% opening:chamber ratio, and regular wave conditions of: (a) Reg01, (b) Reg02, (c) Reg03, (d) Reg04, (e) Reg05, (f) Reg06, (g) Reg07, (h) Reg08, (i) Reg09, (j) Reg11, (k) Reg12, (l) Reg13, (m) Reg16, (n) Reg17, (o) Reg20, (p) Reg21, (q) Reg24, (r) Reg27.

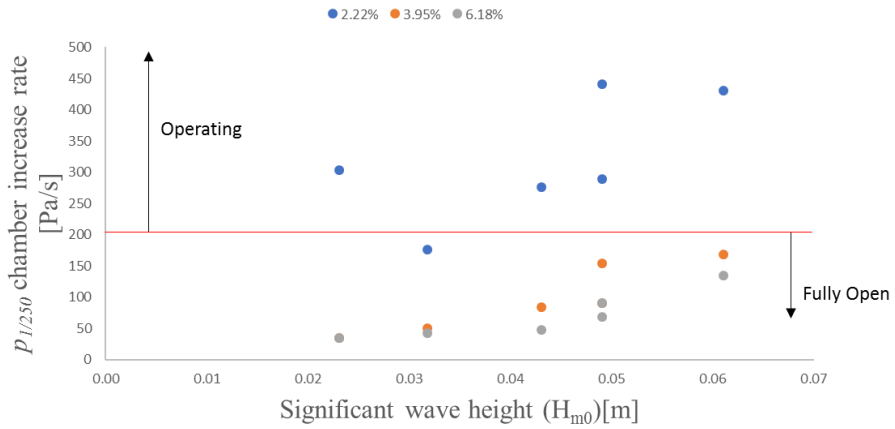

Figure 146 Chamber pressure increase rate for the opening:chamber area ratio of 2.22% (blue solid circle), 3.95% (orange solid circle), and 6.18% (grey solid circle) and irregular wave setting. The solid line represents the cut-off line between the operating condition (above) and fully open condition (below).

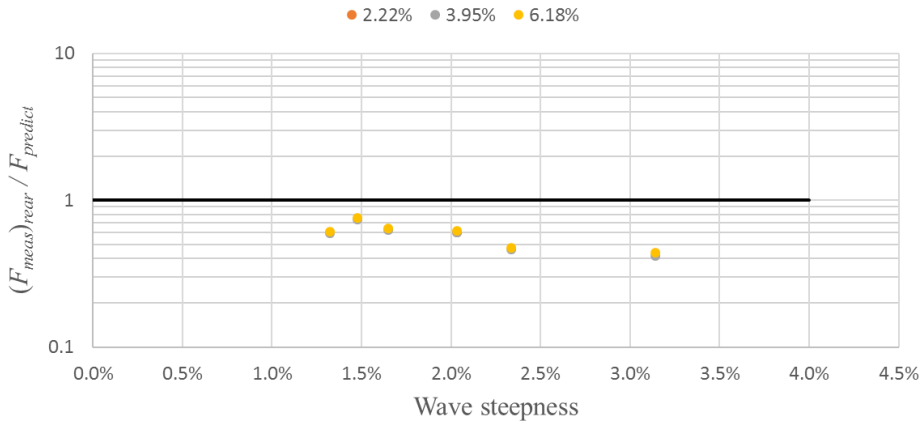

Figure 147 The measurement:prediction ratio of the rear wall landward force for fully open case and irregular wave conditions for various opening:chamber area ratio, small-scale measurements. The solid line represents model prediction.

It is important to note that the air pressure inside the chamber is assumed to be atmospheric or close to atmospheric at all time. The air stiffness characteristic differences between the small-scale and the prototype should be minimal in the fully open condition, as was demonstrated in the regular wave results.

6.2.3 Operating condition case

The operating condition is an intermediate condition between the two extremes. The ratio of measured:predicted chamber pressure maxima are plotted against the wave steepness in Figure 148 for the regular wave condition. As shown in the figure, the prediction model under-estimates the small-scale measurements by a factor between 1.1 and 1.5. The bigger orifiice:chamber area ratio (0.99%) appears to be the closest to the estimation line, with less good agreement to smaller orifice:chamber area ratios, such as: 0.11% (1.44 times), 0.25% (1.51 times), and 0.44% (1.54 times) cases. For the 0.99% (1.1 times) case, however, some of the cases fall below the comparison line, this may happen because in the less steep wave conditions, such an orifice opening may tend more toward the fully open condition than the operating condition.

Note that measurements at the most efficient orifice opening (0.44%) showed in the highest under-estimation by a factor of 1.54. Figure 149 shows the same measurement:prediction comparison of the chamber pressure when plotted against the pressure magnitude. Both Figure 148 and Figure 149 show that the small-scale

physical model results are quite uniformly underestimated by the prediction model (Subchapter 4.1.3 and Equation 17) for higher wave steepness (s_w >1%) and higher chamber pressure generation (p_c >200 Pa).

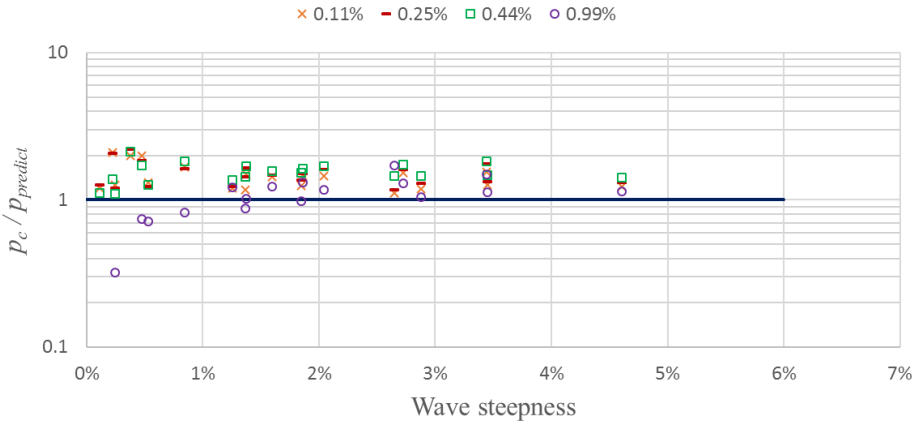

Figure 148 The measurement:prediction ratio of the chamber pressure for the operating condition cases at various opening:chamber ratio for the regular wave conditions vs wave steepness, small-scale measurements. The solid line represents the prediction model.

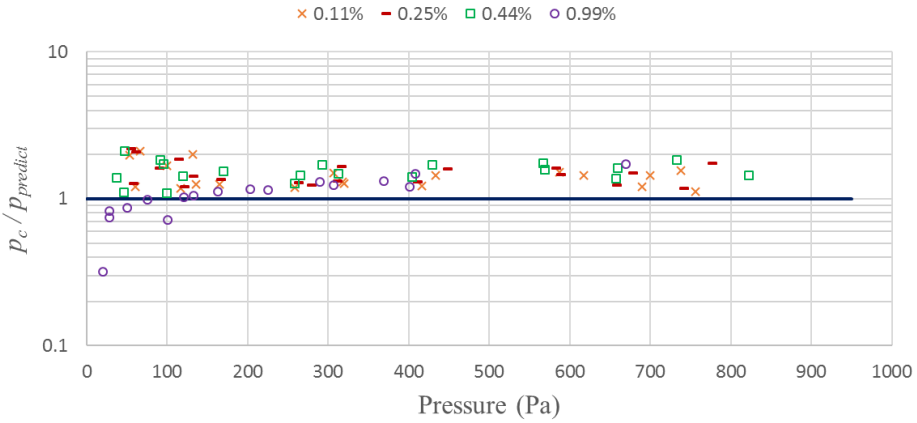

Figure 149 The measurement:prediction ratio of the chamber pressure for the operating chamber cases at various opening:chamber ratio for the regular wave conditions vs pressure magnitude, small-scale measurements. The solid line represents the prediction model.

For the irregular condition, the small-scale measurements and prediction model comparisons show an under-estimation (Figure 150) by a factor of 1.25. The discrepancy between the predicted chamber pressure and the small-scale measurements are consistent across different wave steepnesses, similar to those seen

for the regular wave conditions. In addition to the chamber pressure comparison, Figure 151 and Figure 152 show the rear wall force comparison for the regular and irregular wave conditions respectively. Unlike the large-scale measurements, the pressure transducers in the small-scale measurements are only located below the still water level. Due to this constraint, both the rectangular pressure integration method for measured forces and the prediction model forces are only deployed up to the still water level elevation. It is important to note that the chamber pressure is already retracted from the pressure data for each time step. As can be seen from the regular wave results (Figure 149), the prediction model under-estimates the small-scale measurements, especially for orifice:chamber area ratio of 0.11% and 0.25%, and wave steepness less than 1% by a factor ranging from 1.19 to 2.53. For the higher wave steepness and higher orifice:chamber area ratio, on the other hand, the small-scale seems to have a better agreement with the prediction model. This finding is in line with what is found for the irregular wave condition with the under-estimation factor ranging from 1.14 to 3.24 and with the largest over-estimations occurring at wave steepnesses less than 1% with the highest orifice:chamber area ratio of 0.11%.

The comparison between the predicted pressure distribution and the measured pressure acting on the rear wall of the structure at various elevations can be seen in Figure 153 (a)-(o) for the 0.11% cases, Figure 154 (a)-(o) for the 0.25% cases, Figure 155 (a)-(o) for the 0.44% cases, and Figure 156 (a)-(o) for the 1.0% cases. Unfortunately, there was a sensor failure for both 0.11% cases (Figure 153) and 0.25% cases (Figure 154), so the model is only compared to the measured wave pressure at water elevation of 0.035 m and 0.095 below the still water level (SWL).

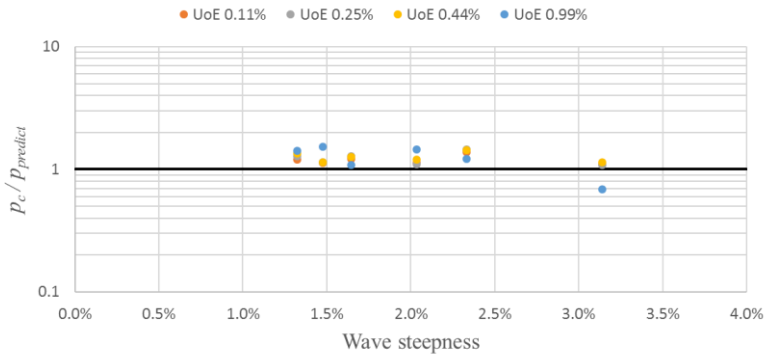

Figure 150 The measurement:prediction ratio of the chamber pressure for operating conditions at various opening:chamber ratio for the irregular wave conditions vs wave steepness, small-scale measurements. The solid line represents the prediction model.

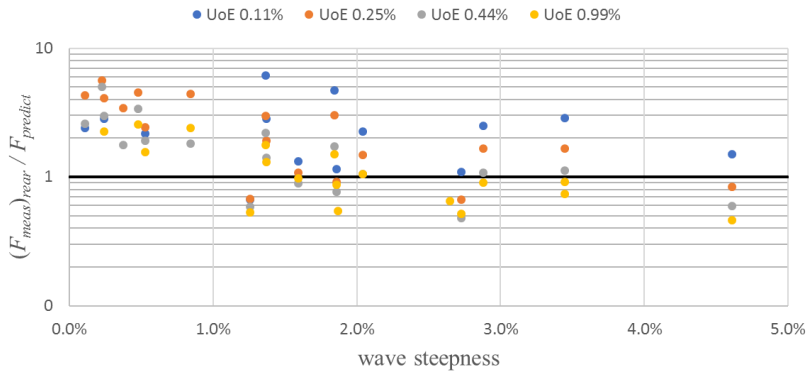

Figure 151 The measurement:prediction ratio of the in-chamber rear wall force for operating conditions at various opening:chamber ratio for the regular wave conditions vs wave steepness, small-scale measurements. The solid line represents the prediction model.

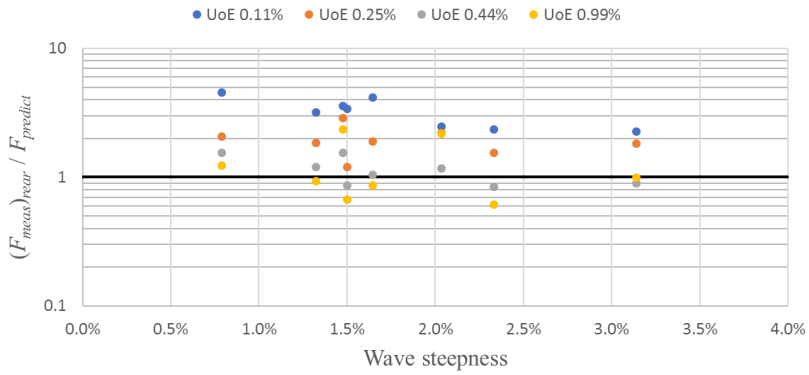

Figure 152 The measurement:prediction ratio of the in-chamber rear wall force for the operating chamber cases at various opening:chamber ratio for the irregular wave conditions vs wave steepness, small-scale measurements. The solid line represents the model prediction.

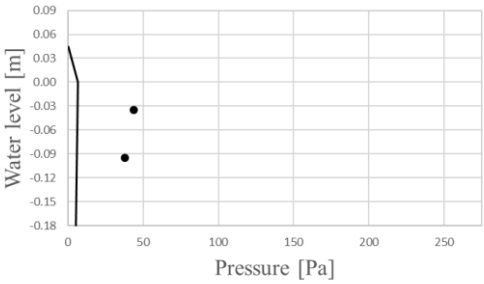
Water level [m]
0.09
0.06
0.03
0.00
-0.03
-0.06
-0.09
-0.12
-0.15
-0.18
0
50
100
150
200
250
Pressure [Pa]

(a)

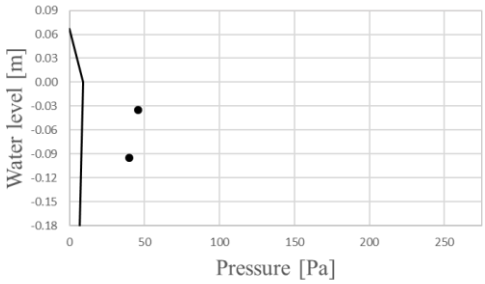
Water level [m]
0.09
0.06
0.03
0.00
-0.03
-0.06
-0.09
-0.12
-0.15
-0.18
0
50
100
150
200
250
Pressure [Pa]

(b)

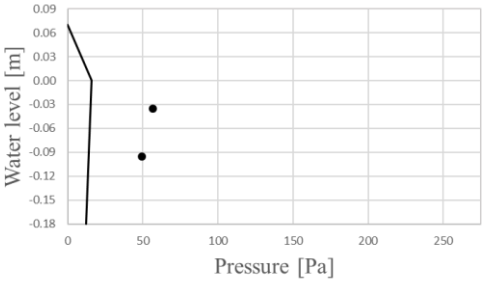
Water level [m]
0.09
0.06
0.03
0.00
-0.03
-0.06
-0.09
-0.12
-0.15
-0.18
0
50
100
150
200
250
Pressure [Pa]

(c)

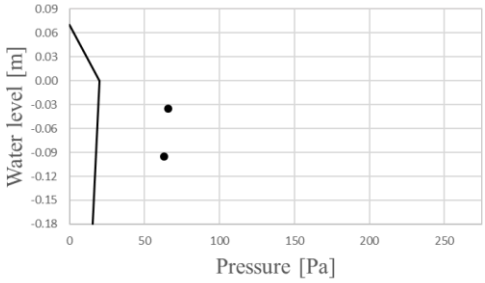
Water level [m]
0.09
0.06
0.03
0.00
-0.03
-0.06
-0.09
-0.12
-0.15
-0.18
0
50
100
150
200
250
Pressure [Pa]

(d)

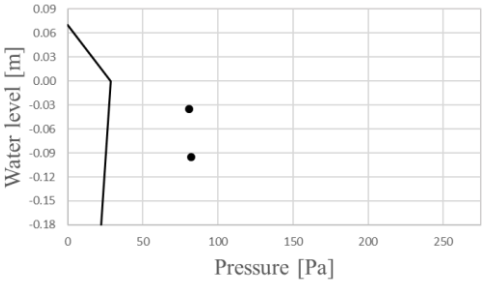
Water level [m]
0.09
0.06
0.03
0.00
-0.03
-0.06
-0.09
-0.12
-0.15
-0.18
0
50
100
150
200
250
Pressure [Pa]

(e)

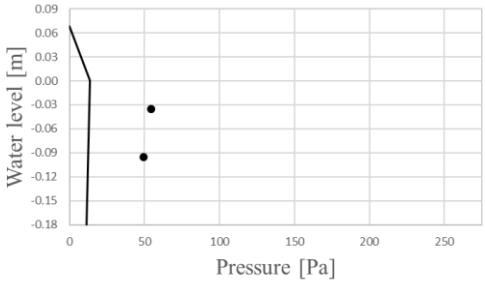
Water level [m]
0.09
0.06
0.03
0.00
-0.03
-0.06
-0.09
-0.12
-0.15
-0.18
0
50
100
150
200
250
Pressure [Pa]

(f)

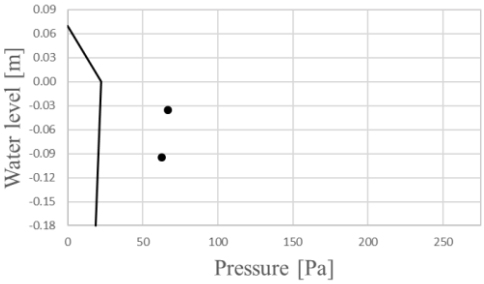
Water level [m]
0.09
0.06
0.03
0.00
-0.03
-0.06
-0.09
-0.12
-0.15
-0.18
0
50
100
150
200
250
Pressure [Pa]

(g)

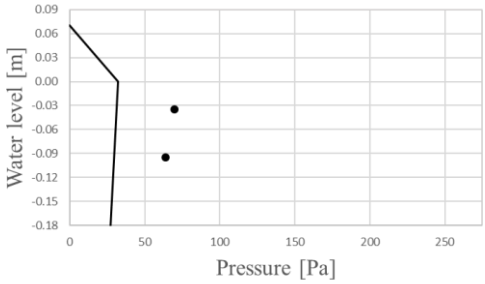
Water level [m]
0.09
0.06
0.03
0.00
-0.03
-0.06
-0.09
-0.12
-0.15
-0.18
0
50
100
150
200
250
Pressure [Pa]

(h)

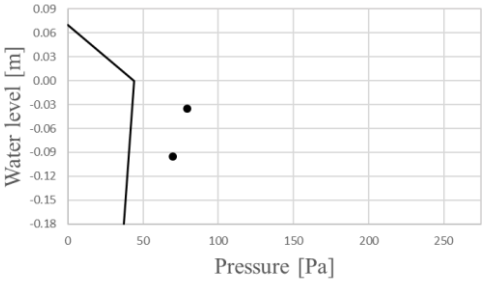

(i)

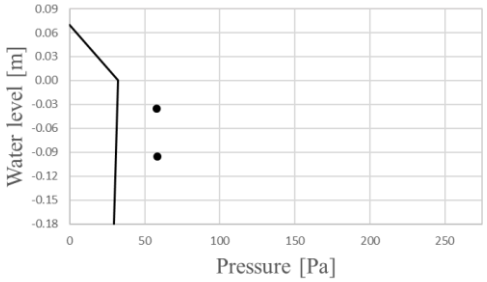

(j)

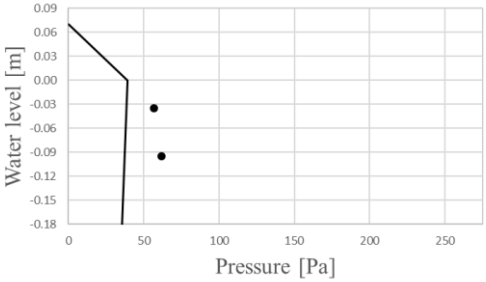

(k)

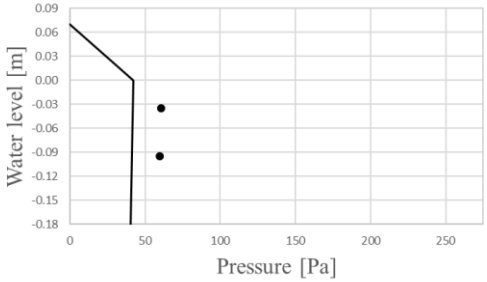

(l)

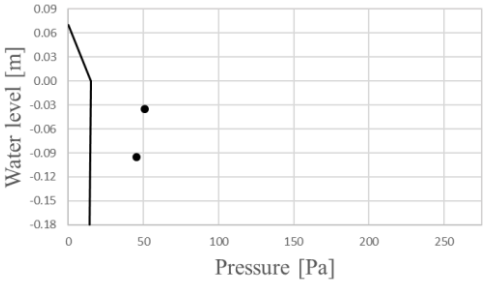

(m)

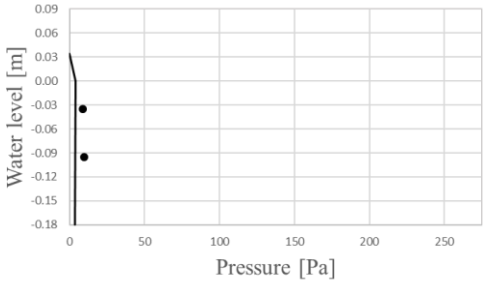

(n)

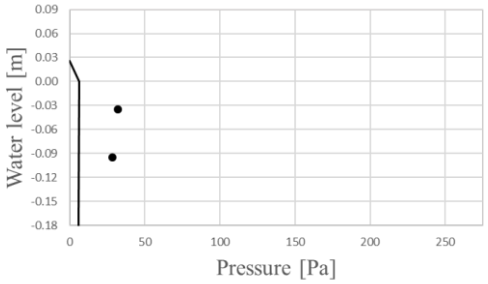

(o)

Figure 153(a)-(o) Measured (solid circle) and predicted (solid line) pressure distributions for operating case, 0.11% opening:chamber ratio, small-scale measurements, and regular wave conditions of: (a) Reg01, (b) Reg02, (c) Reg03, (d) Reg04, (e) Reg05, (f) Reg06, (g) Reg07, (h) Reg08, (i) Reg09, (j) Reg11, (k) Reg12, (l), Reg16 (m) Reg20, (n) Reg24, (o) Reg27.

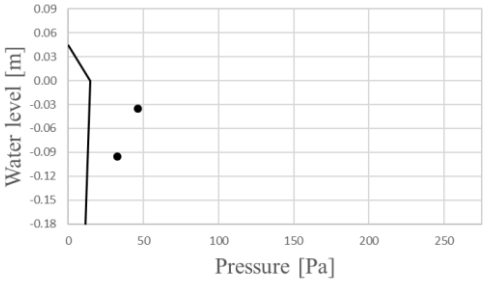
Water level [m]
0.09
0.06
0.03
0.00
-0.03
-0.06
-0.09
-0.12
-0.15
-0.18
0
50
100
150
200
250
Pressure [Pa]

(a)

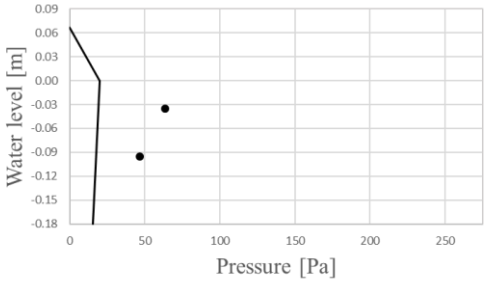
Water level [m]
0.09
0.06
0.03
0.00
-0.03
-0.06
-0.09
-0.12
-0.15
-0.18
0
50
100
150
200
250
Pressure [Pa]

(b)

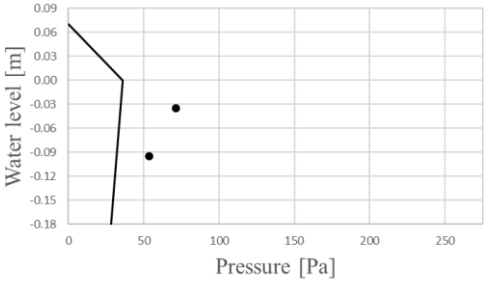
Water level [m]
0.09
0.06
0.03
0.00
-0.03
-0.06
-0.09
-0.12
-0.15
-0.18
0
50
100
150
200
250
Pressure [Pa]

(c)

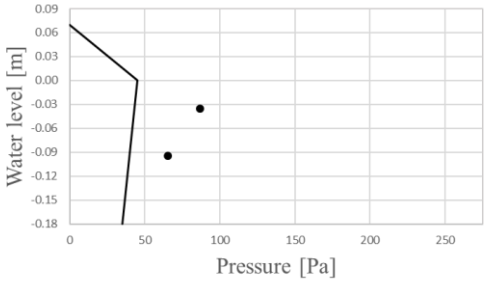
Water level [m]
0.09
0.06
0.03
0.00
-0.03
-0.06
-0.09
-0.12
-0.15
-0.18
0
50
100
150
200
250
Pressure [Pa]

(d)

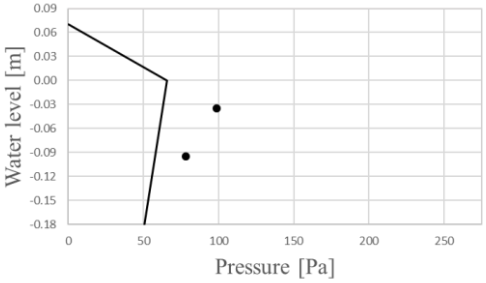
Water level [m]
0.09
0.06
0.03
0.00
-0.03
-0.06
-0.09
-0.12
-0.15
-0.18
0
50
100
150
200
250
Pressure [Pa]

(e)

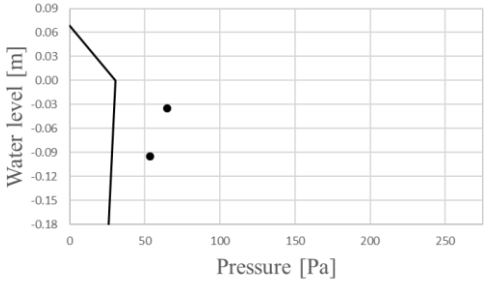
Water level [m]
0.09
0.06
0.03
0.00
-0.03
-0.06
-0.09
-0.12
-0.15
-0.18
0
50
100
150
200
250
Pressure [Pa]

(f)

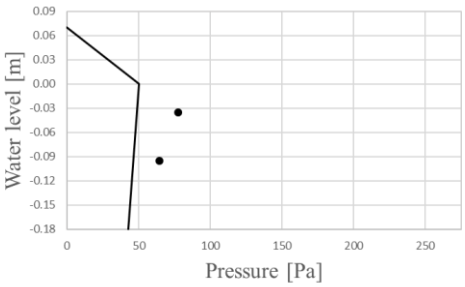
Water level [m]
0.09
0.06
0.03
0.00
-0.03
-0.06
-0.09
-0.12
-0.15
-0.18
0
50
100
150
200
250
Pressure [Pa]

(g)

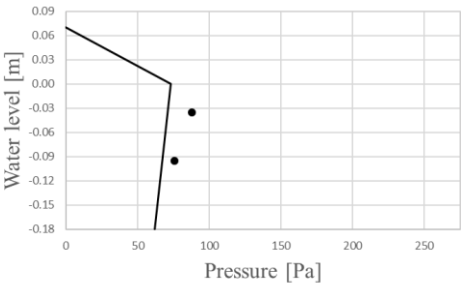
Water level [m]
0.09
0.06
0.03
0.00
-0.03
-0.06
-0.09
-0.12
-0.15
-0.18
0
50
100
150
200
250
Pressure [Pa]

(h)

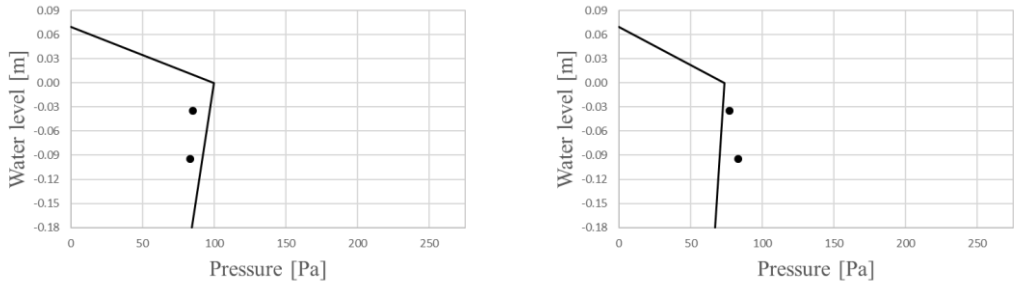

(i) (j)

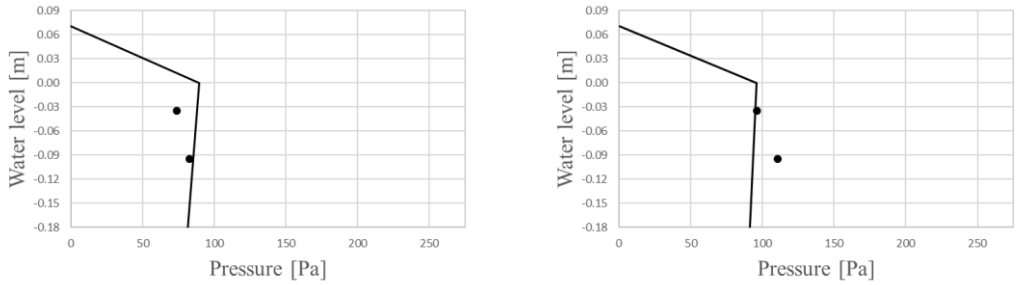

(k) (l)

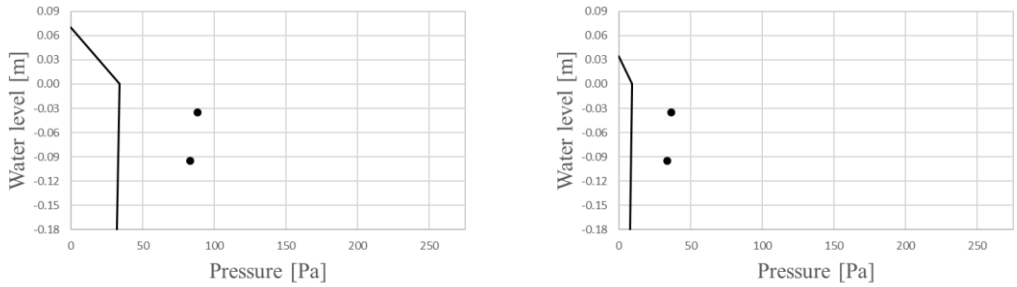

(m) (n)

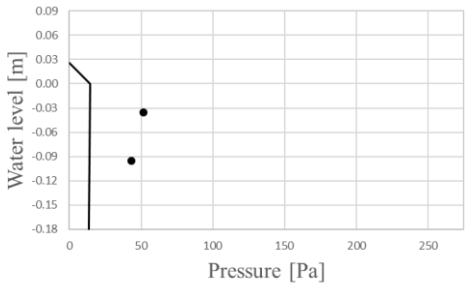

(o)

Figure 154 (a)-(o) Measured (solid circle) and predicted (solid line) pressure distributions for operating case, 0.25% opening:chamber ratio, small-scale measurements, and regular wave conditions of: (a) Reg01, (b) Reg02, (c) Reg03, (d) Reg04, (e) Reg05, (f) Reg06, (g) Reg07, (h) Reg08, (i) Reg09, (j) Reg11, (k) Reg12, (l), Reg16 (m) Reg20, (n) Reg24, (o) Reg27.

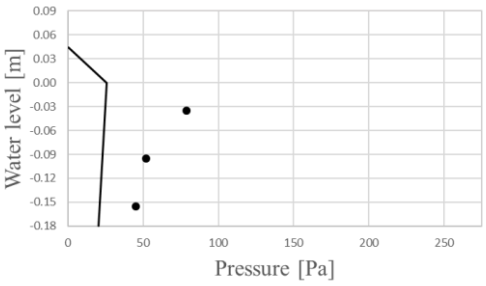
Water level [m]
0.09
0.06
0.03
0.00
-0.03
-0.06
-0.09
-0.12
-0.15
-0.18
0
50
100
150
200
250
Pressure [Pa]

(a)

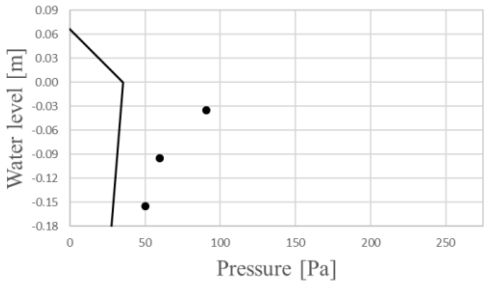
Water level [m]
0.09
0.06
0.03
0.00
-0.03
-0.06
-0.09
-0.12
-0.15
-0.18
0
50
100
150
200
250
Pressure [Pa]

(b)

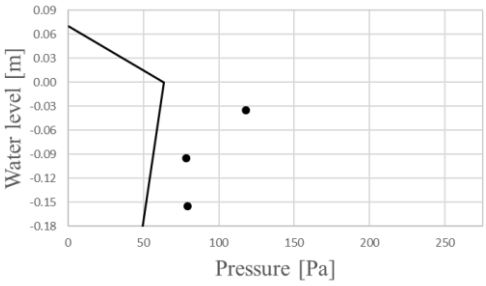
Water level [m]
0.09
0.06
0.03
0.00
-0.03
-0.06
-0.09
-0.12
-0.15
-0.18
0
50
100
150
200
250
Pressure [Pa]

(c)

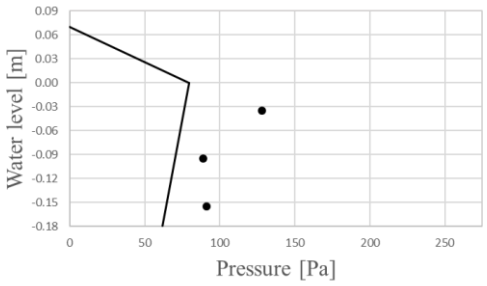
Water level [m]
0.09
0.06
0.03
0.00
-0.03
-0.06
-0.09
-0.12
-0.15
-0.18
0
50
100
150
200
250
Pressure [Pa]

(d)

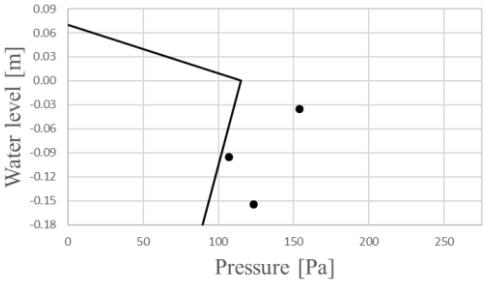
Water level [m]
0.09
0.06
0.03
0.00
-0.03
-0.06
-0.09
-0.12
-0.15
-0.18
0
50
100
150
200
250
Pressure [Pa]

(e)

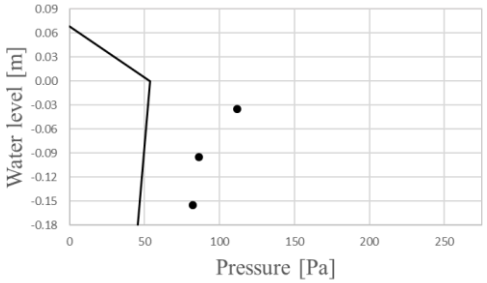
Water level [m]
0.09
0.06
0.03
0.00
-0.03
-0.06
-0.09
-0.12
-0.15
-0.18
0
50
100
150
200
250
Pressure [Pa]

(f)

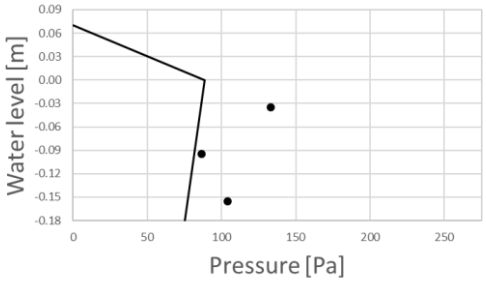
Water level [m]
0.09
0.06
0.03
0.00
-0.03
-0.06
-0.09
-0.12
-0.15
-0.18
0
50
100
150
200
250
Pressure [Pa]

(g)

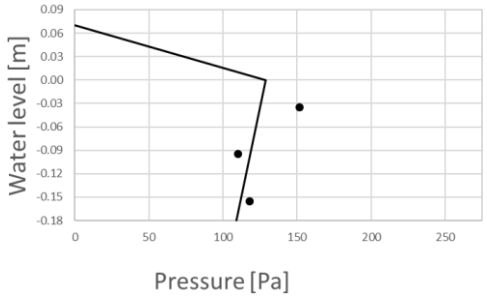
Water level [m]
0.09
0.06
0.03
0.00
-0.03
-0.06
-0.09
-0.12
-0.15
-0.18
0
50
100
150
200
250
Pressure [Pa]

(h)

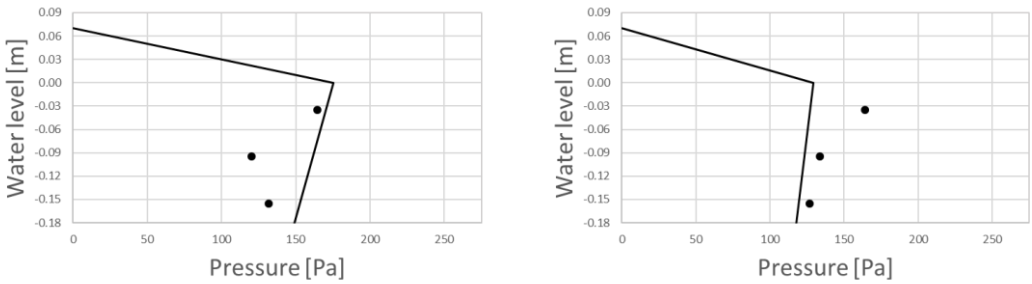

(i)

(j)

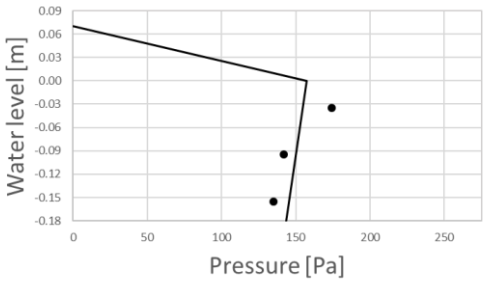

(k)

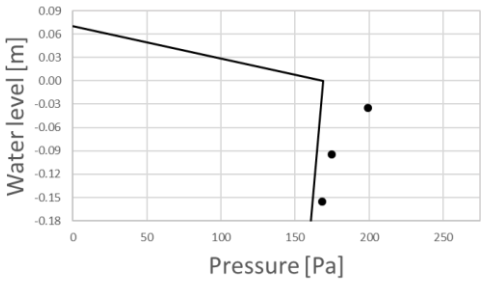

(l)

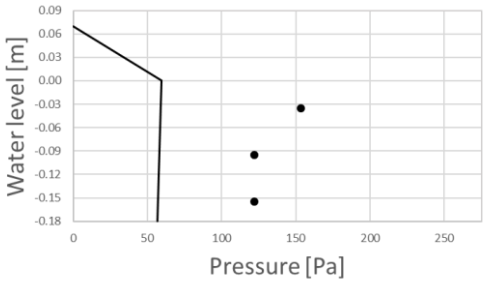

(m)

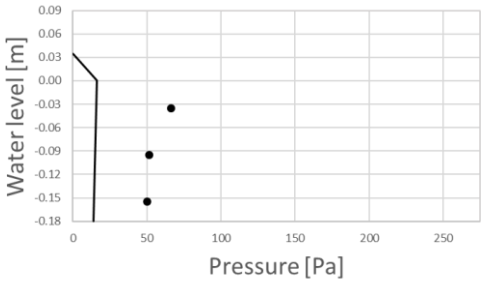

(n)

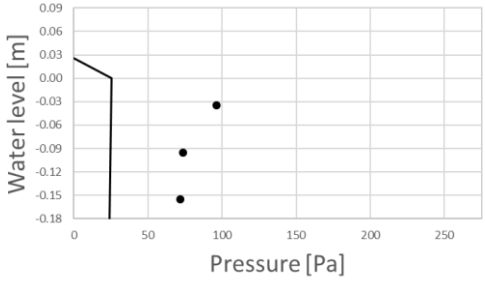

(o)

Figure 155 (a)-(o) Measured (solid circle) and predicted (solid line) pressure distributions for operating case, 0.44% opening:chamber ratio, and regular wave conditions of: (a) Reg01, (b) Reg02, (c) Reg03, (d) Reg04, (e) Reg05, (f) Reg06, (g) Reg07, (h) Reg08, (i) Reg09, (j) Reg11, (k) Reg12, (l), Reg16 (m) Reg20, (n) Reg24, (o) Reg27.

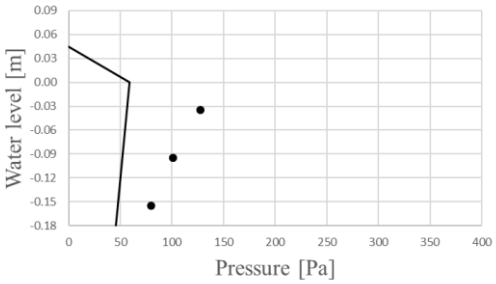
Water level [m]
0.09
0.06
0.03
0.00
-0.03
-0.06
-0.09
-0.12
-0.15
-0.18
0
50
100
150
200
250
300
350
400
Pressure [Pa]

(a)

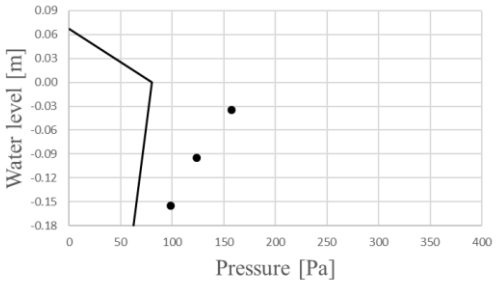
Water level [m]
0.09
0.06
0.03
0.00
-0.03
-0.06
-0.09
-0.12
-0.15
-0.18
0
50
100
150
200
250
300
350
400
Pressure [Pa]

(b)

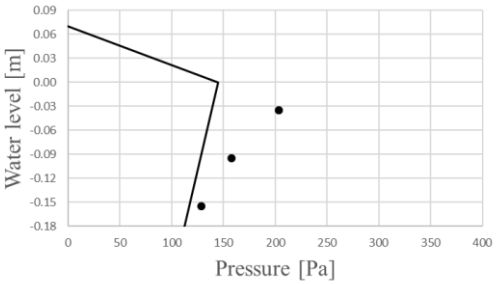
Water level [m]
0.09
0.06
0.03
0.00
-0.03
-0.06
-0.09
-0.12
-0.15
-0.18
0
50
100
150
200
250
300
350
400
Pressure [Pa]

(c)

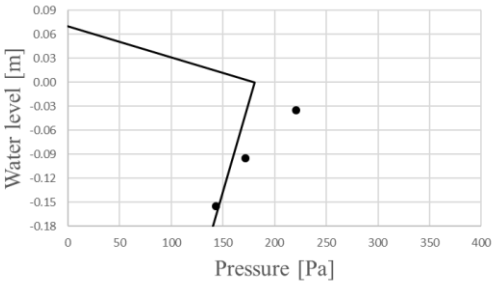
Water level [m]
0.09
0.06
0.03
0.00
-0.03
-0.06
-0.09
-0.12
-0.15
-0.18
0
50
100
150
200
250
300
350
400
Pressure [Pa]

(d)

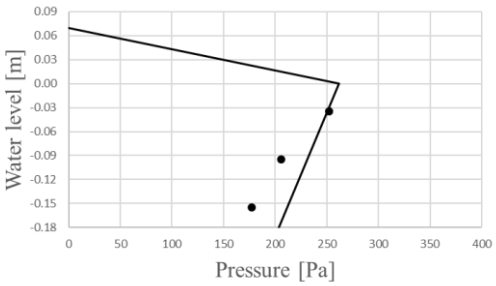
Water level [m]
0.09
0.06
0.03
0.00
-0.03
-0.06
-0.09
-0.12
-0.15
-0.18
0
50
100
150
200
250
300
350
400
Pressure [Pa]

(e)

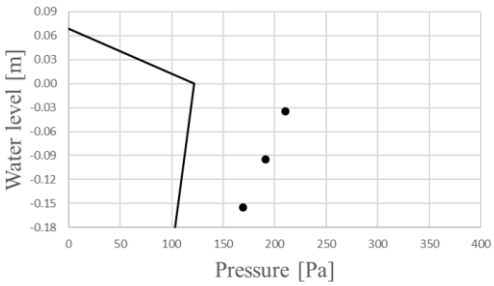
Water level [m]
0.09
0.06
0.03
0.00
-0.03
-0.06
-0.09
-0.12
-0.15
-0.18
0
50
100
150
200
250
300
350
400
Pressure [Pa]

(f)

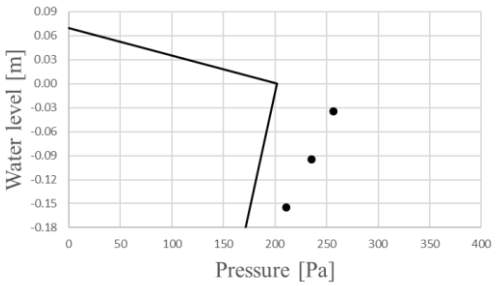
Water level [m]
0.09
0.06
0.03
0.00
-0.03
-0.06
-0.09
-0.12
-0.15
-0.18
0
50
100
150
200
250
300
350
400
Pressure [Pa]

(g)

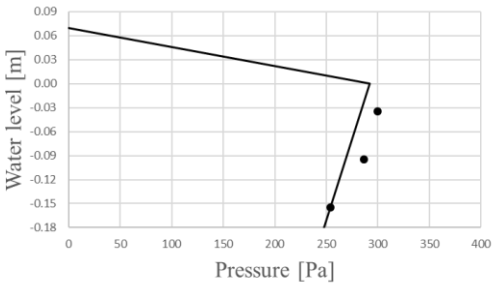
Water level [m]
0.09
0.06
0.03
0.00
-0.03
-0.06
-0.09
-0.12
-0.15
-0.18
0
50
100
150
200
250
300
350
400
Pressure [Pa]

(h)

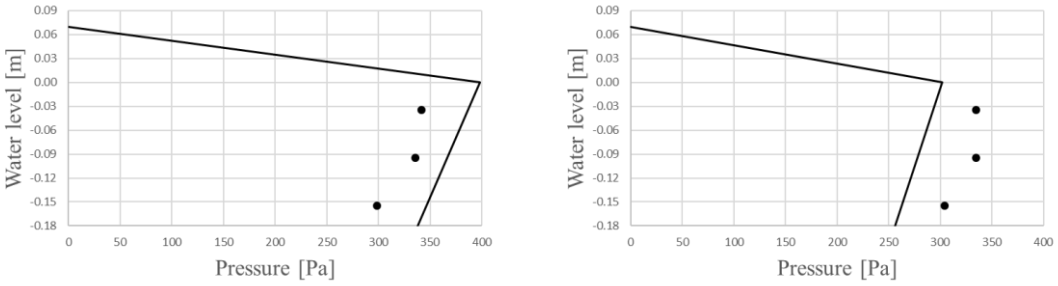

(i)

(j)

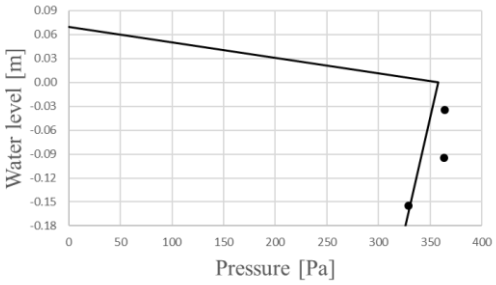

(k)

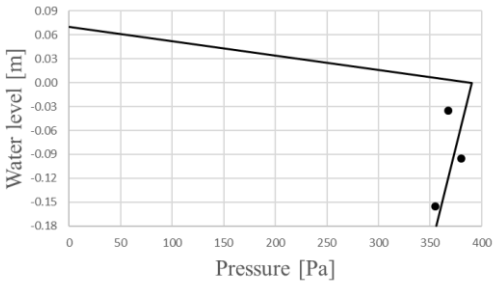

(l)

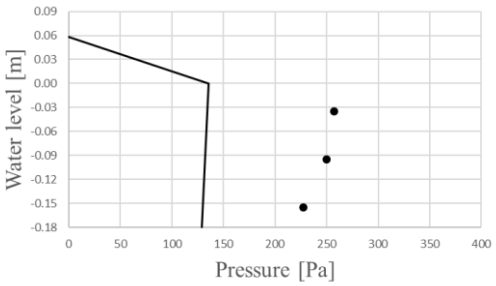

(m)

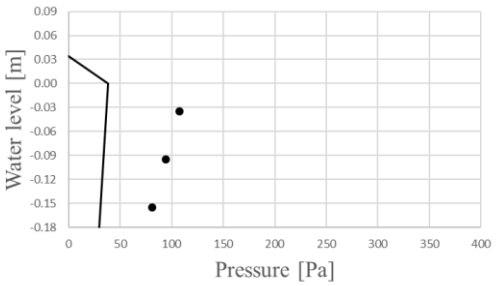

(n)

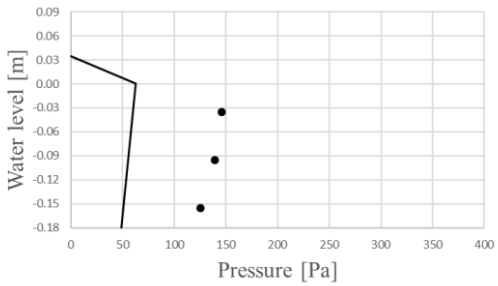

(o)

Figure 156 (a)-(o) Measured (solid circle) and predicted (solid line) pressure distributions for operating case, 1.0% opening:chamber ratio, and regular wave conditions of: (a) Reg01, (b) Reg02, (c) Reg03, (d) Reg04, (e) Reg05, (f) Reg06, (g) Reg07, (h) Reg08, (i) Reg09, (j) Reg11, (k) Reg12, (l), Reg16 (m) Reg20, (n) Reg24, (o) Reg27.

6.2.4 Vertical force calculation

Unlike a conventional vertical breakwater, the chamber inside an OWC installed vertical breakwater will have a vertical force acting on the ceiling generated by the air pressure. It is understood that the same air pressure will provide a counter force to the bottom of the chamber, thus nullifying the total force acting on the structure. This counter acting force, however, will not be available for the open bottom typed breakwater where the chamber floor is not part of the structure, making the calculation of the vertical force necessary. Furthermore, it is also necessary to ensure the chamber roof structure able to withstand the highest chamber pressure generated. One can imagine that the biggest air pressure inside the chamber occurs during the closed chamber case. A comparison between the closed and operating chamber cases for regular waves (Figure 157) supports this argument. Thus, the experiment:prediction vertical force comparison is presented in Figure 158 only for the closed chamber case and the results show that the prediction model has a good agreement for wave steepnesses between 1% and 4% ($1\% \leq s_w \leq 4\%$)with the small-scale measurements. For wave steepnesses outside these range, however, the prediction model under-estimates the less steep wave conditions ($s_w < 1\%$) and over-estimates the steeper one ($s_w > 4\%$).

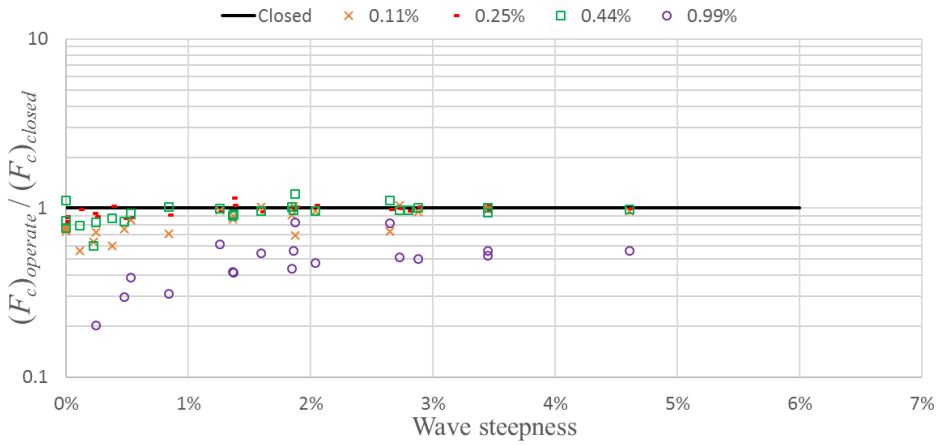

Figure 157 The closed:open chamber ratio comparison of the vertical force for the regular wave conditions at various chamber opening:area ratio, small-scale measurements. The solid line represents the closed chamber.

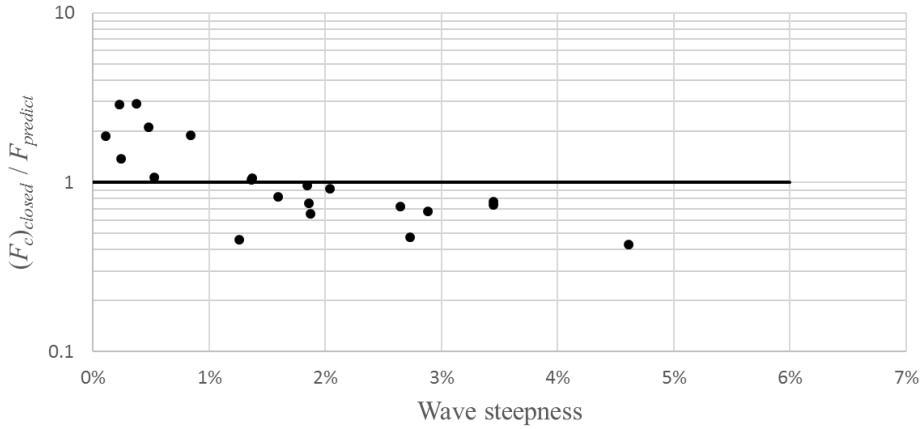

Figure 158 The measurement:prediction ratio of the vertical force for the closed chamber condition cases, regular wave conditions, small-scale measurements. The solid line represents the model prediction.

It is important to remember that the small-scale physical model is scaled down using Froude scaling method which keeps the ratio between the inertia force and gravity force of the model and the prototype. This scaling method, unfortunately, neglects the air stiffness similarity ratio between the scaled model and the prototype. Due to this, the air stiffness characteristic will not be scaled down correctly, except for the ratio equal to 1. It is expected for the physical model to over-estimate the actual pressure occurs on the prototype (Dimakopoulos, *et al.*, 2017).

6.3 Large-scale and small-scale physical model comparison

6.3.1 Large-scale and small-scale physical model dissimilarity

Before discussing the large-scale and the small-scale physical model comparison, it is important to note the difference between the two models. Although the small-scale set up was designed to be maximally similar to the earlier large-scale set up, some differences were inevitable, in wave generation, in the outer shape of the model, and in the instrumentations used. The large-scale experiments, as described in Chapter 3, used a piston type wave generator. This type of wave flume allows the water depth to be changed during the experiment, while the small-scale experiment utilised a flap type paddle wave generator which only calibrated for a single water depth.

For the physical dimensions of the structures, although the chamber dimensions are scaled down correctly following the Froude similitude requirements for reasons of structural strength, the large-scale model employed a separate front wall with the front wall height much higher than the chamber height. The location of the orifice opening was also a bit different. The orifice is located on the centre of the ceiling directly above the Oscillating Water Column (OWC) chamber for the small-scale model, whereas large-scale model orifice is located in the centre of a chimney, about 1.4 m above the OWC chamber. This condition leads to a slight addition on the air volume inside the OWC chamber for the large scale.

The experiments also had different foreshores. The small-scale used two different slopes of 1:10 and 1:16 and the large only used a single slope of 1:6 (for more detail see Chapter 3). The shape of the OWC chamber floor, furthermore, is also slightly different with the small-scale having the same inclination as the foreshore whereas the large-scale had a flat floor. These differences are borne in mind when appraising the comparison that follow.

For the instrumentations, the large-scale measurements quantified the pressure experienced by the front and rear wall using 5 pressure transducers (PTs) located below and above the still water level, whereas the small-scale set-up, only measured the wave pressure below the still water level using 3 PTs, due to the limitation of space. The chamber pressure was measured on the front part and rear part of the chamber using two PTs in the large-scale measurements whereas the small-scale measurements also utilised two PTs, with both located at the centre of the chamber ceiling, but at different lateral positions. Since the pressure generated inside the chamber is assumed to be uniform at all directions, the difference in chamber pressure PT locations between the large-scale measurements and the small-scale measurements should have minimal effect.

6.3.2 Large-scale and small-scale physical model comparison results

Figure 159 shows the measured chamber pressure comparison normalised by the hydrostatic pressure (ρgH) for the closed chamber case. The solid line represents the hydrostatic pressure. As can be seen from the figure, an inconsistent picture emerges.

The cases where the wave steepness is less than 2% show reasonable agreement between the scales, whereas the higher wave steepnesses (s_w > 2%) show that the large-scale tests suggesting much higher pressures than the corresponding small-scale tests. Since the hydrostatic pressure only uses the wave height without considering the front wall penetration, orifice:chamber area ratio condition, or the foreshore inclination, a different normalisation technique is explored in Figure 160. In the figure, both scales are normalised using the prediction model. This method is considered to be more appropriate since the prediction model take into account the chamber bottom shape, orifice:chamber area ratio, and foreshore inclination of the structure. As can be seen, these normalised pressure from large-scale and small-scale tests are close to 1, especially for the wave steepness equal to and bigger than 1%, with the small-scale measurements being approximately 0.9 times the large-scale measurements. This shows that the large-scale air chamber is very close to the incompressible condition of the small-scale air chamber under the closed chamber condition. The rear wall comparison between the two scale models is presented in Figure 161. In the figure, the small-scale is under-estimating the large-scale results by a factor of 0.83. The results show a strong resemblance with the chamber pressure comparison.

Figure 162 plots the force measured on the rear wall of the chamber for the fully open cases normalised using the prediction model. As can be seen, the results from the two scales are very similar. This is as anticipated because the air compressibility differences between the large-scale and the small-scale have the least effect for the fully open chamber.

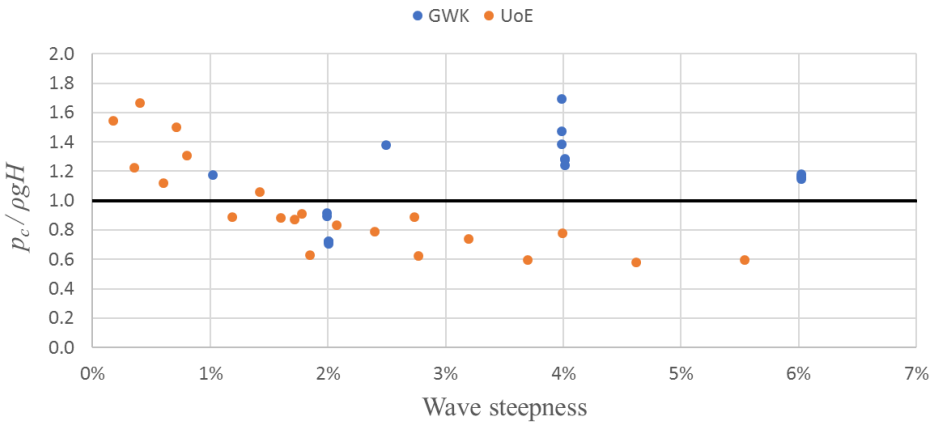

Figure 159 Chamber pressure comparison between the large scale (GWK) and the small scale (UoE) normalised using ρgH for the regular wave condition. Solid line represents the hydrostatic pressure (closed chamber).

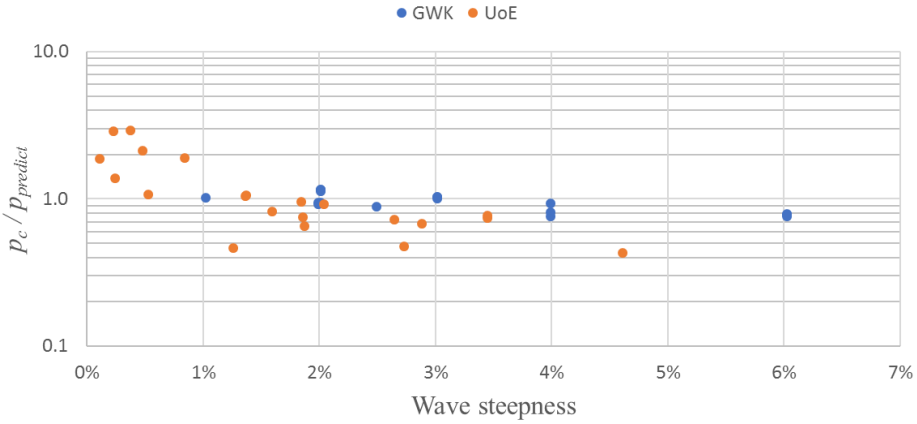

Figure 160 Chamber pressure comparison between the large scale (GWK) and the small scale (UoE) normalised using the prediction model (closed chamber), regular wave condition.

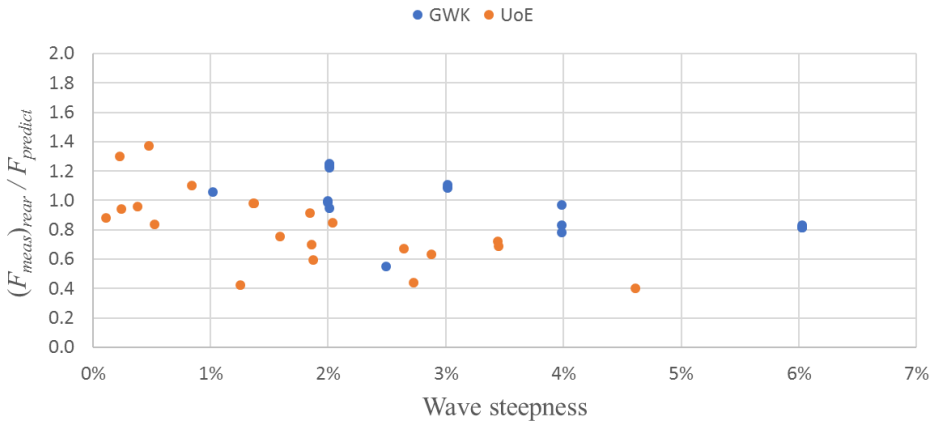

Figure 161 Rear wall landward scale comparison for closed chamber condition normalised using the prediction model, regular wave condition.

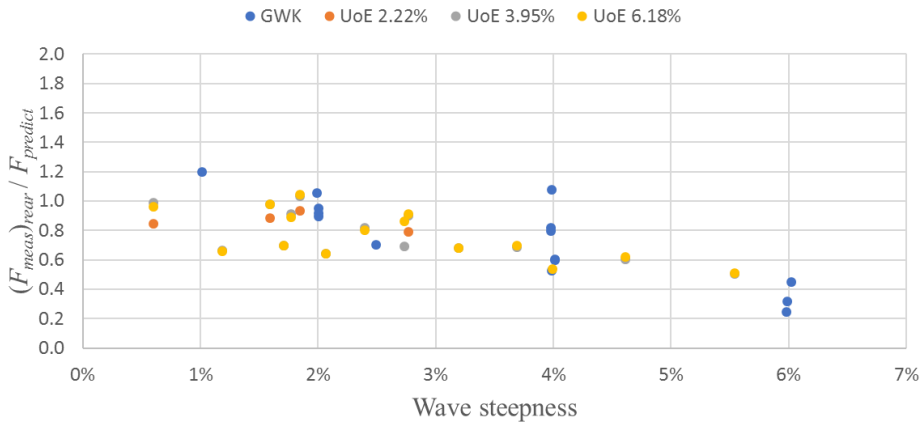

Figure 162 Landward rear wall force comparison between the large scale (GWK) and the small scale (UoE) for the fully-open chamber, normalised using the prediction model, regular wave condition.

Moving now to the operating condition, Figure 163 shows the comparison of measured chamber pressure between the large-scale and the small-scale, normalised using the prediction model. Because the operating chamber openings are different between the two scales, the operating condition comparison will be made based on the most efficient operating condition in each case. Figure 163 shows the large-scale measurement for opening:chamber area ratio of 0.9% since it is the most efficient settings based on the reflection analysis (Viviano *et al.*, 2016), and the small scale measurement for opening:chamber ratio of 0.44% as described in Section 6.1. The

comparison graph shows the small-scale measurements consistently higher than the large-scale data by a factor of 2.45. There does not appear to be any significant influence of wave steepness.

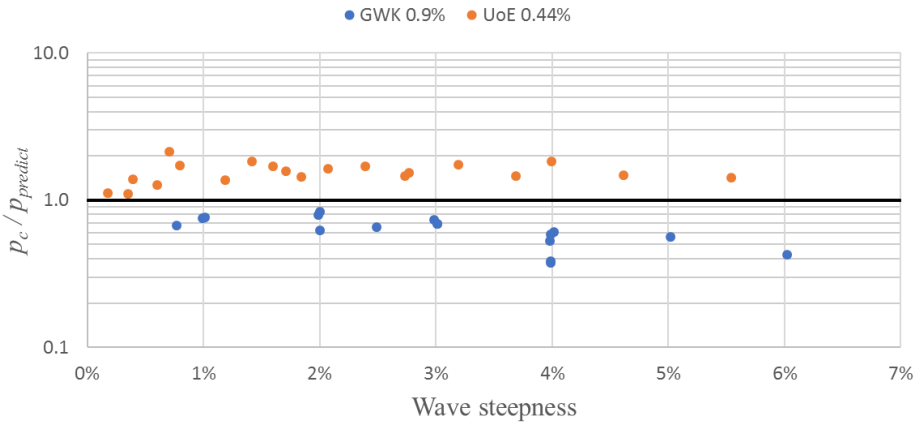

Figure 163 Chamber pressure comparison between the large scale (GWK) and small scale (UoE) for the operating chamber condition with opening:chamber area ratio of 0.9% for the GWK, and 1.0% for the UoE, regular wave condition.

Moving to irregular wave conditions, Figure 164 and Figure 165 show the scale comparison for the closed chamber and fully-open chamber respectively. As can be seen from the figures, the small-scale measurements exceed the large-scale measurements only by a factor of 1.16 for the closed chamber, with a very similar results for the fully open chamber. For the operating condition the chamber pressure comparison is plotted in Figure 166. The figure shows slightly closer agreement compared to the regular wave condition with the small-scale measurements exceeding the large-scale measurements by a factor of 2.00. It can be noted, however, that the large-scale results have a wider scatter compared to the small-scale one. The measured:predicted ratio, however, consistently less than the small-scale physical model measurements.

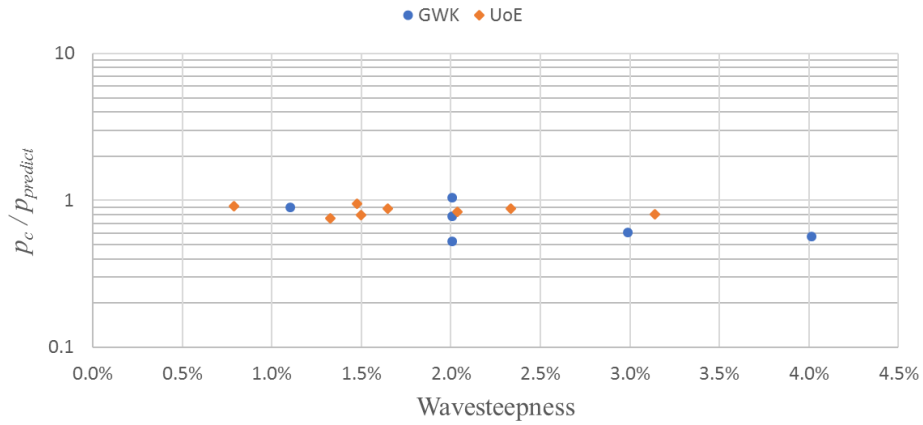

Figure 164 Ratio, chamber pressure measured:predicted, comparison between the large scale (GWK) and the small scale (UoE) normalised using the prediction model (closed chamber), the irregular wave condition.

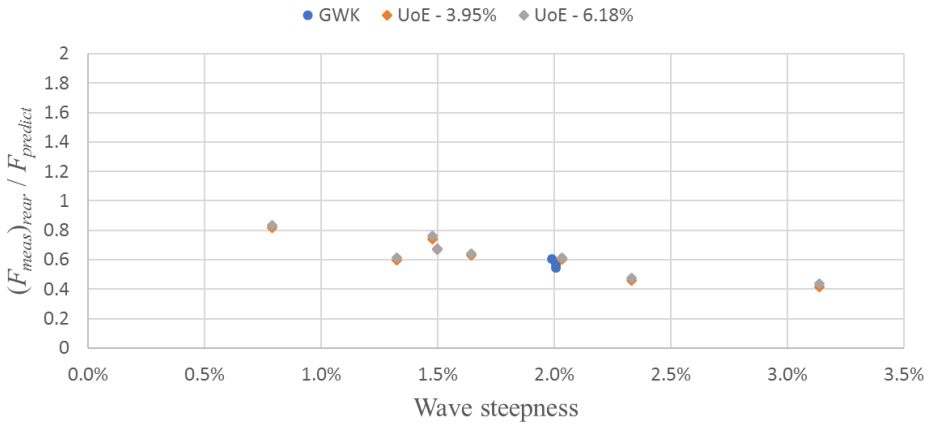

Figure 165 Rear wall force comparison between the large scale (GWK) and the small scale (UoE) for the fully-open chamber, normalised using the prediction model, irregular wave condition.

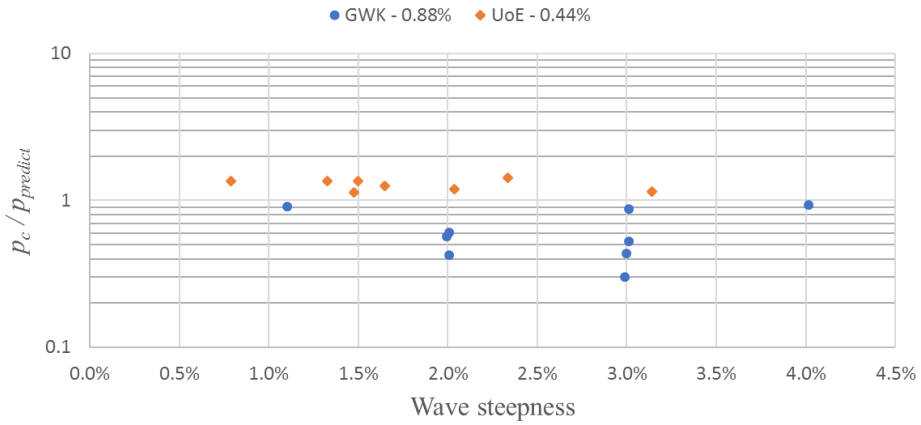

Figure 166 Ratio, chamber pressure measured:predicted, comparison between the large scale (GWK) and small scale (UoE) for the operating chamber condition with opening:chamber area ratio of 0.88% for the GWK and 0.44% for the UoE, irregular wave condition.

6.4 Scaling effect

Figure 163 and Figure 166 show that the operating condition of the small-scale measurements has a higher chamber pressure than the large-scale measurements by a factor between 2.00 - 2.45. This supports the hypothesis that small-scale measurements will over-estimate the prototype scale situation.

The results, however, show that the difference in air stiffnesses have minimal effect for the extreme, fully open chamber case because the air pressure in chamber remains very close to atmospheric. This argument is supported by Figure 162 and Figure 165 with both small-scale and large-scale measurements having overlapping results at wave steepness equal to 2%.

For the fully-closed case, the air compressibility is anticipated to have the most significant effect, Figure 160 and Figure 164, on the other hand, show that the small-scale results are higher compared to the large-scale for low wave steepness (s_w < 2%), very similar for wave steepness around 2%, and lower for higher wave steepness (s_w > 2%). These results show that even the large-scale air chamber may be close to an incompressible condition, similar to the small-scale physical model, for the wave steepness equal to and higher than 2%. This statement is supported for both regular

and irregular wave conditions. This result also supports the conclusion drawn by Dimakopoulos *et al.* (2017).

6.5 Bagnold number application for large-scale and small-scale model adjustment factor (λ)

Takahashi *et al.* (1985) and Takahashi (1988) employed the Bagnold number to predict the pressure increase due to impulsive loads on the front wall inside the wave dissipating chamber and OWC chamber respectively of a hybrid vertical breakwater. Although the method was intended for estimating the entrapped air influence of an impulsive load acting on a vertical breakwater, the idea of air compression due to impinging water mass is not dissimilar with the water column compressing the air chamber in an OWC device. This raises the possibility of the Bagnold number to be applied to calculate the chamber pressure generation maxima in an OWC chamber. Since the initial atmospheric chamber pressure (p_o) and water density (ρ) are the same, parameters *k, D,* and u_o need to be modified for the Bagnold number calculation.

The definition of effective water mass length (k) for this case is adopted from Takahashi *et al.* (1985) and defined as ¼ of an added mass of a plate with length equal to $2B_c$ *(See sub-section 2.6)*. The effective length of air chamber (D) is equal to the ceiling height (h_c) starting from still water level. For the water mass velocity (u_o), instead of the horizontal velocity of propagating wave, the water column vertical velocity considered in this case can be approximated as the incident (significant) wave amplitude (about half the incident wave height) divided by the duration needed for the water elevation to reach that point from still water level (about ¼ of the wave period) and as described in Equation 37.

$$u_o = \frac{2H_{inc}}{T} \tag{37}$$

Based on the large-scale and small-scale measurements observation discussed, the adjustment factor (λ) needed for the small-scale model to estimate the large-scale physical model is equal to the scaling factor 2.0 when the device is tuned to the most efficient wave conditions. Figure 167 shows the large-scale chamber pressure measurement under this condition (circular data point) and the chamber pressure

maxima predicted using small-scale Bagnold number and adjustment factor (dashed line).

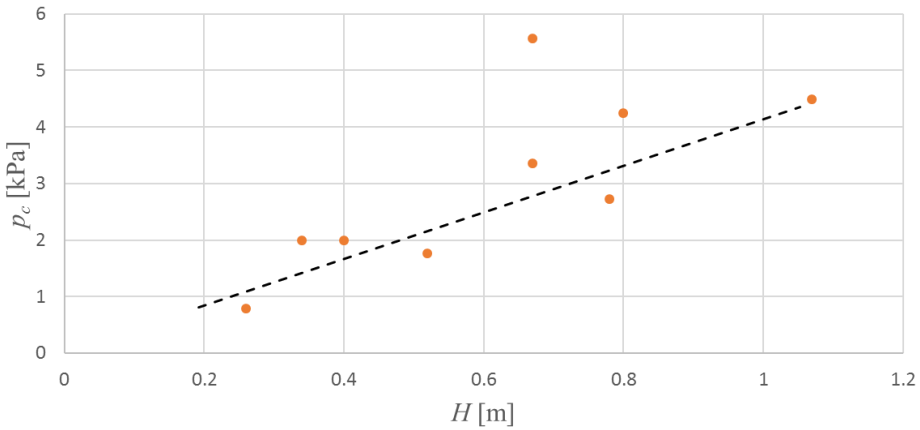

Figure 167 Small-scale chamber pressure Bagnold prediction adjustment factor (λ) of 2.00 (dashed line) compared to the large-scale measurement (circle).

As can be seen from the figure, with the exception of one test, the small-scale Bagnold number prediction has a good agreement with the large-scale measurements. It should be noted that the comparison was done based on the most efficient power-take off settings, and therefore not based on the same orifice:chamber area ratio. It is important to be noted that scaling factor equal to 2.00 is empirically obtained from a 1:9 scale physical model exploration and may be considered as a suggestion in up-scaling pressure measured during a small-scale model experiments.

7 Conclusion

A series of large-scale and small-scale experiments have been done in order to reduce the uncertainty in the design process of an Oscillating Water Column (OWC) installed in a vertical breakwater. A new prediction method to predict the OWC in-chamber vertical and horizontal wave loads has been developed by drawing comparison to the well-established methods in a conventional breakwater design and the method has been validated by means of large-scale measurements comparison *(see Chapter 4, with key Equations 8, 16, and 18).* Both non-impulsive and impulsive wave loads acting on the front wall of the OWC installed vertical breakwater have also been compared with the commonly used prediction methods in a conventional vertical breakwater (*see Chapters 5.1)*. Furthermore, the water column behaviour has been characterised and in-chamber impulsive wave loads have been characterised, classified and quantified by means of in-chamber video camera and pressure transducer (*see Chapter 5.2 and 5.3*). Finally, the large-scale measurements and the small-scale measurements have been compared to check the scaling effect in an OWC installed breakwater physical model testing (*see Chapter 6*).

(In-chamber loads) A new in-chamber loads method for the prediction of in-chamber rear wall and ceiling wave loads experienced by an OWC caisson has been presented. It is based upon the consideration of the physical processes at work, and where possible draws upon established models for conventional breakwaters. The model assumed the water column in the chamber to be well behaved and resulted in a non-impulsive wave load. The prediction model considers three OWC chamber regimes: the closed chamber condition, the fully open condition, and the operating condition. An empirical proportion coefficient, *P*, was introduced to determine the condition of the chamber based on the three chamber regimes considered.

Data from an earlier campaign of large-scale experiments carried out at the Large Wave Flume (GWK) in Hannover, Germany has been used to validate the model. Different orifice settings are deployed to represent the varying power take-off damping characteristics during operation. The model has been tested against multiple chamber conditions in regular waves. For both the chamber pressure measurement and the rear

wall force, the closed chamber model agreed very well with the proposed model, to a factor of 1±0.2 for all of the cases. For the fully open condition, the rear wall measurement:prediction shows somewhat greater scatter across the range of wave steepnesses. The prediction works better for the lower wave steepnesses (within a factor of 1.2) while at higher wave steepnesses, it gives a more conservative prediction with an agreement factor between 0.4 to 0.7. The chamber pressure measured:prediction comparison shows that the model is safer for the higher wave height and under-predicts for the lower wave height. The method works well for the wave steepness of 3% with an agreement factor of 0.9 ± 0.2. The vertical force measured:prediction ratio shows that the structure experience highest vertical force during the closed chamber condition under well behaved water column situation. Here, the method predicts the measured vertical force for the closed chamber to within a factor of 1 ± 0.2.

When the structure is exposed to irregular waves, the method slightly over-predicts the pressure measurements and inferred forces, with predictions lying within a factor between 0.6 to 0.8 for the closed chamber, fully open chamber, and operating conditions. These results indicate a conservative (safe) method. The prediction method can thus be employed as a design tool to predict the pressure distributions, total maximum landward horizontal forces, and caisson chamber vertical forces under non-breaking wave conditions. These parameter predictions can be incorporated into calculations for the over-turning moment and safety against sliding for the whole structure.

(Front wall wave loads) Established design tools for the prediction of wave loads acting on a conventional vertical breakwater were tested against the large-scale measurements of the front wall wave loads. The comparison was done for both non-impulsive and impulsive (breaking) wave loads. Under non-impulsive condition, a comparison between the measurements and Goda's prediction method show that introducing an OWC into a vertical breakwater resulted in a more conservative prediction with the measurement consistently being below the Goda predicted values.

The comparison was then done for impulsive wave loads. Impact force maxima and rise times were shown to follow the relationship proposed by Weggel and Maxwell

(1970). The magnitude and rise time relationship, however, shown to be different with the relationship in a conventional vertical breakwater as shown by Cuomo *et al.* (2010a). The front wall impact loads non-exceedance probability also follows Rayleigh distribution as for conventional vertical breakwater. A change in gradient, on the other hand, does not necessarily indicate a transition between non-impulsive wave loads and impulsive wave loads.

Because the elasticity characteristic of air trapped during an impulsive wave event will not scaled-down correctly in a scale measurement, an adjustment factor needs to be calculated based on the predicted prototype scale impact and the large-scale measurements. The predicted impact wave loads at prototype scale are determined based on Bagnold number (Bagnold, 1939). The result shows an adjustment factor (λ) of 5.3 needs to be used to predict the impact pressure in prototype scale if basing upon 1:9 scale test (as per GWK test here). This number is higher than 3.01 given by Takahashi *et al.* (1985).

The number of front wall impacts observed during the experiment is also compared with Calabrese and Vicinanza (1999)'s method to predict the proportion of wave breaking within an irregular wave train. Based on the results, it can be concluded that the impacts probability method developed for the conventional breakwaters can be used to predict the number of impacts experienced by an OWC installed vertical breakwater with good agreement.

(In-chamber water column behaviour) To check the behaviour of the in-chamber water column during operation, in-chamber video recording was utilised. The in-chamber water column movement can be classified into several intensity level, such as: well-behaved, low movement, medium movement, and violent movement conditions with in-chamber ceiling impacts observed during the violent movement condition. The observations showed that the violent water column movement is more likely to occur with the bigger orifice openings and with higher wave height. A very similar set of behaviour was observed in the equivalent small-scale physical model study. A "venting" phenomenon was also observed during both large-scale and small-scale physical model experiments as suggested by López, *et al.* (2015).

(In-chamber ceiling impacts) Next, the water column behaviour observation was extended to explore, qualitatively and quantitatively, the in-chamber ceiling impacts. The observations resulted in the characterisation of three different types of impact: (a) "single ceiling impact" on the front or the rear part of the ceiling, (b) "successional ceiling impacts" either from the front follow by the rear part of the ceiling or vice versa, and (c) "water column ceiling impact" where the whole water column rose and hit the ceiling. The results showed that "single ceiling impact" gives the highest impact pressures, followed by the "successional ceiling impacts". Recorded in-chamber impact pressure reached up to $12\rho gH$ during the large-scale measurements. When compared with the front wall impact force in the same event, it shows that the in-chamber ceiling impact pressure is at least comparable with that on the front wall.

(Small-scale physical modelling) After the development and validation of the new prediction method for the in-chamber wave loads, attention turned to the small-scale measurements. When compared to the small-scale measurements, the prediction method shows a relatively good agreement, under-estimating the pressures for smaller wave steepness wave conditions (s_w < 1%) and slightly over-estimating higher wave steepness (s_w > 1%) for both closed chamber and fully open conditions. For the operating condition, however, the small-scale tests consistently gave measurement on the upper (unsafe) side of the prediction, except for the largest orifice:chamber ratio (0.99%). This may happen because the small-scale OWC air chamber acts closer to an incompressible fluid compared to the prototype air chamber.

(Large-scale and small-scale comparison) Finally, the large-scale measurements were compared with the small-scale measurements. Both sets of measurements were normalised using the prediction method to minimise the influence of detailing, such as the chamber bottom shape, orifice:chamber area ratio, and foreshore slope. For the closed chamber, the small-scale generated similar normalised chamber pressures compared to the large-scale. The results were the same for both regular and irregular wave conditions. This shows that the large-scale air chamber is actually closer to incompressible during closed chamber condition, just like the small-scale air chamber. Since the chamber pressure generation is expected to be minimum in the fully open chamber condition, the wave loads acting on the structure should be scalable using

Froude scaling with minimum error from any air compressibility effect. The comparison of the large-scale and small-scale measurements of the in-chamber rear wall landward forces reflects this, with the normalised data showing very similar results with several data points over-lapped between the scales. These results supported the argument that the error in scale exploration mainly comes from the air compressibility scaling uncertainty. For the operating condition, the measurements are only compared for the most efficient orifice:chamber area ratio settings, which are the 0.44% for the small-scale measurements and the 0.9% for the large-scale measurements. The results show that the small-scale normalised pressures consistently exceed those measured in the large-scale tests by a factor of 2.45 for the regular wave conditions and by a factor of 2.00 for the irregular wave conditions.

References

Allsop, N.W.H., McKenna, J.E., Vicinanza, D. and Whittaker, T.T.J., 1997. New design methods for wave impact loadings on vertical breakwaters and seawalls. In *Coastal Engineering 1996* (pp. 2508-2521).

Allsop, N. W. H., Vicinanza, D., and McKenna, J. E., (1996). Wave Forces and Vertical and Composite Breakwater.HR Wallingford: Report SR 443. p. 40 – 41

Aqua-RET (2012) wave Technologies available at http://aquaret.com (Acessed at 14 may 2018)

Arena, F., Romolo, A., Malara, G., Fiamma, V. and Laface, V., 2017, June. The First Full Operative U-OWC Plants in the Port of Civitavecchia. In *ASME 2017 36th International Conference on Ocean, Offshore and Arctic Engineering* (pp. V010T09A022-V010T09A022). American Society of Mechanical Engineers.

Ashlin, S.J., Sundar, V. and Sannasiraj, S.A., 2017. Pressures and Forces on an Oscillating Water Column–Type Wave Energy Caisson Breakwater. *Journal of Waterway, Port, Coastal, and Ocean Engineering*, *143*(5), p.04017020.

Bagnold, R.A., 1939. Interim report on wave-pressure research. *Excerpt from the J. of the Institution of Civil Engineers*.

Barstow, S., Mørk, G., Mollison, D. and Cruz, J., 2008. The wave energy resource. In *Ocean wave energy* (pp. 93-132). Springer, Berlin, Heidelberg.

Boccotti, P., 2003. On a new wave energy absorber. *Ocean Engineering*, *30*(9), pp.1191-1200.

Boccotti, P., 2007. Comparison between a U-OWC and a conventional OWC. *Ocean Engineering*, *34*(5-6), pp.799-805.

Bourke, D. (2013). Wave Loading at Breakwater Integrated OWC. MSc. Report. University of Edinburgh.

Bullock, G.N., Obhrai, C., Peregrine, D.H. and Bredmose, H., 2007. Violent breaking wave impacts. Part 1: Results from large-scale regular wave tests on vertical and sloping walls. *Coastal Engineering*, *54*(8), pp.602-617.

Calabrese, M and Vicinanza, D., 1999. Estimation of proportion of impacts. 15 pp.

Cooker, M.J. and Peregrine, D.H., 1991a. A model for breaking wave impact pressures. In *Coastal Engineering 1990* (pp. 1473-1486).

Cooker, M.J. and Peregrine, D.H., 1991b. Violent water motion at breaking-wave impact. In *Coastal Engineering 1990* (pp. 164-176).

Cuomo, G., Allsop, W., Bruce, T. and Pearson, J., 2010a. Breaking wave loads at vertical seawalls and breakwaters. *Coastal Engineering*, *57*(4), pp.424-439

Cuomo, G., Allsop, W. and Takahashi, S., 2010b. Scaling wave impact pressures on vertical walls. *Coastal Engineering*, *57*(6), pp.604-609.

Dimakopoulos, A.S., Cooker, M.J. and Bruce, T., 2017. The influence of scale on the air flow and pressure in the modelling of Oscillating Water Column Wave Energy Converters. *International Journal of Marine Energy*, *19*, pp.272-291.

Evans, D.V. and Porter, R., 1995. Hydrodynamic characteristics of an oscillating water column device. *Applied Ocean Research*, *17*(3), pp.155-164.

Falcão, A.F. and Henriques, J.C., 2016. Oscillating-water-column wave energy converters and air turbines: A review. *Renewable Energy*, *85*, pp.1391-1424.

Falcão, A.F. and Henriques, J.C., 2014. Model-prototype similarity of oscillating-water-column wave energy converters. *International Journal of Marine Energy*, *6*, pp.18-34.

Faraci, C., Scandura, P. and Foti, E., 2014. Reflection of sea waves by combined caissons. *Journal of Waterway, Port, Coastal, and Ocean Engineering*, *141*(2), p.04014036.

Gabbatiss, J. (2018) "A 'hostile environment' for renewables: Why has UK clean energy investment plummeted?", Independent, 19 May. Available at:https://www.independent.co.uk/environment/uk-renewable-energy-investment-targets-wind-solar-power-onshore-a8358511.html (Accessed: 11 June 2019).

Goda, Y., 1975. New wave pressure formulae for composite breakwaters. In *Coastal Engineering 1974* (pp. 1702-1720).

Goda, Y., 2010. *Random seas and design of maritime structures* (Vol. 15). World Scientific Publishing Company.

Gomes, R.P.F., Henriques, J.C.C., Gato, L.M.C. and Falcão, A.D.O., 2011. Design of a floating oscillating water column for wave energy conversion. In *Proceedings of the 9th European Wave and Tidal Energy Conference, Southampton, UK*.

Hattori, M., Arami, A. and Yui, T., 1994. Wave impact pressure on vertical walls under breaking waves of various types. *Coastal Engineering*, *22*(1-2), pp.79-114.

He, F. and Huang, Z., 2016. Using an oscillating water column structure to reduce wave reflection from a vertical wall. *Journal of Waterway, Port, Coastal, and Ocean Engineering*, *142*(2), p.04015021.

Henriques, J.C.C., Cândido, J.J., Pontes, M.T. and Falcão, A.D.O., 2013. Wave energy resource assessment for a breakwater-integrated oscillating water column plant at Porto, Portugal. *Energy*, *63*, pp.52-60.

Hiroi, I., 1919. On a method of estimating the force of waves. *Memoirs of Engineering Facility, Imperial University of Tokyo*, *10*(1), p.19.

Hovart, E. (2009) Wave loading at coastal wave energy converters. MSc Disertation. University of Edinburgh

Hughes, S.A., 1993. *Physical models and laboratory techniques in coastal engineering* (Vol. 7). World Scientific.

Intergovernmental Panel on Climate Change (IPCC) fifth assessment synthesis report - Climate Change 2014 synthesis report (1 November 2014) by Myles R. Allen, Vicente R. Barros, John Broome, et al. edited by Paulina Aldunce, Thomas Downing, Sylvie Joussaume, et al.

Intergovernmental Panel on Climate Change (IPCC) - Special Report on Global Warming of 1.5ºC (7 October 2018). Incheon, Republic of Korea.

IRENA (International Renewable Energy Agency) (2014), Ocean energy technology: Innovation, Patents, Market Status and Trends, International Renewable Energy Agency, June 2014.

Jarlan, G.E., 1961. A perforated vertical wall breakwater. *The Dock and Harbour Authority*, (486), pp.394-398.

Jefferys, R. and Whittaker, T., 1986. Latching control of an oscillating water column device with air compressibility. In *Hydrodynamics of Ocean Wave-Energy Utilization* (pp. 281-291). Springer, Berlin, Heidelberg.

Kirkgöz, M.S., 1995. Breaking wave impact on vertical and sloping coastal structures. *Ocean Engineering*, *22*(1), pp.35-48.

Kisacik, D., Troch, P. and Van Bogaert, P., 2012. Experimental study of violent wave impact on a vertical structure with an overhanging horizontal cantilever slab. *Ocean engineering*, *49*, pp.1-15.

Kriebel, D.L. and Bollmann, C.A., 1997. Wave transmission past vertical wave barriers. In *Coastal Engineering 1996* (pp. 2470-2483).

Kofoed, J.P., Vicinanza, D. and Osaland, E., 2006, January. Estimation of design wave loads on the SSG WEC pilot plant based on 3-D model tests. In *Proc. 16th Int. Offshore and Polar Eng. Conf. International Society of Offshore and Polar Engineers*. San Fransisco.

Kuo, Y.S., Lin, C.S., Chung, C.Y. and Wang, Y.K., 2015. Wave loading distribution of oscillating water column caisson breakwaters under non-breaking wave forces. *Journal of Marine Science and Technology*, *23*(1), pp.78-87.

Laju, K., Sundar, V. and Sundaravadivelu, R., 2005. Studies on pile supported skirt Breakwater. In *Proceedings of the 1st International Conference on Coastal Zone Management and Engineering in the Middle East, Dubai, United Arab Emirates*.

López, I., Castro, A. and Iglesias, G., 2015. Hydrodynamic performance of an oscillating water column wave energy converter by means of particle imaging velocimetry. *Energy*, *83*, pp.89-103.

Ly, D.K., Aboobacker, V.M., Abundo, S.M.L., Srikanth, N. and Tralich, P., 2014, November. Wave energy resource assessment for Southeast Asia. In *Proceedings of the 5th International Conference on Sustainable Energy and Environment (SEE), Science, Technology and Innovation for Association of Southeast Asian Nations (ASEAN) Green Growth, Bangkok, Thailand* (pp. 19-21).

Malara G., Gomes R.P.F., Arena F., Henriques J. C.C., Gato L. M. C., Falão A. F. O., 2015.Hydrodynamic characteristics of a U_OWC plant: comparison between analytical and numerical results. In *Proceedings of the 11st European Wave and Tidal Energy Conference, Nantes, France*.

Mansard, E.P. and Funke, E.R., 1980. The measurement of incident and reflected spectra using a least squares method. In *Coastal Engineering 1980* (pp. 154-172).

Masuda, Y., 1986. An experience of wave power generator through tests and improvement. In *Hydrodynamics of ocean wave-energy utilization* (pp. 445-452). Springer, Berlin, Heidelberg.

McKenna, J. and Allsop, W., 1999. Statistical distribution of horizontal wave forces on vertical breakwaters. In *Coastal Engineering 1998* (pp. 2082-2095).

Medina-Lopez, E., Allsop, N.W.H., Dimakopoulos, A. and Bruce, T., 2015. Conjectures on the Failure of the OWC Breakwater at Mutriku. In *Proceedings of Coastal Structures and Solutions to Coastal Disasters Joint Conference, Boston, Massachusetts*.

Medina-López, E., Ferrando, A.M., Gilabert, M.C., Del Pino, C. and Rodríguez, M.L., 2016. Note on a real gas model for OWC performance. *Renewable Energy*, *85*, pp.588-597.

Mitsuyasu, H., 1967. Shock pressure of breaking wave. In *Coastal Engineering 1966* (pp. 268-283).

Monk, K. (2012) A review of the Pico project 2010 to 2012 - mistake, milestones, and the future [Press Release]. WavEc.

Morris-Thomas, M.T., Irvin, R.J. and Thiagarajan, K.P., 2007. An investigation into the hydrodynamic efficiency of an oscillating water column. *Journal of Offshore Mechanics and Arctic Engineering*, *129*(4), pp.273-278.

Müller, G. and Whittaker, T.J., 1995. Visualisation of flow conditions inside a shoreline wave power-station. *Ocean engineering*, *22*(6), pp.629-641.

Müller, G.U. and Whittaker, T.J.T., 1993. An investigation of breaking wave pressures on inclined walls. *Ocean engineering*, *20*(4), pp.349-358.

Oumeraci, H., 1994. Review and analysis of vertical breakwater failures—lessons learned. *Coastal Engineering*, *22*(1-2), pp.3-29. https://doi.org/10.1016/0378-3839(94)90046-9

Oumeraci, H., Kortenhaus, A., Allsop, W., de Groot, M., Crouch, R., Vrijling, H. and Voortman, H., 2001. *Probabilistic design tools for vertical breakwaters*. CRC Press.

Parkinson, Giles. “Oceanlinx Launches World's First 1MW Wave Energy Machine in S.A.” RenewEconomy, 25 Oct. 2013, reneweconomy.com.au/oceanlinx-launches-worlds-first-1mw-wave-energy-machine-s-88176/.

Patterson, C., Dunsire, R. and Hillier, S., 2010. Development of wave energy breakwater at Siadar, Isle of Lewis. In *Coasts, marine structures and breakwaters: Adapting to change: Proceedings of the 9th international conference organised by the Institution of Civil Engineers and held in Edinburgh on 16 to 18 September 2009* (pp. 1-738). Thomas Telford Ltd.

Poullikkas, A., 2014. Technology Prospects of Wave Power Systems. *Electronic Journal of Energy and Environment*. Vol. 2, No. 1. DOI 10.7770/ejee-V2N1-art662

Preen, S. and Robertshaw, G., 2010. Development of a generic caisson design for an oscillating water column power generator. In *Coasts, marine structures and breakwaters: Adapting to change: Proceedings of the 9th international conference organised by the Institution of Civil Engineers and held in Edinburgh on 16 to 18 September 2009* (pp. 2-266). Thomas Telford Ltd.

Quirapas, M.A.J.R., Lin, H., Abundo, M.L.S., Brahim, S. and Santos, D., 2015. Ocean renewable energy in Southeast Asia: a review. *Renewable and Sustainable Energy Reviews*, *41*, pp.799-817.

Renewables in Numbers 2019, accessed 07 May 2019 (https://www.scottishrenewables.com/forums/renewables-in-numbers/)

Sainflou, G. 1928. Essai sur les digues maritimes verticals. Annales des Ponts et Caausse'es. Paris 98, 11, pp: 5-48 (in French)

Sarmento, A.J. and Falcão, A.D.O., 1985. Wave generation by an oscillating surface-pressure and its application in wave-energy extraction. *Journal of Fluid Mechanics*, *150*, pp.467-485.

Setoguchi, T. and Takao, M., 2006. Current status of self rectifying air turbines for wave energy conversion. *Energy conversion and management*, *47*(15-16), pp.2382-2396.

Setoguchi, T., Takao, M., Kinoue, Y., Kaneko, K., Santhakumar, S. and Inoue, M., 1999, January. Study on an impulse turbine for wave energy conversion. In *The Ninth International Offshore and Polar Engineering Conference*. International Society of Offshore and Polar Engineers.

Sheng, W., Alcorn, R. and Lewis, A., 2013. On thermodynamics in the primary power conversion of oscillating water column wave energy converters. *Journal of Renewable and Sustainable Energy*, *5*(2), p.023105.

Smart, G., Noonan, M., (2018). Tidal stream and wave energy cost reduction and industrial benefit summary analysis. Catapult Offshore Renewable Energy.

Storm wrecks wave-power Osprey (1995) The Herald. 28 August

Takahashi, S., 1989. Hydrodynamic characteristics of wave-power-extracting caisson breakwater. In *Coastal Engineering 1988* (pp. 2489-2503).

Takahashi, S., Tanimoto, K. and Miyanaga, S., 1985. Uplift wave forces due to compression of enclosed air layer and their similitude law. *Coastal Engineering in Japan*, *28*(1), pp.191-206.

The Queen's University of Belfast. Islay Limpet Wave Power Plant [Publishable Report] 1 November 1998 to 30 April 2002

Tomiczek, T., Wyman, A., Park, H. and Cox, D.T., 2018. Application and modification of Goda formulae for nonimpulsive wave forces on elevated coastal structures. Coastal Engineering Proceedings, 1(36), p.48.

Torre-Enciso, Y., Ortubia, I., López de Aguileta, L.I. and Marqués, J., 2009, September. Mutriku wave power plant: from the thinking out to the reality. In *Proceedings of the 8th European wave and tidal energy conference, Uppsala, Sweden* (Vol. 710, p. 319329).

Vicinanza, D., Contestabile, P., Nørgaard, J.Q.H. and Andersen, T.L., 2014. Innovative rubble mound breakwaters for overtopping wave energy conversion. Coastal Engineering, 88, pp.154-170.

Viviano, A., Naty, S. and Foti, E., 2018. Scale effects in physical modelling of a generalized OWC. *Ocean Engineering*, *162*, pp.248-258.

Viviano, A., Naty, S., Foti, E., Bruce, T., Allsop, W. and Vicinanza, D., 2016. Large-scale experiments on the behaviour of a generalised Oscillating Water Column under random waves. *Renewable Energy*, *99*, pp.875-887.

WavEc-Offshore Renewables (2018) Press Release Pico Power Plant [Press release] 23 April 2018. Available at: pico-owc.net/news.php?cat=89&newid=346&wnsid=ffaedab643e41be91f9 eecf88f429ee8 (accessed at 14 May 2018)

Washio, Y., Osawa, H., Nagata, Y., Fujii, F., Furuyama, H. and Fujita, T., 2000, January. The offshore floating type wave power device" Mighty Whale": open sea tests. In *The Tenth International Offshore and Polar Engineering Conference*. International Society of Offshore and Polar Engineers.

Weber, J., 2007, September. Representation of non-linear aero-thermodynamic effects during small scale physical modelling of OWC WECs. In *Proceedings of the 7th European Wave and Tidal Energy Conference* (pp. 11-14).

Weggel, J.R., Maxwell, W.H.C., 1970. Experimental study of wave impact pressures. *Proceedings of the Second Annual Offshore Technology Conference, OTC 1244*, April 23–24, Houston, Texas.

Wiebe, D.M., Park, H. and Cox, D.T., 2014. Application of the Goda pressure formulae for horizontal wave loads on elevated structures. KSCE Journal of Civil Engineering, 18(6), pp.1573-1579.

Wintour, P. and Vaughan, A. (2015) "Tories to end onshore windfarm subsidies in 2016", The Guardian, 18 June. Available at: https://www.theguardian.com/environment/2015/jun/18/tories-end-onshore-windfarm-subsidies-2016 (Accessed: 11 June 2019).

Whittaker, T.J.T., Beattie, W., Folley, M., Boake, C., Wright, A., Osterried, M. and Heath, T., 2004. The Limpet Wave Power Project–the first years of operation. *Renewable Energy*.

World Energy Council (2017) World Energy Resources 2016. Available at: https://www.worldenergy.org/publications/2016/world-energy-resources-2016/ (accessed at 14 May 2018)